Universiteit Gent
Faculteit Ingenieurswetenschappen en Architectuur
Vakgroep Informatietechnologie

Colloïdale quantum dots als lichtbron voor geïntegreerde fotonica in silicium

Colloidal Quantum Dots as Light Emitters for Silicon Photonics

Bram De Geyter

Proefschrift tot het bekomen van de graad van
Doctor in de Ingenieurswetenschappen:
Natuurkunde
Academiejaar 2012-2013

Universiteit Gent
Faculteit Ingenieurswetenschappen en
Architectuur
Vakgroep Informatietechnologie

Promotoren:
prof. dr. ir. Dries Van Thourhout
prof. dr. ir. Zeger Hens

Jury:

prof. dr. ir. Daniël De Zutter (chairman)	Ghent University
prof. dr. ir. Dries Van Thourhout (promotor)	Ghent University
prof. dr. ir. Zeger Hens (promotor)	Ghent University
prof. dr. ir. Günther Roelkens (secretary)	Ghent University
prof. dr. ir. Roel Baets	Ghent University
prof. dr. ir. Edouard Brainis	Université Libre de Bruxelles
prof. dr. ir. Bruno Grandidier	Université de Lille 1
prof. dr. ir. Arjan Houtepen	Delft University of Technology
prof. dr. ir. Philippe Smet	Ghent University

Universiteit Gent
Faculteit Ingenieurswetenschappen en Architectuur

Vakgroep Informatietechnologie
Sint-Pietersnieuwstraat 41, B-9000 Gent, België

Tel.: +32-9-2643316
Fax.: +32-9-2643593

Proefschrift tot het behalen van de graad van
Doctor in de Ingenieurswetenschappen:
Natuurkunde
Academiejaar 2012-2013

Dankwoord

dankwoord...

Gent, augustus 2012
Bram De Geyter

Table of Contents

List of Acronyms

A

AB	Absorption Bleach
AFM	Atomic Force Microscopy

C

CA	Carboxylic Acid
CVD	Chemical Vapour Deposition
CW	continuous wave

D

DOE	Design Of Experiment

E

EDX	Energy Dispersive X-ray spectroscopy

F

FWHM	Full Width at Half Maximum
FSR	Free Spectral Range

H

HOMO	Highest Occupied Molecular Orbital

I

ICPMS	Inductively Coupled Plasma Mass Spectrometry

L

LUMO	Lowest Unoccupied Molecular Orbital

P

PA	Photoinduced Absorption
PbX	Abbreviation for the most common lead chalcogenide QDs. X replaces either S (sulphur), Se (selenium) or Te (tellurium)
PECVD	Plasma Enhanced Chemical Vapour Deposition
PL	photoluminescence

Q

QD	Quantum Dot
QY	Quantum Yield

R

RIE	Reactive Ion Etching
RF	Radio Frequent
rpm	rotations per minute

S

sccm	standard cubic centimeter per minute
SEM	scanning electron microscope
SILAR	Successive Ionic Layer Adsorption and Reaction

T

TA	Transient Absorption spectroscopy
TEM	Transmission Electron Microscopy

W

WGM	Whispering Gallery Modes

Nederlandse samenvatting –Summary in Dutch–

Het onderwerp van deze thesis staat aan de top van het snel groeiende onderzoeksgebied in de nanotechnologie. Dit multidisciplinaire werk brengt de *top down* aanpak van de geïntegreerde fotonica and de *bottom up* aanpak van het onderzoek naar colloïdale nanokristallen samen. De fotonica bestudeert de toepassingen van elementaire lichtdeeltjes of fotonen, net zoals de elektronica de toepassing van elektronen of elektrische stromen bestudeert. Daartoe behoren het genereren, het geleiden, het spectraal scheiden en detecteren van licht in het visueel of infrarood gebied van het elektromagnetische spectrum. Net zoals de verschuiving van de elektronica van aparte elektronische componenten naar geïntegreerde microelektronische chips, streeft de geïntegreerde fotonica naar het samenbrengen van complexe optische toepassingen op één chip. Volledig optische *transceivers* voor *fiber-to-the-home* internetdistributie, optische verbindingen voor communicatie tussen verschillende processorkernen, label-vrije biosensoren voor DNA en andere biochemische stoffen en gassensoren behoren tot de mogelijke toepassingen van geïntegreerde fotonica. Door het grote brekingsindexcontrast en de compatibiliteit van silicium met de huidige CMOS elektronica-industrie legt de *Photonics Research Group* zich toe op het maken van golfgeleiders en complexere optische componenten in silicium. Silicium en silicium-gebaseerde isolatoren hebben het nadeel dat er moeilijk licht mee te genereren valt. Daardoor moeten andere actieve materialen gecombineerd worden met de fotonische circuits in silicium om licht-emitterende diodes (LEDs) en lasers te maken.

Het vakgebied van de colloïdale nanokristallen bestudeert de synthese, de optische en elektrische eigenschappen en de toepassingen van halfgeleiderkristallen met een grootte van enkele nanometers. Door kwantumopsluiting hebben deze nanokristallen bijna atoomachtige energieniveau's. Bovendien is de energiespreiding tussen deze niveau's afhankelijk van de grootte van het nanokristal. Dit maakt dat de golflengte van de emissie

kan gekozen worden door de grootte van het nanokristal te controleren. Voor visuele toepassingen worden in de onderzoeksgroep *Fysica en Chemie van Nanostructuren* vooral cadmiumchalcogeniden (CdS, CdSe, CdTe) gebruikt, voor infrarode toepassingen zijn dit loodchalcogeniden.

Colloïdale *quantum dots* (QDs) zijn erg luminescente materialen met vaak bijna 100% kwantumefficiëntie. Dit, samen met de aanpasbaarheid van de emissiegolflengte met de QD grootte en het gemak van een materiaal dat in oplossing zit voor het verwerken ervan, maakt van colloïdale QDs de perfecte kandidaat voor heterogene integratie op de passieve fotonische circuits in silicium. Colloïdale QDs zijn zeer goede spontane emittoren, maar veel minder geschikt voor gestimuleerde emissie. In het regime waar gestimuleerde emissie winst oplevert — een noodzakelijke voorwaarde voor het maken van een laser — zijn de niet-radiatieve recombinatiemechanismen veel waarschijnlijker dan recombinatie door gestimuleerde emissie.

In deze multidisciplinaire thesis hebben we ons toegelegd op enkele grote hindernissen op de weg naar een competitieve en hoog-performante toepassing van colloïdale QDs in geïntegreerde fotonica.

Een eerste hindernis is het gebrek aan een fundamenteel begrip van de hete-injectiesynthese die gebruikt wordt om de meeste colloïdale QDs te maken. Een goed begrip van deze synthese is nodig om de eigenschappen van QDs op een meer intelligente en kostenbesparende wijze te ontwerpen en ontwikkelen. In dit werk onderzochten we de fysische chemie van de hete-injectiesynthese. We gebruikten daarvoor een theoretisch model voor de nucleatie en groei van deze deeltjes en breidden het uit naar een model dat ook rekening houdt met het genereren van monomeren uit de precursormoleculen. De resultaten van de numerieke simulatie van dit model kwamen zeer goed overeen met de dynamiek van een goed gekende experimentele CdSe synthese. Door simulaties en experimentele resultaten naast elkaar te leggen, konden we bewijzen dat de nucleatie- en groeisnelheid, en de balans tussen beide bepaald wordt door de snelheid waarmee de CdSe-monomeren gegenereerd worden uit de geïnjecteerde precursoren. Vermits de balans tussen nucleatie en groei ook de balans tussen QD concentratie en grootte bepaalt in een synthese waar meer dan 90% van alle precursoren opgebruikt worden, waren we in staat om een nieuwe strategie voor te stellen om de grootte van de QDs bij volledige precursoropbrengst te controleren door de precursorconcentratie te kiezen. We bekeken ook een tweede strategie om de grootte te controleren door de concentratie aan vrije vetzuren aan te passen. Meer vrije vetzuren zorgt voor grotere, maar een lager aantal deeltjes met een hogere spreiding op de grootte. Door eliminatie van an-

dere parameters, zoals de oppervlaktespanning en de adsorptiesnelheid van de monomeren, konden we de rol die vrije vetzuren speelt in het verhogen van de oplosbaarheid, identificeren.

Een tweede obstakel is de snelle niet-radiatieve recombinatiesnelheid van multiexcitonen in QDs. In de literatuur werd een mogelijk strategie voorgesteld om het probleem op te lossen, waarbij twee of meer halfgeleiders een heterostructuur vormen waarbij het elektron en het gat gescheiden worden in de ruimte. Wij onderzochten de optische eigenschappen van een nieuwe klasse PbSe/CdSe heterogestructureerde QDs. We vergeleken de lineaire absorptie van kern/schil QDs met meer conventionele PbSe QDs. We toonden aan dat de relatie tussen de golflengte en de grootte van de QD en de oscillatorsterkte voor absorptie ongewijzigd blijft na het aanbrengen van de CdSe schil. Daarentegen zorgt de verandering in de diëlektrische omgeving door de schil ervoor dat de absorptiecoëfficiënt bij energieën die ver boven de bandkloof liggen afhankelijk wordt van de verhouding tussen het volume van de schil en het volume van de hele QD. Verder bekeken we de eigenschappen van de spontane emissie van deze nieuwe deeltjes. De langere levensduur van de emissie wordt veroorzaakt door een lagere oscillatorsterkte van de emissie in vergelijking met PbSe QDs. Deze verlaging is waarschijnlijk een gevolg van de toegenomen fijnstructuur-splitsing van de achtvoudig ontaarde bandkloof door de CdSe-schil. We maakten ook gebruik van transiënte-absorptiespectroscopie om aan te tonen dat intraband absorptie toegelaten is in colloïdale QDs. De intraband absorptie van PbSe en PbSe/CdSe QDs draagt bij aan de moeilijkheid om transparantie en winst te bereiken in deze QDs. Beneden de bandkloof, tussen 1600 nm en 2200 nm, zou deze intraband absorptie wel kunnen gebruikt worden om verliesloze injectie te realizeren in optische modulatoren. Tot slot bekeken we ook het transiënte absorptiesignaal rond de bandkloof. De levensduur van de Auger-recombinatie is niet verlengd in PbSe/CdSe QDs ten opzichte van PbSe QDs. Verder konden we ook de vorm van het transiënte-absorptiespectrum begrijpen aan de hand van een gevuldetoestandenmodel, waarbij we ook rekening hielden met de effecten van verschuivingen van het spectrum door multi-excitonen en een verhoogde fijnstructuur-splitsing.

Voor de integratie van colloïdale QDs op fotonische circuits is de ontwikkeling van een platformtechnologie nodig die zorgt voor een stabiele integratie van de QDs die de optische eigenschappen bewaart en die de interactie van de QDs met de optische mode maximaliseert. Gezien de makkelijke controle over de emissiegolflengte bij colloïdale QDs, die het

golflengtebereik van 500 nm tot 2500 nm bestrijkt, maakten we gebruik van silicium nitride als golfgeleidermateriaal, omdat het transparant is in dit bereik. Om onze nieuwe platformtechnologie te testen, maakten we gebruik van visueel emitterende cadmium-gebaseerde QDs om vrijstaande *microdisks* te fabriceren. Deze QDs hebben immers verbeterde eigenschappen voor winst. We onderzochten de koppeling van de actieve QDs met de resonator door middel van QD-microdisk tempovergelijkingen. Hiermee konden we aantonen dat de hoeveelheid QDs die gekoppeld zijn met de caviteit een kritieke parameter is om een gepulste laser te maken. Het fabricageproces van de hybride microdisk werd door ons ontwikkeld en op punt gezet. Belangrijk was dat de photoluminescentie behouden bleef na depositie van silicium nitride op de QDs. Tot slot testten we de actieve microdisks met verschillende technieken. De QDs koppelden zeer goed met resonerende modes, maar de hoeveelheid QDs samen met de eigenschappen van de QD winst en de stabiliteit van de QD-silicium nitride lagen zijn onvoldoende om een QD-microdisk laser te maken.

English summary

The subject of this thesis is at the forefront of the booming field of nanotechnology. The multidisciplinary work is at the crossroads between the top down approach of integrated photonics and the bottom up approach of colloidal quantum dot research. The field of photonics studies the application of light quanta or photons in ways similar, but not limited to the mature field of electronics. It therefore deals with generating, transmitting, filtering and detecting light in the visible and infrared region of the electromagnetic spectrum. Similar to the shift of electronics from separate electronic components to integrated microelectronic chips, integrated photonics tries to realize complex optical functions on a single chip. Possible applications include all-optical transceivers for fiber-to-the-home internet distribution, optical interconnects for communication between separate microprocessor cores, label-free biosensing of DNA and other biochemical substances and gas sensing. Due to the large refractive index contrast and the compatibility of the material with the CMOS electronics industry, the *Photonics Research Group* focuses on making waveguides and more complex optical components on silicon based chips. Silicon itself and other silicon based materials have the drawback that it is difficult to generate light. As a consequence, other active materials need to be combined with silicon, which is known as heterogeneous integration, to fabricate light emitting diodes (LED) and lasers.

The field of colloidal nanocrystals studies the wet chemistry based synthesis, the optical and electrical properties and the application of these nanometer sized semiconductor crystals. Due to an effect known as quantum confinement, these nanocrystals have almost atomic like energy levels. Moreover, the separation between these energy levels is tunable with the size of the nanocrystal. This is most obvious in the transition between the band gap energy levels of the semiconductor, which emits light with a wavelength that is determined by the size of the nanocrystal. Here, the material system used is mostly focused on cadmium chalcogenides (CdS, CdSe, CdTe) for visible applications and lead chalcogenides for near-

infrared applications.

Colloidal QDs, synthesized in the proper way, are highly luminescent materials, with quantum yields (QY) often close to 100%. Together with tunability of the emission wavelength with size and the ease of a solution processable material make them ideal candidates for heterogeneous integration onto the passive silicon photonics platform with the aim of generating light. Colloidal QDs are very efficient spontaneous emitters. However as a stimulated emitter, specifically in the regime of gain, where a resonant beam of light is amplified — a necessary condition to make a laser — QDs are very inefficient, meaning that non-radiative pathways of losing the excess energy are very probable.

In this multidisciplinary thesis, we focus on a few major roadblocks on the way to competitive and high performance applications of colloidal QDs in integrated photonic circuits.

A first problem is the lack of fundamental understanding of the hot injection synthesis used to make most colloidal QDs. A profound understanding of this synthesis method is needed as a tool to engineer the properties of QDs in a smarter, more cost-effective and efficient way. We explored the physical chemistry of the hot-injection synthesis of colloidal QDs. We used a theoretical model of QD nucleation and growth and extended it to include the effect of the generation of monomer from precursor molecules. This model was solved numerically and the results of the simulation resemble the dynamics of a well established CdSe QD synthesis. By combining simulations with experimental results, we were able to prove that the rate of nucleation and growth and the balance between both are governed by the formation rate of CdSe monomer from the injected precursors. As the balance between nucleation and growth of the QDs determines the balance between QD concentration and QD size in a synthesis where more than 90% of the precursors are consumed, this result allowed us to explore a new strategy of tuning the size of QDs at full yield by simply changing the precursor concentration. We explored a second common strategy by changing the concentration of free acid in the synthesis. More free acid creates larger, yet less particles with higher size distributions. By eliminating other parameters, such as a change in the surface tension or the monomer adsorption rate, we identified the role of the free acids in raising the solubility of the monomer.

A second hurdle on the way to efficient hybrid colloidal QD-silicon light sources is the fast non-radiative recombination rate of multiexcitons. One possible strategy suggested in literature is the use of two or more semi-

conductors to form a heterostructure in which the electron and hole are spatially separated. We investigated the optical properties of a new near infrared emitting heterostructured PbSe/CdSe QD. We compared the linear absorption of PbSe/CdSe core/shell QDs with the more common PbSe parent QDs. We showed that the sizing curve and the absorption oscillator strength remain unaltered by the addition of a CdSe shell. However, the change in the local dielectric environment by the CdSe shell makes the absorption coefficient at energies well above the band gap dependent on the ratio between the shell volume and the total QD volume V_{shell}/V_{QD}. We further explored the spontaneous emission properties of highly luminescent PbSe/CdSe QDs ($QY \simeq 30 - 60\%$). We showed that the longer emission lifetime is caused by a lower emission oscillator strength compared to PbSe QDs. This reduction is more than likely due to an increased fine-structure splitting of the 8-fold degenerate bulk band gap because of the CdSe shell. We also used transient absorption spectroscopy to show that intraband absorption, forbidden in first order for bulk semiconductors, is allowed in colloidal QDs. The intraband absorption both in PbSe and PbSe/CdSe QDs contributes to the difficulty of achieving transparency and gain in these QDs, yet below the band gap, in the energy range between 1600 nm and 2200 nm, intraband absorption could be used for zero-insertion loss optical modulators. Finally we studied the transient absorption signal around the band gap. By extracting the Auger lifetime for PbSe/CdSe QDs we showed that Auger recombination is not reduced by the addition of the CdSe shell. We further explained the spectral shape of the bleaching signal using a state-filling model including the effects of multi-exciton shifts and increased fine-structure splitting.

Finally, combining colloidal QDs and integrated photonic circuits requires the development of a technology platform that allows a stable integration of the QDs, which preserves the optical properties and provides the maximum interaction with the optical field in the photonic circuits. Given the tunability of colloidal QDs, easily spanning a wavelength range from 500 nm to 2500 nm, we used silicon nitride, which is transparent in that range, as the material system for the integrated circuits. As a demonstrator of our technology platform, we used visibly emitting cadmium based QDs, which were shown to have improved gain properties, to fabricate free-standing microdisks. We investigated the coupling of the active QDs to the resonator using a QD-microdisk rate equation model. Here we showed that the amount of QDs coupled to the cavity is critical to making a pulsed colloidal QD laser. The fabrication flow of the hybrid microdisks was de-

veloped and optimized in house. We showed that the photoluminescence of the QDs remains after silicon nitride deposition. Finally we tested the active microdisks using several techniques. We showed that the QDs couple very well to the whispering gallery modes of the resonators, yet that the loading conditions, the gain properties and the stability of the QD-silicon nitride stack is insufficient to sustain QD-microdisk lasing.

1 Introduction

1.1 Introduction

1.1.1 Nanotechnology

The subject of this thesis is at the forefront of the booming field of nanotechnology. This field is driven by the need to do more — more transistors, more memory, more speed, more bandwith — with less — less material, smaller surface area, smaller form factors. Downsizing is the buzz word, with Moore's famous scaling law as its resounding mantra.

The quest for the ever smaller is not just about putting more transistors on the same microchip. As Moore cleverly realized, nature has set a limit to how far up — or how deep down — Moore's scaling law could go. It was Democritus about 2500 years before Moore who first hypothesized that all things were built up out of indivisible fundamental building blocks or literally atoms (from Greek, $\alpha\tau o\mu o\varsigma$). Although not entirely true, the limit of how far nanotechnology can go in scaling things down is precisely at this atomic level. When a common material, such as silicon, is brought down to a collection of just a few atoms, the properties of the bulk material are no longer valid. Quantum mechanics is needed to understand the new and exciting properties that arise when playing around with just a few of those fundamental building blocks, as wonderfully described in the seminal article *There's Plenty of Room at the Bottom* by Richard Feynman.[1] The visionary future of Feynman[1] is today's present, with a very

rich and broad research field centered around the common denominator of nanotechnology.

The nanometer sized objects that are simulated, fabricated and characterized in this field can be made in two ways, either by putting atom by atom together in a *bottom-up approach* or by cutting a larger block of material to nanometer size in a *top-down approach*. The research in this thesis is at the crossroads between both approaches, combining the field of colloidal quantum dots with integrated nanophotonic circuits.

1.1.2 Integrated Photonics

The field of photonics studies the application of light quanta or photons in ways similar, but not limited to the mature field of electronics. It therefore deals with generating, transmitting, filtering and detecting light in the visible and infrared region of the electromagnetic spectrum. It ranges from very practical applications of light as waves in optical components for the telecommunication industry to theoretical studies of light as particles in quantum cryptography.

Similar to the shift of electronics from separate electronic components to integrated microelectronic chips, integrated photonics tries to realize complex optical functions on a single chip. Possible applications include all-optical transceivers for fiber-to-the-home internet distribution[2], optical interconnects for communication between separate microprocessor cores[3], label-free biosensing of DNA[4] and other biochemical substances and gas sensing[5].

To realize these optical functions on a chip, waveguides are etched into the chip, which by total internal reflection not only confine the light, but guide it around bends and corners. This very basic building block is used to make more advanced components. The most important photonic building blocks are ring resonators, where a ring-shaped waveguide provides the necessary interference to create a very sharp optical filter. Periodic patterns, known as gratings, can be etched in the surface of a waveguide. The coherent scattering from these gratings can send the light in a very specific direction, depending on the wavelength of the light. Gratings are therefore used to couple light in and out of the optical chip to characterize the performance of the optical circuits on the chip.

More than by application, the research of integrated photonics is focused on a specific material used for the optical chip. Therefore, the term *silicon photonics* refers to integrated photonics in silicon. Compared to III-V materials and polymers, silicon has the advantage of having a high refractive index, and hence a high refractive index contrast with both glass

and air, which makes the typical dimensions of the photonic circuit smaller. Moreover, as the preferred material system in the electronics industry, it is fully compatible with the fabrication techniques and facilities used in the mature microelectronics industry and can easily be combined with electronics for richer, more complex applications. The drawback is that silicon is a passive material, meaning that light generation and nonlinear phenomena are inefficient and difficult to achieve. Moreover, silicon is not transparent in the visible range of the electromagnetic spectrum. To solve this latter issue, the field of silicon photonics very recently broadened to include silicon nitride (Si_3N_4) as the material guiding light.

Heterogeneous Integration

To solve the former issue, research has attempted to integrate other active materials on silicon photonic circuits. For the specific application of light generation, significant advances have been made by bonding active III-V chips to the top of a silicon photonic circuit.[6] The success of electrically pumped III-V microdisk lasers coupled to a silicon photonic circuit[7] have made them the work horse of today's silicon photonic circuits. However, the field is still very active, with different designs, working principles and active materials being explored. It is in this philosophy that we look into colloidal quantum dots (QD) as an alternative material for light generation on the silicon photonics platform.

1.1.3 Colloidal Nanocrystal Quantum Dots

What's in a name?

Eventhough the use and application of colloidal nanocrystals goes back thousands of years, it is only until recently — with the advent of nanotechnology — that advances were made to understand, control and engineer these tiny crystals. Brus *et al.*[8;9] and Efros *et al.*[10;11] pioneered the field by studying semiconductor clusters of few hundred to thousand atoms. Eventhough their size was in the 1 to 10 nm range, the atoms still arranged themselves on the regular bulk lattice of the crystal and hence they were called *nanocrystals*. The electronic properties did differ from the bulk crystal. They noticed that the band gap energy shifted towards higher energies (or shorter wavelengths) with decreasing size, an effect known as *quantum confinement*. As such the small nanoscale spherical crystals were coined *quantum dots*. Brus studied colloidal QDs, *i.e.* dispersed in a solvent, while Efros focused on quantum dots in glass solid matrices. It was not until 1993

with the work of Murray, Norris and Bawendi that the modern way of making colloidal nanocrystal QDs *via hot injection* of organo-metallic cadmium chalcogenide precursors was born.[12] This leap forward in the wet chemical synthesis of QDs delivered high quantities of monodisperse (*i.e.* all of similar size) QDs, which were easily tunable in size, absorption and emission wavelength and opened up a completely new field of research on the synthesis[13;14], surface chemistry[15], optical[16], electrical properties[17] and applications of colloidal nanocrystal QDs.[18]

Quantum Confinement

As we confine the movement of an electron to only a few hundred atoms, the quantum confinement will become noticeable below a size known as the *Bohr radius* of the electron. Confining the electron to an infinite spherical potential well leads with the Schrödinger equation to a well known quantized increase of the energy of the electron:

$$E_{well} = \frac{\hbar^2 \beta_{nl}^2}{2m_e L^2} \tag{1.1}$$

Here β_{nl} are the nth roots of the spherical bessel function of the first kind j$_l$(x), n and l are integer quantum numbers, m_e is the electron mass and L is the dimension of the spherical well. Note that a series of discrete energy levels are created within the potential well and the energy spacing of the levels reduces with increasing energy.

In a semiconductor nanocrystal this confinement energy is added to the band gap energy of the electron (or hole) in the bulk semiconductor. Moreover, the confinement of the electron and hole to a small volume leads to non-negligible Coulomb interaction between the electron and hole, and the electron or hole with its own image charge. This usually results in a net-attraction of electron and hole into a quasi-particle known as an *exciton*. This bound electron-hole pair typically has a lower energy. These contributions were summarized by Brus[8] into the *sizing curve* relating energy to QD size:

$$E(R) = E_g + \frac{\hbar^2 \pi^2}{2\mu_{ex} R^2} - \frac{1.8e^2}{4\pi\epsilon R} \tag{1.2}$$

Here $1/\mu_{ex} = 1/m_e^* + 1/m_h^*$ is the effective exciton mass, e is the fundamental charge and ϵ is the dielectric constant of the medium. For small sizes, the confinement energy dominates, resulting in an increasing energy with decreasing diameter. This tunability of the first exciton energy is nicely illustrated by the emission colour of a series of differently sized QDs (see Figure 1.1).

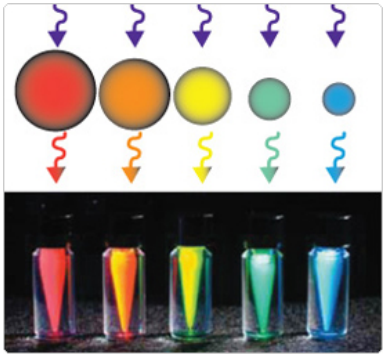

Figure 1.1: Emission colour of a series differently sized CdSe QDs under illumination with a UV lamp shows the effect of quantum confinement.

Types of Colloidal Quantum Dots

From the first CdSe QDs, the field of colloidal semiconductor QDs has significantly advanced. Differents sizes, shapes (dots, rods[19], tetrapods[20], sheets[21],...) and combinations[22;23] of CdX (X=S, Se, Te) in the visible range of the spectrum and PbX in the infrared range of the spectrum dominate the library of materials available today. The toxicity of cadmium and lead are currently driving the field into different material systems, such as CIGS[24] (copper indium gallium selenide/sulfide compounds) or CZTS[25] (copper zinc tin selenide/sulfide). However the main driving forces remain: a material with tunable optical and electrical properties that is easy to make and solution processable. The applications include bio-imaging[26], solar cells[27], light generation for lasers[28] and light-emitting diodes[29;30], nonlinear switching[31] and light detection[32].

1.2 Definition of the Problem

Colloidal QDs, synthesized in the proper way, are highly luminescent materials, with quantum yields (QY) often close to 100%. Together with the tunability of the emission wavelength with size and the ease of a solution processable material make them ideal candidates for heterogeneous integration onto the passive silicon photonics platform with the aim of generating light.

Light generation by a material is a conversion process, where energy is transferred to the material, either by optical pumping (*i.e.* the absorption of a pump photon) or by electrical pumping (*i.e.* the injection of an electron

and/or hole) and subsequently released again by the emission of a photon with an energy specific for that material. The emission process can be either spontaneous or stimulated by another photon.

Colloidal QDs are very efficient spontaneous emitters, meaning that the probability of emission is higher than the probability of losing the energy in any other (non-radiative way). However as a stimulated emitter, specifically in the regime of gain, where a resonant beam of light is amplified — a necessary condition to make a laser — QDs are very inefficient, meaning that non-radiative pathways of losing the excess energy are very probable. This is in the nature of the QD itself, as it needs multiple excitons to be present for gain to appear. Several solutions have been proposed in literature, and all involve making more complex QDs by combining two or more semiconductors in heterostructured QDs, varying the QD composition and changing the QD shape.

1.3 Thesis Outline

In this multidisciplinary thesis, we focus on a few major roadblocks on the way to competitive and high performance applications of colloidal QDs in integrated photonic circuits:

- improving our understanding of the hot-injection synthesis by combining theory with chemical experiments
- optically characterizing PbSe/CdSe heterostructured QDs and linking this to simulations of the opto-electronic properties
- designing and testing a platform technology for embedding colloidal QDs into silicon nitride integrated photonic structures

In Part I we explore the physical chemistry of the hot-injection synthesis of colloidal QDs. A profound understanding of this synthesis method is needed as a tool to engineer the properties of QDs in a smarter, more cost-effective and efficient way. This results in a faster turn-around time of the methodological cycle of designing a synthesis, optimizing the new material, characterizing its properties and feeding the results back into the design phase. We start from a theoretical framework available in literature and combine the formation of monomers, nucleation and QD growth into a single numerical model. We aim to map the parameter space of the model, which includes concepts as monomer solubility, monomer generation rate and surface tension, to the real world parameters of a colloidal chemists, who can tune the temperature, the precursor concentration, the amount of

carboxylic acid, etc in the synthesis. We show that our simulation model agrees very well with the dynamics of an established model CdSe synthesis and are able to link several theoretical parameters to experimental changes.

In Part II we take a new class of infrared emitting QDs, heterostructured PbSe/CdSe dot-in-dot and run them through in-depth optical testing. In Chapter 4 we compare the linear absorption of PbSe/CdSe core/shell QDs with the more common PbSe parent QDs. We show that the sizing curve and the absorption oscillator strength remain unaltered by the addition of a CdSe shell. However, the change in the local dielectric environment by the CdSe shell makes the absorption coefficient at energies well above the band gap dependent on the ratio between the shell volume and the total QD volume V_{shell}/V_{QD}. In Chapter 5 we explore the spontaneous emission properties of highly luminescent PbSe/CdSe QDs ($QY \simeq 30-60\%$). We show that the longer emission lifetime is caused by a lower emission oscillator strength compared to PbSe QDs. This reduction is more than likely due to an increased fine-structure splitting of the 8-fold degenerate bulk band gap because of the CdSe shell. In Chapter 6 we use transient absorption spectroscopy to show that intraband absorption, forbidden in first order for bulk semiconductors, is allowed in colloidal QDs. The intraband absorption both in PbSe and PbSe/CdSe QDs contributes to the difficulty of achieving transparency and gain in these QDs, yet below the band gap, in the energy range between 1600 nm and 2200 nm, intraband absorption could be used for zero-insertion loss optical modulators. Finally we study the transient absorption signal around the band gap. By extracting the Auger lifetime for PbSe/CdSe QDs we show that Auger recombination is not reduced by the addition of the CdSe shell. We further explain the spectral shape of the bleaching signal using a state-filling model including the effects of multi-exciton shifts and increased fine-structure splitting.

In Part III we develop a platform technology for embedding QDs in silicon nitride. We use visibly emitting cadmium based QDs, which were shown to have improved gain properties, to fabricate free-standing microdisks as a demonstrator of this technology. In Chapter 7 we explore the theory of these microdisks and investigate the coupling of the active QDs to the resonator using a QD-microdisk rate equation model. These highlight the conditions needed to achieve lasing using these QDs. In Chapter 8 we elaborate on the newly developed fabrication flow for hybrid QD-silicon nitride photonic structures. Finally we test the active microdisks using several techniques. We show that the QDs couple very well to the whispering gallery modes of the resonators, yet that the loading conditions, the gain properties and the stability of the QD-silicon nitride stack is insufficient to sustain QD-microdisk lasing.

1.4 Publications

1.4.1 International Journals

[1] De Geyter, B.; Houtepen, A. J.; Carrillo, S.; Geiregat, P.; Gao, Y.; ten Cate, S.; Schins, J. M.; Van Thourhout, D.; Delerue, C.; Siebbeles, L. D. A.; Hens, Z. Broadband and Picosecond Intraband Absorption in Lead-Based Colloidal Quantum Dots. *ACS Nano* **2012**, *6*, 6067–6074.

[2] De Geyter, B.; Komorowska, K.; Brainis, E.; Emplit, P.; Geiregat, P.; Hassinen, A.; Hens, Z.; Van Thourhout, D. From Fabrication to Mode Mapping in Silicon Nitride Microdisks with Embedded Colloidal Quantum Dots. *Applied Physics Letters* **2012**, *resubmitted*, year.

[3] Abé, S.; Capek, R. K.; De Geyter, B.; Hens, Z. Reaction Chemistry/-Nanocrystal Property Relations in the Hot Injection Synthesis, the Role of the Solute Solubility. *ACS Nano* **2012**, *under review*, year.

[4] Rodriguez, S.; Lozano, G.; Verschuuren, M.; Gomes, R.; Lambert, K.; De Geyter, B.; Hassinen, A.; Van Thourhout, D.; Hens, Z.; Gomez Rivas, J. Quantum Rod Emission Coupled to Plasmonic Lattice Resonances: A Collective Directional Source of Polarized Light. *Applied Physics Letters* **2012**, *100*, 111103.

[5] Abé, S.; Čapek, R. K.; De Geyter, B.; Hens, Z. Tuning the Postfocused Size of Colloidal Nanocrystals by the Reaction Rate: From Theory to Application. *ACS Nano* **2012**, *6*, 42–53.

[6] De Geyter, B.; Justo, Y.; Moreels, I.; Lambert, K.; Smet, P. F.; Van Thourhout, D.; Houtepen, A. J.; Grodzinska, D.; de Mello Donega, C.; Meijerink, A.; Vanmaekelbergh, D.; Hens, Z. The Different Nature of Band Edge Absorption and Emission in Colloidal PbSe/CdSe Core/Shell Quantum Dots. *ACS Nano* **2011**, *5*, 58–66.

[7] Moreels, I.; Justo, Y.; De Geyter, B.; Haustraete, K.; Martins, J.; Hens, Z. Size-Tunable, Bright, and Stable PbS Quantum Dots: A Surface Chemistry Study. *ACS Nano* **2011**, *5*, 2004–2012.

[8] De Geyter, B.; Hens, Z. The Absorption Coefficient of PbSe/CdSe Core/Shell Colloidal Quantum Dots. *Applied Physics Letters* **2010**, *97*, 161908.

[9] Moreels, I.; Allan, G.; De Geyter, B.; Wirtz, L.; Delerue, C.; Hens, Z. Dielectric Function of Colloidal Lead Chalcogenide Quantum Dots Obtained by a Kramers-Krönig Analysis of the Absorbance Spectrum. *Physical Review B* **2010**, *81*, 235319.

[10] Lambert, K.; De Geyter, B.; Moreels, I.; Hens, Z. PbTelCdTe CorelShell Particles by Cation Exchange, a HR-TEM study. *Chemistry of Materials* **2009**, *21*, 778–780.

[11] Moreels, I.; De Geyter, B.; Van Thourhout, D.; Hens, Z. Transmission of a Quantum-Dot-Silicon-on-Insulator Hybrid Notch Filter. *Journal of the Optical Society of America B-Optical Physics* **2009**, *26*, 1243–1247.

1.4.2 Publications in international conferences

[1] De Geyter, B.; Van Thourhout, D. Silicon compatible laser based on colloidal quantum dots. *ePIXnetSpring School '08, Technology for Photonics Integration*, Elba, Italy, **2008**.

[2] De Geyter, B.; Moreels, I.; Meijerink, A.; Van Thourhout, D.; Hens, Z. Core/shell colloidal quantum dots for silicon compatible lasers. *Proceedings Annual Symposium of the IEEE/LEOS Benelux Chapter*, Enschede, Nederland, **2008**.

[3] Moreels, I.; Knockaert, P.; De Geyter, B.; Van Thourhout, D.; Hens, Z. Colloidal semiconductor quantum dots: from synthesis to photonic applications. *Proceedings Annual Symposium of the IEEE/LEOS Benelux Chapter*, Enschede, Nederland, **2008**.

[4] De Geyter, B.; Justo, Y.; Grodzinska, D.; Moreels, I.; Lambert, K.; Smet, P. F.; Van Thourhout, D.; Meijerink, A.; de Mello Donega, C.; Vanmaekelbergh, D.; Hens, Z. Band Alignment of Colloidal PbSe/CdSe Core/shell Quantum Dots. *NanaX 4*, Munich, Germany, **2010**.

[5] De Geyter, B.; Van Thourhout, D.; Justo, Y.; Moreels, I.; Hens, Z. The Different Nature of Band Edge Absorption and Emission in Colloidal PbSe/CdSe Core/shell Quantum Dots. *E-MRS Spring Meeting 2011*, Nice, France, **2011**.

[6] Abé, S.; Capek, R. K.; De Geyter, B.; Hens, Z. Size Tuning at Full Yield in the Hot Injection Synthesis through a Facile Adjustment of the Nucleation Event. *E-MRS Spring Meeting 2011*, Nice, France, **2011**.

[7] De Geyter, B.; Justo, Y.; Flamée, S.; Hens, Z. The Absorption Coefficient of PbSe/CdSe and PbS/CdS Core/shell Colloidal Quantum Dots. *E-MRS Spring Meeting 2011*, **2011**.

[8] De Geyter, B.; Komorowska, K.; Hens, Z.; Van Thourhout, D. Hybrid Silicon Nitride and Colloidal Nanocrystal Waveguides and Microdisks: A Highly Versatile Test Bed for Visible to near-Infrared Active Integrated Photonics. *MRS Fall Meeting 2011*, Boston, USA, **2011**.

[9] De Geyter, B.; Geiregat, P.; Houtepen, A. J.; Van Thourhout, D.; Siebbeles, L.; Hens, Z. Ultrafast Photoinduced Intraband Absorption in PbS, PbSe and PbSe/CdSe Core/Shell Nanocrystals for near-Infrared to Mid-Infrared All-Optical Signal Processing. *MRS Fall Meeting 2011*, **2011**.

[10] De Geyter, B.; Abé, S.; Hens, Z. Postfocused Nanocrystal Diameter Tuning through Control of the Reaction Rate and the Solubility: Experiment vs. Realistic Modeling. *MRS Fall Meeting 2011*, Boston, USA, **2011**.

[11] Geiregat, P.; De Geyter, B.; Carillo, S.; Houtepen, A.; Gao, Y.; ten Cate, S.; Schins, J. M.; Van Thourhout, D.; Delerue, C.; Siebbeles, L.; Hens, Z. Broadband and Picosecond Intraband Relaxation in Lead Chalcogenide Nanocrystals. *International Quantum Dot Conference*, Santa Fe, USA, **2012**.

[12] De Geyter, B.; Geiregat, P.; Gao, Y.; ten Cate, S.; Houtepen, A. J.; Schins, J. M.; Van Thourhout, D.; Siebbeles, L.; Hens, Z. Broadband and picosecond intraband absorption in lead based colloidal quantum dots. *14th International Conference on Transparant Optical Networks (ICTON 2012) (invited)*, Warwick, United Kingdom, **2012**.

References

[1] Feynman, R. There's plenty of room at the bottom. *Engineering and Science* **1960**, *23*, 22–36.

[2] Vermeulen, D.; Roelkens, G.; Brouckaert, J.; Van Thourhout, D.; Baets, R.; Duijn, R.; Pluk, E.; Van den Hoven, G. Silicon-on-insulator nanophotonic waveguide circuit for fiber-to-the-home transceivers. *Optical Communication, 2008. ECOC 2008. 34th European Conference on*, **2008**; pp 1–2.

[3] Almeida, V.; Barrios, C.; Panepucci, R.; Lipson, M. All-optical control of light on a silicon chip. *Nature* **2004**, *431*, 1081–1084.

[4] Claes, T. Ph.D. thesis, Universiteit Gent, 2012.

[5] Yebo, N.; Taillaert, D.; Roels, J.; Lahem, D.; Debliquy, M.; Van Thourhout, D.; Baets, R. Silicon-on-Insulator (SOI) ring resonator-based integrated optical hydrogen sensor. *Photonics Technology Letters, IEEE* **2009**, *21*, 960–962.

[6] Roelkens, G.; Van Campenhout, J.; Brouckaert, J.; Van Thourhout, D.; Baets, R.; Romeo, P. R.; Regreny, P.; Kazmierczak, A.; Seassal, C.; Letartre, X.; Hollinger, G.; Fedeli, J. M.; Di Cioccio, L.; Lagahe-Blanchard, C. III-V/Si photonics by die to wafer bonding. *Materials Today* **2007**, *10*, 36–43.

[7] Van Campenhout, J.; Rojo-Romeo, P.; Regreny, P.; Seassal, C.; Van Thourhout, D.; Verstuyft, S.; Di Cioccio, L.; Fedeli, J.-M.; Lagahe, C.; Baets, R. Electrically pumped InP-based microdisk lasers integrated with a nanophotonic silicon-on-insulator waveguide circuit. *Optics Express* **2007**, *15*, 6744–6749.

[8] Brus, L. Electronic wave functions in semiconductor clusters: experiment and theory. *The Journal of Physical Chemistry* **1986**, *90*, 2555–2560.

[9] Brus, L. Electron–electron and electron-hole interactions in small semiconductor crystallites: The size dependence of the lowest excited electronic state. *The Journal of chemical physics* **1984**, *80*, 4403.

[10] Ekimov, A.; Efros, A.; Onushchenko, A. Quantum size effect in semiconductor microcrystals. *Solid State Communications* **1985**, *56*, 921–924.

[11] Efros, A.; Efros, A. Interband absorption of light in a semiconductor sphere. *Soviet Physics Semiconductors Ussr* **1982**, *16*, 772–775.

[12] Murray, C.; Norris, D.; Bawendi, M. Synthesis and characterization of nearly monodisperse CdE (E= sulfur, selenium, tellurium) semiconductor nanocrystallites. *Journal of the American Chemical Society* **1993**, *115*, 8706–8715.

[13] Murray, C.; Sun, S.; Gaschler, W.; Doyle, H.; Betley, T.; Kagan, C. Colloidal synthesis of nanocrystals and nanocrystal superlattices. *Ibm Journal of Research and Development* **2001**, *45*, 47–56.

[14] Talapin, D.; Rogach, A.; Haase, M.; Weller, H. Evolution of an ensemble of nanoparticles in a colloidal solution: Theoretical study. *Journal of Physical Chemistry B* **2001**, *105*, 12278–12285.

[15] Moreels, I.; Fritzinger, B.; Martins, J. C.; Hens, Z. Surface Chemistry of Colloidal PbSe Nanocrystals. *Journal of the American Chemical Society* **2008**, *130*, 15081–15086.

[16] Hens, Z.; Moreels, I. Light absorption by colloidal semiconductor quantum dots. *J. Mater. Chem.* **2012**, *22*, 10406–10415.

[17] Talgorn, E.; Gao, Y.; Aerts, M.; Kunneman, L.; Schins, J.; Savenije, T.; van Huis, M.; van der Zant, H.; Houtepen, A.; Siebbeles, L. Unity quantum yield of photogenerated charges and band-like transport in quantum-dot solids. *Nature Nanotechnology* **2011**, *6*, 733–739.

[18] Schmid, G. *Nanoparticles: from theory to application*; Wiley-VCH, 2011.

[19] Justo, Y.; Goris, B.; Kamal, J.; Geiregat, P.; Bals, S.; Hens, Z. Multiple Dot-in-Rod PbS/CdS Heterostructures with High Photoluminescence Quantum Yield in the Near-Infrared. *Journal of the American Chemical Society* **2012**, *134*, 5484.

[20] Manna, L.; Scher, E.; Alivisatos, A. Synthesis of soluble and processable rod-, arrow-, teardrop-, and tetrapod-shaped CdSe nanocrystals. *Journal of the American Chemical Society* **2000**, *122*, 12700–12706.

[21] Ithurria, S.; Tessier, M.; Mahler, B.; Lobo, R.; Dubertret, B.; Efros, A. Colloidal nanoplatelets with two-dimensional electronic structure. *Nature Materials* **2011**.

[22] Pietryga, J.; Werder, D.; Williams, D.; Casson, J.; Schaller, R.; Klimov, V.; Hollingworth, J. Utilizing the Lability of Lead Selenide to Produce Heterostructured Nanocrystals with Bright, Stable Infrared Emission. *Journal of the American Chemical Society* **2008**, *130*, 4879–4885.

[23] Klimov, V. I.; Ivanov, S. A.; Nanda, J.; Achermann, M.; Bezel, I.; McGuire, J. A.; Piryatinski, A. Single-exciton optical gain in semiconductor nanocrystals. *Nature* **2007**, *447*, 441–446.

[24] Panthani, M.; Akhavan, V.; Goodfellow, B.; Schmidtke, J.; Dunn, L.; Dodabalapur, A.; Barbara, P.; Korgel, B. Synthesis of CuInS2, CuInSe2, and Cu (In x Ga1-x) Se2 (CIGS) Nanocrystal "Inks" for Printable Photovoltaics. *Journal of the American Chemical Society* **2008**, *130*, 16770–16777.

[25] Katagiri, H.; Jimbo, K.; Maw, W.; Oishi, K.; Yamazaki, M.; Araki, H.; Takeuchi, A. Development of CZTS-based thin film solar cells. *Thin Solid Films* **2009**, *517*, 2455–2460.

[26] Sharma, P.; Brown, S.; Walter, G.; Santra, S.; Moudgil, B. Nanoparticles for bioimaging. *Advances in colloid and interface science* **2006**, *123*, 471–485.

[27] Nozik, A. Quantum dot solar cells. *Physica E: Low-dimensional Systems and Nanostructures* **2002**, *14*, 115–120.

[28] Klimov, V.; Mikhailovsky, A.; Xu, S.; Malko, A.; Hollingsworth, J.; Leatherdale, C.; Eisler, H.; Bawendi, M. Optical gain and stimulated emission in nanocrystal quantum dots. *Science* **2000**, *290*, 314–317.

[29] Coe, S.; Woo, W.; Bawendi, M.; Bulovic, V. Electroluminescence from single monolayers of nanocrystals in molecular organic devices. *Nature* **2002**, *420*, 800–803.

[30] Wood, V.; Panzer, M.; Caruge, J.; Halpert, J.; Bawendi, M.; Bulovic, V. Air-Stable Operation of Transparent, Colloidal Quantum Dot Based LEDs with a Unipolar Device Architecture. *Nano letters* **2009**, *10*, 24–29.

[31] Moreels, I. Ph.D. thesis, Universiteit Gent, 2009.

[32] Rauch, T.; Böberl, M.; Tedde, S.; Fürst, J.; Kovalenko, M.; Hesser, G.; Lemmer, U.; Heiss, W.; Hayden, O. Near-infrared imaging with quantum-dot-sensitized organic photodiodes. *Nature Photonics* **2009**, *3*, 332–336.

Part I

Theoretical and Experimental Study of Visible to Near-Infrared Absorbing and Emitting Colloidal Quantum Dot Synthesis

2

Kinetics of Colloidal Quantum Dot Formation in the Hot Injection Method

2.1 Introduction

2.1.1 Hot Injection Method

The synthesis of QDs with sharp size distributions at desired mean sizes and high reaction yields is key for the efficient screening of new materials and the development of colloidal QD applications. Until now two concepts, *i.e.* burst nucleation and focusing, are mainly applied in colloidal synthesis to achieve narrow size distributions.[1] In the hot injection synthesis, burst nucleation is supposedly achieved by the injection of reaction precursors at a high temperature, which leads to a high degree of supersaturation. This should result in a short nucleation event, which is stopped by the resulting drop of the supersaturation and the temperature. Next, it is assumed that nucleation is followed by a continuous growth at a lower temperature, thereby maintaining the initial sharp size distribution during the growth phase. In addition, it was shown that specific reaction conditions can even improve an initial size distribution.[2] This so-called focusing is based on the fact that when growth is limited by the diffusion of reagents to the QDs, the increase of the QD radius r_{QD} with time drops as $1/r_{QD}$. Since smaller particles grow faster than bigger particles under this condition, the initial particle size distribution narrows during growth.

2.1.2 Size and Reaction Yield Tuning

The hot injection concept led to the development of synthesis schemes that allow for a control of the mean size of the QDs by the reaction time.[3–10] Although highly successful, these procedures have an intrinsic drawback: QDs with a size smaller than the size reached after focusing (a size referred to as the *post-focused size* d_{PF}), which often coincides with a reaction yield close to unity[2], are only obtained at the expense of a reduced reaction yield and a suboptimal size dispersion. This is problematic when small QDs are targeted or in the context of reaction up scaling. Therefore, the development of strategies enabling the preparation of monodisperse batches of colloidal QDs with different diameters at the end of the reaction is of key importance.

A number of literature examples indicate possible approaches in this respect. Various authors have shown for CdSe and CdS QDs synthesized in non-coordinating solvents that a decrease of the concentration of carboxylic or phosphonic acids leads to a reduction of the QD diameter.[11–15] Alternatively, in the case of InP and CdSe, it was shown that the number of QDs can be tuned by the precursor concentrations[12;16] together with the final QD diameter.[11] In addition to these studies, recent work on the kinetics of the hot injection synthesis showed that the actual solute or monomer is formed in-situ in the reaction mixture out of the injected precursors.[17;18] Although this has been taken into account in rate equation based models for the formation of colloidal nanocrystals,[19] there is as yet no link between these models and the above mentioned strategies for size control. This hampers the development of high yield syntheses, which is an important limiting factor for large-scale applications of colloidal nanocrystals.

2.1.3 Design of Experiment Synthesis

With the advent of high-throughput screening studies[11;20] of the hot injection synthesis, a new direction in the research field aims at finding relations between the reaction conditions and the properties of the synthesized NCs, such as size and size dispersion. Importantly, by means of reaction simulations, this search for reaction chemistry/nanocrystal property relations can be linked to an improved understanding of the hot injection synthesis. As a result, a rational *design of experiment* (DOE) can tailor the synthesis conditions to the specific needs of the application at hand, possibly in more automated and complex ways.

In Section 2.5, we use a comprehensive model of nucleation and growth that combines classical nucleation theory with the concept of monomer formation to demonstrate that the formation rate of the solute can be used to control d_{PF}. Experimentally verifiable fingerprints of this simulated syn-

thesis are a three stage development of the size dispersion from defocusing to focusing to defocusing, where the minimum in the size dispersion is reached close to full yield, and a reaction yield development that is determined by the rate of solute formation. We show that the time-development of a CdSe synthesis, which is optimized for small sizes[21], is fully in line with the basic features of this model synthesis. Based on this correspondence, we explore the tuning of the post-focused size by the reaction rate by varying the precursor concentrations and the reaction temperature. In line with the model predictions, we find that the reaction rate is a powerful reaction variable to steer the outcome of a hot injection synthesis at full yield and narrow size dispersion.

An alternative reaction chemistry/nanocrystal property relation used for nanocrystal size tuning in the hot injection synthesis that often appears in the literature, albeit not always used on purpose, is that between the concentration of the free acid and the nanocrystal size. For various materials, including II-VI,[14;15;20;22] III-V[23;24] and IV-VI[7;25] semiconductors and various metal oxides,[26] it is observed that d_{QD} increases with the carboxylic acid concentration. Several authors interpret this relation as resulting from an enhanced reactivity during the nucleation stage at lower free acid concentrations.[7;15;20;25] Opposite from this, Owen et al.[12] showed in a quantitative study on CdSe QDs synthesized using phosphonic acids, that a reduction of the phosphonic acid concentration systematically leads to the formation of more QDs, while the overall reaction rate remains unchanged.

In Section 2.6, we use a combination of reaction simulations and experimental synthesis screening to understand the role of free acids in the hot injection synthesis. As a starting point, we consider that cation precursors are usually brought in solution as coordinated complexes, where in particular carboxylic (CA) or phosphonic acids are often used complexing agents. Therefore, free acids may also stabilize the actual solute or monomer, thereby enhancing its solubility. In line with this assumption, we use reaction simulations to show that increasing the monomer solubility at constant reaction rate results in larger nanocrystals since monomer consumption by growth is enhanced relative to consumption by nucleation. Next, this size tuning concept is experimentally confirmed again by means of a CdSe synthesis that has been used before to demonstrate high throughput[11] and design-of-experiment synthesis optimization[20]. For this reaction, we find that the reaction rate is independent of the CA concentration while d_{QD} increases with the CA concentration. The correspondence between experiments and simulations indicates that free acids indeed affect the outcome of a hot injection synthesis by changing the monomer solubility.

2.2 Theoretical Model

2.2.1 Evolution of the QD concentration

The modeling approach used here aims at calculating the time evolution of two central quantities. The first is the concentration distribution $c(r,t)$ of QDs, where the product $c(r,t)dr$ yields the concentration of QDs with a radius between r and $r+dr$ at time t. The second is the supersaturation $S(t)$, which is defined as the ratio between the actual concentration of the monomer and its equilibrium concentration. The change of the $c(r,t)$ with time is determined by the nucleation of QDs and by their growth or dissolution. The concentration of QDs with a radius in a control element between r and $r-\Delta r$, written as Δc, at time t is given by:

$$\Delta c = c(r,t)\Delta r \tag{2.1}$$

Focusing first on the change of this concentration within a time span Δt due to QD growth or dissolution, this can be seen as a difference between a flux of QDs entering the control element at $r-\Delta r$ and leaving the control element at $r+\Delta r$. Hence, we have:

$$\begin{aligned} \frac{d\Delta c}{dt}\Delta t &= \frac{\partial c(r,t)}{\partial t}\Delta r \Delta t \\ &= c(r-\Delta r)\left.\frac{dr}{dt}\right|_{r-\Delta r}\Delta t - c(r)\left.\frac{dr}{dt}\right|_{r}\Delta t \end{aligned} \tag{2.2}$$

If we define the QD growth rate j_G as the change of the QD radius with time (i.e., $j_G = dr/dt$), this becomes a simple continuity equation:

$$\frac{\partial c(r,t)}{\partial t} = -\frac{\partial}{\partial r}(j_G c) \tag{2.3}$$

2.2.2 QD Growth Rate

Equations

A general expression for j_G, which takes into account both the diffusion of monomers to the QDs and the reaction of the monomer (adsorption or

desorption) with the QD surface has been proposed by Talapin et al.[27]:

$$\begin{aligned} j_G &= \frac{dr}{dt} \\ &= D\nu_0 N_A [M]_0 \left(\frac{S - \exp\left(\frac{2\gamma\nu_0}{rk_BT}\right)}{r + \frac{D}{k_g^\infty} \exp\left(\alpha \frac{2\gamma\nu_0}{rk_BT}\right)} \right) \\ &= D\nu_0 N_A [M]_0 \left(\frac{S - \exp\left(\frac{2\gamma\nu_0}{rk_BT}\right)}{r + \frac{D[M]_0}{k_d^\infty} \exp\left(\alpha \frac{2\gamma\nu_0}{rk_BT}\right)} \right) \end{aligned} \tag{2.4}$$

Here,

D is the monomer diffusion coefficient

ν_0 is the molecular volume of the QD material,

N_A is Avogadro's number,

$[M]_0$ is the solubility of the monomer,

γ is the surface tension of the QD,

k_B is Boltzmann's constant,

k_g^∞ / k_d^∞ are the rate constants for crystal growth (g) and dissolution (d) for a flat (∞) surface

α is the transfer coefficient of the crystal growth reaction.

Interpretation

Although this expression has been extensively discussed in literature, it remains instructive to take a look at its main features. As shown in Figure 2.1a, equation 2.4 accounts both for the dissolution (negative growth rates) and the growth (positive growth rates) of the QDs. The radius at which j_G is zero is the so-called critical radius r_c. Looking more closely at the positive growth rates, one sees that it is composed of a region with positive slope followed by a region with negative slope. In the former region, the larger a QD, the higher its growth rate, which leads to a *defocusing* of the size distribution. In the latter region, smaller particles grow faster, meaning that the size distribution *focuses*. Importantly, the initial defocusing regime spreads over a wider diameter range with lower supersaturation (see Figure 2.1b).

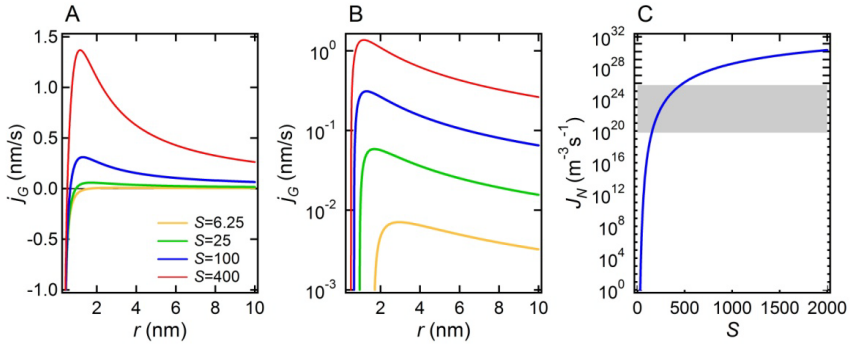

Figure 2.1: (a) Quantum dot growth rate calculated according to eq. 2.2 with the parameters as given in Table 2.1 for different values of the supersaturation S. (b) idem in logarithmic scale. (c) Nucleation rate calculated according to eq. 2.4 with the parameters as given in Table 2.1. The grey region indicates nucleation rates from 0.1 M/s to 0.1 μM/s.

2.2.3 QD Nucleation Rate

Equations

In classical nucleation theory, the formation of nuclei at the critical radius r_c follows from the build-up of a steady state concentration of embryos, *i.e.*, particles with a radius smaller than r_c. We will not attempt to describe this embryo concentration, yet we include nucleation in the model as a source term that describes the formation of QDs with a radius r_c at a rate J_N. Doing so, the overall time evolution of $c(r)$ reads (the indices G and N refer to growth and nucleation, respectively):

$$\frac{\partial c}{\partial t} = \left.\frac{\partial c}{\partial t}\right|_G + \left.\frac{\partial c}{\partial t}\right|_N = -\frac{\partial}{\partial r}(j_G c) + J_N \delta(r - r_c) \tag{2.5}$$

For r_c and J_N, we take the expressions of classical nucleation theory, which read:[28]

$$r_c = \frac{2\gamma\nu_0}{k_B T \ln S} \tag{2.6}$$

$$J_N = \frac{2D}{\nu_0^{5/3}} \exp\left(-\frac{16\pi\gamma^3\nu_0^2}{3(k_B T)^3(\ln S)^2}\right) \tag{2.7}$$

Interpretation

Also in this case, it is instructive to look at the dependence of J_N on S. Presuming that a QD synthesis yields about 100 μmol of particles in 10 mL (*i.e.*, 10^{-2} M), nucleation will take from 0.1 s to about 1 hour for nucleation rates ranging from 0.1 M/s to 0.1 μM/s. Due to the extremely high prefactor in eq. 2.7, these nucleation rates are obtained for supersaturations where the exponential term is much smaller than one. As a result, small changes in S will strongly affect the nucleation rate. As shown in Fig 2.1c, a change of S from about 150 to about 450 suffices to sweep the nucleation rate from the lower limit of 0.1 μM/s to the upper limit of 0.1 M/s.

2.2.4 Precursors, Monomers and Supersaturation

From precursor to monomer

Importantly, both j_G, r_c and J_N depend on the supersaturation S, which is a time-dependent quantity itself. Following recent literature results,[12;17;18] we assume that the time evolution of S is determined by the generation of the monomer from the precursors and by its consumption through the nucleation and the growth of nuclei. To simplify, we regard the precursors and the monomer as the monomolecular species P and M, respectively, without specifying their chemical nature. In this way, the formation of QDs can be described as:

$$\mathrm{P} \rightarrow \mathrm{M} \leftrightarrow \mathrm{QD} \tag{2.8}$$

Following this overall reaction scheme, we can define S more precisely as the ratio between the monomer concentration $[M]$ and the monomer solubility $[M]_0$:

$$S = \frac{[M]}{[M]_0} \tag{2.9}$$

Evolution of the Monomer Concentration

The concentration of monomers changes due to the generation of new monomers and due to a change of the number of monomers incorporated in the QDs, a number we will call M_{QD}. This number can be linked to the concentration distribution $c(r,t)$ as follows:

$$M_{QD} = \int_0^\infty \frac{4\pi r^3}{3\nu_0} c(r,t)dr \tag{2.10}$$

By means of eq. 2.5, the time derivative dM_{QD}/dt can be obtained as follows:

$$\begin{aligned}\frac{dM_{QD}}{dt} &= \int_0^\infty \frac{4\pi r^3}{3\nu_0} c(r,t)dr \\ &= \frac{4\pi r^3}{3\nu_0} J_N - \int_0^\infty \frac{4\pi r^3}{3\nu_0} \frac{\partial}{\partial r}(j_G c(r,t))dr \end{aligned} \tag{2.11}$$

Using this expression, the time derivative dS/dt is readily obtained as:

$$\frac{dS}{dt} = \frac{1}{[M]_0}\left(G_M - \frac{4\pi r^3}{3\nu_0} J_N + \int_0^\infty \frac{4\pi r^3}{3\nu_0} \frac{\partial}{\partial r}(j_G c)dr\right) \tag{2.12}$$

Ostwald Ripening and QD dissolution

Since the expression for j_G (see Eq. 2.4) covers both QD dissolution and growth, stopping the integration in the last term of the right hand side of eq. 2.8 at r_c describes the rate of monomer formation $J_{M,diss}$ due to the dissolution of QDs with a radius smaller than r_c:

$$J_{M,diss} = -\frac{1}{[M]_0} \int_0^{r_c} \frac{4\pi r^3}{3\nu_0} \frac{\partial}{\partial r}(j_G c)dr \tag{2.13}$$

This expression can be used to estimate the rate of *Ostwald ripening*, the effect where larger QDs grow at the expense of dissolving smaller QDs.

Evolution of the Precursor Concentration

Finally, the monomer generation rate G_M also determines the change of the precursor concentration $[P]$ with time:

$$\frac{d[P]}{dt} = -G_M = -k_1[P] \tag{2.14}$$

To concentrate on concepts rather than on the details of a specific synthesis, we assume in the above expression that the generation rate depends in first order on the precursor concentration $[P]$.

2.3 Simulated Synthesis

2.3.1 Implementation and Parameters

The coupled differential equations as outlined in the manuscript were implemented in COMSOL Multiphysics. A one-dimensional simulation domain for the nanocrystal radius ranging from 0 to 4 nm was divided in

Symbol	Parameter description	Value	Unit
D	monomer diffusion coefficient	$1\ 10^{-9}$	m^2/s
ν_0	molecular volume	$5.6\ 10^{-29}$	m^3
$[M]_0$	monomer solubility	$4\ 10^{-8}$	mol/m^3
γ	QD surface tension	0.2	J/m^2
T	temperature	$533.15/260$	K/°C
k_g^∞	surface growth rate constant	50	m/s
k_1	first order monomer generation rate constant	0.08333	s^{-1}
$[P]_i$	initial precursor concentration	0.01667	mol/L

Table 2.1: Parameter values used for the reference simulation as shown in Figure 2.2

512 elements. From 0 to 0.2 nm an absorbing boundary condition was implemented to account for nanocrystal dissolution into monomers. The nucleation term was implemented as a Gaussian function with a width of 0.01 nm, centered 0.1 nm above the critical radius. The monomer diffusion coefficient D was chosen according to literature values for free oleic acid ligands obtained from diffusion NMR. The molecular volume ν_0 is the volume of a single CdSe unit in the zincblende CdSe unit cell. The surface tension γ and the monomer solubility $[M]_0$ were adjusted to yield a realistic nucleation radius of ∼0.5 nm and a final QD concentration and radius comparable to what is obtained in the experiments. The surface tension was kept constant for all simulations. The surface growth rate constant k_g^∞ was chosen to be in the diffusion limited growth regime. However, the ratio of the surface dissolution rate constant and the surface growth rate constant equals the monomer solubility.[27] To model the effect of variations of the solubility, we have assumed that a change in the solubility results in a change of the surface growth rate constant, and not the surface dissolution rate constant, rationalized by the concept that the rate of dissolution is influenced mostly by the ligands bound to the surface, not the ligands in solution. The magnitude of the first order monomer generation rate constant was set equal to the experimental value for the product $k_2[P_{Se}]$ obtained from the experimental yield development. Especially in terms of reaction speed, the values for k_1 (0.0833 s^{-1}) and $[M]_0$ (2 10^{-10} mol/L) imply a fast reaction with a low monomer solubility. For the initial precursor concentration used, a supersaturation S of 100 is reached within 10 μs and a reaction yield of 99% within about 1 minute.

Symbol	Parameter description	Value	Unit
D	monomer diffusion coefficient	$0.5\ 10^{-9}$	m^2/s
ν_0	molecular volume	$1.33\ 10^{-29}$	m^3
$[M]_0$	monomer solubility	$2\ 10^{-8}$	mol/m^3
γ	QD surface tension	0.2	J/m^2
T	temperature	$508.15/235$	K/°C
k_g^∞	surface growth rate constant	$5\ 10^{-7}/[M]_0$	m/s
k_1	first order monomer generation rate constant	0.02333	s^{-1}
$[P]_i$	initial precursor concentration	0.01667	mol/L

Table 2.2: Parameter values used for the simulations as shown in Figure 2.16,2.17 and 2.18

2.3.2 Typical Simulation Result

Figure 2.2 represents the outcome of a typical model synthesis, representative of a fast reaction with a low monomer solubility (see Table 2.1 for the parameter values used). Apart from the nucleation stage, the time evolution of the concentration distribution $c(r,t)$ (see Figure 2.2a) resembles the result obtained by Rempel et al. [19] who kept track of all possible n-clusters in the system. Looking at the development of the QD concentration, [QD] (see Figure 2.2b), one sees that there are two main regions in the reaction development: a first in which [QD] increases because of nucleation of new QDs (region 1) and a second where [QD] decreases due to Ostwald ripening (regions 2a and 2b).

Nucleation

In the initial stage of the nucleation (region 1), the generated monomers are mainly consumed by the nucleation of QDs (Figure 2.2d). Importantly, this implies that the initial nucleation rate and therefore S and r_c are set by the rate of the monomer formation. As a result, [QD] increases with time and the initial size distribution is narrow and centered around a fixed radius.

Reaction Driven Growth

With the rise of [QD], an increasing part of the generated monomers is used for the growth of existing QDs at the expense of nucleation. The dropping nucleation rate results in a reduction of S, and thus an increase of r_c (see Figure 2.2c). When r_c falls within the concentration distribution

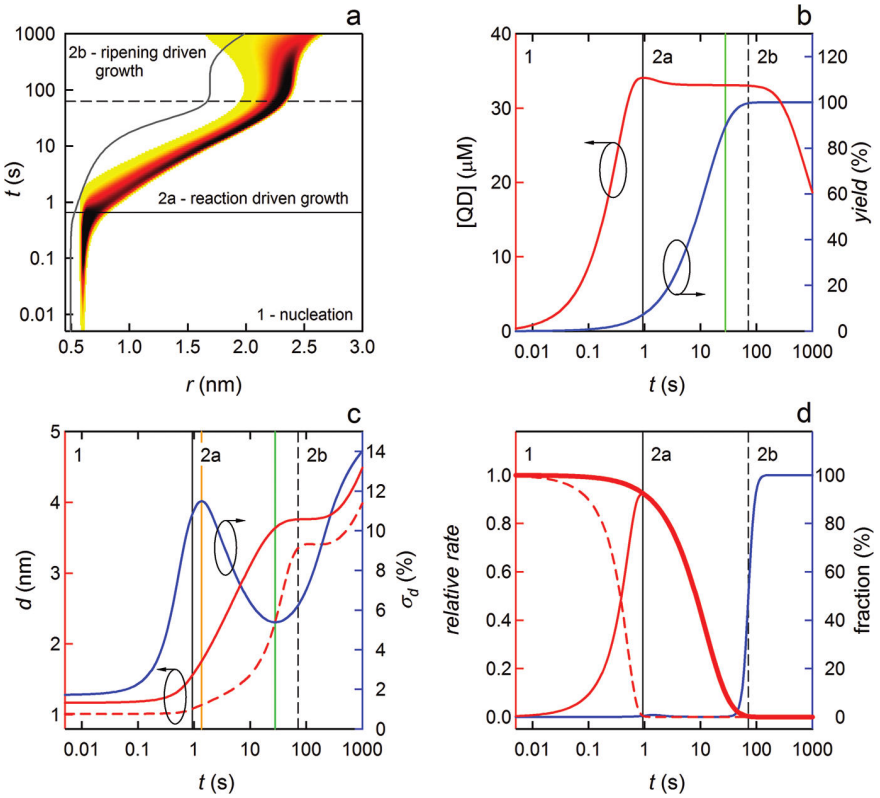

Figure 2.2: (a) Concentration distribution $c(r,t)$ obtained with the initial parameters as given in Table 2.1. The color scale indicates an increase of c in the direction yellow-orange-red-black. The gray line marks the critical radius, r_c. (b) Change of (red) QD concentration and (blue) reaction yield as a function of time. (c) Change of (full red) QD diameter, (dashed red) critical radius, and (blue) size dispersion as a function of time. Indicated are (orange) the maximum and (green) the minimum of the size dispersion. (d) (bold red line) Monomer generation rate, (dashed red line) monomer consumption rate by nucleation, and (red line) monomer consumption rate by growth. All rates are given relative to the initial monomer formation rate. (blue) Fraction of the monomer generation resulting from particle dissolution.

(Figure 2.2a), particles with a radius r_{QD} below r_c will dissolve (Ostwald ripening). This results in a maximum [QD], determined by a balance between the dissolution of existing QDs and the nucleation of new QDs. This indicates that Ostwald ripening may occur in parallel with nucleation and is not limited to the end of the reaction, when the monomer concentration is depleted.[29] Opposite of Kwon et al.[1] we find no bimodal concentration distribution in the nucleation region. Since for radii close to r_c, the QD growth rate dr_{QD}/dt increases with r_{QD} (see Figure 2.1),[27] the onset of QD growth leads to a strong increase of the size dispersion, σ_d, defined here as the ratio between standard deviation of the particle size distribution and r_{QD} (defocusing, Figure 2.2c).

After the concentration maximum, the contribution of nucleation to the consumption of monomers becomes negligible and the reaction enters a regime in which the monomer generation mainly drives nanocrystal growth (region 2a). This results in a pronounced increase of r_{QD} and a reduction of σ_d (focusing, between orange and green lines in Figure 1c), which is linked to an increasing difference between r_{QD} and r_c (Figure 2.2c). Opposite of the original description of size distribution focusing,[29] Ostwald ripening is not absent during focusing, but its effect is small and [QD] is almost constant.

Ripening Driven Growth

With increasing reaction time, the monomer generation rate drops, which results in a reduction of the QD growth rate and a progressive decrease of S. Therefore, the difference between r_{QD} and r_c goes down again (Figure 2.2c) and Ostwald ripening becomes the dominant growth process (region 2b). Hence, σ_d reaches a minimum and further QD growth occurs only at the expense of defocusing and a drop in [QD] (Figure 2.2b,c). Importantly, the minimum of σ_d corresponds to a reaction yield of 90%. In view of size control at almost full yield, this is an ideal point to stop the reaction, especially since the transition from reaction-driven growth to Ostwald ripening shows a relatively wide time span in which the reaction has reached almost full yield, r_{QD} rises slowly, and σ_d is close to its minimum. This shows the relevance of strategies to tune the diameter at the end of the focusing, *i.e.*, the *postfocused diameter* d_{PF}.

The Focusing Criterion r_{QD}/r_c

The connection between size distribution focusing and the difference between r_{QD} and r_c that follows from the modeling (Figure 2.2c) has been

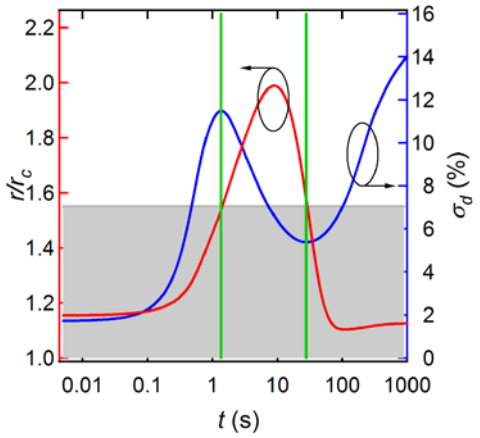

Figure 2.3: (Blue) size dispersion σ_d and (red) size-focusing coefficient r/r_c as obtained for the model synthesis shown in Figure 2.2. The green lines indicate the points where size distribution focusing starts (maximum of σ_d) and ends (minimum of σ_d). The gray line separates the region with $r/r_c < 1.55$ from that with $r/r_c > 1.55$. One sees that focusing occurs when $r/r_c > 1.55$

proposed before by Sugimoto [30] and was the subject of a recent theoretical study on focusing during nanocrystal growth by Clark et al. [31]. Briefly, these authors argue that focusing will occur when r_{QD}/r_c exceeds 2.

In Figure 2.3, we plot the ratio r/r_c found for the model synthesis shown in Figure 2.2. The green lines indicate the moments where size distribution focusing starts and ends. At both turnover points, we find a size-focusing coefficient of about 1.55, which shows that the size distribution broadens when $r/r_c < 1.55$ (grey background), while it sharpens when $r_c > 1.55$ (white background). Hence, it appears that both regimes are indeed associated to different values of r/r_c . On the other hand, a critical size-focusing coefficient of about 1.55 is smaller than the value of 2 predicted by Clark et al. [31] Possibly, this is related to the different expression we use here to express the nanocrystal growth rate.

Limiting Monomer Formation Rate

Figure 2.2d represents the three terms contributing to the change of the monomer concentration: monomer generation (G_M, bold line) and monomer

consumption by growth (J_G, full line) and by nucleation (J_N, dashed line). One sees that for the fast reaction modeled here, the sum of J_N and J_G is always equal to G_M. Returning to the model, this implies that the supersaturation S is quasi-stationary; that is, dS/dt is small with respect to these three rates. Therefore, the initial nucleation rate is set by the initial monomer generation rate. This implies that the latter may be used to adjust the total number of particles nucleated and, therefore, d_{PF}, a concept we will further explore in Section 2.5.

2.4 Experimental CdSe Synthesis

To verify the predictions of the simulations, we use a synthesis for zinc-blende CdSe QDs, based on the injection of trioctylphosphine selenide (TOP-Se) in a solution of Cd stearate ($Cd(StA)_2$), hexadecylamine (HDA), and stearic acid (StA) in octadecene (ODE).[21] The typical development of the absorption spectra during the synthesis is shown in Figure 2.4a. A relatively sharp absorption peak corresponding to the first exciton transition ($\lambda_{1S\text{-}1S}$) is observed even in the beginning of the reaction. With increasing reaction time, $\lambda_{1S\text{-}1S}$ shifts to longer wavelengths, reflecting QD growth. Figure 2.4b gives the corresponding change of d_{QD} and σ_d with time. In line with the model synthesis, the growth almost stops after σ_d has reached its minimum. Further, a pronounced increase of n_{QD} is observed in the beginning, accompanied by an increase of σ_d. When this defocusing turns into focusing, n_{QD} remains largely constant within the errors of the measurement, in line with the reaction-driven growth regime that appeared in the model synthesis. Moreover, at the end of the focusing regime, the reaction has reached almost full yield. With such a high yield at the postfocused diameter and the almost perfect agreement with the model synthesis, this particular reaction is well suited to investigate the modeling results in terms of tuning d_{PF} by the reaction rate.

2.4.1 CdSe Formation Rate

A key element of the modeling work is that a change of the monomer formation rate enables a tuning of d_{PF}. Hence to implement and understand this tuning strategy, the kinetics of the monomer formation reaction must be known. In the model synthesis, the rate at which CdSe is formed (the CdSe formation rate) equals the rate of monomer generation. To verify this for the experimental synthesis, Figure 2.5a plots the amount of TOP-Se ($n_{\text{TOP-Se}}$) - as determined using ^{31}P NMR - and CdSe (n_{CdSe}) in the reaction mixture as a function of time. Since the sum of both is a constant,

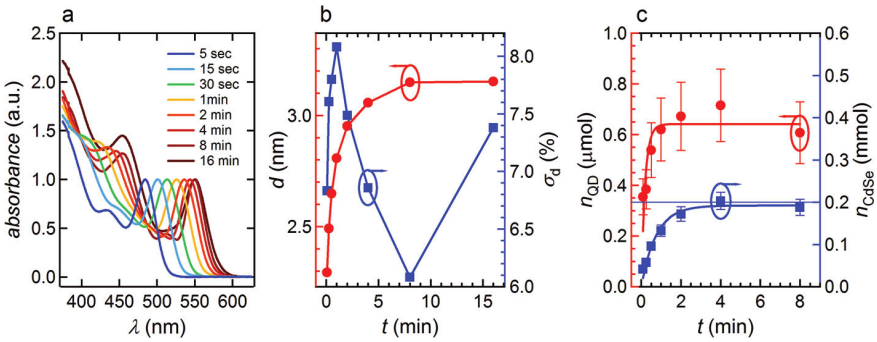

Figure 2.4: (a) Development of the absorption spectrum of CdSe QDs during a standard synthesis ($n_{\mathrm{Cd,0}} = 0.2$ mmol, $n_{\mathrm{Se,0}} = 2$ mmol, 245°C /230°C injection/growth temperature). (b) Time development of (red circles) the QD diameter d and (blue squares) the size dispersion. (c) Time development of the number of QDs (n_{QD}, red circles) and the amount of CdSe formed (n_{CdSe}, blue squares). The full lines are guides to the eye. The horizontal blue line indicates the 100% yield level.

the disappearance of TOP-Se is balanced by the formation of CdSe. This means that the monomer concentration is quasi-stationary, in line with the model synthesis, and that the time development of n_{CdSe} reflects the kinetics of the monomer generation in the experimental synthesis. Figure 2.5b shows n_{CdSe} as a function of time for three different combinations of $n_{\mathrm{Cd,0}}$ and $n_{\mathrm{Se,0}}$ under conditions of a 10-fold excess of Se. The thin horizontal lines indicate the 100% yield level for the different reactions (Cd-based), confirming that the Cd precursor is almost completely converted into CdSe for all three reactions. The full lines represent best fits of the experimental data to a model where the formation of CdSe depends in first order on n_{Cd}:

$$n_{\mathrm{CdSe}}(t) = n_{\mathrm{Cd,0}}(1 - e^{-k_1 t}) \tag{2.15}$$

The correspondence between this simple build-up model and the experimental data is surprisingly good.

A closer look at the fitting parameters represented in Figure 2.5c shows that the fitted value of $n_{\mathrm{Cd,0}}$ almost corresponds to the experimental one, as expected for a yield close to 100%. More importantly, we find that the rate constant k_1 increases proportionally to the precursor concentration. Since the ratio $n_{\mathrm{Cd,0}}$:$n_{\mathrm{Se,0}}$ was kept constant during these experiments, this suggests that the formation of CdSe is determined by a second-order monomer generation rate, which is proportional either to n_{Cd}^2 or to $n_{\mathrm{Cd}} \times n_{\mathrm{Se}}$.

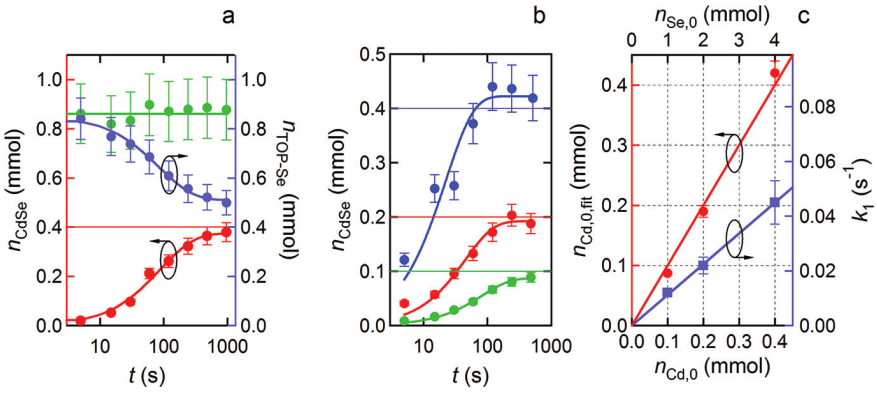

Figure 2.5: (a) Time evolution of the amount of (red) CdSe (n_{CdSe}), (blue) TOP-Se ($n_{\mathrm{TOP\text{-}Se}}$), and (green) the sum of both ($n_{\mathrm{Cd,0}}$, 0.4 mmol; $n_{\mathrm{Se,0}}$, 1 mmol, 245 °C /230 °C injection/growth temperature). The red and blue fitting lines are guides to the eye, whereas the green line indicates the number of moles of TOP-Se effectively injected (0.86 mmol). The horizontal red line shows the 100% yield level. (b) Time evolution of the amount of CdSe (n_{CdSe}) for reactions with a $n_{\mathrm{Cd,0}} : n_{\mathrm{Se,0}}$ ratio of 1:10, $n_{\mathrm{Cd,0}}$ ranges from (green) 0.1 mmol to (red) 0.2 mmol to (blue) 0.4 mmol, 245 °C /230 °C injection/growth temperature. The full lines through the data points represent best fits to eq 2.15. The horizontal lines indicate the respective 100% yield levels. (c) Fitting parameters, (red) $n_{\mathrm{Cd,0}}$ and (blue) k_1, obtained from a best fit of the data shown in (b) to a first-order buildup curve.

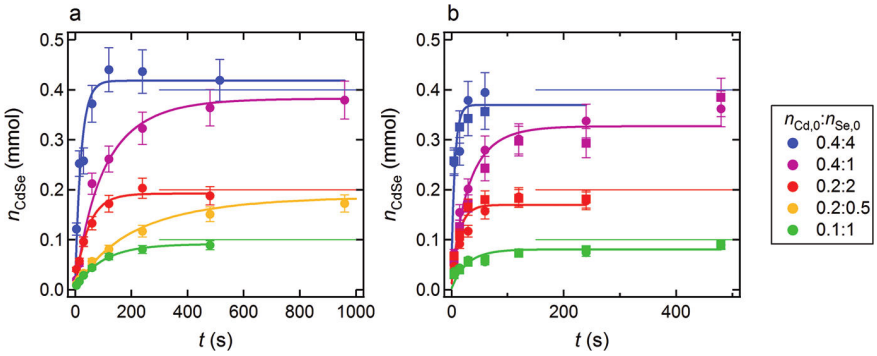

Figure 2.6: (a) Time evolution of the amount of CdSe formed (n_{CdSe}) for reactions with initial amounts $n_{\mathrm{Cd,0}}$ and $n_{\mathrm{Se,0}}$ as indicated in the legend (all numbers in mmol), 245 °C /230 °C injection/growth temperature. The horizontal lines indicate the respective 100% yield levels. The full lines through the data points represent best fits using a monomer generation rate that is first order in P_{Cd} and P_{Se}. (b) The same as in (a) using 280 °C /260 °C as injection/growth temperature. Note the different scale in the horizontal axis. The squares and the circles indicate different runs of the same experiment.

To investigate this more closely, the development of n_{CdSe} with time was determined at two different temperatures and for various combinations of $n_{\mathrm{Cd,0}}$ and $n_{\mathrm{Se,0}}$ (Figure 2.6a and b). For these experiments, the concentration of StA and HDA was adjusted proportionally to $n_{\mathrm{Cd,0}}$. As demonstrated in Figure 2.7, the reaction rate does not depend on the concentration of StA or HDA. Thus, differences in the yield development between different experiments directly reflect the influence of the precursor concentration on the reaction rate. Figure 2.6a and b show that reactions where the product $n_{\mathrm{Cd,0}} \times n_{\mathrm{Se,0}}$ is the same (purple and red data, orange and green data) have a coinciding slope dn_{CdSe}/dt at $t = 0$ and, thus, an identical initial reaction rate. Furthermore, for reactions with the same $n_{\mathrm{Cd,0}}$, the initial rate dn_{CdSe}/dt increases proportionally to $n_{\mathrm{Se,0}}$ (see Figure 2.6a, b and Figure 2.8). Both elements point towards a rate equation that depends in first order on n_{Cd} and n_{Se}.

To corroborate this conclusion, we have fitted the experimental development of $n_{\mathrm{CdSe}}(t)$ to a buildup curve based on a formation rate that is proportional to $n_{\mathrm{Cd,0}} \times n_{\mathrm{Se,0}}$ (see Figure 2.8). In these fits, a single value is used for the second-order rate constant k_2 and $n_{\mathrm{Cd,0}}$ is taken as an adjustable variable to compensate for reaction yields slightly different from 100%. As shown in Figure 2.6a and b, the agreement between the data and the best fit is remarkable and results in second-order rate constants of 0.14 ± 0.01 L/(s mol) at 230 °C and 0.56 ± 0.05 L/(s mol) at 260 °C . The fact that the formation of CdSe with time follows this simple second-order rate law, which is independent of the QD size and concentration, confirms that the CdSe formation is dominated by a monomer generation in solution and barely by a surface reaction of the separate precursors. Moreover, the first-order dependence of the CdSe formation rate on n_{Cd} and n_{Se} excludes the possibility that the monomers are in quasi-equilibrium with the precursors. Indeed, if this would be true, the rate of CdSe formation can be proportional to $n_{\mathrm{Cd,0}} \times n_{\mathrm{Se,0}}$ only if the rate of monomer consumption by nucleation and growth depends in first order on the monomer concentration, which is not the case (see Eq. 2.7 and 2.1) .

Steckel et al.[17] and Liu et al.[18] proposed a possible mechanism for the monomer formation in reactions similar to the one used here, involving the formation of a cadmium selenide complex (binding reaction), which decomposes further to a CdSe monomer (cleavage reaction):

$$\mathrm{Cd(OOCR)_2} + \mathrm{SePR_3} \underset{k_{-b}}{\overset{k_b}{\longleftrightarrow}} [\mathrm{Cd(OOCR)(SePR_3)}]^+[\mathrm{OOCR}]^- \quad (2.16)$$

$$[\mathrm{Cd(OOCR)(SePR_3)}]^+[\mathrm{OOCR}]^- \xrightarrow{k_c} \mathrm{CdSe{+}OPR_3{+}O(OCR)_2} \quad (2.17)$$

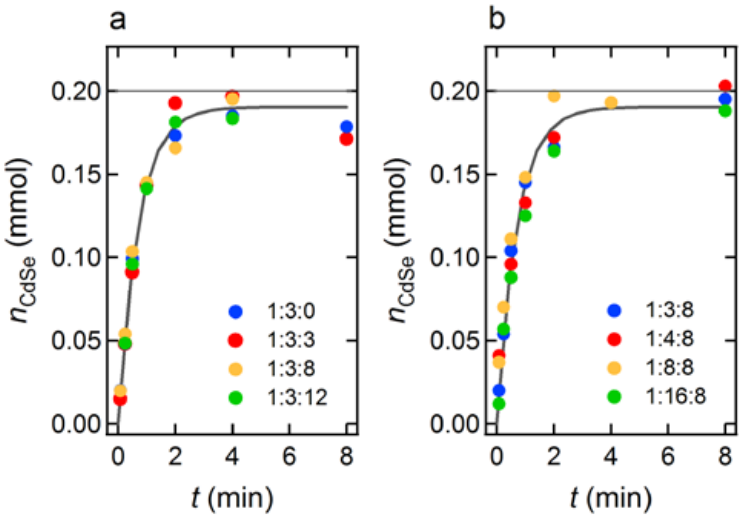

Figure 2.7: Time evolution of the amount of CdSe (n_{CdSe}) for (a) reactions with fixed initial concentrations of $Cd(StA)_2$, TOP-Se and StA, and different concentrations of HDA and (b) reactions with fixed initial concentrations of $Cd(StA)_2$, TOP-Se and HDA, and different concentrations of StA. The legends give the respective ratios $n_{Cd,0}$:n_{StA}:n_{HDA}. The horizontal lines indicate the 100% yield levels and the full line is a fit through the data points following a mixed second order monomer generation rate model[32]. $n_{Cd,0}$=0.2, $n_{Se,0}$=2, 245 °C /230 °C injection/growth temperature.

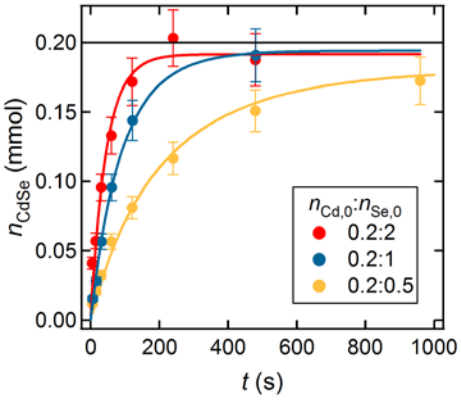

Figure 2.8: (a) Time evolution of the amount of CdSe formed (n_{CdSe}) for reactions with initial amounts $n_{\mathrm{Cd,0}}$ and $n_{\mathrm{Se,0}}$ as indicated in the legend (all numbers in mmol), 245 °C /230 °C injection/growth temperature. The horizontal line indicates the 100% yield level. The full lines through the data points represent best fits using a monomer generation rate that depends in first order on n_{Cd} and n_{Se} (see text).

In line with this mechanism, we find that the disappearance of TOP-Se results in the formation of an equivalent amount of TOPO (see Figure 2.9b). Hence, assuming that the above reaction scheme applies, the experimentally observed second-order rate equation indicates that the concentration of the complex is quasi-stationary, which leads to an effective second-order rate constant, $k_{2,eff} = k_c k_b/(k_c + k_{-b})$. In the limit $k_c \gg k_{-b}$, this implies that the binding reaction is rate determining, while if $k_c \ll k_{-b}$, the binding reaction (eq. 2.16) is in rapid, quasi-equilibrium and the cleavage reaction is rate determining. A similar result was found by Owen et al. [12] for cadmium phosphonate/TOPSe-based hot injection reactions. However, the fact that the CdSe formation rate does not depend on the concentration of added carboxylic acid or alkyl amines (see Figure 2.7) – which are both nucleophiles that can enhance the cleavage reaction – suggests that in this case the binding reaction is rate limiting.

With the monomer formation rate depending in first order on both precursors, the particular CdSe synthesis used here represents an ideal system for investigating the tuning of d_{PF} by the reaction rate. In the case of a Se excess for example, the pseudo-first-order rate constant of the monomer formation reaction is proportional to $n_{\mathrm{Se,0}}$ (Figure 2.5). Therefore, changing $n_{\mathrm{Se,0}}$ suffices to analyze the predicted link between the monomer formation

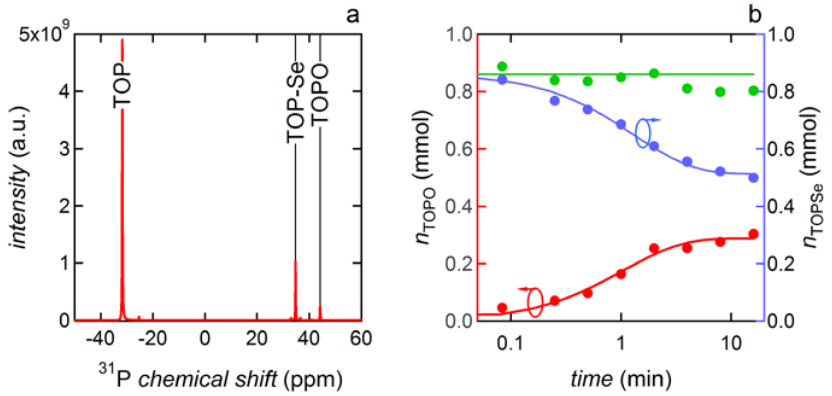

Figure 2.9: (a) ^{31}P NMR spectrum of the reaction mixture dissolved in toluene-$d8$ ($n_{\mathrm{Cd},0} = 0.4$ mmol, $n_{\mathrm{Se},0} = 1$ mmol, 245 °C /230 °C injection/growth temperature, sample taken after 1 min of reaction time) indicating the ^{31}P resonances of TOP , TOP-Se and TOPO. (b) Time evolution of the concentrations of (red) TOPO, (blue) TOP-Se and (green) their sum. The red and blue full lines are guides to the eye, the full green line indicates the initial amount of TOP-Se in the reaction mixture.

rate and d_{PF}.

2.5 Size Tuning by the Monomer Formation Rate

Using the typical simulated synthesis we showed in Section 2.3.2 that the initial nucleation rate is set by the initial monomer generate rate, and hence that the latter may be used to adjust the total number of particles nucleated, and, therefore, d_{PF}.

2.5.1 Simulation

Figure 2.10a shows G_M, J_N, and J_G for different monomer generation rates (*i.e.*, different first-order rate constants k_1 for the monomer generation reaction). As expected, G_M drops faster for higher reaction rates and the initial nucleation rate changes proportionally to k_1. However, changing k_1 has only a minor effect on the moment that Ostwald ripening exceeds nucleation. This results from the extreme dependence of the nucleation rate on S (see Figure 2.1), which implies that a change of G_M hardly affects the initial supersaturation and, thus, the initial r_c. Therefore, not only J_N but

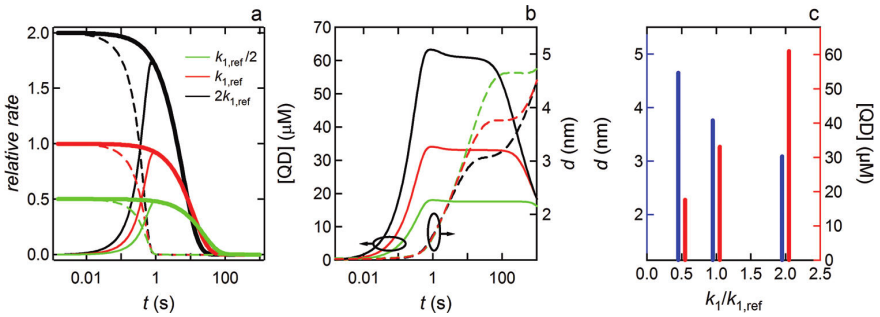

Figure 2.10: (a) (boldlines) Monomer generation rate; (full lines) rate of monomer consumption by growth; (dashed lines) rate of monomer consumption by nucleation for three different values of the first-order rate constant of monomer generation. Red: the value used in Figure 2.2 (k_1). Green: $k_1/2$. Black: $2k_1$. (b) (full lines) Change of the QD concentration and (dashed lines) the average QD diameter as a function of time. (c) (blue bars) QD diameter and (red bars) QD concentration at the end of the focusing regime.

also the number of particles formed by nucleation is proportional to G_M. This implies that also monomer consumption by growth scales proportionally to G_M and, thus, that the takeover of nucleation by growth hardly changes. The net effect is an increase of the QD concentration during the reaction-driven growth regime with increasing k_1 (Figure 2.10b). As the total amount of precursor stays constant, this implies that d_{PF} decreases if k_1 is raised. Since a 4-fold increase of k_1 leads to a significant reduction of d_{PF} in the model synthesis, this clearly is a potentially powerful tuning strategy.

2.5.2 Role of the Precursor Concentration

Figure 2.11 shows the development of n_{QD} and σ_d for three reactions with constant $n_{\mathrm{Cd,0}}$, while $n_{\mathrm{Se,0}}$:$n_{\mathrm{Cd,0}}$ is increased from 2.5 to 5 to 10. All reactions follow the general behavior of the model synthesis, with σ_d reaching its minimum at almost full yield. Moreover, in line with the model predictions (Figure 2.10), n_{QD} goes down when $n_{\mathrm{Se,0}}$ is decreased, and a larger d_{PF} is hence obtained for lower reaction rates (Figure 2.11c). Obviously, the time at which d_{PF} is reached increases when the reaction rate is reduced (Figure 2.11b).

As shown in Figure 2.12, this result can be generalized to different ini-

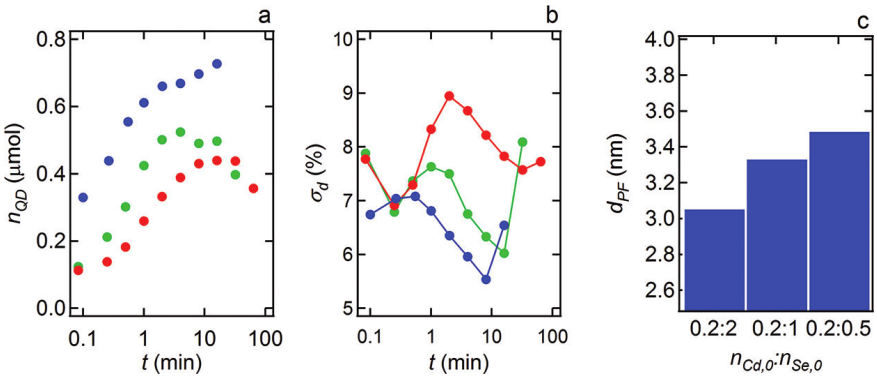

Figure 2.11: (a) Time evolution of the amount of QDs for reactions with $n_{\mathrm{Cd,0}}$:$n_{\mathrm{Se,0}}$ of (blue) 0.2:2, (green) 0.2:1, and (red) 0.2:0.5 (numbers in mmol), 245 °C /230 °C injection/growth temperature. (b) Time evolution of the size dispersion for the same reactions as in (a). (c) Postfocused diameter of the different reactions.

tial precursor concentrations. Doubling $n_{\mathrm{Cd,0}}$ and $n_{\mathrm{Se,0}}$ roughly leads to a 3-fold increase of the number of QDs. As expected from the CdSe formation kinetics, a separate increase of the cadmium, or the selenium precursor, leads to an increase of the number of nuclei as well, which is more pronounced when increasing the cadmium concentration. However, since the selenium precursor was kept in excess during this study, the absolute reaction yield goes up as well when the cadmium precursor concentration is increased. This makes size control by adjusting the selenium precursor concentration more efficient. Overall, changing the product $n_{\mathrm{Cd,0}} \times n_{\mathrm{Se,0}}$ by a factor of 64 allows us to vary the QD diameter from 2.8 to 4.1 nm and the position of the first electronic transition ($\lambda_{\mathrm{1S\text{-}1S}}$) from 529 to 601 nm with reaction yields in the range of 90% and low size dispersions (Figure 2.12). Hence, this approach represents a simple yet powerful strategy to tune d_{PF} in a hot injection synthesis, albeit at the expense of an increased reaction time and a reduction of the amount of material produced for larger sizes.

In the simulations, reducing k_1 by a factor of 4 increases d_{PF} by about 50% from 3.0 to 4.6 nm. Experimentally, a more moderate increase from 2.8 to 4.1 nm is achieved by changing $n_{\mathrm{Se,0}}$ and $n_{\mathrm{Cd,0}}$ over a range that approximately corresponds to a 16-fold increase of the pseudo-first-order rate constant. This more limited tuning in the experimental system can be linked to the duration of the nucleation. Opposite of the simulations, Figure 2.11a and b indicate that the rise of n_{QD} and the initial defocusing last longer

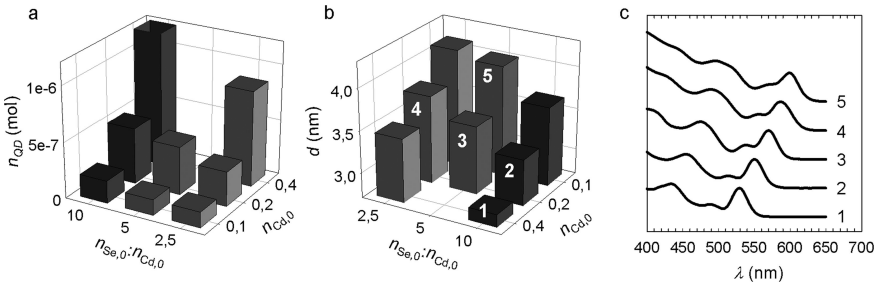

Figure 2.12: (a) Concentration of QDs formed as a function of $n_{\text{Cd,0}}$ and the $n_{\text{Se,0}}$:$n_{\text{Cd,0}}$ ratio; 280 °C /260 °C injection/growth temperature. (b) Postfocused diameter obtained as a function of $n_{\text{Cd,0}}$ and the $n_{\text{Se,0}}$:$n_{\text{Cd,0}}$ ratio. Note that the direction of each axis is swapped with respect to (a). (c) Absorption spectrum corresponding to the samples as indicated in (b).

if the monomer generation rate is reduced. For example, the moment the maximum in the size dispersion is reached increases from 15 s up to 1 min when $n_{\text{Se,0}}$ is reduced from 2 to 0.5 mmol. This prolonged nucleation implies that a reduction of the monomer formation rate reduces n_{QD} less than predicted by the modeling, which leads in turn to a smaller than expected increase of d_{PF}. Within the logic of the simulations, the experimentally observed prolonged nucleation indicates that the dependence of the nucleation rate on S is less extreme than expressed by Eq. 2.7, an expression typically used to describe the nucleation event in a hot injection synthesis.[1;33;34] According to classical nucleation theory, the nucleation rate is linked to the free energy barrier $\Delta_N G$ for nucleation:

$$\Delta_N G = \frac{16\pi\gamma^3\nu_0^2}{3(k_bT)^2(\ln S)^2} = \frac{4\pi}{3}\gamma r_c^2 \tag{2.18}$$

Hence, the experimentally observed persistence of the nucleation at larger r_c (or lower supersaturation) implies that $\Delta_N G$ increases less strongly than assumed with increasing r_c. Following Eq. 2.18, this could for example result from a reduction of the surface tension with increasing QD diameter, which is not unexpected given the strong reduction of the surface curvature that accompanies QD growth. The occurrence of a prolonged nucleation also indicates that hot injection followed by burst nucleation is not required to obtain narrow size distributions, opposite of what is often proposed in the description of the hot injection synthesis.[33]

2.5.3 Role of Temperature

A classical description of the hot injection synthesis is that the rapid injection of precursors into a hot (surfactant) solution produces a high degree of supersaturation, resulting in a burst nucleation by relieving the excess free energy of the supersaturation.[33] Looking at the expression for the critical radius and the nucleation rate, this should result in the formation of more and smaller nuclei at higher temperature and, thus, a decrease of d_{PF}. A similar conclusion could follow from the viewpoint that the nucleation rate is set by the monomer generation rate, since the second-order rate constant of this reaction increases with temperature. Opposite of this expected trend, Figure 2.13 shows that the reaction temperature has no significant effect on d_{PF} and thus on the QD concentration. Similarly, Joo et al.[34] observed that in the case of the PbSe synthesis, increasing the injection temperature leads to a decrease of the QD concentration during growth and an increase of the QD diameter. These contradictions are hard to reconcile with the classical description linking hot injection to burst nucleation. On the other hand, they can be understood by considering that, next to the monomer formation rate, also the rate of QD nucleation and growth depend on temperature. For example, if an increase of the temperature significantly enhances the growth rate, *e.g.*, linked to an increase of the monomer solubility, the time span of nucleation will be reduced. Since the total number of particles formed during the nucleation stage depends on both the nucleation rate and the time span of nucleation, the net effect of a temperature change on the final QD concentration and diameter is difficult to predict. For the present synthesis, it appears that the net effect of the change of nucleation rate and nucleation time span is that d_{PF} is almost insensitive to a change in temperature. Importantly, this lack of temperature dependence explains the high reproducibility of the postfocused diameter for given conditions as shown in Figure 2.12. Clearly, this is an important advantage of the reaction presented here.

2.6 Size Tuning at Constant Formation Rate

2.6.1 Experimental CdSe Synthesis

We establish the influence of the free acid concentration on nanocrystal size in an experimental hot injection synthesis and try to link it to a simulation parameter. We study the relation between the concentration of free acid, the reaction rate and the QD diameter in a typical zincblende CdSe QD synthesis, very similar to the synthesis used in the previous section. This involves

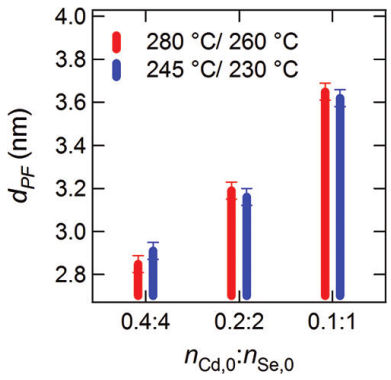

Figure 2.13: Postfocused diameter obtained for different initial concentrations at two different combinations of injection and growth temperature.

the injection of trioctylphosphine selenide (TOP-Se) in a hot mixture of cadmium oleate ($Cd(OA)_2$), oleic acid (OA) and hexadecylamine (HDA) in octadecene (ODE).[11;20] Different reactions are characterized by the ratio $Cd(OA)_2$:total OA:HDA, where total OA refers to the sum of the OA used to coordinate the Cd^{2+} and excess, free OA. For the different reactions, only total OA is changed by changing the amount of free OA.

Figure 2.14a gives an example of absorption spectra recorded on aliquots for a 1:4:3 (Cd:OA:HDA) synthesis. In line with previously published data on this synthesis, the absorption peak of the first exciton ($\lambda_{1S\text{-}1S}$) progressively shifts to longer wavelengths and tends towards a limiting value at 480 s. Obviously, d_{QD} follows the same trend (Figure 2.14b). The size dispersion on the other hand reaches a minimum value at around 240 s — indicative of size focusing — and slightly increases afterwards.

Figure 2.15a shows the absorption spectra of aliquots taken after 480 s of reaction time for syntheses where the Cd:OA:HDA ratio is progressively raised from 1:4:3 to 1:64:3. The red shift and broadening of the first exciton absorption peak already indicates that this results in a concomitant increase of both d_{QD} and σ_d , which change from about 3.1 to 5.1 nm and 6.3 to 16.9%, respectively (Figure 2.15b). For three different Cd:OA:HDA ratios, we have determined the time development of n_{CdSe}, d_{QD} and the number of QDs n_{QD} by taking aliquots and analyzing the respective absorption spectra. As indicated in Figure 2.14c, the time development of n_{CdSe}, which directly reflects the reaction rate, is almost independent of the amount of OA. A global fit of the three curves assuming G_M to be first order in TOP-Se and

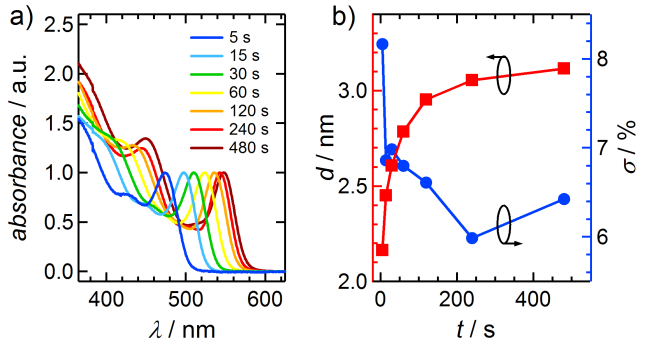

Figure 2.14: (a) Absorption spectrum of aliquots taken at the indicated times after injection for a CdSe synthesis using $Cd(OA)_2$ and TOP-Se as precursors in ODE. Cd:OA:HDA = 1:4:3. (b) Evolution of (red) d_{QD} and (blue) σ_d with time as calculated from the spectra shown in (a).

$Cd(OA)_2$ yields a second order rate constant of 0.11 L/(mol·s), a number in line with the values obtained in Section 2.6. On the other hand, raising [OA] significantly reduces the amount of QDs formed (see Figure 2.14d), and thus the final QD diameter. Figure 2.14d indicates that this change in diameter is linked to a reduction of the nucleation time. Whereas for the 1:32:3 synthesis n_{QD} is within 5% of the final value after 30-60 s, this takes 2-4 minutes for the 1:4:3 synthesis.

The increase of d_{QD} — and decrease of n_{QD} — with increasing acid concentration as shown here for a particular CdSe QD synthesis has been reported for a wide range of colloidal nanocrystals, including both semiconductors and metal oxides. This relation is typically seen as counterintuitive. Since free acids are supposed to act as ligands, raising their concentration should increase the ligand density on the QD surface and thus hamper nanocrystal growth.[25] Several authors therefore proposed that the increase of the number of nanocrystals formed when lowering the free acid concentration reflects an enhanced reactivity during the nucleation stage. Opposite from this, we find that the free acid concentration does not affect the overall reaction rate, which indicates that the observed size tuning does not result from an enhanced reactivity. This conclusion is supported further by literature results on ligand densities. Irrespective of the QD material and the free acid concentration during synthesis, these typically yield 3-5 nm^{-2},[35–37] which questions the conjecture that raising the free acid concentration has

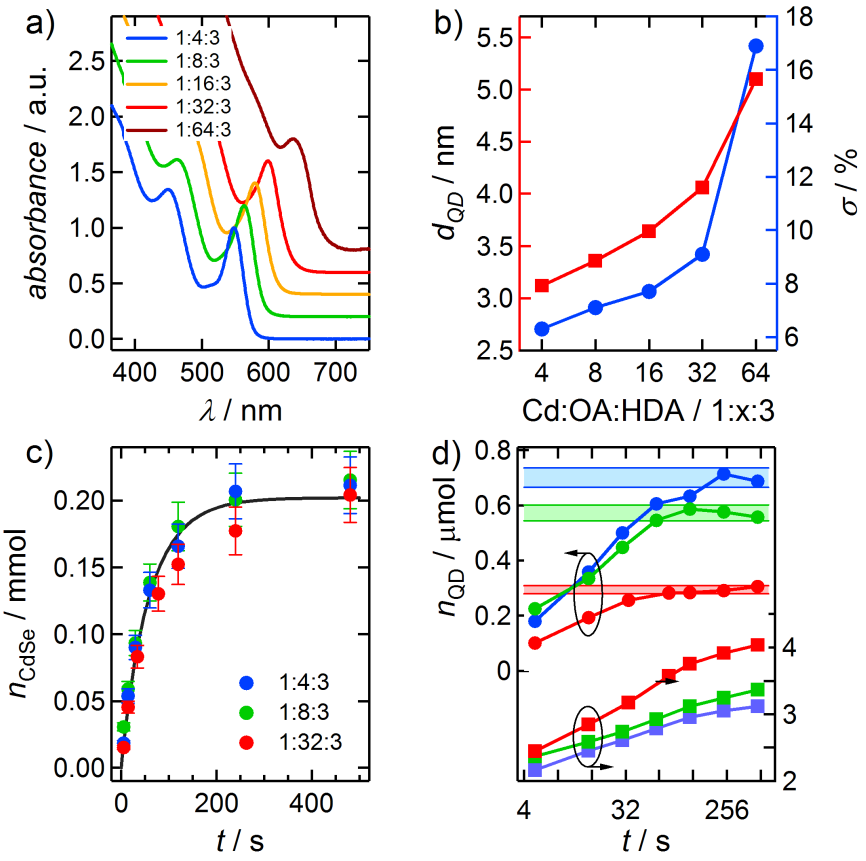

Figure 2.15: (a) Absorption spectrum of aliquots taken after 480 s of reaction time for different Cd:OA:HDA ratios. (b) (red) d_{QD} and (blue) σ_d after 480 s reaction time for the different reactions shown in (a). (c) Amount of CdSe formed as a function of time for three different Cd:OA:HDA ratios as indicated. The full line is a best global fit assuming G_M to be first order in $Cd(OA)_2$ and TOP-Se. (d) Time evolution (log2 scale) of (circles) amount of QDs and (squares) QD diameter for the same reactions as in (c). The same color code applies. The shaded regions indicate a range of $\pm 5\%$ around the final QD concentration.

a significant effect on the ligand density.

2.6.2 Simulated Synthesis

According to the simulations, size tuning at constant reaction rate is possible by accelerating or delaying the takeover of nucleation by growth, where an earlier takeover leads to less and thus larger nanocrystals. This is achieved by varying the monomer solubility $[M]_0$. In principle, $[M]_0$ corresponds to the amount of unreacted Cd at the end of the reaction. However, regardless of the oleic acid concentration, the CdSe synthesis we use has a yield of about 100%. This indicates that $[M]_0$ is considerably smaller than the initial concentration of $Cd(OA)_2$, which unfortunately prevents a reliable determination of $[M]_0$ by directly measuring it. The same effect of size tuning at constant reaction rate can result from an increase of the free energy barrier for nucleation, which implies that nucleation requires a higher supersaturation — and thus favors growth — or from an increase of the monomer adsorption rate.

Influence of the Surface Tension γ

Figure 2.16 shows the results of simulations where starting from the reference values for the different parameters (see Table 2.2), the surface tension has been progressively increased. Following Eq. 2.7, a higher surface tension implies that a higher supersaturation is required to achieve the same nucleation rate. Again, this enhances the growth rate and thus expedites the takeover of nucleation by growth. The simulations are in line with this description. As can be seen in Figure 2.16(a), the higher the surface tension, the lower the nanocrystal concentration and the larger their size. Due to the exponential dependence of the nucleation rate on the surface tension, nanocrystal concentration and size are very sensitive to the surface tension (see Figure 2.16(b)). Since the ratio D/k_g^∞ stays put in these simulations, the enhanced growth rate strongly promotes size distribution focusing (see Figure 2.16(c)), opposite from the effect an increase of the carboxylic acid concentration has on a real nanocrystal synthesis (see Figure 2.16(d)), as will be discussed in more detail in Section 2.6.

Influence of the Rate Constant for Nanocrystal Growth k_g^∞

Figure 2.17 shows the results of simulations where starting from the reference values for the different parameters (see Table 2.2), the growth rate k_g^∞ has been progressively increased. Following Eq. 2.7, this implies that

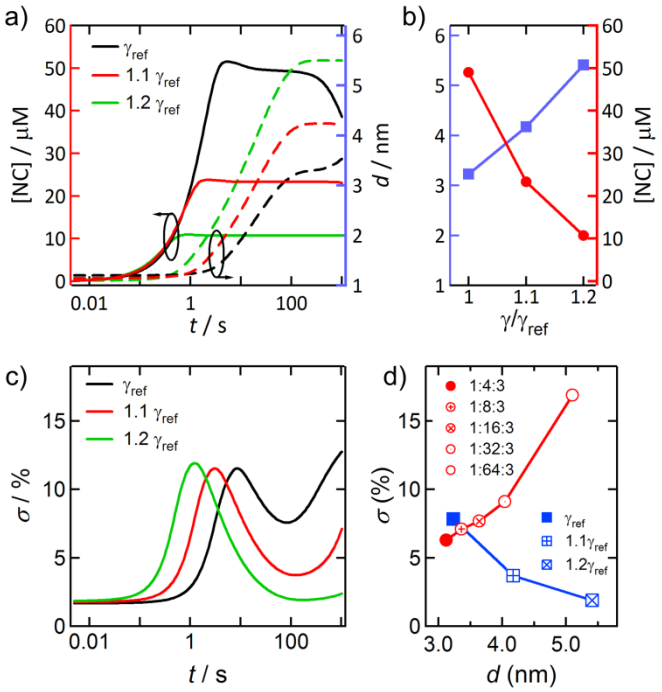

Figure 2.16: (a) Nanocrystal concentration and diameter for simulations where relative to the reference values, the surface tension has been increased as indicated. (b) Size and concentration after 128 s as a function of the surface tension. (c) Evolution of the size dispersion for the same simulations as shown in Figure 2.17a). (d) (blue) Size dispersion vs. size after 128 s for the same series of simulations as shown in (a), (b) and (c). (red) Experimental data obtained by varying the acid concentration (same data as in Figure 2.15).

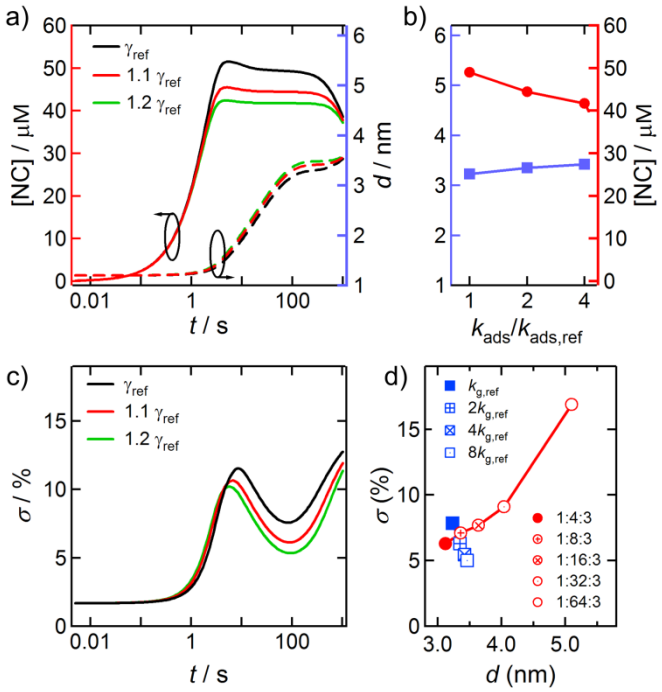

Figure 2.17: (a) Nanocrystal concentration and diameter for simulations where relative to the reference values, the rate constant for growth has been increased as indicated. (b) Size and concentration after 128 s as a function of the surface tension. (c) Evolution of the size dispersion for the same simulations as shown in (a). (d) (blue) Size dispersion vs. size after 128 s for the same series of simulations as shown in (a), (b) and (c). (red) Experimental data obtained by varying the acid concentration (same data as in Figure 2.15).

the growth rate goes up, while the reaction is pushed into the diffusion limited regime even further. Again, the enhanced growth rate expedites the takeover of nucleation by growth, which leads to larger particles. In this case, the effect is limited since the reference simulation is already close to diffusion limitation. However, also in this case, larger sizes correspond to more narrow size distributions, opposite from the experimental observation (see Section 2.6).

Influence of the Solubility $[M]_0$

Equation 2.4 for the growth rate of a colloidal nanocrystals was derived within a framework where the rate of monomer incorporation in the nanocrystals j_g and of monomer dissolution j_d are written as first and zeroth order in the monomer concentration, respectively:

$$j_g = 4\pi r^2 k_g^\infty e^{-\alpha \frac{2\gamma\nu_0}{r k_b T}} [M] \quad (2.19)$$

$$j_d = 4\pi r^2 k_d^\infty e^{1-\alpha \frac{2\gamma\nu_0}{r k_b T}} [M] \quad (2.20)$$

Here, k_g^∞ and k_d^∞ are the rate constants for growth and dissolution for a flat surface, while the exponential factors take the effect of the curved surface of the nanocrystal into account. Importantly, both rate constants are related to the monomer solubility $[M]_0$ according to:

$$\frac{k_d^\infty}{k_g^\infty} = [M]_0 \quad (2.21)$$

Hence, if the monomer solubility changes, either k_g^∞, k_d^∞ or both must change as well.

The effect a change of the solubility has on the rate constants for adsorption and desorption as expressed by Eq. 2.22 can be understood from the thermodynamic scheme shown in Figure 2.18(a). A change in solubility is a result of a change in the standard free energy of dissolution $\Delta_{sol}G^\circ = \mu_{sol}^0 - \mu_s^0$ of the solute, where an increased solubility corresponds to a lowering of $\Delta_{sol}G^\circ$. Comparing two solubilities $[M]_0$ and $[M]_{0,ref}$ one has:

$$\Delta_{sol}G^0 = \mu_{sol}^0 - \mu_{sol}^0 = \Delta_{sol}G_{0,ref}^\circ - RT \ln \frac{[M]_0}{[M]_{0,ref}} \quad (2.22)$$

Since the chemical potential of the solid remains fixed, an increase of the solubility corresponds to a lowering of the standard chemical potential of the solute. As shown in Fig 2.18(a), this results in an increase of the activation barrier for the growth process. We thus expect that k_g^∞ goes down if $[M]_0$ is raised.

Assuming that a transfer coefficient β determines how a change in the free energy of dissolution is distributed over the free energy barrier for growth and dissolution (see Figure 2.18(a)), one gets:

$$k_g^\infty = k_{g,ref}^\infty \left(\frac{[M]_{0,ref}}{[M]_0} \right)^\beta \quad (2.23)$$

$$k_d^\infty = k_{d,ref}^\infty \left(\frac{[M]_{0,ref}}{[M]_0} \right)^{\beta-1} \quad (2.24)$$

In our simulations, we have assumed — as indicated in Table 2.2 — that k_g^∞ is inversely proportional to $[M]_0$, *i.e.*, we take $\beta = 1$. The decrease of the rate constant for growth with increasing solubility means that the ratio D/k_g^∞ will go up. This implies that the reaction shifts from the regime of diffusion control to the regime of kinetic control, with a concomitant loss of size-focusing. This is crucial to retrieve the experimentally observed loss of size focusing in the modeling. Figure 2.18(b) and (c) represents simulation results for different values of $[M]_0$, while k_g^∞ is kept fixed. One clearly sees that this results in a pronounced size tuning, yet with size dispersions that go down with increasing solubility. On the other hand, when k_g^∞ goes down with increasing $[M]_0$, larger solubilities imply larger sizes and deteriorated size dispersions (see Figure 2.18(d), (e) and (f)).

Linking Free Acid Concentration to Solubility

In the previous paragraphs we showed simulation results where we changed either the free energy barrier for nucleation, by varying the QD surface tension γ (on p. 45), or the monomer adsorption rate by varying k_g^∞ (on p. 45). The key result is summarized in Figure 2.19. We find that an increase of both γ and k_g^∞ lead to larger nanocrystals. However, the increase of d_{QD} comes with a marked reduction of the size dispersion σ_d . This effect can be understood by considering that the enhanced consumption of monomers by growth is achieved either by raising the supersaturation (due to an increase of γ) or k_g^∞. Both conditions enhance the size focusing, which leads to a reduction of σ_d for larger diameters. Opposite from this, increasing the free acid concentration in the CdSe synthesis studied deteriorates the size dispersion (see Figure 2.15(b) and Figure 2.19), a result also reported in the literature for other material systems.[15]

As outlined in Section 2.6.2 (on p. 48), an increase in solubility shifts the reaction from diffusion control ($D/k_g^\infty \ll 1$) towards kinetic control ($D/k_g^\infty \gg 1$), *i.e.*, out of the size-focusing regime.[27] As confirmed by the simulation results shown in Figure 2.19 (blue markers), this leads to an increase of d_{QD} with a concomitant deterioration of the size dispersion in agreement with the experimental results. The decrease of k_g^∞ with increasing $[M]_0$ is therefore essential to retrieve a deteriorated size dispersion for larger diameters.

We thus conclude that free acids raise d_{QD} since they increase the monomer solubility. This promotes monomer consumption by growth over consumption by nucleation. As a result, less nanocrystals are formed, which thus grow to larger sizes while the reaction rate remains fixed.

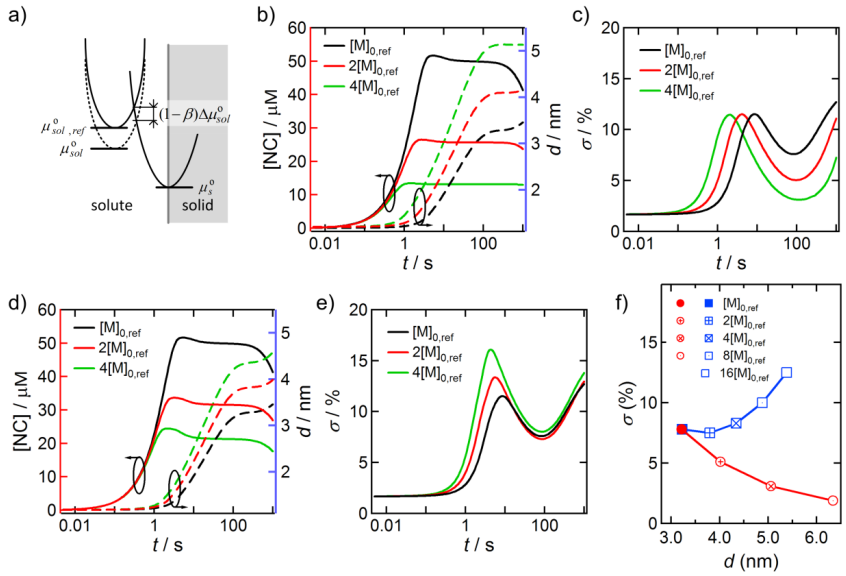

Figure 2.18: (a) Thermodynamic scheme illustrating the effect of an enhanced stabilization of the solute on the free energy barrier for growth (left to right) and dissolution (right to left). (b) Nanocrystal concentration and mean diameter for simulations where relative to the reference value, the solubility is raised as indicated while the rate constant for growth is kept constant. (c) Size disperions for the same series of simulations as shown in (b). (d) Nanocrystal concentration and mean diameter for simulations where relative to the reference value, the solubility is raised as indicated and the rate constant for growth is changed according $\sim 1/[M]_0$. (e) Size disperions for the same series of simulations as shown in (d). (f) Size dispersion *vs.* diameter after 128 s for the reaction simulations shown in (red) (b) and (c) and (blue) (d) and (e).

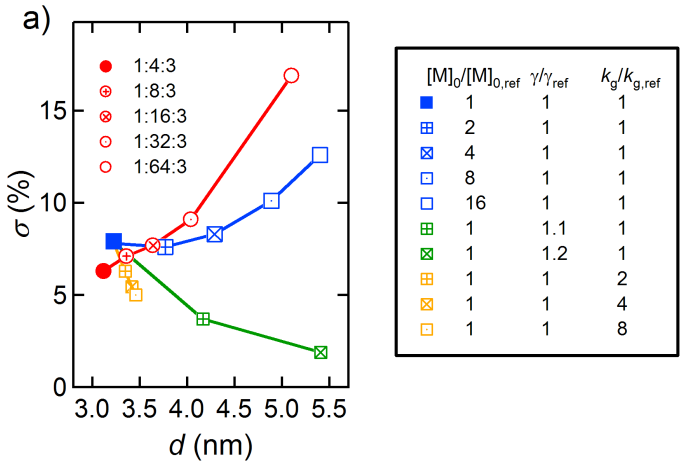

Figure 2.19: Size dispersion as a function of diameter for reaction simulations as a function of (blue) $[M]_0$, (green) γ and (orange) k_g^∞ (data taken after 128 s) and (red) experimental synthesis for the indicated Cd:OA:HDA combinations (data taken after 480 s). The table lists the particular parameter values used in each simulation.

2.7 Size Focusing in the PbSe and PbTe Synthesis

The synthesis of PbSe[8] and PbTe[38] is an extreme example of the role of the monomer generation rate in high-quality syntheses. The most common synthetic schemes were optimized for size tuning and sharp size distributions at the cost of very low reaction yields in the order of a few percent. Joo et al.[34] showed that the injected precursors — lead oleate (Pb|OA) and trioctylphosphine selenide (TOPSe) or telluride (TOPTe) — are not directly incorporated into the QDs, but go through a reduction reaction first. Since in the normal synthetic schemes, the reducing agent needed for this reaction is only present in the form of impurities, the monomer generation rate is low, resulting in a low reaction yield. As shown by Joo et al.[34] a controlled addition of these impurities can significantly improve the chemical yield, while still providing sufficient control over size and size dispersion.

2.7.1 Ostwald Focusing

Besides the low reaction yield, the common lead chalcogenide synthesis shows a continuous dissolution of particles all throughout the reaction, even during the growth and focusing stage. We illustrate this using an optimized form of the PbTe synthesis[38], where we inject 0.5 mmol of TOPSe into 1 mmol of Pb|EA (lead erucitate), dissolved in ODE at 145 °C . Figure 2.20 shows the evolution of the size d_{QD}, size dispersion σ_d, the amount of QDs formed n_{QD} and the amount of PbTe formed n_{PbTe}. As expected from the low amount of impurities driving the monomer generation reaction, n_{PbTe} is much lower than the amount of injected precursors and increases approximately linearly in time (as the precursor concentration remains almost constant throughout the reaction). Figure 2.20(a) shows the gradual increase of the QD diameter with time from 4 to 8 nm and a concomitant reduction of the size dispersion from 9 to 5%, indicative of size focusing. At the same time however, the amount of QDs (see Figure 2.20(b)) reduces from 3.5 nmol to 1.4 nmol.

As explained in Section 2.2.4 (p. 24), dissolution of QDs is known as Ostwald ripening, an effect where smaller QDs dissolve and feed growth of the larger QDs. This is usually considered an adverse effect, as the size dispersion increases simultaneously. The regime where QDs grow, focus and dissolve all at the same time is different from typical focusing in QDs and has never been described in literature before.

We postulate here a second focusing criterion (see Section 2.2.4) to explain this new focusing mechanism, which we coin *Ostwald focusing*. The first criterion for classical focusing stated that the ratio of the QD radius

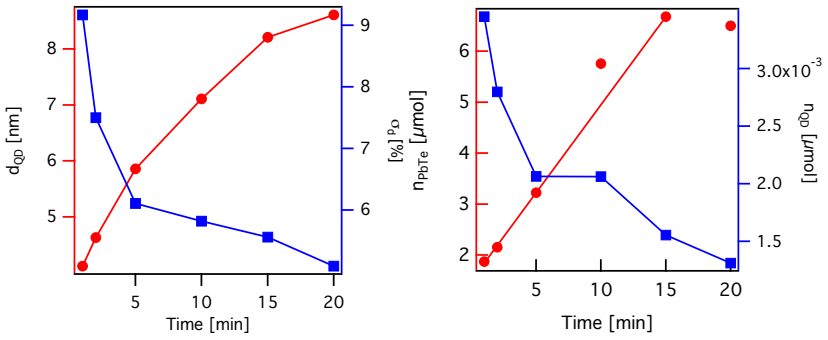

Figure 2.20: (a) The PbTe QD diameter (red) increases with reaction time as the size dispersion (blue) reduces, as expected from a size focusing synthesis (b) The amount of PbTe (red) increases linearly (except for the last data point). The red line is a linear fit to all data points but the last. The number of QDs (blue) reduces with reaction time.

to the critical radius needs to be larger than 1.55. Ostwald focusing can only occur when, regardless of the expression or exact shape of the growth rate function, the critical radius moves faster than the average QD radius:

$$\frac{dr_c}{dt} > \frac{dr_{QD}}{dt} \tag{2.25}$$

Only then will the dissolution of smaller particles result in a more narrow size distribution. The mathematics and physical chemistry of this radical new focusing concept remain to be explored.

In a first attempt, we show that at least qualitatively our simulation model is able to combine QD dissolution with size focusing. Under conditions of a constant monomer generation rate with a lower solubility $[M]_0 = 8\ 10^{-9}$ mol/m^3, a lower reaction temperature $T = 135$ °C and a lower surface tension $\gamma = 0.092$ J/m^2, Figure 2.21(a) shows that the size dispersion decreases for $r/r_c < 1.55$ and hence that another focusing mechanism plays a role. Figure 2.21 then shows that this size focusing occurs simultaneously with QD dissolution.

2.8 Conclusion

In this Chapter we combined the outcome of model cadmium and lead chalcogenide QD syntheses with a continuum simulation model, that includes monomer generation and depletion, QD nucleation and growth. We

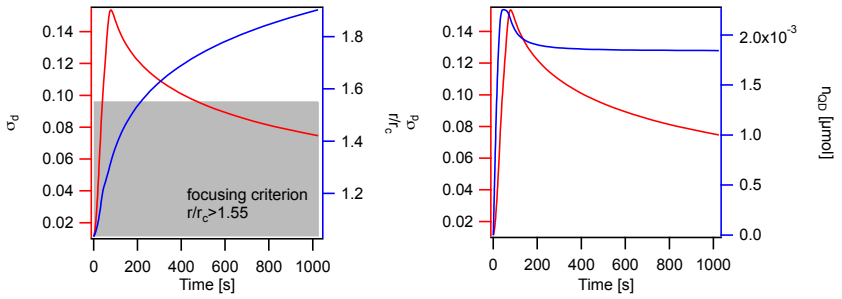

Figure 2.21: (a) Size dispersion (red) decreases with increasing time. The focusing parameter r/r_c (blue), together with the criterion $r/r_c > 1.55$ shows that it does not hold for this simulation. (b) Size focusing occurs together with dissolution of the number of QDs n_{QD} (blue).

showed that the simulation model yields similar dynamics as experimental syntheses and systematically investigated the influence of the simulation parameters, such as the monomer reaction rate constant, the monomer solubility, the surface tension and the rate constant for nanocrystal growth.

Comparing this with a model CdSe synthesis, we were able to link two experimental reaction chemistry parameters — the precursor concentration and the free acid concentration — to two distinct simulation model parameters — the monomer generation rate and the solubility.

We now understand that the initial precursor concentration changes the rate of the monomer generation. In turn, more QDs can nucleate during the nucleation stage, leaving less monomer avaible for growth. As a result, higher initial precursor concentrations yield more, yet smaller QDs.

The signature influence of a change in the free acid concentration — more free acid yields larger and more polydisperse QDs — we clearly identified as a increase of the monomer solubility (and a concomitant decrease of the rate constant for nanocrystal growth).

Finally we showed that the peculiar focusing mechanism of lead chalcogenide QDs, *i.e.* dissolution-aided QD focusing, is reproduced in part by our simulation model by lowering the solubility, the reaction temperature and the surface tension.

Our results have identified the first set of reaction chemistry/nanocrystal property relations, a key to designing size tuning strategies at full yield. It proves the validity of our simulation model and highlights its importance as a tool for more model-driven design of experiment syntheses.

References

[1] Kwon, S. G.; Piao, Y.; Park, J.; Angappane, S.; Jo, Y.; Hwang, N.-M.; Park, J.-G.; Hyeon, T. Kinetics of monodisperse iron oxide nanocrystal formation by "heating-up" process. *Journal of the American Chemical Society* **2007**, *129*, 12571–12584.

[2] Li, J. J.; Wang, Y. A.; Guo, W. Z.; Keay, J. C.; Mishima, T. D.; Johnson, M. B.; Peng, X. G. Large-scale synthesis of nearly monodisperse CdSe/CdS core/shell nanocrystals using air-stable reagents via successive ion layer adsorption and reaction. *Journal of the American Chemical Society* **2003**, *125*, 12567–12575.

[3] Murray, C. B.; Norris, D. J.; Bawendi, M. G. Synthesis and Characterization of Nearly Monodisperse CdE (E = S, Se, Te) Semiconductor Nanocrystallites. *Journal of the American Chemical Society* **1993**, *115*, 8706–8715.

[4] Li, L.; Daou, T. J.; Texier, I.; Chi, T. T. K.; Liem, N. Q.; Reiss, P. Highly Luminescent CuInS2/ZnS Core/Shell Nanocrystals: Cadmium-Free Quantum Dots for In Vivo Imaging. *Chemistry of Materials* **2009**, *21*, 2422–2429.

[5] Xie, R.; Battaglia, D.; Peng, X. Colloidal InP nanocrystals as efficient emitters covering blue to near-infrared. *Journal of the American Chemical Society* **2007**, *129*, 15432–+.

[6] Jasieniak, J.; Bullen, C.; van Embden, J.; Mulvaney, P. Phosphine-free synthesis of CdSe nanocrystals. *Journal of Physical Chemistry B* **2005**, *109*, 20665–20668.

[7] Hines, M. A.; Scholes, G. D. Colloidal PbS nanocrystals with size-tunable near-infrared emission: Observation of post-synthesis self-narrowing of the particle size distribution. *Advanced Materials* **2003**, *15*, 1844–1849.

[8] Murray, C. B.; Sun, S. H.; Gaschler, W.; Doyle, H.; Betley, T. A.; Kagan, C. R. Colloidal synthesis of nanocrystals and nanocrystal superlattices. *Ibm Journal of Research and Development* **2001**, *45*, 47–56.

[9] Peng, Z. A.; Peng, X. G. Formation of high-quality CdTe, CdSe, and CdS nanocrystals using CdO as precursor. *Journal of the American Chemical Society* **2001**, *123*, 183–184.

[10] Talapin, D. V.; Rogach, A. L.; Kornowski, A.; Haase, M.; Weller, H. Highly luminescent monodisperse CdSe and CdSe/ZnS nanocrystals synthesized in a hexadecylamine-trioctylphosphine oxide-trioctylphospine mixture. *Nano Letters* **2001**, *1*, 207–211.

[11] Chan, E. M.; Xu, C.; Mao, A. W.; Han, G.; Owen, J. S.; Cohen, B. E.; Milliron, D. J. Reproducible, High-Throughput Synthesis of Colloidal Nanocrystals for Optimization in Multidimensional Parameter Space. *Nano Letters* **2010**, *10*, 1874–1885.

[12] Owen, J. S.; Chan, E. M.; Liu, H.; Alivisatos, A. P. Precursor Conversion Kinetics and the Nucleation of Cadmium Selenide Nanocrystals. *Journal of the American Chemical Society* **2010**, *132*, 18206–18213.

[13] van Embden, J.; Mulvaney, P. Nucleation and growth of CdSe nanocrystals in a binary ligand system. *Langmuir* **2005**, *21*, 10226–10233.

[14] Bullen, C. R.; Mulvaney, P. Nucleation and growth kinetics of CdSe nanocrystals in octadecene. *Nano Letters* **2004**, *4*, 2303–2307.

[15] Yu, W. W.; Peng, X. G. Formation of high-quality CdS and other II-VI semiconductor nanocrystals in noncoordinating solvents: Tunable reactivity of monomers. *Angewandte Chemie-International Edition* **2002**, *41*, 2368–2371.

[16] Xie, R.; Li, Z.; Peng, X. Nucleation Kinetics vs Chemical Kinetics in the Initial Formation of Semiconductor Nanocrystals. *Journal of the American Chemical Society* **2009**, *131*, 15457–15466.

[17] Steckel, J. S.; Yen, B. K. H.; Oertel, D. C.; Bawendi, M. G. On the mechanism of lead chalcogenide nanocrystal formation. *Journal of the American Chemical Society* **2006**, *128*, 13032–13033.

[18] Liu, H.; Owen, J. S.; Alivisatos, A. P. Mechanistic study of precursor evolution in colloidal group II-VI semiconductor nanocrystal synthesis. *Journal of the American Chemical Society* **2007**, *129*, 305–312.

[19] Rempel, J. Y.; Bawendi, M. G.; Jensen, K. F. Insights into the Kinetics of Semiconductor Nanocrystal Nucleation and Growth. *Journal of the American Chemical Society* **2009**, *131*, 4479–4489.

[20] Protière, M.; Nerambourg, N.; Renard, O.; Reiss, P. Rational design of the gram-scale synthesis of nearly monodisperse semiconductor nanocrystals. *Nanoscale Research Letters* **2011**, *6*, 472.

[21] Capek, R. K.; Lambert, K.; Dorfs, D.; Smet, P. F.; Poelman, D.; Eychmueller, A.; Hens, Z. Synthesis of Extremely Small CdSe and Bright Blue Luminescent CdSe/ZnS Nanoparticles by a Prefocused Hot-Injection Approach. *Chemistry of Materials* **2009**, *21*, 1743–1749.

[22] Dai, Q.; Kan, S.; Li, D.; Jiang, S.; Chen, H.; Zhang, M.; Gao, S.; Nie, Y.; Lu, H.; Qu, Q.; Zou, G. Effect of ligands and growth temperature on the growth kinetics and crystal size of colloidal CdSe nanocrystals. *Materials Letters* **2006**, *60*, 2925 – 2928.

[23] Battaglia, D.; Peng, X. Formation of high quality InP and InAs nanocrystals in a noncoordinating solvent. *Nano Letters* **2002**, *2*, 1027–1030.

[24] Baek, J.; Allen, P.; Bawendi, M.; Jensen, K. Investigation of Indium Phosphide Nanocrystal Synthesis Using a High-Temperature and High-Pressure Continuous Flow Microreactor. *Angewandte Chemie* **2011**, *123*, 653–656.

[25] Dai, Q.; Zhang, Y.; Wang, Y.; Wang, Y.; Zou, B.; Yu, W. W.; Hu, M. Z. Ligand Effects on Synthesis and Post-Synthetic Stability of PbSe Nanocrystals. *The Journal of Physical Chemistry C* **2010**, *114*, year.

[26] Jana, N.; Chen, Y.; Peng, X. Size-and shape-controlled magnetic (Cr, Mn, Fe, Co, Ni) oxide nanocrystals via a simple and general approach. *Chemistry of materials* **2004**, *16*, 3931–3935.

[27] Talapin, D. V.; Rogach, A. L.; Haase, M.; Weller, H. Evolution of an ensemble of nanoparticles in a colloidal solution: Theoretical study. *Journal of Physical Chemistry B* **2001**, *105*, 12278–12285.

[28] Nielsen, A. *Kinetics of precipitation*; International series of monographs in analytical chemistry; Pergamon Press; [distributed in the Western Hemisphere by Macmillan, New York], 1964.

[29] Peng, X. G.; Wickham, J.; Alivisatos, A. P. Kinetics of II-VI and III-V colloidal semiconductor nanocrystal growth: "Focusing" of size distributions. *Journal of the American Chemical Society* **1998**, *120*, 5343–5344.

[30] Sugimoto, T. Preparation of Monodispersed Colloidal Particles. *Advances in Colloid and Interface Science* **1987**, *28*, 65–108.

[31] Clark, M. D.; Kumar, S. K.; Owen, J. S.; Chan, E. M. Focusing Nanocrystal Size Distributions via Production Control. *Nano Letters* **2011**, *11*, 1976–1980.

[32] Abe, S.; Čapek, R. K.; De Geyter, B.; Hens, Z. Tuning the Postfocused Size of Colloidal Nanocrystals by the Reaction Rate: From Theory to Application. *ACS Nano* **2012**, *6*, 42–53.

[33] Park, J.; Joo, J.; Kwon, S. G.; Jang, Y.; Hyeon, T. Synthesis of monodisperse spherical nanocrystals. *Angewandte Chemie-International Edition* **2007**, *46*, 4630–4660.

[34] Joo, J.; Pietryga, J. M.; McGuire, J. A.; Jeon, S.-H.; Williams, D. J.; Wang, H.-L.; Klimov, V. I. A Reduction Pathway in the Synthesis of PbSe Nanocrystal Quantum Dots. *Journal of the American Chemical Society* **2009**, *131*, 10620–10628.

[35] Moreels, I.; Justo, Y.; De Geyter, B.; Haustraete, K.; Martins, J.; Hens, Z. Size-tunable, bright, and stable PbS quantum dots: A surface chemistry study. *ACS nano* **2011**.

[36] Fritzinger, B.; Moreels, I.; Lommens, P.; Koole, R.; Hens, Z.; Martins, J. In situ observation of rapid ligand exchange in colloidal nanocrystal suspensions using transfer NOE nuclear magnetic resonance spectroscopy. *Journal of the American Chemical Society* **2009**, *131*, 3024–3032.

[37] Moreels, I.; Fritzinger, B.; Martins, J. C.; Hens, Z. Surface Chemistry of Colloidal PbSe Nanocrystals. *Journal of the American Chemical Society* **2008**, *130*, 15081–15086.

[38] Murphy, J.; Beard, M.; Norman, A.; Ahrenkiel, S.; Johnson, J.; Yu, P.; Micic, O.; Ellingson, R.; Nozik, A. PbTe colloidal nanocrystals: Synthesis, characterization, and multiple exciton generation. *Journal of the American Chemical Society* **2006**, *128*, 3241–3247.

Part II

Optical Properties of Near-Infrared Emitting Colloidal Quantum Dots

3

Interactions of Colloidal Quantum Dot Charge Carriers with Matter and Field

3.1 Introduction

In this chapter we set the scene for the coming chapters on the optical studies we performed during this PhD research. We aim to introduce the different processes that charge carriers in QDs undergo, when interacting with the optical field and with themselves. Figure 3.1 gives a graphical overview of all the processes involved. The radiative transitions will be discussed in Section 3.2 and non-radiative transitions in Section 3.3. Finally, we devote Section 3.4 to the problems and solution strategies for realizing optical gain in colloidal QDs.

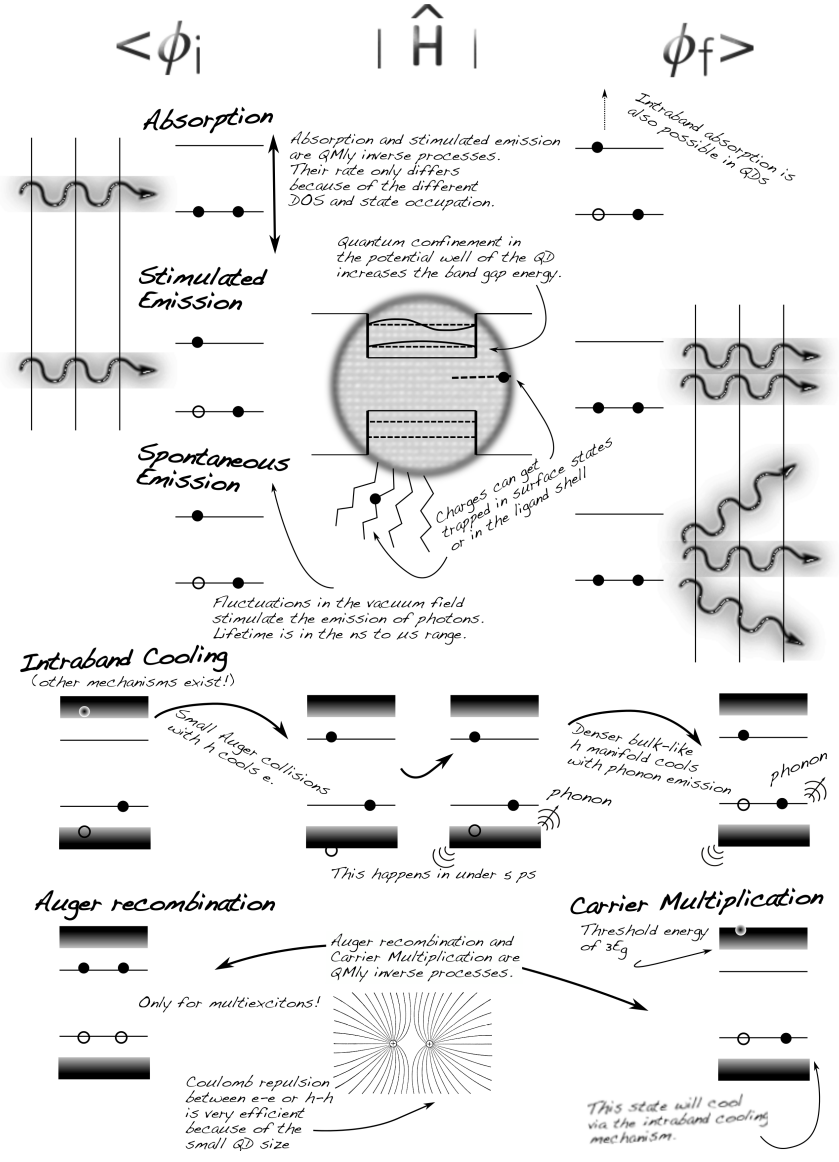

Figure 3.1: Overview of Radiative and Non-radiative Transitions in QDs

3.2 Optical Transitions

3.2.1 Oscillator Strength

The collection of atoms that make up a QD are not arranged randomly, but on particular points of a lattice. The electron clouds that surround the atoms can connect to form a large cloud throughout the QD. Electrons can bounce around freely, but the forces of the positively charged atomic cores on the negatively charged electron are analogous to springs with different spring constants connected to a mass. When an electric field exerts a force and distorts the electron cloud in the QD, much like a harmonic oscillator, the electron cloud will vibrate as a standing wave with a certain resonance frequency that is determined by the different spring constants.

The collection of different spring constants allows for many different resonance frequencies. In a QD, where the electron is confined to a finite size, the possibilities to form a standing wave inside the QD are limited. Therefore only a finite number of resonance frequencies can exist in a QD. In a much larger bulk crystal, where the electron does not feel boundaries, a quasi-continuum of frequencies exist.

When we shine light on a QD, the electromagnetic wave that makes up the light beam will distort the electrons in the QD in a periodic way. When the frequency at which this happens reaches one of these resonant frequencies, the electron will start to bounce around at that particular frequency. The work that the electromagnetic wave does in displacing the electron reduces the energy stored in the electromagnetic wave. As energy cannot be created nor lost, the energy is now stored in the movement of the electron.

Since an electron can vibrate at many different frequencies, we define a relative strength for which each of the vibrating modes can be activated by an oscillating electromagnetic field: the oscillator strength f_{if}.

$$f_{if} = \frac{2m_e\omega}{3\hbar}|\langle\psi_f|\mathbf{r}|\psi_i\rangle|^2 \tag{3.1}$$

Here m_e is the free electron mass, ω is the frequency of the transition and $\langle\psi_f|\mathbf{r}|\psi_i\rangle$ the dipole matrix element of the transition.

For one electron, the sum of the oscillator strengths for all resonant frequencies has to equal one:

$$\sum_{if} f_{if} = 1$$

This law is known as the *Thomas-Reiche-Kuhne sum rule*.

3.2.2 Fermi's Golden Rule

While the oscillator strength is a measure for how strongly a given quantum mechanical state (or vibrational electron mode) is activated by the electrical field, the transition probability per unit time for a quantum system to go from an initial state i to a final state f under the perturbation of the electrical dipole by a harmonically oscillating field $\widehat{\mathbf{H}}' = q\widehat{\mathbf{r}} \cdot \mathbf{E} \cos \omega t$ is given by Fermi's Golden Rule:

$$w_{if} = \frac{2\pi}{\hbar} |\langle \psi_f | \widehat{H}' | \psi_i \rangle|^2 g_f \delta(E_i - E_f - \hbar\omega) \tag{3.2}$$

where $\hbar\omega$ is the photon energy, $E_{i,f}$ are the energies of the initial and final states, $\widehat{H}' = |\widehat{\mathbf{H}}'|$ and g_f is the density of final states.

3.2.3 Spontaneous Emission

Spontaneous emission is the quantum mechanical process whereby the excited QDs lose energy by emitting a photon, seemingly without external perturbation. This process cannot be fully described and understood without using a full quantum mechanical description of the interaction between the harmonically oscillating electron and the photon radiation field. In this quantum electrodynamical description of the interaction, small fluctuations in the vacuum can occur that stimulate the emission of a photon from the excited QD.

While essentially spontaneous emission is the same process as stimulated emission, they are still treated as separate processes, based on the type of photons they emit. In stimulated emission, photons are emitted that have exactly the same polarization, phase and direction of propagation as the *real* photons already present in the radiation field. Spontaneously emitted photons have a random polarization, phase and direction, since they are caused by *virtual* photons — with random polarization, phase and direction — that appear and disappear extremely fast.

The transition rate from an initial state i to the final state f is given by Fermi's golden rule (see Section 3.2.2). From this definition, we see immediately that the rate of stimulated emission and absorption can be calculated using the semi-classical approach, since the electric field is non-zero in both processes. However, for spontaneous emission no external field is present, and hence the rate of spontaneous emission needs to be derived with a different approach. The most rigorous approach takes into account the quantum nature of the optical field, but the rate of spontaneous emission can also be derived from the laws of thermodynamics.

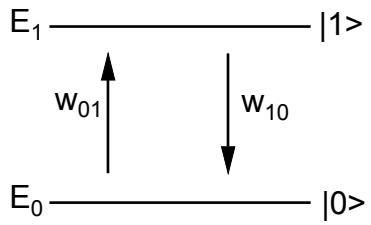

Figure 3.2: Two level system

Assuming we have an ensemble of a two-level system (Figure 3.2), the population in each level is determined by Boltzmann statistics:

$$N_1/N_0 = \exp\left(-\frac{\Delta E}{kT}\right) \tag{3.3}$$

When the system is in thermal equilibrium, the upward and downward rate are equal:

$$w_{01} = w_{10} \tag{3.4}$$
$$N_0 B_{01}\rho(\omega_{01}) = N_1 B_{10}\rho(\omega_{01}) \tag{3.5}$$

Here we defined the Einstein coefficients $B_{01} = B_{10}$, and $\rho(\omega)$ is the spectral energy density at a given angular frequency ω.

Since for a finite temperature $N_0 \neq N_1$ according to Eq. 3.3 , another emission path (*i.e.* spontaneous emission) must be present that is independent of the photon energy density:

$$N_0 B_{01}\rho(\omega_{01}) = N_1(A_{10} + B_{10}\rho(\omega_{01}))$$

Equating for the Einstein coefficient for spontaneous emission A_{10} we get:

$$A_{10} = B_{10}\rho(\omega_{10})(e^{\frac{\hbar\omega_{10}}{kT}} - 1)$$

where we can use Planck's formula for the energy density of blackbody radiation:

$$\rho(\omega) = \frac{\hbar\omega^3}{\pi^2 c^3}\frac{1}{e^{\frac{\hbar\omega_{10}}{kT}} - 1}$$

so:

$$A_{10} = \tau_{sp}^{-1} = \frac{\hbar\omega^3}{\pi^2 c^3} B_{10} \tag{3.6}$$

The probability for stimulated emission can be derived from Fermi's Golden Rule:

$$w_{if} = \frac{\pi\rho(\omega)}{3\varepsilon_0\hbar^2}\left|\langle\psi_f|q\widehat{\mathbf{r}}|\psi_i\rangle\right|^2 \quad (3.7)$$

$$= B_{10}\rho(\omega) \quad (3.8)$$

$$\text{with} \quad g_f = \frac{\rho(\hbar\omega)}{\frac{1}{2}\varepsilon_0|\mathbf{E}|^2}$$

Here we use the relation that the density of final states g_f is the spectral energy density ρ of the electric field at a given energy, divided by the energy of a single energy state $1/2\varepsilon_0|\mathbf{E}|^2$. The factor $1/3$ comes from replacing the scalar product $\mathbf{r}\cdot\mathbf{E}$ in the hamiltonian $\widehat{\mathbf{H}}'$ with the product of its norms. Note that the harmonic factor $\cos\omega t$ is split up in two exponential terms, one for absorption and one for stimulated emission. These exponential factors disappear for each process in taking the norm of the matrix element.

Combining Eq. 3.8 with Eq. 3.6, we find the expression for the Einstein coefficient for spontaneous emission A_{10}:

$$A_{10} = \tau_{rad}^{-1} = \frac{\omega^3}{3\varepsilon_0\pi\hbar c^3}\left|\langle\psi_f|q\widehat{\mathbf{r}}|\psi_i\rangle\right|^2 \quad (3.9)$$

We can now relate the rate of spontaneous emission τ_{rad}^{-1} to the oscillator strength of the transition between two levels i and f:

$$A_{10} = \tau_{rad}^{-1} = \frac{e^2\omega^2}{2\pi\varepsilon_0 c^3 m_e} f_{if} \quad (3.10)$$

Note that we have not included the screening of the electrical field inside the QDs in this definition.

3.2.4 Interband Absorption and Stimulated Emission

By definition the Einstein coefficients for interband absorption B_{01} and stimulated emission B_{10} of a two-level system are the same. The expression for the Einstein coefficients was derived in the previous section:

$$B_{10} = B_{01} = \frac{\pi}{3\varepsilon_0\hbar^2}\left|\langle\psi_f|q\widehat{\mathbf{r}}|\psi_i\rangle\right|^2$$

so the stimulated emission and absorption transition rate for monochromatic light ($\rho(\omega) = \hbar\omega n_{if} g(\omega)$) is:

$$w_{if} = \frac{\pi e^2}{2\varepsilon_0 m_e} f_{if} n_{if} g(\omega) \quad (3.11)$$

Here $g(\omega)$ is the lineshape function of the transition, which has units of ω^{-1} and n_{if} is the photon density in cm^{-3}. Note that the transition rate for a single electron to make a transition by absorption or stimulated emission, scales with the energy density (*i.e.* the number of photons per unit volume in the photon field at the location of the QD).

Balance between Spontaneous and Stimulated Emission into a Cavity Mode

Using the Boltzmann distribution above, we derived that the ratio between the rate of stimulated emission and the rate of spontaneous emission equals:

$$\frac{B_{10}\rho_{\omega_{10}}}{A_{10}} = \frac{1}{e^{\frac{\hbar\omega_{10}}{kT}} - 1}$$

the average number of photons with energy $\hbar\omega$ present in a single free space mode with frequency ω. A fundamental result from quantum electrodynamics is that this balance between the spontaneous and stimulated emission rates is not limited to free space modes, but also holds for confined fields (for a more extensive review we refer to Milonni and Eberly [1] or Hilborn [2]):

$$R_{stim} = qR_{spon} \tag{3.12}$$

where q is the number of photons in this mode. However, rewriting B_{if} and $\rho(\omega)$ in the transition rate from stimulated emission yields:

$$\begin{aligned} w_{10} &= B_{10}\rho(\omega) \\ &= \left(\frac{\lambda}{2}\right)^2 \frac{cg(\omega)}{V_{mode}} qA_{10} \end{aligned} \tag{3.13}$$

where we have used:

Eq.3.6

$$\begin{aligned} \frac{\omega}{c} &= \frac{2\pi}{\lambda} \\ \rho(\omega) &= \hbar\omega n_{if} g(\omega) \\ n_{if} &= \frac{q}{V_{mode}} \end{aligned}$$

The paradox between Equation 3.12 and Equation 3.13 lies in the fact that we are relating the stimulated emission due to a monochromatic beam (*i.e.* a single field mode) to the spontaneous emission to all free space (black

body) modes. The density of states of a single mode (*eg.* in a cavity) is different than in free space, from Eq. 3.13:

$$R_{spon,mode} = \underbrace{\left(\left(\frac{\lambda}{2}\right)^2 c\right)}_{\text{free space mode density}} \underbrace{\frac{g(\omega)}{V_{mode}}}_{\text{cavity mode density}} A_{10}$$

where we have identified the free space mode density $\left(\frac{2}{\lambda}\right)^2 \frac{1}{c}$ and the cavity mode density. This leads to the Purcell effect, where the spontaneous emission rate is altered in a cavity compared to free space.

Assuming the lineshape function $g(\omega)$ is a Lorentzian, and evaluating it at the maximum $g(\omega_{if}) = \frac{2}{\pi\Gamma}$, we easily obtain the ratio between the rate of spontaneous emission in the cavity to the rate of spontaneous emission in free space, *i.e.* the Purcell factor F_p:

$$F_p = \frac{3}{4\pi^2}\lambda^2 \frac{Q}{V_{mode}}$$

where $Q = \omega/\Gamma_\omega$. The added factor of 3 means that we assume the emitting dipole to be oriented parallel to the mode field in the cavity. For random emitters, like spherical QDs, this assumption is not correct.

With these equations, we can write the cavity rate equations as:

$$\frac{dN}{dt} = -\frac{N}{\tau_{spon}} - \frac{(N-1)q}{\tau_{spon}} + P \tag{3.14}$$

where N is the number of excitons per QD, $\tau_{spon} = R^{-1}_{spon,mode}$ and P is the pump rate.

Degeneracy

The rate at which a QD absorbs or emits photons is proportional to the degeneracy g, *i.e.* the number of degenerate transitions that exist at a given energy:

$$w_{if,QD} = g w_{if}$$

For PbX semiconductors, where the band gap is in the L-point of the Brillouin zone[3], $g = 64$. Note that in general, quantum confinement will lift the degeneracy. The degree of this lifting depends on the size, composition and shape of the QDs.

Cross section

The absorption or stimulated emission cross section σ of a QD is a convenient quantity when dealing with population dynamics. By definition:

$$\sigma\psi = w_{if,QD} \tag{3.15}$$

the cross section is the proportionality constant that relates the rate at which photons are absorbed (and excitons created) $w_{if,QD}$ to the photon flux ψ (number of photons per unit area and per unit time). The photon flux is a common measure, when using lasers for optical pumping of QDs. The cross section has units of area (cm^2). Intuitively, when a photon passes through this area around the QD, it will be absorbed or it will stimulate emission of an identical photon.

With $\psi = cn$, we rewrite Eq 3.15:

$$\sigma(\omega) = \frac{w_{if,QD}}{\psi} = \frac{\hbar\omega}{c} B_{if} g(\omega) = \frac{\pi e^2}{2\varepsilon_0 c m_e} f_{if} g(\omega) \tag{3.16}$$

For colloidal QDs, with a large inhomogeneous broadening due to size dispersion, often the energy integrated cross section over the band gap transition is given[4]. With $g(\omega)d\omega = g(E)dE$, this becomes:

$$\sigma_{QD,eV} = \frac{\hbar\pi e}{2\varepsilon_0 c m_e} f_{if} \tag{3.17}$$

Absorption Coefficient

When dealing with densely packed layers of QDs, typical in the design of integrated photonic structures activated with QDs, the intrinsic linear absorption coefficient μ_i is a more convenient measure. It is defined as the characteristic decay length of a beam through a hypothetical QD medium with volume fraction one. By definition:

$$\mu_{i,eV} = \frac{\sigma_{QD,eV}}{V_{QD}} = \frac{\hbar\pi e}{2\varepsilon_0 c m_e} \frac{f_{if}}{V_{QD}} \tag{3.18}$$

where V_{QD} is the QD volume. Note that this has units [eV/cm].

Local Field Effects

The calculations above were done for QDs in vacuum. Usually colloidal QDs are studied in suspension in a non-polar solvent. Therefore in all formulas, ε_0 needs to be replaced by $\varepsilon_0\varepsilon_s$ and c by c/n_s. Note that $\varepsilon_s = n_s^2$,

where ε_s and n_s are the dielectric constant and refractive index of the solvent.

Since QDs are small dielectric objects, a homogeneous external field (such as visible or near-infrared light with a wavelength much larger than the QD size) will polarize the QD. The resulting polarisation field effectively reduces the field strength inside the QD. This reduction is quantized by the *local field factor* $f_{LF} = E_{QD}/E_0$. As we have derived above, the rate of absorption and stimulated emission are directly proportional to the square of the field at the location of the dipole E_{QD}. Therefore, $B_i f$ (in Eq. 3.9-3.11,3.16-3.18) needs to be multiplied by $|f_{LF}|^2$. The calculation of the local field factor for core and spherical heterostructured QDs is dealt with in more detail in Section 4.2 on p. 89. For a more comprehensive review, we refer to Hens and Moreels [4].

3.2.5 Intraband Absorption

Intraband absorption is forbidden in first order in bulk semiconductors, because of momentum conservation. The three-particle process, in which the creation or absorption of a phonon provides the necessary momentum for the transition, is called *free carrier absorption*. This process, together with *free carrier refraction* is important for integrated optical modulators.

In QDs, momentum conservation is relaxed. The band itself is split into well separated atomic-like energy states, close to the band gap. At higher energies, these states form a quasi-continuum. Most studies have focused on the transition between the 1S and the 1P state, both in PbSe and CdSe QDs. In Chapter 6, we investigate intraband absorption in lead-based colloidal QDs using transient absorption spectroscopy. This study is relevant for the design of new colloidal heterostructure with improved gain performance and for applications in all-optical modulators.

3.3 Non-radiative Transitions

3.3.1 Intraband cooling

As photons with an energy much larger than the band gap energy are absorbed by a QD, an electron-hole pair is created in a higher energy state. In bulk semiconductors, the coupling of these states to the phonon bath is very efficient. As a result, the electron-hole pair loses its energy to the creation of phonons and eventually ends up at the lowest non-occupied state near the band gap. Here, no phonon has sufficient energy to facilitate the transition. This process is called *intraband cooling*.

In QDs, because of quantum confinement, the energy between different energy states is large. In the beginning of experimental QD research, it was assumed that the lack of phonons with sufficiently large energy would prevent intraband cooling and result in a so-called *phonon bottleneck* or long lifetime of high energy states. With the first experimental results from transient absorption spectroscopy, it became clear that this bottleneck did not exist and that the average intraband cooling time was in the sub-ps to a few ps range.

Currently, two theories try to explain this unexpected behaviour. The first theory credits the vibrational modes of the ligand molecules on the colloidal QD surface for the absence of the phonon bottleneck.[5] The second theory claims that the hole manifold is much denser and can cool in the traditional phonon-assisted way. Subsequently, inelastic collisions between the hole and the electron (*i.e.* Auger-like Coulomb interaction) aid the electron in cooling to the band gap.[6]

3.3.2 Multi-exciton Coulomb interactions

Auger Recombination

Auger recombination is a non-radiative recombination mechanism, in which carriers collide and transfer both momentum and energy. As a result of this inelastic scattering process, one of the carriers goes from the bottom of the conduction band to the top of the valence band, while a second carrier transfers to a higher energy state in the conduction band or in extreme cases is ejected out of the atom or crystal. In fact, the observation of secondary photoelectric electrons or beta-radiation upon excitation of a gas using X-rays led Pierre Victor Auger in 1923 to the discovery of the effect. The Auger effect was later applied in Auger photo-electron spectroscopy, a nowadays common technique in material science.

In bulk semiconductors, Auger recombination is a three-particle effect, where an electron-hole pair collides with a free electron or hole, and recombines. The free carrier subsequently loses its energy in the form of heat by colliding with the lattice (i.e. emission of phonons). In most applications, the effect is therefore undesirable, but since the interaction requires three particles, it is usually weak, unless for very high carrier densities. The rate of Auger recombination is proportional to the carrier density n cubed:

$$\Gamma_{n,A} = C_A n^3 \tag{3.19}$$

Here C_A is the Auger constant, for which values can be found in literature for most common semiconductors.

Robel et al.[7] followed a phenomenological approach to study Auger recombination in QDs. Assuming the same dependence on carrier density as above, they show that the Auger constant scales with the QD size as:

$$\begin{aligned} C_A &= \gamma R^3 \\ &\text{with} \quad \gamma = 0.4 - 2.3 \times 10^{-9} \mathrm{cm}^3 \mathrm{s}^{-1} \end{aligned} \tag{3.20}$$

Surprisingly, the proportionality constant γ is universal to different materials, suggesting that not the energy gap or electronic structure, but rather the QD size is the main influence on the Auger effect.

For QDs, the carrier density n is often replaced by the number of excitons per QD $N = V_{QD}n$. The rate $\Gamma_{N,A}$ at which excitons disappear from a QD through Auger recombination therefore becomes:

$$\begin{aligned} \Gamma_{N,A} &= \frac{dN}{dt} \\ &= V_{QD}\frac{dn}{dt} \\ &= \frac{C_A}{V_{QD}^2}N^3 \\ &= \frac{3}{4\pi}\frac{\gamma}{V_{QD}}N^3 \end{aligned} \tag{3.21}$$

Here we have used Equation 3.20 to show that the Auger rate in QDs is inversely proportional to the QD volume. We note that the cubic dependence on N has been the subject of some debate in literature[8]. Other authors have reported quadratic[9] (N^2) and statistical[10] ($N^2(N-1)$) scaling based on both phenomenological as theoretical arguments, depending on the size, shape and electronic structure of the QDs under study. While experiments mostly rule out the quadratic model, which assumes excitons are quasiparticles (two excitons need to collide to give rise to the Auger effect), there is little experimental ground to clearly distinguish between statistical (assuming both exciton and free carrier interactions) or cubic (only bulk-like free carrier interaction) scaling laws.

Equation 3.21 shows that for the same amount of carriers per QD, Auger recombination is enhanced in small QDs. In quantum mechanical terms, Auger recombination is Coulomb coupling between the charge carriers. The Auger rate is described by Fermi's Golden Rule:

$$\Gamma_{N,A} = \frac{2\pi}{\hbar}|M_{if}|^2\rho(E_f)\delta(E_i - E_f)$$

Note that the use of the density of final state $\rho(E_f)$ indicates that we assume the final states to be a continuum. The matrix element is:

$$|M_{if}|^2 = \langle \Psi_i | \widehat{V}(\mathbf{r}_1 - \mathbf{r}_2) | \Psi_f \rangle$$

The wavefunction of the initial state Ψ_i is the antisymmetrized product of two ground state hole wave functions. The wavefunction of the final state Ψ_f is the product of a ground state electron wavefunction (i.e. the complex conjugate of the hole ground state wavefunction) and a higher energy hole wavefunction.

$$|M_{if}|^2 = \langle \psi_h^0(\mathbf{r}_1)\psi_h^0(\mathbf{r}_2) | \widehat{V}(\mathbf{r}_1 - \mathbf{r}_2) | \psi_e^0(\mathbf{r}_1)\phi_h^f(\mathbf{r}_2) \rangle$$

The potential energy operator $\widehat{V}$ is the Coulomb potential between two holes.

$$|M_{if}|^2 = \langle \Psi_i | \frac{e^2}{4\pi\epsilon|\mathbf{r}_1 - \mathbf{r}_2|} | \Psi_f \rangle$$

The magnitude of the matrix element and hence the Auger rate is on the one hand increased by the spatial overlap of the ground state electron and hole wavefunctions $\psi_{e,h}^0$, which increases with r^{-1}. Hence spatial confinement of the carriers in the QD enhances the Auger rate. On the other hand, the high energy hole (ϕ_h^f) has acquired significant momentum $\hbar k_f$ in the collision process. The rapid oscillations of its wavefunction ϕ^f decrease the overlap with the ground state hole wavefunction ψ_h^0. The matrix element thus becomes much smaller than the typical Coulomb interaction energy $e^2/4\pi\epsilon d$. Taking the fourier transform of ψ_h^0, the main contribution to the matrix element comes from high spatial frequency components in the ground state wavefunction, close to k_f. Hence high frequency overlap of the initial and final state wavefunctions enhances Auger recombination[11]. These high frequency components mainly come from abrupt changes in the confinement potential at interfaces or at the QD surface. Control over the confinement potential by interfacial alloying[11;12] or large gradient heterostructures[13] is therefore essential in reducing the negative effects of enhanced Auger recombination in QDs. For these alloyed heterostructures, deviations from the volume scaling law (Equation 3.21) were observed[12].

Carrier Multiplication

CM or MEG has attracted a lot of research interest for its (arguable[14–16]) potential in solar energy conversion. Carrier multiplication (CM) or multiple exciton generation is quantum-mechanically the inverse process of

Auger recombination: an excited electron collides with a ground state electron, passing its excess energy. The final state of this process is two band gap electron-hole pairs. Since it is formally the same process as Auger recombination, its efficiency in quantum dots can be understood with the same arguments (see Section 3.3.2). If we assume that the energy of the exciting photon is divided equally over electron and hole ($m_e \simeq m_h$), the process has a threshold photon energy of $3E_g$. The reason is that the excited electron needs to have an excess energy of E_g above the band gap to be able to transfer enough energy to stimulate a ground state electron across the band gap.

3.3.3 Carrier Trapping

Given the high surface-to-volume ratio in QDs, trapping of carriers at the QD surface or in the organic ligand shell is often used to explain low QY, poor stability, unexpected positive or negative differential absorption signals in transient absorption spectroscopy, higher than expected CM-QY and other processes. The nature of these states is not fully understood and probably depends on QD composition, the nature of the ligand molecules and the environmental conditions. Several authors have contributed to increasing the understanding of these surface and ligand shell states.[5;17–22]

3.4 Gain in Colloidal QDs

3.4.1 Problems

From the very start of colloidal QD research, the promise of a solution-processable and wavelength tunable material providing optical gain was a driving force for research. Over the years, however, it became clear that optical gain was not easy to achieve in colloidal QDs. We highlight the three main problems.

Short gain lifetime

Since the band gap in colloidal QDs is two-fold degenerate for CdX and eight-fold for PbX QDs, the necessary requirement of population inversion for optical gain is by default the highly unstable multi-excitonic state. As discussed in Section 3.3.2 (p. 71), non-radiative decay through Auger recombination is enhanced in colloidal QDs. The lifetime of the biexciton state is in the 100 ps range, and the rate scales cubically with exciton multiplicity. As such, the gain lifetime is limited by the multiexciton lifetime.

As will be discussed in more detail later, this has a profound impact on the continuous wave (CW) gain and lasing threshold.

High charge density

Because of their small size, the charge density is very high. For one exciton, the charge density ranges between $10^{18} - 10^{21}$ cm^{-3} for QDs with a diameter between 10 nm and 1 nm. Together with the local field effect, which reduces the effective field inside the QD, the energy or power densities of the laser sources needed to pump the QDs are very high and far from trivial to achieve. Moreover, at these energy densities, sample stability becomes an issue. Moreover, many non-linear processes of other materials, including silicon are not negligible at these energy or power densities.

Carrier trapping and intraband absorption

Often, in experiments[17;23], the gain magnitude is smaller than expected or sometimes gain cannot be achieved. Also, often the threshold exciton multiplicity is higher than expected. These effects are usually attributed to carriers getting trapped at the QD surface or in the ligand shell. Furthermore, intraband absorption, resonant with band gap, reduces the gain performance.

3.4.2 Strategies for Improving Gain

Since gain in colloidal QDs is hard to achieve, several authors have directed their efforts to engineering new QDs with improved gain performance. Three general strategies can be identified.

Reducing the Auger Recombination Rate

This strategy tackles the problem of the efficient Auger recombination rate directly. The first, obvious approach is to increase the QD volume. In order to keep the wavelength tunability, heterostructured QDs are made with a smaller band gap core material and a larger band gap shell material. If at least one of the charge carriers leaks into the shell volume, the effective Auger recombination rate is reduced accordingly. A succesful example of this approach are the CdSe/CdS dot-in-rod structures.[24].

The second approach adds a gradient between core and shell material to obtain a smooth potential well. García-Santamaría et al. [13] showed that their *giant* CdSe/CdS QDs have a long biexciton lifetime and therefore boost the optical gain performance of these QDs.

Single-exciton Gain

The seminal article by Klimov et al.[25] introduced the idea of *single exciton gain*. In these so-called type-II heterostructures, the electron and hole are spatially separated. As charge neutrality is broken, the Coulomb attraction between electron and hole does not cancel out the Coulomb repulsion between two electrons or holes. This positive energy contribution is added to the energy of the biexciton state. Therefore, the biexciton state is not degenerate with the ground and the single exciton state and the threshold exciton multiplicity is lowered from one (in CdX) to below one. As gain is now provided by single excitons, the gain lifetime is dominated by the radiative lifetime of the single exciton. Besides the original CdS/ZnSe dot-in-dot structure, a decrease in the Auger recombination rate was observed for CdTe/CdSe QDs[26;27]. For CdSe/CdTe heteronanocrystals[28;29] and ZnTe/ZnSe QDs[30], long radiative lifetimes, indicative of charge separation, and a strong redshift of the exciton transitions were reported.

The degenerate band gap of bulk materials is naturally split in QDs, through other effects than Coulomb repulsion between multiexcitons. This fine structure splitting is usually smaller than the inhomogeneous linewidth of the QD ensemble. Several authors have investigated this fine structure in an attempt to understand and engineer the magnitude of the splitting.[31–38]

Doping and the Four-Level System QD

Inherently, a QD is a three-level system. Recently, doping of colloidal QDs was suggested as a new strategy to solve the issues relating to QD gain.[39] The dopant (Cu) creates an optically active hole in the band gap, and thus provides a fully transparent four-level system, where the creation of single exciton (or even the injection of a single electron) is enough to provide gain. This completely removes the gain threshold. However, the lifetime of this transition is much longer than the band gap transition, so the maximum gain is expected to be lower for this new class of materials.

3.4.3 Benchmarking

The maximum possible material gain from colloidal QD films is:

$$G_{max} = \mu_{gap,eV} \frac{1}{\sqrt{2\pi}\sigma} f$$

where $\mu_{gap,eV}$ is the energy integrated absorption coefficient (see Eq 3.18), σ is the width of the first exciton peak and f is the volume fraction of

material in the film. In both CdX[40;41] and PbX[42;43],

$$\mu_{gap,eV} \sim 1/A_{QD}$$

is inversely proportional with the QD surface area. Typical values for the maximum gain are in the range of $10^4 - 10^5$ cm^{-1} for both CdX and PbX QD closest packed films (*i.e.* f = 0.2 - 0.75).

The high material gain comes at a cost of very high carrier densities. One exciton per QD, the theoretical threshold for a two-level system, puts the threshold carrier density n_{th} between $10^{18} - 10^{21}$ cm^{-3} for QD diameters between 10 nm and 1 nm. From the threshold carrier density, we can estimate the threshold photon flux (or power density) ϕ_P for gain under CW conditions:

$$\phi_P = \frac{n_{th}}{\mu_{i,P}\tau_{A,2}} \sim \frac{1}{V_{QD}^2} \tag{3.22}$$

where $\mu_{i,P}$ is the absorption coefficient at the pump wavelength and $\tau_{A,2}$ is the biexciton lifetime. At high energies well above the band gap, $\mu_{i,P}$ is constant in QDs, so the threshold photon flux increases quadratically with decreasing QD volume ($\sim d^{-6}$). The combination of the high carrier densities required for population inversion and the short lifetime of the multiexciton states means that high pump power densities ($\sim$MW/cm^2) are required for QD gain. This power is equivalent to 1 mW of optical power in a standard silicon photonic wire with a 200 nm by 500 nm cross section.

QD engineering could reduce this minimum threshold pump power. Single exciton gain would reduce the threshold by 1 to 2 orders of magnitude for CdX and 4 orders of magnitude for PbX. It comes at a cost of reducing the maximum gain, by a factor of two for CdX and a factor of four for PbX. Strategies to reduce the Auger rate directly typically use larger particles to exploit the volume scaling. Doubling the diameter yields a 2 orders of magnitude reduction in the threshold, but again lowers the maximum gain by a factor of 4. Creating heterostructures with a small core and a much larger shell is a good strategy to keep the wavelength tunability, while also reducing the pump threshold. However, the smaller volume fraction of active material due to the *inactive* shell makes the maximum gain scale inversely with the total QD volume (instead of the QD area). By far the most promising strategy is to use doping to create a four-level system in which the threshold can be completely removed. This comes at the cost of, probably, lower gain and less wavelength tunability.

III-V gain materials

A competing and much more mature technology to bring gain to the silicon photonics platform uses bonded III-V dies to silicon.[44] In Figure 3.3(a) we compare the theoretical maximum gain (*i.e.* the absorption coefficient with $f = 1$) for PbSe QDs ($d = 3.4$ nm, $\lambda = 1200$ nm) with calculated data by Asada et al.[45] for a GaInAs/InP bulk heterojunction, quantum well, quantum wire and quantum dot[1]. PbSe QDs have higher gain than all four III-V configurations. A large difference however is that the 4 nm PbSe QDs require a charge density of 4×10^{20} cm^{-3} to reach gain, two orders of magnitude higher than the III-V material. Clearly, a larger QD will result in a lower threshold charge density. The large charge densities needed for colloidal PbSe QDs become even clearer in Figure 3.3(b). Here we plot the maximum material gain as a function of injection current density (*i.e.* the current actually going into the gain material). For the III-V heterostructure, again the data was taken from Asada et al.[45]. They assume that, despite the $f = 0.25$, all the current is injected into the QDs. For 3.4 nm PbSe QDs ($\lambda = 1200$), we define the current density for optical pumping (black in Figure 3.3(b)) as the number of excitons created by the pump source per second (*i.e.* $e\phi_P$, see Eq. 3.22), where we have taken the absorption cross section as the active QD area. The dramatic effect of the efficient non-radiative Auger recombination on the transparency threshold is obvious in Figure 3.3(b). The threshold current density is more than four orders of magnitude larger. Note that, because of the local field factor, the absorption cross section, which was used to calculate the current density, is smaller than the QD area. Hence, for electrical injection, where we use the QD area instead of the absorption cross section (grey curve in Figure 3.3(b)), the theoretical threshold is lower by more than an order of magnitude. A slightly larger QD ($d = 5.3$ nm, $\lambda = 1570$ nm) brings the theoretical threshold down by another order of magnitude, but also shifts the operational wavelength by 300 nm.

3.4.4 Conclusion

The great benefits of using colloidal QDs as a gain material are their wavelength tunability, the accuracy, flexibility and easy with which they can be synthesized, the QD densities that can be reached with simple wet deposition techniques and the possibility to embed them into the core of an active waveguide. However, their extremely small size together with the increased efficiency of non-radiative Auger recombination that accompanies

[1] Note that for the quantum dots, Asada et al.[45] used a fill-factor of $f = 0.25$.

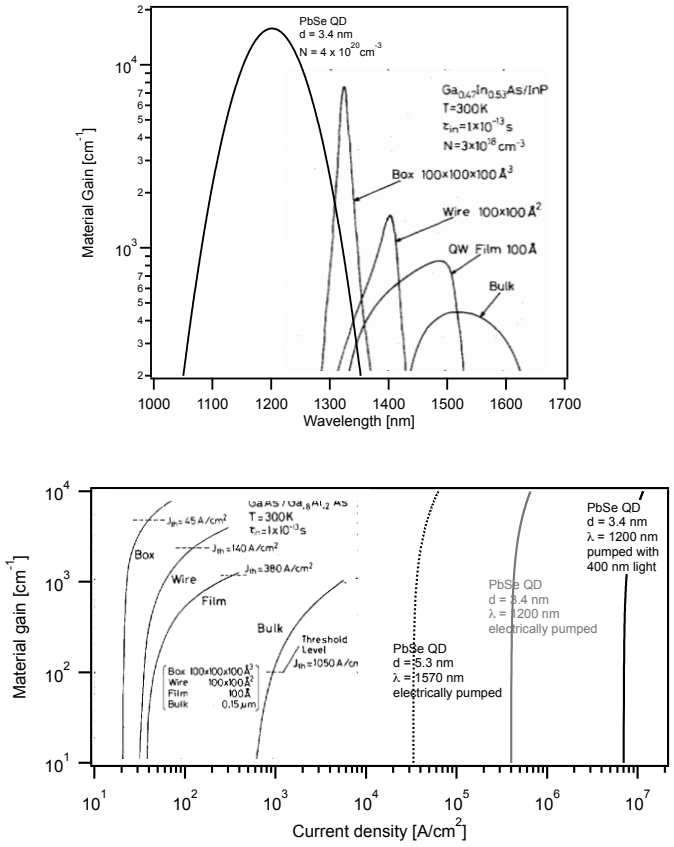

Figure 3.3: (a) Comparison between the gain spectra of PbSe QDs ($d = 3.4$ nm) and III-V gain structures (reproduced from Asada et al.[45]) with different confinement. (b) Maximum material gain as a function of the injection current density. The data for the III-V structures is reproduced from Asada et al.[45] and shows the clear difference with the very high threshold current density needed for PbSe QDs. The current density for 3.4 nm PbSe QDs in black has the meaning of the number of excitons created per second by a 400 nm CW optical pump source (multiplied by e) per unit area. The grey ($d = 3.4$ nm) and the dotted ($d = 5.3$ nm) curves plot the material gain vs. the current density for electrical injection.

it, demand very high optical or electrical pump power densities to achieve transparency or gain. Therefore, their application is limited to very small, integrated devices in which these densities can be reached more easily. Several strategies have been proposed in literature to overcome this problem. It is however questionable that any of these strategies will result in a gain material that is, if not better, at least as good as the current state-of-the-art in III-V gain media in terms of performance. Possibly, the simple processing could then provide more cost effective devices, or its tunability could cater to much larger wavelength regions.

3.5 This work

As is clearly evident from this introduction, the optical performance of core-only colloidal QDs is not sufficient to make a competitive laser. In this work, we therefore focused on material science to engineer and study a new class of infrared emitting heterostructures, PbSe/CdSe QDs, as possible candidates for NIR lasing. In the coming Chapters, we report on the optical properties of PbSe/CdSe core/shell heterostructured QDs.

In Chapter 4 we study how the CdSe shell influences the linear band gap absorption of the PbSe core. We show that both the relation between band gap energy and core size is not altered by the CdSe shell. However, as our work on both PbSe/CdSe and PbS/CdS shows, the local field experienced by the QDs is altered by the CdX shell in a non-trivial way. We explain our results using the Maxwell-Garnett effective medium theory.

In Chapter 5 we study the spontaneous emission properties. We show that fine structure splitting of the PbSe band gap is significantly increased by the CdSe shell. We back up our experimental results with theoretical calculations using the effective mass model and tight-binding. Our results pertain to the strategy of single-exciton gain as a way of boosting the gain performance of these QDs.

The gain performance and charge dynamics are studied in Chapter 6 using transient absorption spectroscopy. We show that the increased splitting and partial lifting of the degeneracy is not yet sufficient to provide optical gain. Moreover, gain is further hampered by resonant intraband absorption. This type of transition was never studied for this particular energy range before. We back up our results with tight binding simulations, in cooperation with Université de Lille 1, and go on to show that the adverse effect intraband absorption has on gain, could be useful for integrated high speed optical modulators.

References

[1] Milonni, P.; Eberly, J. *Laser Physics*; John Wiley & Sons, 2010.

[2] Hilborn, R. Einstein coefficients, cross sections, f values, dipole moments, and all that. *Arxiv preprint physics/0202029* **2002**.

[3] An, J. M.; Franceschetti, A.; Dudiy, S. V.; Zunger, A. The peculiar electronic structure of PbSe quantum dots. *Nano Letters* **2006**, *6*, 2728–2735.

[4] Hens, Z.; Moreels, I. Light absorption by colloidal semiconductor quantum dots. *J. Mater. Chem.* **2012**, *22*, 10406–10415.

[5] Guyot-Sionnest, P.; Wehrenberg, B.; Yu, D. Intraband relaxation in CdSe nanocrystals and the strong influence of the surface ligands. *Journal of Chemical Physics* **2005**, *123*, 074709.

[6] Klimov, V.; McBranch, D.; Leatherdale, C.; Bawendi, M. Electron and hole relaxation pathways in semiconductor quantum dots. *Physical Review B* **1999**, *60*, 13740–13749.

[7] Robel, I.; Gresback, R.; Kortshagen, U.; Schaller, R. D.; Klimov, V. I. Universal Size-Dependent Trend in Auger Recombination in Direct-Gap and Indirect-Gap Semiconductor Nanocrystals. *Phys. Rev. Lett.* **2009**, *102*, 177404.

[8] Klimov, V. I.; McGuire, J. A.; Schaller, R. D.; Rupasov, V. I. Scaling of multiexciton lifetimes in semiconductor nanocrystals. *Phys. Rev. B* **2008**, *77*, 195324.

[9] Klimov, V.; Mikhailovsky, A.; McBranch, D.; Leatherdale, C.; Bawendi, M. Quantization of multiparticle Auger rates in semiconductor quantum dots. *Science* **2000**, *287*, 1011–1013.

[10] Barzykin, A.; Tachiya, M. Stochastic models of charge carrier dynamics in semiconducting nanosystems. *Journal of Physics: Condensed Matter* **2007**, *19*, 065105.

[11] Cragg, G. E.; Efros, A. L. Suppression of Auger Processes in Confined Structures. *Nano Letters* **2010**, *10*, 313–317.

[12] García-Santamaría, F.; Brovelli, S.; Viswanatha, R.; Hollingsworth, J. A.; Htoon, H.; Crooker, S. A.; Klimov, V. I. Breakdown of Volume Scaling in Auger Recombination in CdSe/CdS

Heteronanocrystals: The Role of the CoreShell Interface. *Nano Letters* **2011**, *11*, 687–693.

[13] García-Santamaría, F.; Chen, Y.; Vela, J.; Schaller, R. D.; Hollingsworth, J. A.; Klimov, V. I. Suppressed Auger Recombination in Giant Nanocrystals Boosts Optical Gain Performance. *Nano Letters* **2010**, *9*, 3482–3488.

[14] Schaller, R.; Klimov, V. High efficiency carrier multiplication in PbSe nanocrystals: Implications for solar energy conversion. *Physical Review Letters* **2004**, *92*, 186601.

[15] McGuire, J.; Sykora, M.; Joo, J.; Pietryga, J.; Klimov, V. Apparent versus true carrier multiplication yields in semiconductor nanocrystals. *Nano letters* **2010**, *10*, 2049–2057.

[16] Schaller, R.; Sykora, M.; Pietryga, J.; Klimov, V. Seven excitons at a cost of one: Redefining the limits for conversion efficiency of photons into charge carriers. *Nano Letters* **2006**, *6*, 424–429.

[17] Malko, A.; Mikhailovsky, A.; Petruska, M.; Hollingsworth, J.; Klimov, V. Interplay between optical gain and photoinduced absorption in CdSe nanocrystals. *Journal of Physical Chemistry B* **2004**, *108*, 5250–5255.

[18] McGuire, J. A.; Sykora, M.; Robel, I.; Padilha, L. A.; Joo, J.; Pietryga, J. M.; Klimov, V. I. Spectroscopic Signatures of Photocharging due to Hot-Carrier Transfer in Solutions of Semiconductor Nanocrystals under Low-Intensity Ultraviolet Excitation. *ACS Nano* **2010**, *4*, 6087–6097.

[19] Padilha, L. A.; Robel, I.; Lee, D. C.; Nagpal, P.; Pietryga, J. M.; Klimov, V. I. Spectral Dependence of Nanocrystal Photoionization Probability: The Role of Hot-Carrier Transfer. *ACS Nano* **2011**, *5*, 5045–5055.

[20] Stouwdam, J. W.; Shan, J.; van Veggel, F. C. J. M.; Pattantyus-Abraham, A. G.; Young, J. F.; Raudsepp, M. Photostability of Colloidal PbSe and PbSe/PbS Core/Shell Nanocrystals in Solution and in the Solid State. *The Journal of Physical Chemistry C* **2007**, *111*, 1086–1092.

[21] An, J. M.; Franceschetti, A.; Zunger, A. Pauli blocking versus electrostatic attenuation of optical transition intensities in charged PbSe quantum dots. *Physical Review B* **2007**, *76*, 161310.

[22] Liu, H.; Guyot-Sionnest, P. Photoluminescence Lifetime of Lead Selenide Colloidal Quantum Dots. *The Journal of Physical Chemistry C* **2010**, *114*, 14860–14863.

[23] Cooney, R.; Sewall, S.; Sagar, D.; Kambhampati, P. Gain Control in Semiconductor Quantum Dots via State-Resolved Optical Pumping. *Physical review letters* **2009**, *102*, 127404.

[24] Zavelani-Rossi, M.; Lupo, M.; Tassone, F.; Manna, L.; Lanzani, G. Suppression of biexciton Auger recombination in CdSe/CdS dot/rods: role of the electronic structure in the carrier dynamics. *Nano letters* **2010**, *10*, 3142–3150.

[25] Klimov, V. I.; Ivanov, S. A.; Nanda, J.; Achermann, M.; Bezel, I.; McGuire, J. A.; Piryatinski, A. Single-exciton optical gain in semiconductor nanocrystals. *Nature* **2007**, *447*, 441–446.

[26] Oron, D.; Kazes, M.; Banin, U. Multiexcitons in type-II colloidal semiconductor quantum dots. *Physical Review B* **2007**, *75*, 035330.

[27] Dorfs, D.; Franzl, T.; Osovsky, R.; Brumer, M.; Lifshitz, E.; Klar, T. A.; Eychmueller, A. Type-I and type-II nanoscale heterostructures based on CdTe nanocrystals: A comparative study. *Small* **2008**, *4*, 1148–1152.

[28] Jones, M.; Kumar, S.; Lo, S. S.; Scholes, G. D. Exciton trapping and recombination in type IICdSe/CdTe nanorod heterostructures. *Journal of Physical Chemistry C* **2008**, *112*, 5423–5431.

[29] de Mello Donegá, C. Formation of nanoscale spatially indirect excitons: Evolution of the type-II optical character of CdTe/CdSe heteronanocrystals. *Physical Review B* **2010**, *81*, 165303.

[30] Bang, J. et al. ZnTe/ZnSe (Core/Shell) Type-II Quantum Dots: Their Optical and Photovoltaic Properties. *Chemistry of Materials* **2010**, *22*, 233–240.

[31] Johnson, J. C.; Gerth, K. A.; Song, Q.; Murphy, J. E.; Nozik, A. J. Ultrafast exciton fine structure relaxation dynamics in lead chalcogenide nanocrystals. *Nano Letters* **2008**, *8*, 1374–1381.

[32] Norris, D.; Efros, A.; Rosen, M.; Bawendi, M. Size dependence of exciton fine structure in CdSe quantum dots. *Physical Review B* **1996**, *53*, 16347–16354.

[33] Biadala, L.; Louyer, Y.; Tamarat, P.; Lounis, B. Band-Edge Exciton Fine Structure of Single CdSe/ZnS Nanocrystals in External Magnetic Fields. *Phys. Rev. Lett.* **2010**, *105*, 157402.

[34] Schaller, R. D.; Crooker, S. A.; Bussian, D. A.; Pietryga, J. M.; Joo, J.; Klimov, V. I. Revealing the Exciton Fine Structure of PbSe Nanocrystal Quantum Dots Using Optical Spectroscopy in High Magnetic Fields. *Physical Review Letters* **2010**, *105*, 067403.

[35] Wong, C. Y.; Scholes, G. D. Using two-dimensional photon echo spectroscopy to probe the fine structure of the ground state biexciton of CdSe nanocrystals. *Journal of Luminescence* **2010**, *131*, 366–374.

[36] Accanto, N.; Masia, F.; Moreels, I.; Hens, Z.; Langbein, W.; Borri, P. Engineering The Spin-Flip Limited Exciton Dephasing in Colloidal CdSe/CdS Quantum Dots. *ACS nano* **2012**, *6*, 5227–5233.

[37] Raino, G.; Stöferle, T.; Moreels, I.; Gomes, R.; Hens, Z.; Mahrt, R. Controlling the Exciton Fine Structure Splitting in CdSe/CdS Dot-in-Rod Nanojunctions. *ACS nano* **2012**, *6*, 1979–1987.

[38] Moreels, I.; Rainò, G.; Gomes, R.; Hens, Z.; Stöferle, T.; Mahrt, R. Band-Edge Exciton Fine Structure of Small, Nearly Spherical Colloidal CdSe/ZnS Quantum Dots. *ACS nano* **2011**, *5*, 8033–8039.

[39] Viswanatha, R.; Brovelli, S.; Pandey, A.; Crooker, S.; Klimov, V. Copper-doped inverted core/shell nanocrystals with permanent optically active holes. *Nano Letters* **2011**, *11*, 4753–4758.

[40] Capek, R. K.; Moreels, I.; Lambert, K.; De Muynck, D.; Zhao, Q.; Vantomme, A.; Vanhaecke, F.; Hens, Z. Optical Properties of Zincblende Cadmium Selenide Quantum Dots. *Journal of Physical Chemistry C* **2010**, *114*, 6371–6376.

[41] Leatherdale, C.; Woo, W.; Mikulec, F.; Bawendi, M. On the absorption cross section of CdSe nanocrystal quantum dots. *Journal of Physical Chemistry B* **2002**, *106*, 7619–7622.

[42] Moreels, I.; Lambert, K.; De Muynck, D.; Vanhaecke, F.; Poelman, D.; Martins, J. C.; Allan, G.; Hens, Z. Composition and size-dependent extinction coefficient of colloidal PbSe quantum dots. *Chemistry of Materials* **2007**, *19*, 6101–6106.

[43] Moreels, I.; Lambert, K.; Smeets, D.; De Muynck, D.; Nollet, T.; Martins, J. C.; Vanhaecke, F.; Vantomme, A.; Delerue, C.; Allan, G.;

Hens, Z. Size-Dependent Optical Properties of Colloidal PbS Quantum Dots. *Acs Nano* **2009**, *3*, 3023–3030.

[44] Roelkens, G.; Van Campenhout, J.; Brouckaert, J.; Van Thourhout, D.; Baets, R.; Romeo, P. R.; Regreny, P.; Kazmierczak, A.; Seassal, C.; Letartre, X.; Hollinger, G.; Fedeli, J. M.; Di Cioccio, L.; Lagahe-Blanchard, C. III-V/Si photonics by die to wafer bonding. *Materials Today* **2007**, *10*, 36–43.

[45] Asada, M.; Miyamoto, Y.; Suematsu, Y. Gain and the threshold of 3-dimensional quantum-box lasers. *Ieee Journal of Quantum Electronics* **1986**, *22*, 1915–1921.

4

Linear Absorption of PbSe and PbSe/CdSe

4.1 Sizing Curve - Relating Band Gap Energy and Size

PbSe/CdSe core/shell QDs were made by cation exchange on PbSe QDs as described by Pietryga *et al.*[1]. The cation exchange does not alter the total QD size and original size distribution[2], and yields PbSe/CdSe core/shell QDs with tunable core size and shell thickness. This is corroborated by the absorption spectra (see Figure 4.1(a)), which show an increasing blueshift with increasing exchange time. The blueshift can be attributed to the shrinking of the PbSe core and the simultaneous increase of the CdSe shell thickness. Using high resolution transmission electron microscopy (HR-TEM), we showed that the cation exchange process is quite anisotropic[2], partially leading to particles with eccentric and non-spherical cores. This heterogeneity accounts for the broadening of the absorption and PL spectra with increasing exchange time (see Figure 4.1(a)).

Knowledge of the core diameter and shell thickness is important for the present study of the QD optical and electronic properties. Although HR-TEM (see Figure4.1(b)) can be used for this purpose, it is not a practical technique for the analysis of a large number of samples in a short time span. Moreover, even when the boundary between core and shell can be distin-

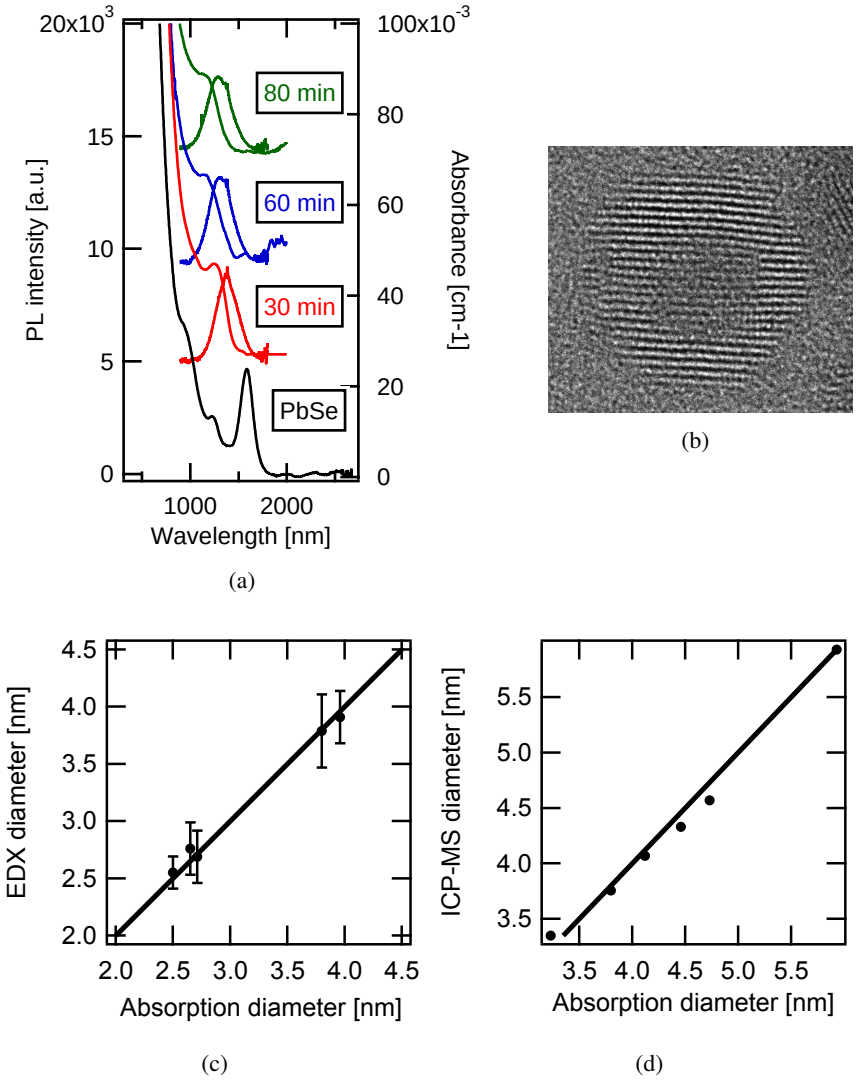

Figure 4.1: (a) Absorption and luminescence spectra of PbSe/CdSe QDs in C_2Cl_4 for increasing exchange times. (b) HR-TEM image of a PbSe/CdSe core/shell QD, clearly showing the PbSe core and the CdSe shell. (c) PbSe/CdSe QDs: diameter determined from EDX vs. diameter determined from the position of the first absorption peak, using the PbSe sizing curve.[3] (d) PbS/CdS QDs: diameter determined from ICPMS vs. diameter determined from the position of the first absorption peak, using the PbS sizing curve.[4] In both figures, the black line indicates a 1-to-1 relationship.

guished, it is not clear whether to place it on a cation or anion plane. Therefore, we measured the Pb/Se ratio of the original PbSe core QDs and of the derived PbSe/CdSe QDs by TEM-based energy dispersive x-ray spectroscopy (EDX). Since the Se-content stays constant, we can calculate the amount of Pb in the PbSe/CdSe core, taking the nonstoichiometry [3;5] of the parent PbSe QDs into account. Since the stoichiometry of the core is not known, we assume the PbSe core is terminated by Pb-planes and therefore has the stoichiometry of PbSe QD with the same diameter:

$$[Pb] \quad = \quad \underbrace{4\frac{4\pi}{3}(\frac{d}{2a})^3}_{\text{volume term}} - \underbrace{Ad^2}_{\text{surface term}}$$

with $A = 6.8$ an empirical constant relating the Pb excess to the QD surface area[3], a the lattice constant of PbSe and d the diameter. This effective diameter for the PbSe core, determined with EDX, is in good agreement with the diameter determined using the PbSe QD sizing curve[3](see Figure 4.1(c)). A similar approach was followed for PbS/CdS QDs, where we used inductively-coupled plasma mass spectrometry (ICPMS) to measure the absolute Pb and S content before and after shell growth. Again, the core diameter from ICPMS and from the PbS sizing curve[4] match well. It shows that the Pb content of the PbSe/CdSe and PbS/CdS QDs determines the bandgap and hence we justify using the PbSe and PbS QD sizing curve to estimate the PbSe (PbS) effective core diameter in PbSe/CdSe (PbS/CdS) core/shell QDs respectively.

Recent work by Zhang et al.[6] using a SILAR approach for the CdSe growth confirms this result. They observe a shift of only 32 nm in the absorption spectra upon growth of three CdSe monolayers ($\sim$ 1 nm shell thickness), which corresponds to a shift in the diameter of just 0.17 nm, less than a Cd or Se monolayer.

4.2 Absorption Coefficient of Heterostructured QDs

4.2.1 Local Field Effects in Colloidal QDs

Since colloidal QDs are made in a wet chemical synthesis, the basic characterization is mostly done on QDs suspended in an organic solvent. Because of their small size, the macroscopic optical properties of suspended QDs are determined both by the intrinsic optical properties and by the surrounding medium. This effect is typically described by the Maxwell-Garnett effective medium theory. The importance of this effect can hardly be underestimated, as it will alter the absorbance, the photoluminescence (PL) peak

position and emission rate and the PL quantum yield[7], depending on the surrounding medium or solvent. For example, Moreels et al.[8] used this theory to calculate the dielectric function of PbSe, PbS and PbTe colloidal QDs and study the effect of quantum confinement on these elementary material properties. This effect is typically described by the local field factor f_{LF}, which is the ratio of the field inside the QD and the field in the surrounding medium. We analyze the effect of the effective medium on the absorbance (A) of core/shell PbSe/CdSe and PbS/CdS QDs, where not only the solvent, but also the inorganic core/shell structure determines the local field factor. For a more comprehensive review, we refer to Hens and Moreels[9].

4.2.2 Absorption Coefficient of Core-Only QDs

To quantify the spectrum of the absorbance (A), it is converted to the spectrum of the intrinsic absorption coefficient μ_i. For this, the QD volume fraction f and the cuvette length L are needed:

$$\mu_i = \frac{\ln 10 A}{f L} \tag{4.1}$$

The intrinsic absorption coefficient μ_i provides the characteristic decay length of the light intensity in a hypothetical medium with a QD volume fraction of one.

For PbSe[3], PbS[4], wurtzite and zincblende CdSe[10–12], InAs[13] and ZnO[14] QDs, it was shown that at high energies (3.1 eV for PbSe and PbS, 3.54 eV for CdSe, 2.76 eV for InAs, 5.0 eV for ZnO), μ_i is independent of the QD size. Moreover, it generally coincides with the theoretical value calculated using bulk optical constants and the Maxwell-Garnett effective medium theory[15;16]:

$$\mu_i = \frac{2\pi}{\lambda n_s} Im(\epsilon_c) \left| f_{LF} \right|^2 \tag{4.2}$$

Here, n_s is the solvent refractive index, ϵ_c and ϵ_s the complex dielectric function of the QD material and the solvent, respectively, and λ the wavelength. For spherical particles, the local field factor reads:

$$f_{LF} = \frac{3\epsilon_s}{\epsilon_c + 2\epsilon_s} \tag{4.3}$$

The fact that at short wavelengths a bulk-like absorption coefficient is found, means that the electronic states at high energies are not quantum confined, but form a continuum in these QDs. Hence the QD concentration

[QD], an essential quantity to assess synthesis quality and to control deposition, can be determined from the absorbance at high energies, irrespective of size dispersion, using the Beer-Lambert law and μ_i as calculated above:

$$[\mathrm{QD}] = \frac{A}{\varepsilon L} = \frac{A \ln 10}{\mu_i N_A V_{QD} L}$$

Here ε is the molar exctinction coefficient, N_A is Avogadro's constant and V_{QD} the volume of the QD.

4.2.3 Absorption Coefficient of Heterostructured QDs

For core/shell QDs, both core and shell contribute to the screening of an external electric field. With a homogeneous external field, this more complex screening only leads to a homogeneous local field in the core, not in the shell (see Figure 4.2(a)-(b)). Thus, when the shell contributes to the absorbance, Eq. 4.2 can no longer be used. An expression for the absorption coefficient of core/shell particles was proposed by Neeves et al.[17;18]. If the volume fraction of core/shell particles in solution is small, it reads:

$$\begin{aligned} \mu_i \quad &= \quad \frac{2\pi}{\lambda n_s} Im(3\epsilon_s \beta) \\ &\text{with} \quad \beta = \left(\frac{\epsilon_{sh}\epsilon_a - \epsilon_s \epsilon_b}{\epsilon_{sh}\epsilon_a + 2\epsilon_s \epsilon_b} \right) \\ &\qquad \epsilon_a = \epsilon_c (3 - 2\frac{V_{sh}}{V_{QD}}) + 2\epsilon_{sh}\frac{V_{sh}}{V_{QD}} \\ &\qquad \epsilon_b = \epsilon_c \frac{V_{sh}}{V_{QD}} + \epsilon_{sh}(3 - \frac{V_{sh}}{V_{QD}}) \end{aligned} \tag{4.4}$$

Here, ϵ_{sh} denotes the complex dielectric function of the shell. Importantly, μ_i becomes dependent on the ratio between the shell and the total QD volume for core/shell heterostructures. This is purely an effect of the change in the effective medium and not an effect of quantum confinement. Hence, to compare theory with experiment, a precise knowledge of the core diameter and shell thickness is essential for QD heterostructures.

4.2.4 Experiment *vs.* Theory

We take the example of PbSe/CdSe and PbS/CdS QDs made by cation exchange on PbSe or PbS QDs[1], to study the absorption coefficient of QD heterostructures. They offer an ideal test case, since the total QD diameter and the concentration remains constant throughout the exchange procedure.

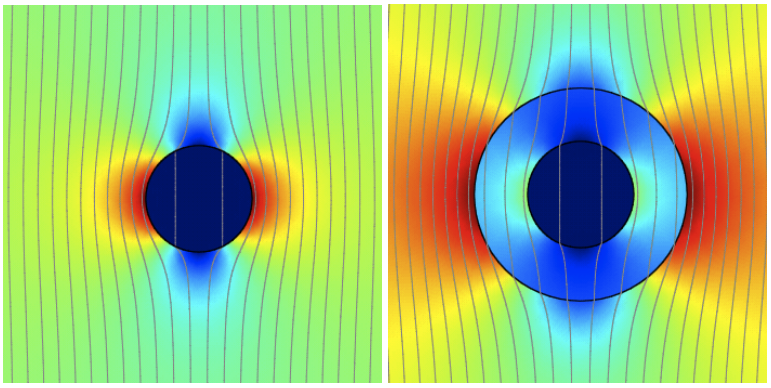

(a) (b)

Figure 4.2: Intensity of the electric field (colour, increasing from blue to red) and (grey) equipotential lines in and around a dielectric sphere exposed to a constant (vertical) external field (a) for a core-only QD (b) and core/shell QD ($\epsilon_c > \epsilon_{sh} > \epsilon_s$)

Indeed, as Pb atoms in the PbSe lattice are gradually replaced by Cd atoms, a CdSe shell with increasing thickness is formed for prolonged exchange times. This is confirmed by high-resolution transmission electron microscope (HR-TEM) images (see Figure 4.1(b)), which clearly show the CdSe shell around the PbSe core. To determine the core diameter, we use the PbSe or PbS sizing curve, as outlined in Section 4.1.

Under the assumption that the initial, known QD volume fraction does not change during the cation exchange process, the spectrum of μ_i (see Figure 4.3(a)) is readily obtained from the absorption spectrum of a PbSe/CdSe suspension (see Eq. 4.1). In Figure 4.3(a), spectra for several differently sized PbSe QDs clearly coincide at energies far above the bandgap, whereas the spectra for PbSe/CdSe QDs show a broad band of values due to the influence of the CdSe shell. Figure 4.3(c) shows a set of experimentally determined intrinsic absorption coefficients at 3.1 eV ($\mu_{3.1\mathrm{eV}}$) and 3.5 eV ($\mu_{3.5eV}$) for PbSe/CdSe QDs with different total diameter, core diameter and shell thickness as a function of the shell/quantum dot volume ratio V_{sh}/V_{QD}. For small shells μ_i slightly increases, reaching a maximum value. For larger shells, μ_i decreases rapidly. The lines represent $\mu_{i,th}$ values calculated with bulk PbSe and CdSe optical constants at 3.1 eV (400 nm) and 3.5 eV (355 nm).[19;20]. Similar results are obtained with a more limited data set from PbS/CdS QDs (see Figure 4.3(d)). Clearly, we find an

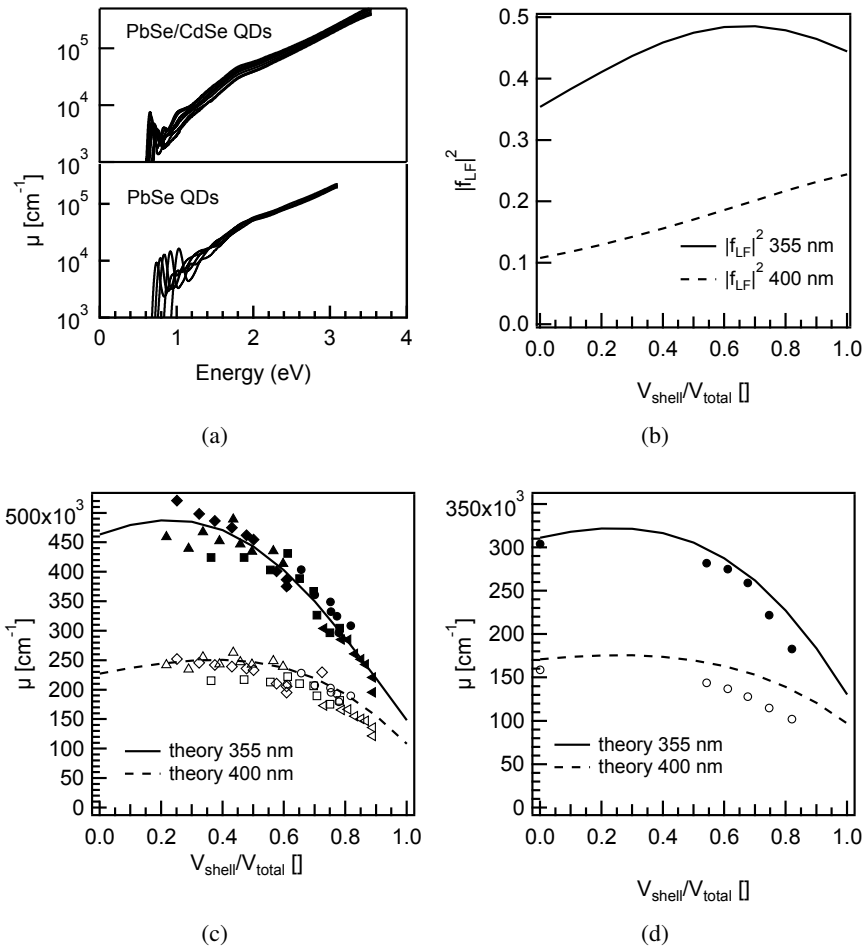

Figure 4.3: (a) Spectra of μ_i for PbSe/CdSe QDs with constant V_{QD} and increasing V_{sh} and PbSe QDs with varying diameters. (b) Local field factor calculated for PbSe/CdSe core/shell QDs at 355 nm and 400 nm. In the limiting case it becomes the local field factor for PbSe QDs($V_{sh} = 0$) or CdSe QDs ($V_{sh} = V_{total}$). (c) Intrinsic absorption coefficient $\mu_{3.5eV}$ at 355 nm and $\mu_{3.1eV}$ at 400 nm for PbSe/CdSe core/shell QDs as predicted by theory (black line) and as measured (with total diameter of circles = 5.2 nm, squares = 5.8 nm, triangles = 7.8 nm, leftarrows = 4.5 nm and diamonds = 7.5 nm). (d) and for PbS/CdS QDs (with total diameter = 5.9 nm)

excellent agreement between these theoretical values and the experimental results for $\mu_{3.1\mathrm{eV}}$ (dashed line) and $\mu_{3.5eV}$ (full line) for both PbSe/CdSe (see Figure 4.3(c)) and PbS/CdS QDs (see Figure 4.3(d)).

4.2.5 Local Field Factor of Heterostructured QDs

Following Neeves et al., the local field factor in the core of a core/shell QD reads[17]:

$$f_{LF} = \frac{9\epsilon_{sh}\epsilon_s}{\epsilon_{sh}\epsilon_a + 2\epsilon_s\epsilon_b} \tag{4.5}$$

At 3.1 eV, $|f_{LF}|^2$ gradually increases from the value of PbSe core QDs to that of CdSe core QDs, which accounts for the initial rise of the intrinsic absorption coefficient of PbSe/CdSe core/shells for small shells (see Figure 4.3(b)). With thicker shells, μ_i decreases, because the contribution of the CdSe shell, which absorbs less than the PbSe core, becomes more important. The great correspondence between the experimental and theoretical values for μ_i proves that the Maxwell-Garnett effective medium theory can adequately describe the absorption of QD heterostructures at high energies. At these energies, the energy levels of both the PbSe core and the CdSe shell form a continuum, allowing us to treat the absorption of these QD heterostructures using bulk values.

4.2.6 Conclusion

Calculating μ_i using the Maxwell-Garnett effective medium theory and bulk values for the dielectric function offers an elegant and reliable way to determine the QD concentration of suspensions of QD heterostructures (see Eq. 4.4), based on a straightforward absorbance measurement and knowledge of the core and shell size. This is essential for the succesfull integration of these QDs in applications such as LEDs and lasers. In typical synthesis schemes for core/shell growth, where the concentration remains constant, it also allows for direct monitoring of the dynamics of shell growth. For studies on the intrinsic carrier dynamics in QD heterostructures, the contribution of the change in the local field can be taken into account, using this effective medium theory.

4.3 Absorption Oscillator Strength

The first exciton transition is characterized by its energy and its oscillator strength $f_{if,abs}$. To obtain the oscillator strength, we use the energy-

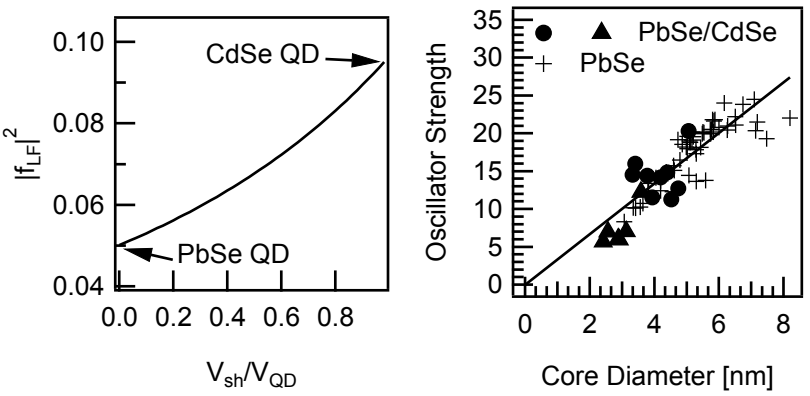

Figure 4.4: (a) Local field factor at the band edge for PbSe/CdSe QDs as a function of the ratio V_{sh}/V_{QD}. (b) Absorption oscillator strength $f_{if,abs}$ for PbSe QDs (crosses) and PbSe/CdSe QDs (full markers). The circles are values for PbSe/CdSe with a total diameter of 5.83 nm and the triangles a total diameter of 4.57 nm. The full black line is a guide to the eye.

integrated absorption coefficient $\mu_{\text{gap,eV}}$ (see Eq. 3.18) calculated from the spectrum of μ_i (see Eq. 4.1 and Fig. 4.3(a)), in analogy with calculations for PbSe[3] and PbS[4] QDs: .

$$f_{if,abs} = \frac{2\epsilon_0 c m_e n_s}{\pi \hbar e} \frac{V_{QD}}{|f_{LF}|^2} \mu_{\text{gap,eV}} \tag{4.6}$$

Here, ϵ_0 stands for the permittivity of the vacuum, c is the speed of light, m_e the electron mass, n_s the solvent refractive index (1.53 for C_2Cl_4), $\hbar$ Planck's constant, e the unit charge, f_{LF} the local field factor at the band gap (see Eq. 4.5 on p. 94).

Using $\epsilon_c = 25.7$[19] and $\epsilon_{sh} = 8.3$[20], we find that $|f_{LF}|^2$ gradually increases from the value for PbSe QDs to the value for CdSe QDs with increasing shell thickness (see Figure 4.4(a)). Because of the significant broadening of the first exciton peak at long reaction times, μ_{gap} is obtained by fitting a series of gaussian functions with a polynomial background function to the μ spectrum and taking the area under the first gaussian function. The combination of $|f_{LF}|^2$ with the values for $\mu_{\text{gap,eV}}$ enables us to calculate $f_{if,abs}$ of PbSe/CdSe QDs. Figure 4.4(b) shows that in the size range of 2.5 to 5 nm, we obtain similar values as a function of core diameter d_c as for PbSe QDs. This correspondence confirms that the nature of the first

absorption feature remains largely unchanged when adding a shell of CdSe.

4.4 Conclusion

In this chapter, we showed that the sizing curve of core-only PbSe and PbS QDs can be used to determine the core diameter of PbX/CdX (X = S, Se) core/shell QDs. Since the total diameter and concentration remains constant throughout the cationic exchange procedure, we used PbSe/CdSe and PbS/CdS QDs as a model system to test the validity of the Maxwell-Garnett model for colloidal core/shell QDs. We have shown that their intrinsic absorption coefficient at energies well above the band edge can be predicted using the Maxwell-Garnett effective medium theory and bulk values for the dielectric function. At the band gap, the energy-integrated absorption coefficient was used to calculate the oscillator strength of the band gap exciton transitions of core/shell QDs. We showed that the addition of CdX shell does not alter the oscillator strength of the absorbing transitions.

The validity of the Maxwell-Garnett model has important implications for colloidal QD heterostructure research, since the local field influences all optical characterization methods. It changes for example the magnitude of the absorption spectrum and the photoluminescence decay rate. Hence this model not only offers an easy way to determine concentrations of QD suspensions, but has to be taken into account when extracting the intrinsic physics of colloidal QD heterostructures from standard optical measurements.

References

[1] Pietryga, J.; Werder, D.; Williams, D.; Casson, J.; Schaller, R.; Klimov, V.; Hollingworth, J. Utilizing the Lability of Lead Selenide to Produce Heterostructured Nanocrystals with Bright, Stable Infrared Emission. *Journal of the American Chemical Society* **2008**, *130*, 4879–4885.

[2] Lambert, K.; De Geyter, B.; Moreels, I.; Hens, Z. PbTelCdTe CorelShell Particles by Cation Exchange, a HR-TEM study. *Chemistry of Materials* **2009**, *21*, 778–780.

[3] Moreels, I.; Lambert, K.; De Muynck, D.; Vanhaecke, F.; Poelman, D.; Martins, J. C.; Allan, G.; Hens, Z. Composition and size-dependent extinction coefficient of colloidal PbSe quantum dots. *Chemistry of Materials* **2007**, *19*, 6101–6106.

[4] Moreels, I.; Lambert, K.; Smeets, D.; De Muynck, D.; Nollet, T.; Martins, J. C.; Vanhaecke, F.; Vantomme, A.; Delerue, C.; Allan, G.; Hens, Z. Size-Dependent Optical Properties of Colloidal PbS Quantum Dots. *Acs Nano* **2009**, *3*, 3023–3030.

[5] Dai, Q.; Wang, Y.; Li, X.; Zhang, Y.; Pellegrino, D. J.; Zhao, M.; Zou, B.; Seo, J.; Wang, Y.; Yu, W. W. Size-Dependent Composition and Molar Extinction Coefficient of PbSe Semiconductor Nanocrystals. *ACS Nano* **2009**, *3*, 1518–1524.

[6] Zhang, Y.; Dai, Q.; Li, X.; Cui, Q.; Gu, Z.; Zou, B.; Wang, Y.; Yu, W. W. Formation of PbSe/CdSe Core/Shell Nanocrystals for Stable Near-Infrared High Photoluminescence Emission. *Nanoscale Research Letters* **2010**, *5*, 1279–1283.

[7] Kigel, A.; Brumer, M.; Maikov, G. I.; Sashchiuk, A.; Lifshitz, E. Thermally Activated Photoluminescence in Lead Selenide Colloidal Quantum Dots. *Small* **2009**, *5*, 1675–1681.

[8] Moreels, I.; Allan, G.; De Geyter, B.; Wirtz, L.; Delerue, C.; Hens, Z. Dielectric function of colloidal lead chalcogenide quantum dots obtained by a Kramers-Krönig analysis of the absorbance spectrum. *Phys. Rev. B* **2010**, *81*, 235319.

[9] Hens, Z.; Moreels, I. Light absorption by colloidal semiconductor quantum dots. *J. Mater. Chem.* **2012**, *22*, 10406–10415.

[10] Leatherdale, C.; Woo, W.; Mikulec, F.; Bawendi, M. On the absorption cross section of CdSe nanocrystal quantum dots. *Journal of Physical Chemistry B* **2002**, *106*, 7619–7622.

[11] Jasieniak, J.; Smith, L.; van Embden, J.; Mulvaney, P. Re-examination of the Size-Dependent Absorption Properties of CdSe Quantum Dots. *Journal of Physical Chemistry C* **2009**, *113*, 19468–19474.

[12] Capek, R. K.; Moreels, I.; Lambert, K.; De Muynck, D.; Zhao, Q.; Vantomme, A.; Vanhaecke, F.; Hens, Z. Optical Properties of Zincblende Cadmium Selenide Quantum Dots. *Journal of Physical Chemistry C* **2010**, *114*, 6371–6376.

[13] Yu, P.; Beard, M.; Ellingson, R.; Ferrere, S.; Curtis, C.; Drexler, J.; Luiszer, F.; Nozik, A. Absorption cross-section and related optical properties of colloidal InAs quantum dots. *Journal of Physical Chemistry B* **2005**, *109*, 7084–7087.

[14] Lommens, P.; Lambert, K.; Loncke, F.; De Muynck, D.; Balkan, T.; Vanhaecke, F.; Vrielinck, H.; Callens, F.; Hens, Z. The growth of Co : ZnO/ZnO core/shell colloidal quantum dots: Changes in nanocrystal size, concentration and dopant coordination. *Chemphyschem* **2008**, *9*, 484–491.

[15] Ricard, D.; Ghanassi, M.; Schanneklein, M. Dielectric confinement and the linear and nonlinear-optical properties of semiconductor-doped glasses. *Optics Communications* **1994**, *108*, 311–318.

[16] Sihvola, A. Two main avenues leading to the Maxwell Garnett mixing rule. *Journal of Electromagnetic Waves and Applications* **2001**, *15*, 715–725.

[17] Neeves, A.; Birnboim, M. Composite structures for the enhancement of nonlinear-optical susceptibility. *Journal of the Optical Society of America B-Optical Physics* **1989**, *6*, 787–796.

[18] Sihvola, A. *Electromagnetic mixing formulas and applications*; IET: London, UK, 1999.

[19] Suzuki, N.; Sawai, K.; Adachi, S. Optical-properties of pbse. *Journal of Applied Physics* **1995**, *77*, 1249–1255.

[20] Ninomiya, S.; Adachi, S. Optical-properties of cubic and hexagonal cdse. *Journal of Applied Physics* **1995**, *78*, 4681–4689.

5

Spontaneous Emission of PbSe and PbSe/CdSe

5.1 Comparison of Absorption and Emission between PbSe and PbSe/CdSe QDs

5.1.1 Classification of Heterostructured QDs

Compared to plain core QDs, core/shell QDs offer an enhanced stability and tunability of the optical and electronic properties. This difference arises from the spatial distribution of electron and hole wave functions in the QD heterostructures.

Based on the bulk band alignment and the effective mass theory in a quantum confined heterostructure, three regimes of core/shell QDs can be distinguished, depending on the localization of the charge carrier wave functions (see Figure 5.1). In a **type-I localization regime**, the electron and hole are both localized in the core, resulting in chemically stable and well passivated QDs with high photoluminescence (PL) quantum yield (QY). In a **type-II regime** the electron and hole are spatially separated. In a **quasi-type-II**[1] localization regime, one of the carriers is fully delocalized, while the other remains localized.

As amply demonstrated with QD heterostructures emitting in the visible, this opens up new possibilities for engineering the intrinsic opto-

electronic properties of nanomaterials. For instance, a five-fold reduction of the gain threshold was demonstrated with CdS/ZnSe dots, due to repulsive biexciton interaction of spatially separated excitons[2]. Similar effects, combined with a decrease in the Auger recombination rate were observed for CdTe/CdSe QDs[3;4]. For CdSe/CdTe heteronanocrystals[5;6] and ZnTe/ZnSe QDs[7], long radiative lifetimes, indicative of charge separation, and a strong redshift of the exciton transitions were reported.

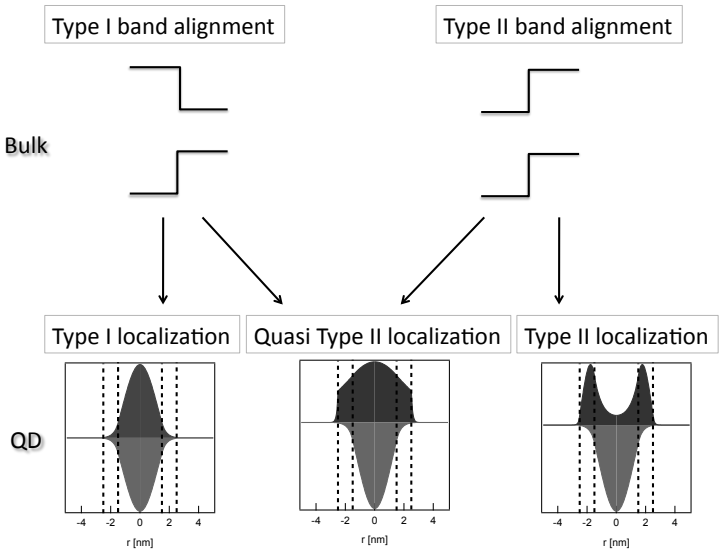

Figure 5.1: Core/shell QDs can be divided in three types, depending on the localization of the electron and hole wave function. In type-I, electron and hole are confined in the same region (either core or shell), in type-II, they are spatially separated. In a quasi-type-II one carrier is fully delocalized over the entire volume and one is localized in one region.

Previous work on colloidal type-II heteronanocrystals has focused primarily on compositions emitting in the visible spectral range. Colloidal core/shell heterostructures active in the near-infrared wavelength range (1000-3000 nm, NIR) have been scarcely investigated. For example, it has been recently shown that PbSe/PbS core/shell QDs with outer diameters below 10 nm behave like single composition QDs, where electron and hole are delocalized over the entire heterostructure[8]. Colloidal synthesis techniques were recently extended to concentric PbX/CdX (X=S, Se, Te) core/shell

QDs[9;10].

In this thesis we focus on PbSe/CdSe QDs, investigating their carrier distribution by absorption and photoluminescence (PL) spectroscopy and attempt to understand the electronic nature of the lowest absorbing and emitting states.

5.1.2 Steady-state and Time-resolved PL

Relative QY

Next to the absorbance spectrum, Figure 4.1(a) shows the PL spectrum for three different suspensions of PbSe/CdSe QDs. Due to the lack of efficient and reliable infrared reference dyes, the quantum yield (QY) is hard to determine. The QY is defined as the ratio of the emitted photon flux to the absorbed photon flux:

$$\begin{aligned} QY &= \frac{\Phi_{em}}{\Phi_{abs}} \\ &= \frac{\int \frac{P(E)}{E} dE}{\frac{P_{ex}}{E_{ex}}(1 - T(E_{ex}))} \\ &= \frac{\int \frac{P(E)}{E} dE}{\frac{P_{ex}}{E_{ex}}(1 - 10^{-\alpha(E_{ex})l})} \end{aligned}$$

with P_{ex} the excitation power, E_{ex} the excitation energy, $\alpha(E_{ex})$ the absorbance at the excitation energy and l the path length through the cuvette. Care is taken to avoid exposure to air of the PbSe QD samples. The PL spectrum is corrected for the grating and detector efficiency and converted to an energy scale, using the formula:

$$P(E) = P(\lambda)\frac{\lambda^2}{hc}$$

with $P(\lambda)$ the intensity spectrum on a wavelength scale as measured on the PL setup. A gaussian is fitted to the $P(E)$ spectrum and the area under the gaussian is determined.

Since P_{ex} is not known in absolute value, but is kept constant for all measurements, we can make a relative comparison between the QY of different samples. In Figure 5.2 we see the relative QY for PbSe and PbSe/CdSe QDs, by assigning a value of 100 to the most luminescent sample. We make sure to normalize them relative to the absorbance at the excitation wavelength and keep all settings of the spectrofluorometer the same. The

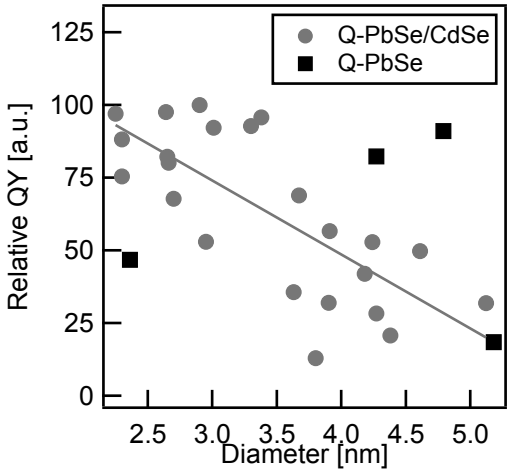

Figure 5.2: Relative QY for PbSe/CdSe (grey dots) and PbSe (black squares) as a function of the core diameter. The grey line is a guide to the eye.

QY for PbSe/CdSe QDs and PbSe QDs is comparable. Although a trend of increasing QY with decreasing core size is present for PbSe/CdSe QDs, the large scatter on these data suggests that sample preparation and surface quality have a large influence on the observed QY for PbSe/CdSe QDs.

From time-resolved PL to radiative lifetime estimates

We complemented the steady state PL results with PL lifetime measurements for different samples of PbSe/CdSe QDs, suspended in C_2Cl_4. The steady-state PL spectrum was broadened considerably for all samples to about 250 nm (full width at half maximum). Hence each sample was probed at several wavelengths. Figure 5.3(a) shows a typical decay curve for PbSe/CdSe QDs and its PbSe QD parent. From this logarithmic plot, we clearly see that the PbSe QD decay is monoexponential. It is considerably faster than the decay of PbSe/CdSe QDs, which is multiexponential.

From a single exponential fit to the decay curves of a 4.6 nm PbSe QD sample (see Figure 5.3(a)), we obtain an experimental lifetime τ_0 of 0.969 ± 0.002 μs, 0.979 ± 0.002 μs and 1.067 ± 0.002 μs respectively at a wavelength of 1375, 1425 and 1500 nm. These results agree with the 1.04 μs measured by Kigel *et al.*[11] for 4.7 nm PbSe QDs in chloroform. The decay curves of the different PbSe/CdSe QD samples were fitted

with a double exponential, a stretched exponential function and a lognormal distribution of decay rates[12]. The stretched exponential function and the lognormal distribution resulted in a much poorer fit than the double exponential function. For all samples, the double exponential fit yields two decay constants differing by about a factor of 10. However, the intensity (area under decay curve) of the slow decay was 5 to 20 times higher than the intensity of the fast decay. For this reason, we will focus our analysis on the slow component of the decay.

Figure 5.3(b) shows the results of the fit procedure (open light-grey squares, open black and grey markers). The lifetime differs significantly for different samples, ranging from 1.5 to 7 μs. The fact that PbSe/CdSe QDs from different suspensions, yet with comparable core diameters and shell thicknesses yield strongly different lifetimes suggests that the experimental lifetime τ_0 depends on the QY of each sample. In that case, the radiative lifetime τ_{rad} follows from:

$$\tau_0 = (\tau_{rad}^{-1} + \tau_{nrad}^{-1})^{-1} = \tau_{rad} QY \tag{5.1}$$

Since we are not able to determine the absolute QY, we cannot determine the τ_{rad} of the QDs. However, the relative QY allows us to rescale the values of τ_0, so we can compare the lifetimes of different QD suspensions. In Figure 5.3(b) the arrows illustrate that by rescaling the lifetime of each of the open red and open blue markers to the QY of the sample with full green squares, we obtain a one-to-one relation between core size and lifetime. We note that these values, between 4 and 7 μs, are a lower limit of τ_{rad}. From Figure 5.3(b), we see that the lifetime decreases with increasing core diameter. This was predicted by Moreels *et al.*[13] using the molar extinction coefficient at the band gap for PbSe QDs up to 5 nm. Kigel *et al.*[11] measured a similar decreasing trend. For all wavelengths, the values are at least 4 to 6 times higher for PbSe/CdSe QDs than for PbSe QDs[11;14;15].

5.1.3 Emission Oscillator Strength

From the lower limit of the radiative lifetime obtained above for PbSe/CdSe QDs and literature values for PbSe QDs[11;14], we can calculate an upper limit of the oscillator strength $f_{if,PbSe/CdSe,em}$ and $f_{if,PbSe,em}$ of the emitting transition.

$$f_{if,em} = \frac{2\pi\varepsilon_0 c^3 m_e}{e^2} \frac{g}{n_s \left| f_{LF} \right|^2 \omega^2} \tau_{rad}^{-1} \tag{5.2}$$

Dielectric screening will affect the radiative lifetime. Therefore we correct for this local field effect with f_{LF}. While the absorption oscillator strength

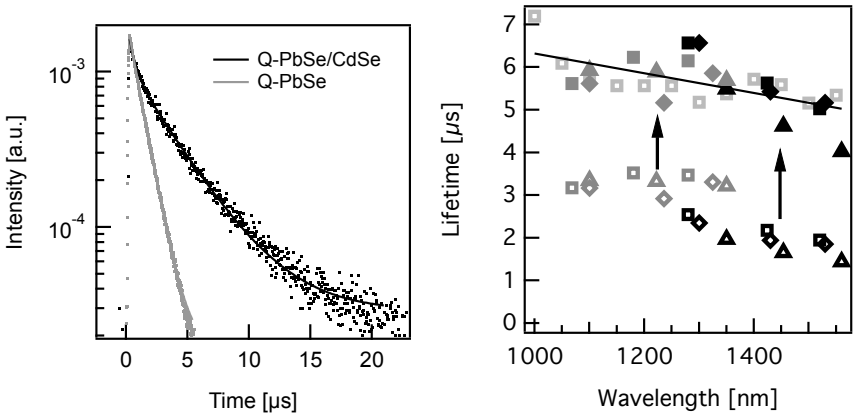

(a) (b)

Figure 5.3: (a) Typical decay curve for PbSe/CdSe QDs and their PbSe QD parent, shown on a logarithmic scale illustrates the longer lifetime of PbSe/CdSe QDs. A single exponential fit is shown for PbSe and a biexponential fit for PbSe/CdSe. (b) Lifetime for 7 samples of PbSe/CdSe QDs. Each sample is probed at different wavelengths (markers with equal colour and symbol). Light gray squares have a PbSe QD parent diameter of 6.09 nm, black markers a PbSe QD parent diameter of 5.83 nm and grey markers a parent diameter of 4.57 nm. Open symbols give the decay constant for the slow component obtained from a bi-exponential fit to experimental decay curves. Closed symbols give the fitted values rescaled according to the QY of each individual sample, taking the sample with open light-gray squares as the standard.

is the sum of the transition strengths of all exciton states f_k:

$$f_{if,abs} = \sum_{k=1}^{g} f_k \tag{5.3}$$

the emission oscillator strength is, taking into account possible splitting between the states, a Boltzmann weighted average of the transition strength of each exciton state[16]:

$$f_{if,em} = g\frac{\sum_{k=1}^{g} f_k e^{\frac{-\Delta E_k}{kT}}}{\sum_{k=1}^{g} e^{\frac{-\Delta E_k}{kT}}} \tag{5.4}$$

Effectively, this yields the average transition strength of the states that contribute to emission. Since emission comes from radiative decay of a single exciton, which occupies only one of all possible ground exciton states, and absorption involves all exciton states, we multiply in Eq. 5.4 by the total number of exciton states $g = 64$ to obtain a total emission oscillator strength. This is equivalent to compressing the fine structure to one single emitting state with degeneracy g and oscillator strength $f_{if,em}$.

The resulting values for $f_{if,PbSe/CdSe,em}$ and $f_{if,PbSe,em}$ are represented by the open markers in red and blue respectively in Figure 5.4. The values for $f_{if,PbSe,em}$ are similar to the values obtained from the absorption spectrum $f_{if,PbSe,abs}$. Values smaller by at least 75% are found for the emission oscillator strength $f_{if,PbSe/CdSe,em}$.

5.1.4 Discussion

PL Quenching

The quantitative analysis of the absorption and luminescence data yields contradictory outcomes. While the energy and the absorption oscillator strength of the band gap transition in PbSe/CdSe are indicative of a type-I localization regime, the sensitivity of the emission QY and the increase in exciton lifetime associated with a decrease in emission oscillator strength suggest that one of the carriers is delocalized over the entire QD (quasi-type-II) or even localized in the CdSe shell (type-II). To pinpoint the localization regime, we added dodecanethiol (DDT), a well-known hole scavenger for CdSe[17;18] and PbSe[19;20]and methyl viologen (MV^{2+}), an electron scavenger[21;22], to PbSe/CdSe suspensions and analyzed their effect on the photoluminescence.

Adding DDT (150μM) to a PbSe/CdSe suspension does not affect the QY (Figure 5.5(a)). It redshifts the emission spectra by 20-40 nm (see Figure 5.5(b)), indicating interaction of at least one of the charge carriers with

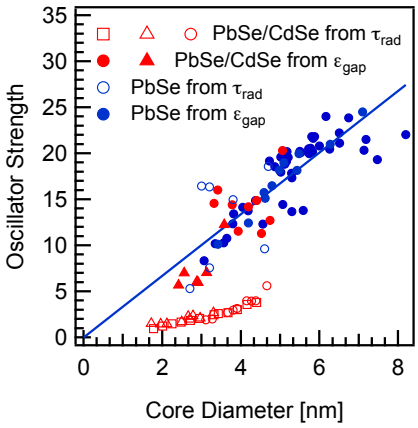

Figure 5.4: Absorption oscillator strength $f_{if,abs}$ for PbSe QDs (full blue markers) and PbSe/CdSe QDs (full red markers) and emission oscillator strength $f_{if,em}$ for PbSe QDs[11;14] (empty blue markers) and PbSe/CdSe QDs (empty red markers) as a function of the core diameter. The red squares are values for PbSe/CdSe with a total diameter of 6.09 nm, the red dots a total diameter of 5.83 nm and the red triangles a total diameter of 4.57 nm.

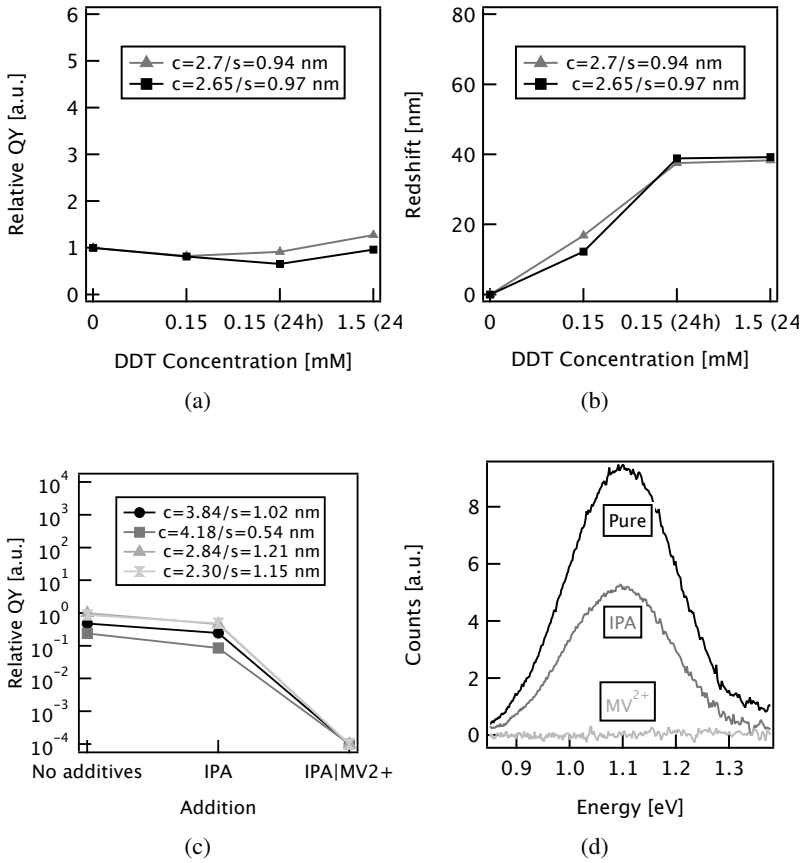

Figure 5.5: (a) Relative QY and (b) PL redshift before and after adding thiols (c) Relative QY (log-scale) and (d) PL spectra before and after adding IPA and MV^{2+}/IPA. The graphs show the clear difference between the addition of a hole acceptor and an electron acceptor to PbSe/CdSe QDs.

	PbSe[25]	cubic CdSe[26;27]
m_e	0.047	0.12
m_h	0.040	0.8

Table 5.1: Effective masses of PbSe and cubic CdSe.

the surface[23;24]. In contrast, addition of DDT to a PbSe QD sample resulted in significant quenching of the PL. Methylviologen dichloride was dissolved in isopropanol (IPA) and the MV^{2+}/IPA mixture was added in a 1:33 (v:v) ratio to obtain a 150μM MV^{2+} concentration. As a reference, we added the same amount of pure IPA to an identical QD sample, which resulted in a 50% drop of the QY. Adding the MV^{2+} mixture however immediately quenches the PL signal to values below the detection limit (Figure 5.5(c) and Figure 5.5(d)). The same result was obtained for a PbSe QD reference sample. This shows that PbSe/CdSe QDs emit from a state in which the electron wave function reaches the surface and the hole wave function is well confined to the core. It confirms that PbSe/CdSe are in the (quasi)-type-II localization regime. The delocalization of the electron will reduce the wavefunction overlap to some extent. However, these measurements are not sufficient to conclude that this reduction in overlap fully accounts for the reduction in emission oscillator strength. In addition, they do not explain why the absorption oscillator strength essentially remains unchanged.

Effective Mass Modelling

Atomistic calculations that reconcile the experimental results are not yet available. Therefore, we interpret our results in terms of an effective mass model, based on literature data of the bulk band alignment and the effective masses[25–27]. In addition, we use the energy criterion introduced by Klimov *et al.* to classify quantum confined heterojunctions based on their carrier localization[28]. This criterion can best be appreciated by means of the square of the wavenumber for electron (k_e^2) and hole (k_h^2):

$$k_{e,h}^2 = \frac{2m_{e,h}}{\hbar^2}(E_{e,h} - V_{e,h})$$

Here, $V_{e,h}$ denotes the potential (i.e., the position of the bulk energy bands) in each region and $m_{e,h}$ the effective mass for electron and hole. If k^2 is negative, the wavenumber is imaginary, resulting in an exponentially decaying wave function. Provided that the characteristic decay length k^{-1}

is sufficiently small, this means that a charge carrier is preferentially found in that region of the heterostructure where k^2 is positive and the resulting wave number is real. Hence, looking at binary heterostructures, we talk about type-I regime, if k_e^2 and k_h^2 have the same sign in each region of the heterostructure. For type-II regime, k_e^2 and k_h^2 have opposite sign in every region. Finally, for quasi-type-II regime, k_e^2 and k_h^2 have the same sign in one of the regions, and opposite sign in the other region (see Figure 5.6(a)).

According to Michaelson[29], bulk PbSe and CdSe have a type-I bulk band alignment with a valence band offset of 0.78 eV and conduction band offset of 0.70 eV. Using the effective masses of PbSe and CdSe as summarized in Table 5.1, we obtain the wave function of a PbSe/CdSe QD with a core radius of 1.5 nm and a shell thickness 1 nm as plotted in 5.6(b). Due to the difference in effective mass between electron and hole in CdSe, we find that the electron wave function spreads throughout the entire QD, while the hole wave function is confined to the core. Taking the band offset Δ as an adjustable parameter, we find that PbSe/CdSe QDs are at the boundary between the type-I and quasi-type-II regime. The overlap integral slightly drops from a value close to one for large band offsets to about 0.8 when Δ equals zero. Since the overlap integral is directly proportional to the oscillator strength, this confirms the experimental result that $f_{if,PbSe/CdSe,abs}$ does not significantly differ from $f_{if,PbSe,abs}$.

Eventhough there is only a small reduction in overlap, the electron wavefunction does have a non-zero value at the QD outer surface, while the hole wavefunction is negligible at the QD outer surface. This overall picture is confirmed by the PL quenching experiments, which show that the electron is transferred to the electron acceptor at the surface, while the hole does not transfer to the hole acceptor.

This simple model fails to explain why $f_{if,PbSe/CdSe,em}$ is reduced. The fact that the QY of PbSe/CdSe QDs is comparable to and often higher than that of PbSe QDs and the clear dependence of $f_{if,PbSe/CdSe,em}$ on the QD diameter indicate that this is most likely an intrinsic PbSe/CdSe QD property, and not an artefact due to surface-state mediated radiative recombination. Therefore, it suggests that the fine structure of PbSe/CdSe QDs, which our model cannot resolve, is more complex. Looking at Eq. 5.3 and Eq. 5.4, $f_{if,abs}$ and $f_{if,em}$ will only differ significantly, when (a) the energy splitting is much larger than the thermal energy kT and (b) the emitting states have a much lower oscillator strength than the absorbing states. Therefore, the band edge emission in PbSe/CdSe QDs comes from states, that are fundamentally different from the bright absorbing states.

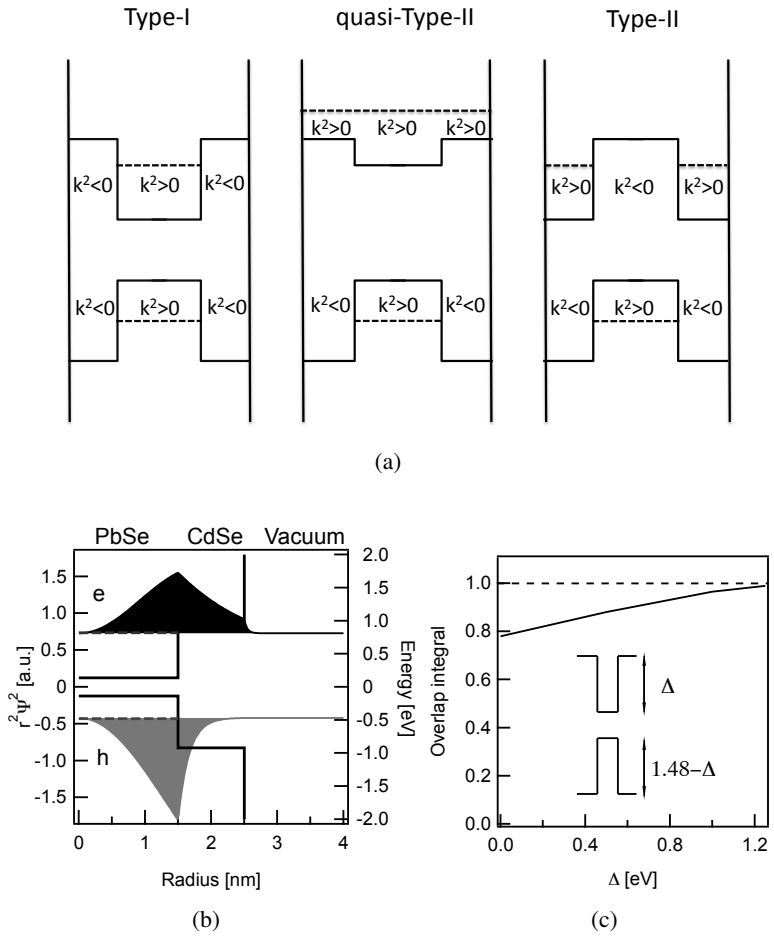

Figure 5.6: (a) Definition of types of localization regimes in core/shell quantum dots in terms of the square of the wavenumber k^2.(b) Electron and hole wave functions ($r^2\Psi^2$) for PbSe/CdSe QDs (green and red) in a simple effective mass model illustrate the delocalized electron wave function. The confinement energy (striped) is drawn within the bulk band diagram. (c) Overlap integral as a function of the conduction band offset Δ. The dotted line shows the overlap integral for PbSe QDs shows that even for zero offset the overlap only reduces by 20%.

Stokes shift

A splitting of the band edge in a lower energy dark and higher energy bright state due to the exchange interaction was predicted for PbSe QDs by An *et al.*[16]. This so-called exchange splitting however is only between 0 and 20 meV. Hence, at room-temperature these states are both populated due to thermal excitation, resulting in similar values for $f_{if,PbSe,abs}$ and $f_{if,PbSe,em}$. According to An *et al.*[16], the exchange splitting, together with the intervalley splitting, explains the non-resonant Stokes shift in PbSe QDs. Figure 5.7(b) shows the Stokes shift of PbSe QDs (blue squares) and PbSe/CdSe QDs (red dots) as a function of absorption energy or core size. Our values for PbSe QDs extrapolate well to the theoretical values reported for small QDs[16;30;31].

Like the band gap energy, the PbSe/CdSe QD Stokes shift depends only on the core size, but it exceeds that for PbSe QDs by 50 to 100 meV. For small cores, it reaches a value of 200 meV. The molar extinction coefficient at energies well above the bandgap is typically volume dependent for colloidal QDs. Therefore a broad size distribution can result in a shift in the PL spectrum, because larger particles are excited more than smaller particles. To quantify this effect, we write the PL intensity ϕ_{em} proportional to the Gaussian concentration distribution G and the molar extinction coefficient ϵ:

$$\phi_{em} \sim c_0 G\left(\mu_d, \sigma_d\right) \epsilon\left(E_{ex}\right) \sim c_0 G\left(\mu_d, \sigma_d\right) d^3$$

Here c_0 is the total QD concentration, μ_d the average QD diameter and σ_d the QD diameter standard deviation. Using the raw moments of the gaussian distribution the relative shift in mean diameter in the PL spectrum can be obtained:

$$\frac{\Delta\mu_d}{\mu_d} = \frac{3\sigma_d^4 + 3\sigma_d^2}{3\sigma_{d^2} + 1}$$

This shift is indeed highly dependent on the size distribution. Using the sizing curve of PbSe, we calculated the energy shift in the PL spectrum as a function of the QD diameter for three different size distributions (see Figure 5.7(a). For small size distributions (5%) the shift is about 5 meV and hence not enough to explain the PbSe Stokes shift.

For PbSe/CdSe QDs, we showed in Section 4.2 (see p. 89) that the molar extinction coefficient is largely determined by the total QD volume with only a small dependence on the ratio V_{shell}/V_{QD}.[32] Since the total volume and total size dispersion remain constant for these QDs throughout the exchange procedure[9], we expect an increase in the Stokes shift due to non-uniform excitation of maximum 10 meV for the most broadened sample. The large Stokes shift is therefore not an artefact of size broadening, but

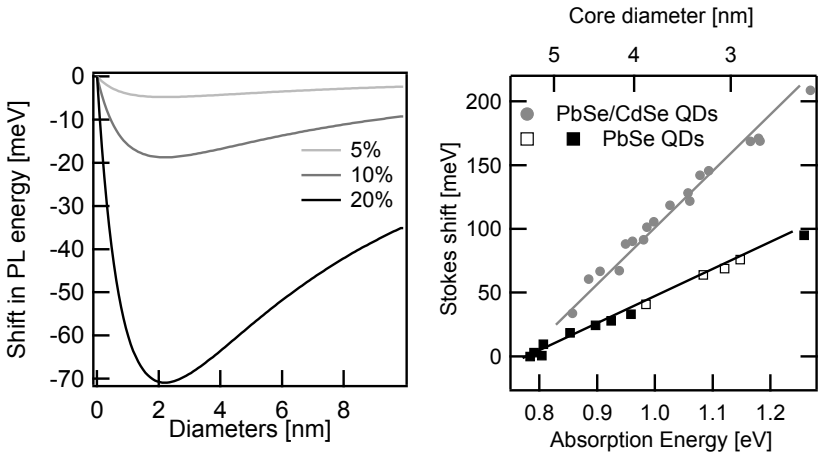

(a) (b)

Figure 5.7: (a) The shift in the PL mean energy as a function of the PbSe QD diameter for three different size distributions shows that the size distribution can result in an apparent Stokes shift (b)Stokes shift for PbSe QDs (full and open [11] black squares) is much smaller than for PbSe/CdSe QDs (full grey squares).

due to an intrinsic physical effect. Increased splitting in the fine structure will according to Boltzmann statistics result in an increased Stokes shift. Hence, it confirms that the band edge emission results mostly from lower energy states with reduced oscillator strength as compared to the higher energy absorbing states.

This fine structure cannot be understood without extensive modelling. The nature of the interface, both in the real and in the reciprocal lattice (the band edge states are around the L-point for PbSe and the Γ-point for CdSe) probably has a strong influence on the electronic properties of these heterostructures. This could result in increased exchange and intervalley splitting, or might induce states at the PbSe/CdSe interface. For PbTe/CdTe however, theoretical calculations did not yield such interfacial states [33], because the atomic structure of the lattice at the interface is virtually unperturbed.

5.1.5 Conclusion

In conclusion, we show that both the energy and the absorption oscillator strength of the first absorption peak in PbSe/CdSe quantum dots follow the same trend with core diameter as PbSe QDs. On the other hand, PL lifetime measurements yield an oscillator strength in emission that is reduced by at least 75%, compared to the PbSe/CdSe oscillator strength from absorption and the PbSe QD oscillator strength in absorption and emission. Moreover, the addition of an electron scavenger leads to a complete quenching of the PbSe/CdSe QD PL, while a hole scavenger does not. These results can be rationalized by an effective mass model that depicts a PbSe/CdSe QD as a quantum confined heterostructure at the boundary between a type-I and a quasi-type-II localization regime. They show that the absorbing states essentially remain unchanged by the addition of a CdSe shell. However, they do not explain the reduction of the oscillator strength of the band gap emission. In combination with the significantly increased Stokes shift, we conclude that the band gap emission in PbSe/CdSe QDs comes from fundamentally different states with lower oscillator strength that are energetically well separated from the absorbing states at room temperature. Moreover, these emitting states are different than the emitting states in PbSe QDs. Depending on the degeneracy of the emitting states, these binary heterostructures could allow lasing in the NIR wavelength range using single excitons.

References

[1] Ivanov, S. A.; Piryatinski, A.; Nanda, J.; Tretiak, S.; Zavadil, K. R.; Wallace, W. O.; Werder, D.; Klimov, V. I. Type-II core/shell CdS/ZnSe nanocrystals: Synthesis, electronic structures, and spectroscopic properties. *Journal of the American Chemical Society* **2007**, *129*, 11708–11719.

[2] Klimov, V. I.; Ivanov, S. A.; Nanda, J.; Achermann, M.; Bezel, I.; McGuire, J. A.; Piryatinski, A. Single-exciton optical gain in semiconductor nanocrystals. *Nature* **2007**, *447*, 441–446.

[3] Oron, D.; Kazes, M.; Banin, U. Multiexcitons in type-II colloidal semiconductor quantum dots. *Physical Review B* **2007**, *75*, 035330.

[4] Dorfs, D.; Franzl, T.; Osovsky, R.; Brumer, M.; Lifshitz, E.; Klar, T. A.; Eychmueller, A. Type-I and type-II nanoscale heterostructures based on CdTe nanocrystals: A comparative study. *Small* **2008**, *4*, 1148–1152.

[5] Jones, M.; Kumar, S.; Lo, S. S.; Scholes, G. D. Exciton trapping and recombination in type IICdSe/CdTe nanorod heterostructures. *Journal of Physical Chemistry C* **2008**, *112*, 5423–5431.

[6] de Mello Donegá, C. Formation of nanoscale spatially indirect excitons: Evolution of the type-II optical character of CdTe/CdSe heteronanocrystals. *Physical Review B* **2010**, *81*, 165303.

[7] Bang, J. et al. ZnTe/ZnSe (Core/Shell) Type-II Quantum Dots: Their Optical and Photovoltaic Properties. *Chemistry of Materials* **2010**, *22*, 233–240.

[8] Bartnik, A. C.; Wise, F. W.; Kigel, A.; Lifshitz, E. Electronic structure of PbSe/PbS core-shell quantum dots. *Physical Review B* **2007**, *75*, 245424.

[9] Pietryga, J.; Werder, D.; Williams, D.; Casson, J.; Schaller, R.; Klimov, V.; Hollingworth, J. Utilizing the Lability of Lead Selenide to Produce Heterostructured Nanocrystals with Bright, Stable Infrared Emission. *Journal of the American Chemical Society* **2008**, *130*, 4879–4885.

[10] Zhang, Y.; Dai, Q.; Li, X.; Cui, Q.; Gu, Z.; Zou, B.; Wang, Y.; Yu, W. W. Formation of PbSe/CdSe Core/Shell Nanocrystals for Sta-

ble Near-Infrared High Photoluminescence Emission. *Nanoscale Research Letters* **2010**, *5*, 1279–1283.

[11] Kigel, A.; Brumer, M.; Maikov, G. I.; Sashchiuk, A.; Lifshitz, E. Thermally Activated Photoluminescence in Lead Selenide Colloidal Quantum Dots. *Small* **2009**, *5*, 1675–1681.

[12] van Driel, A. F.; Nikolaev, I. S.; Vergeer, P.; Lodahl, P.; Vanmaekelbergh, D.; Vos, W. L. Statistical analysis of time-resolved emission from ensembles of semiconductor quantum dots: Interpretation of exponential decay models. *Physical Review B* **2007**, *75*, 035329.

[13] Moreels, I.; Lambert, K.; Smeets, D.; De Muynck, D.; Nollet, T.; Martins, J. C.; Vanhaecke, F.; Vantomme, A.; Delerue, C.; Allan, G.; Hens, Z. Size-Dependent Optical Properties of Colloidal PbS Quantum Dots. *Acs Nano* **2009**, *3*, 3023–3030.

[14] Schaller, R. D.; Crooker, S. A.; Bussian, D. A.; Pietryga, J. M.; Joo, J.; Klimov, V. I. Revealing the Exciton Fine Structure of PbSe Nanocrystal Quantum Dots Using Optical Spectroscopy in High Magnetic Fields. *Physical Review Letters* **2010**, *105*, 067403.

[15] Oron, D.; Aharoni, A.; Donega, C. d. M.; van Rijssel, J.; Meijerink, A.; Banin, U. Universal role of discrete acoustic phonons in the low-temperature optical emission of colloidal quantum dots. *Physical Review Letters* **2009**, *102*, 177402.

[16] An, J. M.; Franceschetti, A.; Zunger, A. The excitonic exchange splitting and radiative lifetime in PbSe quantum dots. *Nano Letters* **2007**, *7*, 2129–2135.

[17] Aldana, J.; Wang, Y.; Peng, X. Photochemical instability of CdSe nanocrystals coated by hydrophilic thiols. *Journal of the American Chemical Society* **2001**, *123*, 8844–8850.

[18] Wuister, S. F.; Donega, C. D.; Meijerink, A. Influence of thiol capping on the exciton luminescence and decay kinetics of CdTe and CdSe quantum. *Journal of Physical Chemistry B* **2004**, *108*, 17393–17397.

[19] Wang, C.; Kwon, K.-W.; Odlyzko, M. L.; Lee, B. H.; Shim, M. PbSe nanocrystal/TiOx heterostructured films: A simple route to nanoscale heterointerfaces and photocatalysis. *Journal of Physical Chemistry C* **2007**, *111*, 11734–11741.

[20] Luther, J. M.; Law, M.; Song, Q.; Perkins, C. L.; Beard, M. C.; Nozik, A. J. Structural, Optical, and Electrical Properties of Self-Assembled Films of PbSe Nanocrystals Treated with 1,2-Ethanedithiol. *ACS Nano* **2008**, *2*, 271–280.

[21] Burda, C.; Green, T.; Link, S.; El-Sayed, M. Electron shuttling across the interface of CdSe nanoparticles monitored by femtosecond laser spectroscopy. *Journal of Physical Chemistry B* **1999**, *103*, 1783–1788.

[22] Matylitsky, V. V.; Dworak, L.; Breus, V. V.; Basche, T.; Wachtveitl, J. Ultrafast Charge Separation in Multiexcited CdSe Quantum Dots Mediated by Adsorbed Electron Acceptors. *Journal of the American Chemical Society* **2009**, *131*, 2424–2425.

[23] Koole, R.; Luigjes, B.; Tachiya, M.; Pool, R.; Vlugt, T. J. H.; Donega, C. D. M.; Meijerink, A.; Vanmaekelbergh, D. Differences in cross-link chemistry between rigid and flexible dithiol molecules revealed by optical studies of CdTe quantum dots. *Journal of Physical Chemistry C* **2007**, *111*, 11208–11215.

[24] Talgorn, E.; Moysidou, E.; Abellon, R. D.; Savenije, T. J.; Goossens, A.; Houtepen, A. J.; Siebbeles, L. D. A. Highly Photoconductive CdSe Quantum-Dot Films: Influence of Capping Molecules and Film Preparation Procedure. *Journal of Physical Chemistry C* **2010**, *114*, 3441–3447.

[25] Martinez, G.; Schlüter, M.; Cohen, M. L. Electronic structure of PbSe and PbTe. I. Band structures, densities of states, and effective masses. *Physical Review B* **1975**, *11*, 651–659.

[26] Dalven, R. Calculation of effective masses in cubic CdS and CdSe. *Physica Status Solidi B-Basic Research* **1971**, *48*, 13.

[27] Nikitine, S.; Dimmock, J.; Wheeler, R. Exciton structure and zeeman effects in cadmium selenide. *Journal of Applied Physics* **1961**, *32*, 2271–2277.

[28] Piryatinski, A.; Ivanov, S. A.; Tretiak, S.; Klimov, V. I. Effect of quantum and dielectric confinement on the exciton-exciton interaction energy in type II core/shell semiconductor nanocrystals. *Nano Letters* **2007**, *7*, 108–115.

[29] Michaelson, H. B. Relation between an atomic electronegativity scale and the work function. *IBM Journal of Research and Development* **1978**, *22*, 72–80.

[30] Leitsmann, R.; Bechstedt, F. Characteristic Energies and Shifts in Optical Spectra of Colloidal IV-VI Semiconductor Nanocrystals. *ACS Nano* **2009**, *3*, 3505–3512.

[31] Franceschetti, A. Structural and electronic properties of PbSe nanocrystals from first principles. *Physical Review B* **2008**, *78*, 075418.

[32] De Geyter, B.; Hens, Z. The absorption coefficient of PbSe/CdSe core/shell colloidal quantum dots. *Applied Physics Letters* **2010**, *97*, 161908.

[33] Leitsmann, R.; Bechstedt, F.; Groiss, H.; Schaeffler, F.; Heiss, W.; Koike, K.; Harada, H.; Yano, M. Structural and electronic properties of PbTe (rocksalt)/CdTe (zinc-blende) interfaces. *Applied Surface Science* **2007**, *254*, 397–400.

6

Transient Absorption and Stimulated Emission in PbSe and PbSe/CdSe

6.1 Transient Absorption Spectroscopy

6.1.1 The TA setup

Understanding the dynamics of charge carriers in QDs is essential to design the next generation of high performance optical materials for applications in integrated photonics. An indispensable technique to monitor the dynamics of charge carriers is transient absorption spectroscopy[1]. In this measurement, a short laser pulse excites carriers to a higher energy level. The population of carriers in a certain QD state is subsequently monitored by measuring the change in transmission over time of a probe laser resonant with a transition from or to this state (see Figure 6.2).

To access the ultrafast timescale that governs the dynamics of the charge carriers in QDs, a femtosecond pulsed laser is needed. Moreover, to get the excitation densities high enough to study the interactions of multiple excitons, the energy of the pulse needs to be sufficiently high. Currently, only one type of laser satisfies these requirements: the optically pumped and amplified femtosecond titanium-sapphire laser, emitting a maximum of a few mJ of energy per pulse around 800 nm.

Figure 6.1 shows the layout of the setup at TUDelft that was used in this thesis. A commercial Ti:S laser system (Mira- Legend USP, Coherent

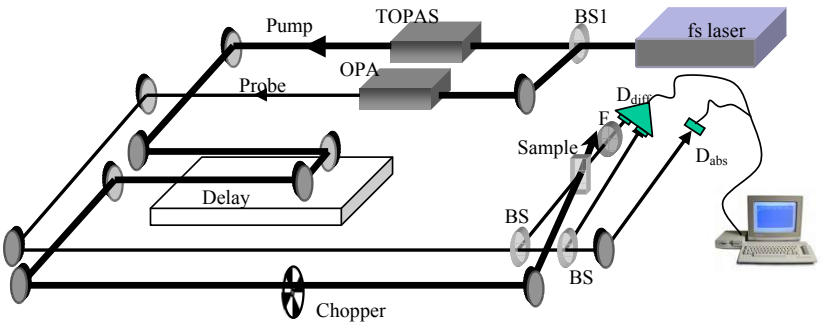

Figure 6.1: Scheme of the transient absorption spectroscopy setup. BS1, BS are beam splitters; OPERA and TOPAS are optical parametric amplifiers; F: filter; D_{diff} and D_{abs}: difference and absolute detector (reprinted from Trinh[2])

Inc.) seeds a separate optical parametric amplifier for the pump (Topas-800-fs, Coherent Inc.) and probe beams (Opera, Coherent Inc.). These OSA's convert the pump and probe to the desired energy. Pump and probe beams overlap under a small angle (3°) in a cuvette of 10 mm path length (see Figure 6.2) and are imaged onto InGaAs pin photodiodes (Hamamatsu G5853-23, G8605-23). The polarization of the pump and probe is made orthogonal so that pulses of similar photon energy can be separated with polarization filters.

The delay stage in the setup (see Figure 6.1) permits variation in the delay time between the pump and probe pulses in a temporal window extending to 1 ns. The measured fractional transmission signals, called transient absorption (*TA*) in the following, may be written as $TA = \frac{T_{on}-T_{off}}{T_{off}}$, where T_{on} denotes the probe transmission with pump on and T_{off} the probe transmission with pump off. With this definition, bleach and emission yield positive *TA* signals while an increase in absorption yields negative *TA* signals.

The TA signal can easily be converted to a differential absorption signal $\Delta\alpha$:

$$\Delta\alpha = \alpha_{off} - \alpha_{on} = \log\frac{T_{on}}{T_{off}} = \log(1 + TA)$$

where α_{off} and α_{on} are the absorbance with the pump off and on respec-

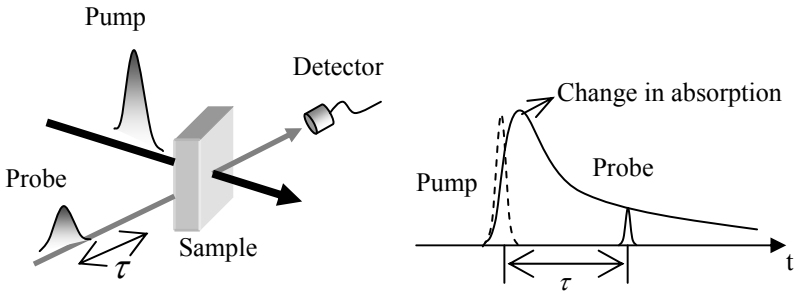

Figure 6.2: Principle of a pump-probe experiment. Pump causes a change of absorption of the probe pulse, which is measured by a detector as a function of time delay between the pump and probe pulses.(reprinted from Trinh[2])

tively. Gain occurs when $\Delta\alpha > \alpha_{off}$. Note that this requires a separate measurement of α_{off} (or α_0), usually with a regular absorption spectrometer.

6.1.2 From TA transients to QD Population Dynamics

The operating principle and resulting time transient is illustrated in Figure 6.2. To relate the recorded time transients to the population dynamics, the first step is to convert the excitation power to the number of excitons created by the pump pulse. This can be done by measuring the pump laser power P and the diameter of the pump spot d_{spot} entering the sample, to extract the photon flux density Φ_0:

$$\Phi = \frac{P}{f_{rep}} \frac{1}{\hbar\omega} \frac{4}{\pi d_{spot}^2}$$

Here f_{rep} is the repetition rate of the laser (typically 1 KHz) and $\hbar\omega$ the energy of the pump photon. The average number of excitons created by the pulse N_{eh} then becomes, with the absorption cross section at the pump wavelength σ_{pump}:

$$N_{eh} = \frac{1}{L} \int_0^L \Phi(z)\sigma_{pump} \tag{6.1}$$

$$= \Phi_0 \frac{1 - 10^{-\alpha_0 L}}{\langle QD \rangle L} \tag{6.2}$$

Here we have used the relation between the absorbance and the QD cross section (see Eq. 4.1 where $\sigma = \mu_i V_{QD}$). L is the cuvette length and $\langle QD \rangle$ is the QD concentration in the sample.

The probability that a QD has n excitons for a given average N_{eh} number of excitons is described by the Poisson distribution[3]:

$$\mathcal{P}(n, N_{eh}) = \frac{N_{eh}^n e^{-N_{eh}}}{n!} \tag{6.3}$$

This we can use to get a more accurate measurement of N_{eh}. As N_{eh} depends quadratically on d_{spot} and the differential absorption signal depends on the overlap of the pump and probe beam, it is more precise to derive N_{eh} from a pump-dependent measurement of the differential absorption at the bandgap, when all multi-excitons have recombined through Auger recombination and a population of single excitons remains, according to the following distribution:

$$\Delta\alpha_{500ps} = \frac{2\alpha_0}{g}(1 - e^{-N_{eh}}) = A\left(1 - e^{-BP}\right)$$

Here g is the degeneracy of the level. A global fit to the differential absorption *vs* pump power around the bandgap yields a relation between N_{eh} and P with the fit parameter B. To illustrate the necessity of this correction, we obtain for the PbSe QDs, used in Section 6.2, the cross section $\alpha_{pulse} = 0.132$ cm^{-1} , which differs from the value measured in the linear absorption spectrum $\alpha_{pulse} = 0.180$ cm^{-1}, because of errors in the spot size and the overlap between pump and probe beam.

At early delay times (typically 5 to 10 ps), the carriers have cooled to the band gap, but have not yet recombined through Auger recombination. This therefore gives a direct measurement of the average number of excitons $\widetilde{n}$ around the band gap

$$\begin{aligned} \Delta\alpha_{5ps} &= \frac{2\alpha_0}{g}\widetilde{n} \\ &= \frac{2\alpha_0}{g}\left(\sum_{n=1}^{g} n\mathcal{P}(n, N_{eh}) + \sum_{n=g+1}^{\infty} g\mathcal{P}(n, N_{eh})\right) \end{aligned} \tag{6.4}$$

This is a so-called state-filling model[3], where $\widetilde{n}$ cannot exceed the degeneracy g of that level.

The ratio of $\Delta\alpha_{5ps}/\Delta\alpha_{500ps}$ of the differential absorption at early and late delay times is a measure of the average number of excitons per excited QD. In the limit of high fluences, this ratio will approach g. In the limit of

low fluence, the lower limit is one. This ratio is heavily used in the context of carrier multiplication in QDs. It will exceed one, even for very low fluences, if carrier multiplication is significant (i.e. when the pump energy exceeds 3 E_g[2;4]).

Finally, the TA transients at different pump powers can be used to extract the Auger lifetimes of multi-excitons. We use an adapted fitting procedure, similar to the procedure by Klimov et al.[5]. Figure 6.3 illustrates the fitting procedure. It shows the differential absorption vs log(time) for different pump fluences (N_{eh}) for PbSe QDs around the band gap. First a single exponential is fit to a low pump fluence trace ($N_{eh} = 0.8$), dominated by single excitons and biexcitons to extract the biexciton lifetime. Next the $N_{eh} = 1.6$ trace is fitted with a biexponential, but keeping the biexciton lifetime constant, as to extract the triexciton lifetime. This scheme is continued until the highest pump fluence is reached.

As a disclaimer, we would like to add that extracting relevant data from TA measurements not only requires a good knowledge of the underlying QD physics, but also of the intricate details of the measurement setup. Many details, including overlap of the pump and probe beam, pump and probe beam spot size, stability of the optical delay stage, laser prepulses, coherent effects of the pump pulse, laser and sample stabilty, shaken or stirred samples[6] etc, can influence the shape and magnitude of TA transients, without being obvious. Therefore, care (and thus time) has to be taken to understand and elliminate the effect of each of these artefacts before interpreting TA results.

6.2 Intraband Absorption

6.2.1 Introduction

Literature Study

The design of efficient and competitive materials for the photonics industry based on QDs requires a precise understanding of the electronic states involved in light-matter interaction and the decay dynamics of photogenerated carriers. In the case of QDs with their first exciton absorption in the near infrared (800–2000 nm), most studies have focused on interband transitions and intraband relaxation.[7–10] On the other hand, a few literature studies indicate that additional electronic transitions are relevant in excited QDs. Intraband absorption between the 1S and 1P state has been studied extensively for CdSe,[11–13] PbSe[10;14] and PbS,[15] with good agreement between experiment and theory. In the case of CdSe QDs, several authors[16–19]

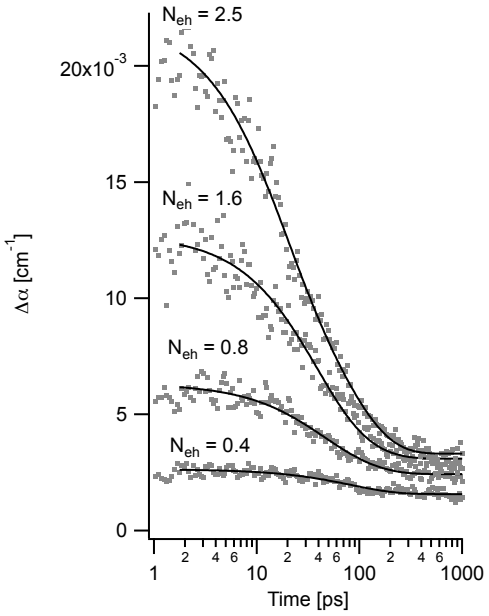

Figure 6.3: Differential absorption vs log(time) for PbSe QDs under different pump power (N_{eh}) and probed at 1550 nm illustrates the fitting procedure used to extract the multi-excitonic lifetimes. First the lowest fluences traces ($N_{eh} = 0.4, 0.8$) are fitted using a single exponential to extract the biexciton lifetime. Next the $N_{eh} = 1.6$ trace is fitted with a sum of two exponentials, where we keep the biexciton lifetime constant, as to extract the triexciton lifetime, etc.

reported photoinduced absorption (*PA*) at wavelengths directly below the band gap, which they attributed to absorption from excited trap states at the QD surface. Recent work on CdSe QDs[20] and CdSe/CdS QDs[21] identified absorption from holes to be the main contribution to this signal. For PbS QDs coupled to nanostructured metal oxides,[22;23] a similar broad *PA* feature below the band gap was observed, though its origin remained unclear.

In this Section we report on strong, broadband photo-induced absorption (*PA*) in lead chalcogenide QDs, starting at photon energies directly below the bandgap. Using femtosecond transient absorption (*TA*) spectroscopy, we find that the decay of the *PA* matches the recovery of the band gap absorption. Therefore, we interpret the *PA* in terms of transitions of excited electrons and holes from the lowest conduction (LUMO) and the highest valence band state (HOMO) to the conduction and valence band continuum, respectively. Moreover, we demonstrate that this broad intraband absorption is a characteristic of several Pb chalcogenide QDs, including PbSe and PbS core QDs and PbSe/CdSe core/shell QDs. Using tight-binding[24] calculations — in collaboration with Universit de Lille 1 — on PbSe QDs, we show agreement between the observed *PA* and the calculated intraband absorption spectrum. The calculations shed light on the initial and final states involved in the photoinduced absorption process.

Rationale

Because of intraband absorption, excited Pb chalcogenide QDs absorb light in a wavelength range where ground state QDs are transparent. Depending on the size of the QDs, this wavelength range can be tuned to cover wavelengths around 1300 and 1550 nm, which are widely used in optical communication. Since intraband transitions have a strong absorption coefficient and are followed by picosecond intraband cooling, our findings show that Pb chalcogenide QDs are highly relevant materials for telecom applications. Free carrier absorption (*FCA*), the equivalent process in bulk semiconductors, is nowadays widely studied for optical modulation.[25;26] However, momentum conservation forbids intraband transitions in this case, which makes that a phonon is needed for *FCA*. This results in a relatively low absorption coefficient and makes applications in ultrafast optical switching sensitive to the device temperature. Hence, by proving that intraband absorption is an allowed process in Pb chalcogenide QDs over a broad wavelength range, our results are a particular example of how size quantization affects the properties of materials up to a level where they outperform bulk materials.

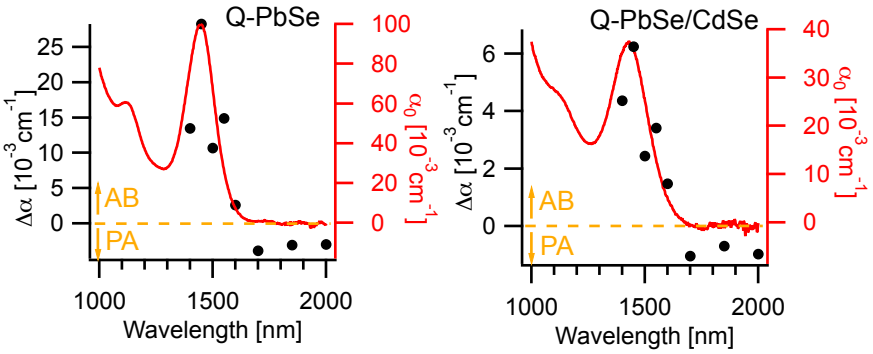

Figure 6.4: Steady state (red line, right axis) and differential transient absorption spectrum (black dots, left axis) of PbSe QDs (left graph) and PbSe/CdSe (right graph) 5 ps after the pump pulse shows absorption bleach (*AB*) of the band gap absorption ($\Delta\alpha = \alpha_0 - \alpha > 0$) and wavelength-independent photoinduced absorption (*PA*, $\Delta\alpha < 0$) below the band gap.

6.2.2 Experimental Results

TA Measurements and Analysis

Figure 6.4 shows the change in absorption of PbSe core ($d = 4.6\,\mathrm{nm}$) and PbSe/CdSe core/shell QDs ($4.5\,\mathrm{nm}$ core, $0.5\,\mathrm{nm}$ shell) following excitation with a 50 fs pump pulse (λ_{pump} =790 nm). This resulting excited state cools down rapidly.[1] A buildup of carriers at the band gap reduces the band gap absorption (absorption bleach, *AB*), as can be seen in Figure 6.4. Here, a bleach is indicated by a positive value for $\Delta\alpha = \alpha_0 - \alpha$, where α_0 is the steady state absorbance and α is the absorbance after the pump pulse. However, below the bandgap (1700 nm to 2000 nm) we observe a negative $\Delta\alpha$ for both materials, indicating photoinduced absorption (*PA*).

To gain insight into the nature and strength of the *PA*, we performed power and wavelength dependent measurements. At high fluences, when more than one exciton is created per QD, the distribution of multiexcitons is Poissonian and the decay of the *TA* signal is governed by Auger recombination.[5] After 500 ps all multiexcitons have recombined, leaving a population of singly excited QDs. Assuming an initial Poissonian distribution of carriers, the normalized differential absorption after 500 ps becomes:

$$\frac{\Delta\alpha_{500ps}}{\alpha_0} = \frac{2}{g}(1 - e^{-N_{eh}}) \tag{6.5}$$

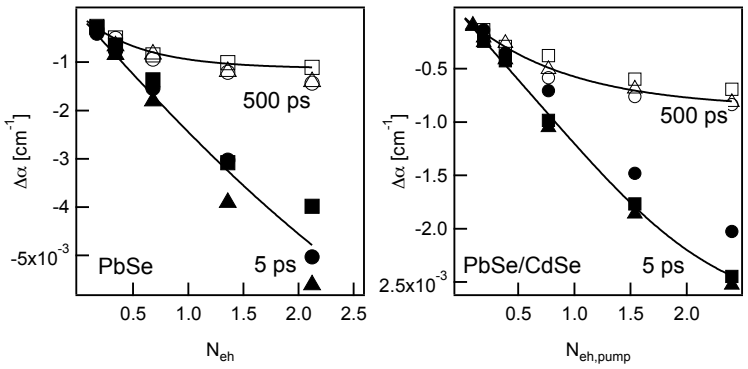

Figure 6.5: Differential absorption as a function of average number of excitons N_{eh} 5ps after the pump pulse (red) and 500 ps after the pump pulse (blue) at 1700 nm (triangles), 1850 nm (squares) and 2000 nm (circles) for (a) PbSe QDs and (b) PbSe/CdSe QDs. The full lines are fits to a Poissonian state filling model.

Here we have expressed the pump power as the average number N_{eh} of excitons that are created per QD by the pump pulse (see Section 6.1). g is the degeneracy of the LUMO and the HOMO. The factor two accounts for both electrons and holes, since the differential absorption is proportional to the sum of all involved carriers.[27]

The power dependence of the *PA* for short and long times after the pump pulse is given in Figure 6.5(a) for PbSe. A similar behaviour is observed for PbSe/CdSe (see Figure 6.5(b)). At short delay times (red curves), the *PA* is linear with N_{eh} within the given power range, in agreement with a Poisson distribution of the initial excitons. At long times, we observe a trend, which fits well to Equation 6.5.

Based on these traces, we quantify the strength of the *AB* and *PA* transition as the absorbance per exciton $\alpha_{AB,ex}$ and $\alpha_{PA,ex}$ respectively. $\alpha_{PA,ex}$ is the maximum *PA* after long delay, obtained from fitting Equation 6.5 to the blue curves in Figure 6.5 (see Table 6.1). For PbSe $\alpha_{AB,ex}$ (obtained in the same way) is $16.9 \cdot 10^{-3}\mathrm{cm}^{-1}$ (FWHM=81 meV). The intraband transition is about 10 times weaker. The *PA* per exciton $\alpha_{PA,ex}$ in PbSe/CdSe is also about 10 times weaker than the $\alpha_{AB,ex}$ ($88 \cdot 10^{-4}\mathrm{cm}^{-1}$, FWHM=105 meV). To compare both materials, the absorption coefficient μ[28] and the cross section $\sigma = \mu V_{QD}$ for the *PA* are also given in Table 6.1. The cross sections are very similar for both materials. The larger volume of PbSe/CdSe results in a lower μ than PbSe QDs with similar core size. μ is proportional to the oscillator strength and the local field factor.[29] Given

	PbSe		
λ_{probe}	$\alpha_{PA,ex}$	$\mu_{PA,ex}$	$\sigma_{PA,ex}$
[nm]	$[cm^{-1}]$	$[cm^{-1}]$	$[cm^2]$
1700	$1.54 \cdot 10^{-3}$	187	$9.2 \cdot 10^{-18}$
1850	$1.29 \cdot 10^{-3}$	157	$7.7 \cdot 10^{-18}$
2000	$1.57 \cdot 10^{-3}$	190	$9.7 \cdot 10^{-18}$
	PbSe/CdSe		
λ_{probe}	$\alpha_{PA,ex}$	$\mu_{PA,ex}$	$\sigma_{PA,ex}$
[nm]	$[cm^{-1}]$	$[cm^{-1}]$	$[cm^2]$
1700	$8.6 \cdot 10^{-4}$	92	$8.0 \cdot 10^{-18}$
1850	$5.6 \cdot 10^{-4}$	82	$7.1 \cdot 10^{-18}$
2000	$8.6 \cdot 10^{-4}$	92	$8.0 \cdot 10^{-18}$

Table 6.1: Photoinduced absorbance for a population of one exciton in the initial state $\alpha_{PA,ex}$, derived from a Poissonian fit, together with the absorption coefficient for PbSe and PbSe/CdSe QDs.

the increasing local field factor in core/shell QDs compared to core only QDs,[30] a lower μ translates in a lower oscillator strength for PbSe/CdSe QDs.

Figure 6.6 shows that after 10 ps delay the transient absorption for PbSe at the band gap maximum (red trace) and below the band gap (black traces, inverted for clarity) follow a very similar time dependence for three different values of the pump power. This decay is due to Auger recombination. Fitting a sum of three exponentials to the absorption transients[31] yields a biexciton lifetime of 82 ps, a triexciton lifetime of 32 ps and a quadrexciton lifetime of 13 ps for the PbSe QDs at the bandgap. The *PA* transients differ from the transients at the band gap for early delay times. The onset is much steeper, which is clearest for the highest pump power (see Figure 6.6c). For both high and for low pump powers, an initial decay is present, which we do not observe in the differential absorption transients around the bandgap. The fitting procedure[31] yields a lifetime of 1.2 ps for this initial decay. Similar dynamics are observed for PbSe/CdSe QDs, as summarized in Table 6.2.

The band gap bleach only develops when hot carriers have cooled to the band gap. However the fast rise of the *PA* suggests that hot carriers also exhibit *PA* (see Figure 6.6b). To corroborate this, we measured the *TA* of very small PbS QDs (2.45 nm), for which the pump is resonant with the band gap transition (see Figure 6.6b). In this case, no fast initial decay component is observed, which corroborates the assumption that hot electrons and

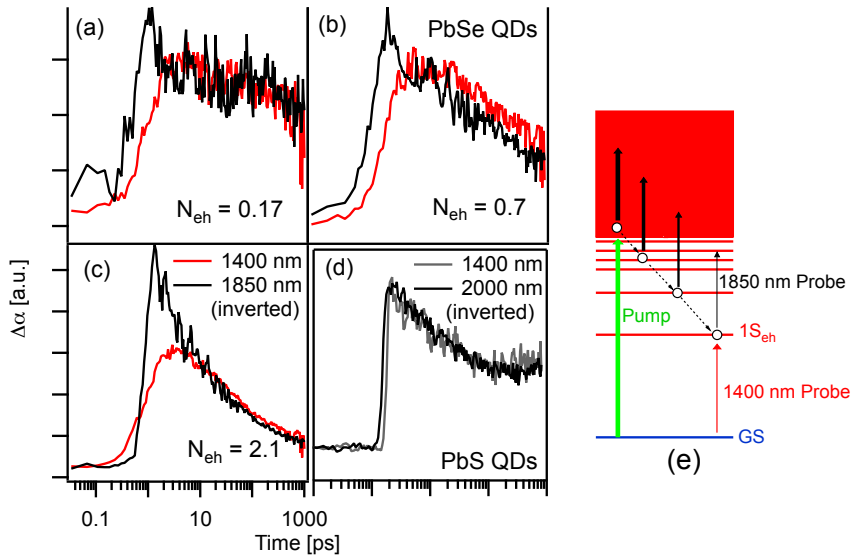

(e) The diagram illustrates the intraband transitions probed by the sub gap probe (black). These transitions cause the fast initial decay component in the sub gap transients (black) for non-resonantly excited PbSe QDs. The band gap probe (red) will only register the band gap bleach after carriers have cooled to the band gap.

Figure 6.6: (a,b,c) Absorption transients for the differential absorption at the band gap (1450 nm, red) and below the band gap (1850 nm, black, inverted for clarity) for PbSe QDs show similar decay dynamics after 10 ps for three different values of the pump power (a) $N_{eh} = 0.17$, b) $N_{eh} = 0.7$ and c) $N_{eh} = 2.1$). An initial faster decay is present in the *PA* transients for all three pump powers shown. (d) Absorption transients for very small PbS QDs (2.45 nm) for which the pump is resonant with the band gap transition (780 nm) show *PA* ($\Delta\alpha < 0$), yet no fast initial decay component.

[ps]	PbSe	PbSe/CdSe
$\tau_{A,n=2}$	82 ± 7.7	84 ± 6.4
$\tau_{A,n=3}$	32 ± 8.9	16 ± 0.84
$\tau_{A,n=4}$	13 ± 3.5	-
τ_{hot}	1.2 ± 0.13	1.3 ± 0.24

Table 6.2: Auger decay times and initial decay times for PbSe and PbSe/CdSe QDs, as extracted by the fitting proceduce.

holes also show *PA*.

Interpretation of the Results

The wavelength-independent *PA* we observe in these near-infrared QDs could have different origins, such as

1. Coulomb shifts in the multiexcitonic absorption spectrum,[32–37]
2. absorption from surface-localized states or defects,[18;38–40]
3. intraband absorption.[10;13;19;41]

Coulomb shifts can be excluded, since the *PA* is observed up to 2000 nm, well below the band gap. Moreover, a Coulomb shift would result in a characteristic anti-symmetric *TA* spectrum,[27] not the broadband signal we observe here (see Figure 6.7).

Malko *et al.*[16]reported *PA* in absorption transients of colloidal CdSe QDs. An extensive study revealed a strong dependence on solvent and surface passivation, along with a limited size dependence of the *PA* cross section. This study indicates a strong influence of the QD surface. Given the high cross section, Malko *et al.* attributed the *TA* to transitions from dangling surface bonds to excited states in the capping or surrounding matrix, rather than intraband absorption. Since we work with a considerably lower photon energy (0.5 to 0.8 eV vs. 2.0 to 2.5 eV), a transition to a final state in the surrounding matrix is unlikely at these low energies. Furthermore, since the dynamics and strength of the *PA* of PbSe and PbSe/CdSe QDs are very similar, despite having very distinct surface properties, makes *PA* from surface defects improbable. Moreover, the *PA* we observe at long delay times saturates with increasing pump power, similar to the bleach of the band gap absorption. This shows that the initial state of the *PA* after carrier cooling is in fact the band gap exciton. That QD core states are involved, instead of surface states, is further confirmed by the Auger dynamics of the *PA* signal.

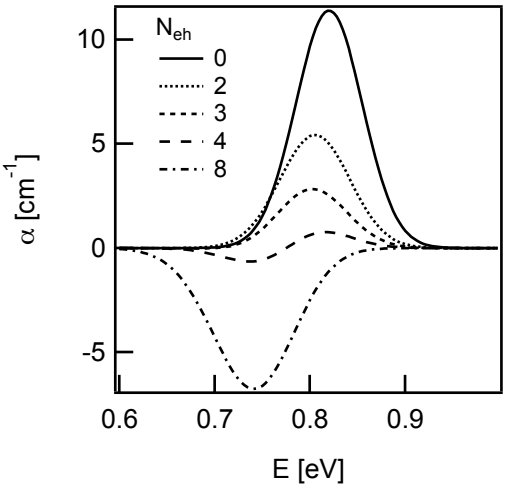

Figure 6.7: Simulation of the nonlinear absorption spectrum for $N_{eh} = 0$, 2, 3, 4 and 8 for a spectral redshift of 10 meV/exciton.

We therefore conclude that the *PA* observed here finds its origin in intraband absorption. This is in line with a recent study of photocharging[6;42] of PbSe QDs, where pumping with 1.5 eV photons did not result in significant photocharging. Based on the interpretation of the *PA* as intraband absorption, we attribute the quick rise time to intraband transitions from higher energy excited states (see Figure 6.6.a). The correspondence between the time constant of the initial decay (see Figure 6.2) we measure and literature values for intraband carrier cooling[8;9;43] corroborates this interpretation.

6.2.3 Tight-binding Calculations

The tight-binding calculations in this Section were kindly provided through a cooperation with Sergio Carrillo and Christophe Delerue from Université de Lille 1.

Theory of Intraband Absorption in QDs

Intraband absorption is forbidden in first order for bulk semiconductors. In order to conserve the crystal momentum, phonon absorption or emission is needed. The process is commonly called free carrier absorption (*FCA*) and is well described by a Drude model. In the case of a particle in an infinite spherical potential well, only transitions with orbital angular momentum $\Delta l = \pm 1$ are allowed. Here, we find experimentally that both

the conservation of crystal momentum and orbital angular momentum are relaxed in Pb chalcogenide QDs, resulting in a non-zero probability for intraband absorption. This confirms that in quantum dots the deviations from the ideal infinite spherical potential well cause the electronic states to be superpositions of states with different crystal momentum and orbital angular momentum.[14] To investigate this further, we perform tight-binding simulations of the absorption cross section for intraband absorption for PbSe QDs.

Simulating QDs using the Tight Binding Model

To simulate the electronic structure and the strength of the optical transitions of QDs, the Schrödinger equation needs to be solved for the collection of atoms that make up the QD. Three numerical methods are used often. They differ in the way they approximate the interaction of the atomic nuclei and electrons with eachother.

The $\mathbf{k} \cdot \mathbf{p}$ theory assumes a periodic potential in the Hamiltonian and a linear combination of Bloch waves for the wavefunctions describing the electron.[44] This theory is also known as the effective mass approximation. The density functional theory and atomistic pseudopotential theory are so called first principle methods, which make no (or few) assumptions and solve the Schrödinger equation for the entire collection of atomic nuclei and electrons.[14;45;46] It is therefore computationally very demanding and can only be done for small QDs. Finally, the tight binding theory assumes that the Hamiltonian and the wavefunctions of the QD are linear combinations of the atomic Hamiltonian and wavefunctions. Small perturbations on the Hamiltonian and wavefunctions account for the interaction of the atoms with eachother (usually only with their nearest neighbours). The perturbations are fitting parameters, for which values are obtained by fitting the theory to experimental data.

In this thesis we use the tight-binding model. The single-electron states and energies of PbSe QDs are calculated using the $sp^3d^5s^*$ tight-binding model of Allan and Delerue[24] including spin-orbit coupling. Since many states are needed to calculate the optical spectra, the matrix of the tight-binding Hamiltonian is fully diagonalized even for diameters up to 4.5 nm ($\approx$1600 atoms). The absorption cross section for an optical transition of a single QD at the photon energy $\hbar\omega$ is written as:

$$\sigma(\hbar\omega) = |f_{LF}|^2 \sum_{ij} \frac{4\pi^2 \omega_{ij} e^2 |\langle i|\mathbf{r}\cdot\mathbf{e}|j\rangle|^2}{cn} L\left(\hbar\omega - \hbar\omega_{ji}\right)\left[f_i - f_j\right] \quad (6.6)$$

where **e** is the polarization vector of the electric field, **r** is the electron position vector, $|j\rangle$ and $|i\rangle$ are electronic states with respective populations f_j and f_i, $\hbar\omega_{ji}$ is the energy of transition between the two states, $|f_{LF}|^2$ is the local-field factor and n is the refractive index of Cl_2Cl_4. The cross section is averaged over all the orientations of the electric field. The function L in Equation 6.6 describes the lineshape of each individual transition. We have considered a Gaussian lineshape, i.e., $L(x) = \frac{1}{\sigma\sqrt{2\pi}} \exp(-\frac{x^2}{2\sigma^2})$.

In the ground state, i.e. without exciton, the population of the initial states f_i is set to one for all the valence states and to zero for all the conduction states. This is the interband absorption cross section.

The intraband cross section in the presence of an exciton is calculated assuming that an electron has been excited from a valence state to a conduction state. Excitonic effects are neglected.

Simulation Results

Tight-binding calculations[241] on 4.5 nm PbSe QDs support our observations of PA in PbSe and PbSe/CdSe QDs. We simulate the spectrum of the absorption cross section without and with an exciton in the HOMO-LUMO. Our simulations substantiate earlier atomistic pseudopotential calculations[47] of the *AB* at the band gap and intraband absorption between the 1S and 1P state[14] (see Figure 6.8(a)).

Moreover, they predict previously unreported non-zero oscillator strength for intraband transitions between the HOMO-LUMO and higher energy states, in the energy range between the 1S-to-1P and the band gap transition. Our experimental data qualitatively agree with the tight-binding results, taking the local field factor ($|f_{LF}|^2 = 0.059$[30;48] in C_2Cl_4) into account (see Figure 6.9). Uncertainty of the local field factor or excitonic effects which are missing in the calculations could explain the difference between theory and experiment. Electron and hole transitions contribute equally to the cross section (see Figure 6.8(b)). This is in line with the similar bulk effective masses, but contradicts the prediction of a denser hole manifold.[14]

Tight-binding calculations also predict a higher intraband absorption cross section for carriers in the higher energy P-state (see Figure 6.10 between 0.5 and 0.8 eV). This confirms our interpretation of the quick rise time and fast initial decay (see Figure 6.6(a-c) and Table 6.2) as intraband absorption from carriers cooling to the band gap.

[1]Calculations were performed by Sergio Carillo and Christophe Delerue from Universit de Lille 1

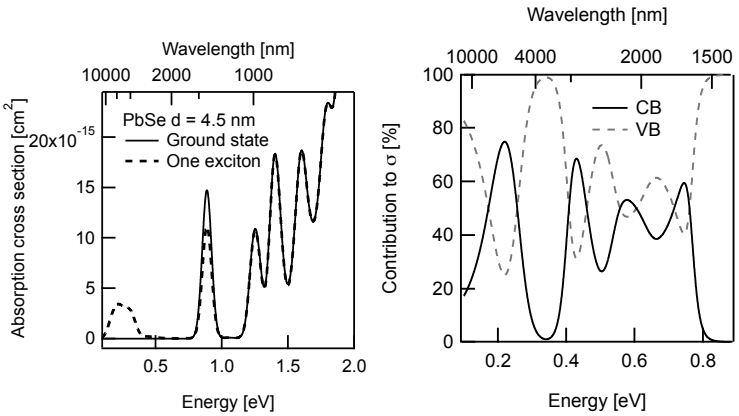

Figure 6.8: (a) Theoretical absorption cross section for a 4.5 nm PbSe QD in the ground state and with a single exciton in the 1S state confirms earlier calculations on PbSe for both band gap AB and mid-infrared PA. (b) The percentage for which initial states in the conduction band (red curve) and valence band (blue curve) contribute to the absorption cross section below the band gap shows that valence and conduction band state contribute almost equally in the energy range between 0.4 and 0.8 eV.

In Figure 6.11(a) we compare the absorption cross section of PbSe with similarly sized wz-CdSe QDs. Despite the order of magnitude difference in the local field factor for both materials, we observe similar cross sections for intraband absorption directly below the band gap. In the wavelength range studied, wz-CdSe has a factor of 5 to 10 higher absorption cross section than PbSe QDs. We stress that this result however highly depends on the local field factor, and hence the environment in which the QDs are intended to be used.

However, the predicted ratio between *AB* and *PA*, due in part to the lower degeneracy of HOMO-LUMO in CdSe, is much higher ($\sim$400), making it harder to distinguish the *PA* in a *TA* experiment. This is shown in Figure 6.11(b), where we plot the differential absorption for both materials, normalized to the intraband absorption directly below the band gap. Moreover, the reported cross sections for *PA* in CdSe are much higher than the theoretical values predicted by tight-binding calculations. This highlights the clear difference between the *PA* in CdSe as reported in literature, which can be attributed to nanocrystal charging and the *PA* in PbSe reported here, which is due to intraband transitions.

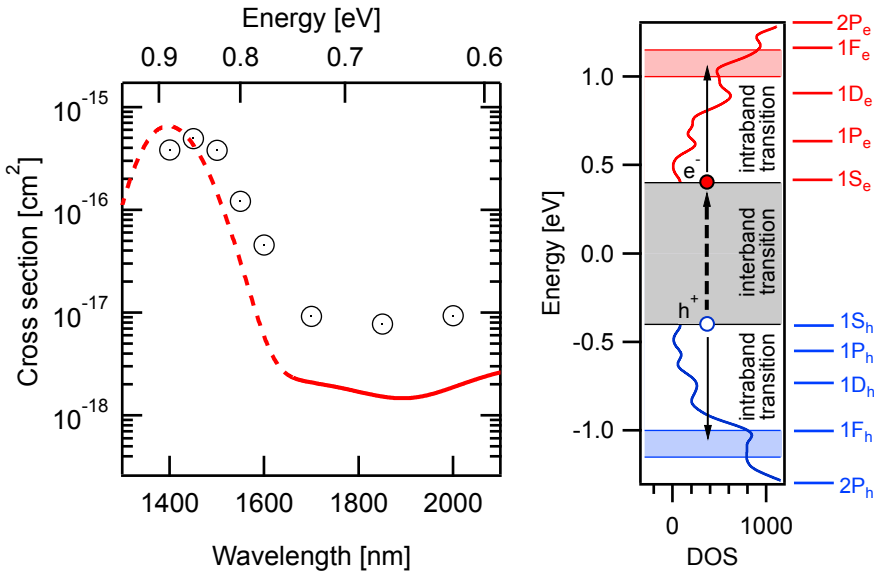

Figure 6.9: (a) The absorption cross section in the presence of an exciton for PbSe QDs (4.5 nm) as calculated by tight-binding (red trace) agrees well qualitatively with the values measured using *TA* spectroscopy (black circles). (b) Graphical representation of the transitions which give the strongest contribution to the absorption cross section in the presence of an exciton for energies below the band gap (full lines) and at the band gap (dashed lines). The same symbolism is used in the curve representing the tight-binding absorption cross section.

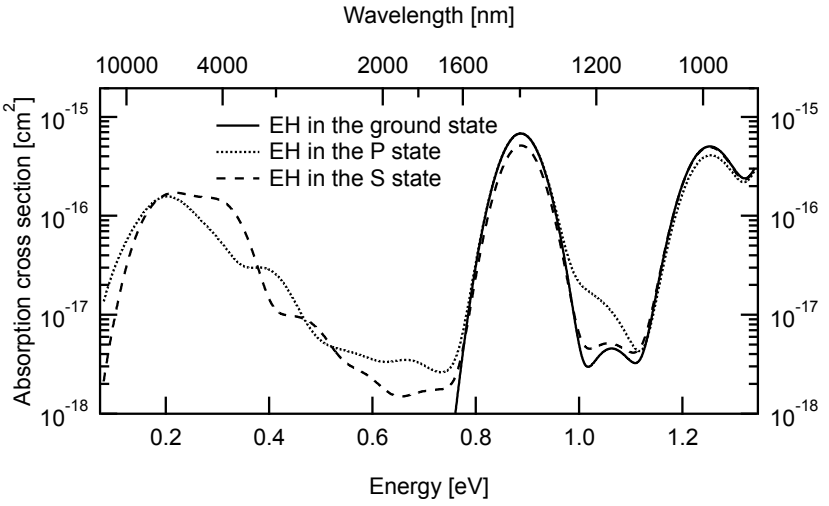

Figure 6.10: Theoretical absorption cross section for a 4.5 nm PbSe QD in the ground state and with a single exciton in the 1S state, in the lower energy P state and in a higher energy P state shows that intraband absorption in the region 0.5 to 0.8 eV is higher for the P state than for the S state.

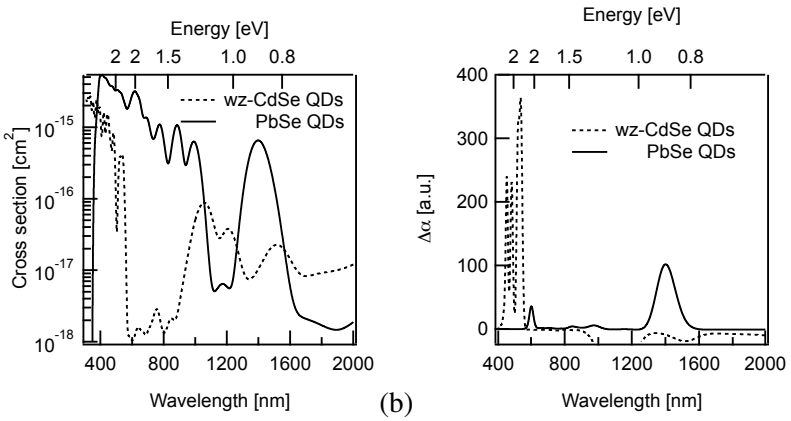

Figure 6.11: (a) The absorption cross section for wurtzite (wz) CdSe QDs and PbSe QDs with a diameter of 4.5 nm, as calculated by tight-binding and corrected for the local field factor in C_2Cl_4 (0.339 and 0.059 for CdSe and PbSe resp.) (b) Differential absorption, normalized to the intraband absorption directly below the band gap (600 nm for wz-CdSe, 1700 nm for PbSe) shows the higher contrast of the AB and PA expected for CdSe as compared to PbSe.

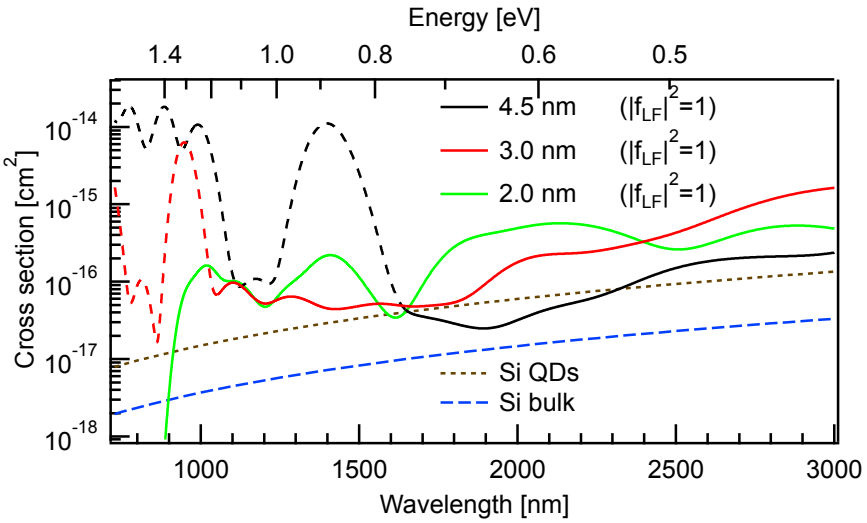

Figure 6.12: The absorption cross section in the presence of an exciton for PbSe QDs (black, d=4.5 nm, $E_g = 0.89eV$; red, d=3.0 nm, $E_g = 1.3eV$; green, d=2.0 nm, $E_g = 1.92eV$) as calculated by tight-binding, taking no local field factor into account, shows size-dependent intraband absorption that cannot be explained by a simple Drude model ($\sim \lambda^2$). The cross section dominated by intraband transitions is marked with a full line, whereas the cross section dominated by interband transitions is marked by a dashed line. For comparison with materials which operate in the same wavelength range, the absorption cross section for *FCA* in bulk silicon[50] (blue stripes) and silicon nanocrystals[52] (brown dots) are shown.

6.2.4 Benchmarking Intraband Absorption with FCA in silicon

FCA and *FCR* (free carrier refraction) in silicon have been studied extensively for applications in ultrafast signal processing at telecom wavelengths.[49] In bulk silicon *FCA* is well understood and its cross section has a λ^2 dependence in line with the predictions of the Drude model.[49;50] Silicon nanocrystals (NCs, $d = 5$ nm) in silicon-rich-oxide, which operate in the same wavelength range, were shown to have an order of magnitude higher cross sections for *FCA*, both in the visible[51] and in the near-infrared[52] region, yet with a similar λ^2 dependence. The result was explained by considering that the mean free path of the carriers was limited to the QD size, increasing the scattering cross section.

In Figure 6.12 we compare the *FCA* cross section of bulk-Si and Si-

NCs with the calculated spectrum of the absorption cross section of excited PbSe QDs of three different sizes. Since a typical application will require a densely packed layer of QDs, we do not take the local field factor into account ($|f_{LF}|^2 = 1$). Depending on the QD diameter, the intraband absorption cross section is one to two orders of magnitude larger than in bulk-Si. Around 1550 nm, an important telecom wavelength, the cross section is comparable to the Si-NC cross section. As the origin of the absorption is a direct intraband absorption, without interaction of phonons, the wavelength dependence differs from a Drude model and strongly depends on the QD diameter.

Implications for QD gain

As highlighted by Kekatpure and Brongersma[51], the higher *FCA* cross section has important implications for gain at telecom wavelengths using Si-NCs in erbium-doped silica. For the erbium gain to exceed the *FCA* loss, *FCA* cannot be larger than 10^{-18} cm^2. A similar upper limit to the photoinduced loss of QDs doped with erbium exists, making gain in hybrid erbium-QD systems impossible.

The use of QDs directly for gain will be affected as well. Assuming a similar ratio between the gain cross section and the intraband absorption cross section at the band gap as the ratio $\alpha_{AB,ex}/\alpha_{PA,ex} \simeq 10$ we observed experimentally, we can define a condition for the gain threshold in the presence of intraband absorption:

$$\begin{aligned} n\sigma_{ex} &= (n-\gamma/2)\sigma_{AB,ex} \\ n_{threshold} &= (\gamma/2)\frac{\sigma_{AB,ex}}{\sigma_{AB,ex}-\sigma_{PA,ex}} \end{aligned}$$

Here n is the number of excitons per QD and γ is the degeneracy. For the measured values, the theoretical threshold for gain would increase by about 11% to $N_{eh} = 4.45$. Similarly, the maximum gain value will decrease by 20%.

Note that in colloidal QDs the rate of multi-exciton decay (a necessary condition to obtain population inversion) is dominated by the non-radiative Auger recombination rate, which is 4 to 6 orders of magnitude larger than the spontaneous emission recombination rate.[53] Therefore a high QD density and large total number of QDs coupled to the laser cavity will be required for the stimulated emission rate to overcome the non-radiative recombination rate.[54] In turn, this requires very high pump fluences, essentialy making CW lasing impossible. Moreover, in the case of non-resonant

excitation the Auger recombination rate for $N_{eh} \simeq 4$ approaches the rate of carrier cooling to the band gap. This inhibits gain altogether, as the condition of population inversion is never reached.

6.2.5 Intraband Absorption for Integrated Optical Modulators

The intraband absorption observed in lead-salt colloidal QDs can be beneficial for other applications. Silicon-based electro-optical modulators typically do not use *FCA*, since the effect is too weak to make small modulators with easily achievable doping levels. Modulators are then based on free-carrier refraction (*FCR*), where a trade-off is made between an optimized modulation depth and minimal insertion loss because of *FCA*. Moreover, the phase shift that *FCR* induces requires these type of modulators to have an interferometric design, which limits the spectral bandwidth at which they can be used. The intraband absorption of lead-salt colloidal QDs is a first step towards a zero-insertion loss optical modulator. The small size, together with the high intraband absorption cross section makes high absorption coefficients in the order of a few 100 to 1000 cm^{-1} easily achievable with doping or electrical injection.[55] Modulators with footprints between 10 and 100 μm, an order of magnitude smaller than current interferometric designs are therefore possible. Moreover, the extremely large absorption cross section at and above the band gap (see Figure 6.9), together with the tunability of band gap with size make optical excitation of the intraband absorption, as demonstrated here, very easy. It opens the way for all optical signal processing using lead-salt QDs.

6.2.6 Conclusion

In conclusion we have shown that intraband absorption in the telecom wavelength range is universal to lead chalcogenide QDs. The absorption is strong, only 10 times weaker than the band gap absorption bleach. The intraband absorption is broadband and nearly constant over a large wavelength range. This range can be tuned easily by changing the QD size. The intraband absorption has ultrafast dynamics in the one to tens of picoseconds range, governed by carrier cooling and Auger recombination. Tight-binding modeling of the absorption cross section of excited QDs confirm our experimental observation of intraband absorption in this wavelength range.

Our work is essential to understand the response of QDs as gain media and ultrafast nonlinear media for photonic applications. Moreover, our measurements are a clear manifestation that the selection rules for the bulk

crystal momentum and for the angular momentum in spherically confined structures as mentioned above are relaxed in QDs and are therefore very interesting from a theoretical standpoint. They go beyond intersubband absorption [10–13;15] and cover a new wavelength range directly below the band gap. Intraband absorption offers a nice way to study the dynamics of carrier cooling [7–9] and multiple-exciton generation [4;56] in a direct way, free from possible Coulomb shifts or redistribution over dark and bright band gap states, which complicate typical *TA* measurements at the band gap.

6.3 Interband Absorption and Stimulated Emission

As discussed in Chapter 5, a CdSe shell around PbSe QDs changes the electronic fine structure around the band gap, mainly by increasing the fine structure splitting. These results drew from measurements of the linear absorption and spontaneous emission. In this Section we will compare the carrier dynamics of PbSe and PbSe/CdSe QDs around the band gap, and the effect of fine structure splitting on the nonlinear absorption and stimulated emission.

The population dynamics of PbSe QDs were studied by several authors using TA. Recently, PbSe and PbS QDs have been of great interest to study carrier multiplication in QDs [2;2;4;57–65]. These studies are typically performed at low fluences. Other studies have focused on the dynamics at higher fluences, reporting the lifetimes of multi-excitons [2;6;37;53;61;64;66;67] and spectral shifts due to biexciton attraction [2;37;64;65]. To date, only one, somewhat controversial, report of gain in PbSe QDs, observed using TA, was published by Schaller et al. [66] in 2003. For a somewhat outdated, yet still relevant and interesting review, we refer to the article by Klimov [61].

6.3.1 The Auger Rate of Multiexcitons in PbSe and PbSe/CdSe QDs

As discussed in Section 3.3.2 on p. 71, the Auger rate in QDs increases cubically with the number of excitons and is inversely proportional to the QD volume. With this dependence and a biexciton lifetime of $\sim$100 ps, the lifetime of the QD state containing 5 excitons, needed to reach population inversion and provide gain in the 8-fold degenerate PbSe QDs, becomes:

$$\tau_{A,5} = \frac{8}{125}\tau_{A,2} \simeq 6.4\, ps$$

This is very similar to the intraband carrier cooling time of 2-5 ps [8;10;68]. In short, excitons recombine faster than they can cool to the band gap, where

	PbSe	PbSe	PbSe/CdSe	PbSe/CdSe
$d_{QD}/d_{shell}[nm]$	4.6	4.0	4.5/0.5	4.6/2.0
λ_g [nm]	1442	1324	1429	1460
$\tau_{A,n=2}$ [ps]	82	150	84	100
$\tau_{A,n=3}$ [ps]	32	42	16	15
$\tau_{A,n=4}$ [ps]	13	12	-	-

Table 6.3: Auger decay times and initial decay times for PbSe and PbSe/CdSe QDs, as extracted by the fitting proceduce.

they can participate in stimulated emission.

We use the fitting procedure, outlined in Section 6.1.2 on p. 121 to extract the Auger lifetimes of multiexcitons. The results are summarized in Table 6.3. There is no large difference in the biexciton lifetimes of PbSe and PbSe/CdSe QDs with similar core or total QD size and the triexciton lifetime of PbSe/CdSe QDs is shorter than for PbSe QDs. There is currently not enough data to draw any solid conclusions. Possibly, the abrupt interface between PbSe and CdSe could be the origin of an increased efficiency of Auger recombination for triexcitons.[69]

In Figure 6.13 we combine our data with literature values. Figure 6.13(a) illustrates the large scattering on the lifetime data reported in literature. Probably the ill-defined nature of fitting sums of exponentials is the chief reason for the large scattering. Few data is available for the triexciton state. No other authors report a quadrexciton lifetime. Despite the scattering on the data, as outlined in Section 3.3.2, the Auger constant C_A, relating the rate of Auger recombination to the carrier density, scales with the volume of the QDs. This is illustrated in Figure 6.13(b) for PbSe and PbSe/CdSe QDs. According to Robel et al.[53], the scaling constant γ is universal to all QD materials within a given range, indicated by the shaded area in Figure 6.13(b). Our limited data on PbSe/CdSe QDs, combining two common QD materials, seems to confirm this law.

6.3.2 Transient Absorption Spectra of PbSe and PbSe/CdSe QDs

Effect of carrier cooling, multi-exciton shifts and fine structure on $\Delta\alpha/\alpha_0$

The normalized differential absorbance $\Delta\alpha/\alpha_0$ as a function of power N_{eh} at short (5 ps) and long (500 ps) delay time provides insight into the carrier decay processes and the nature of the states these carriers are in. Figure 6.14(a) shows the state-filling model of Equation 6.4 for three different

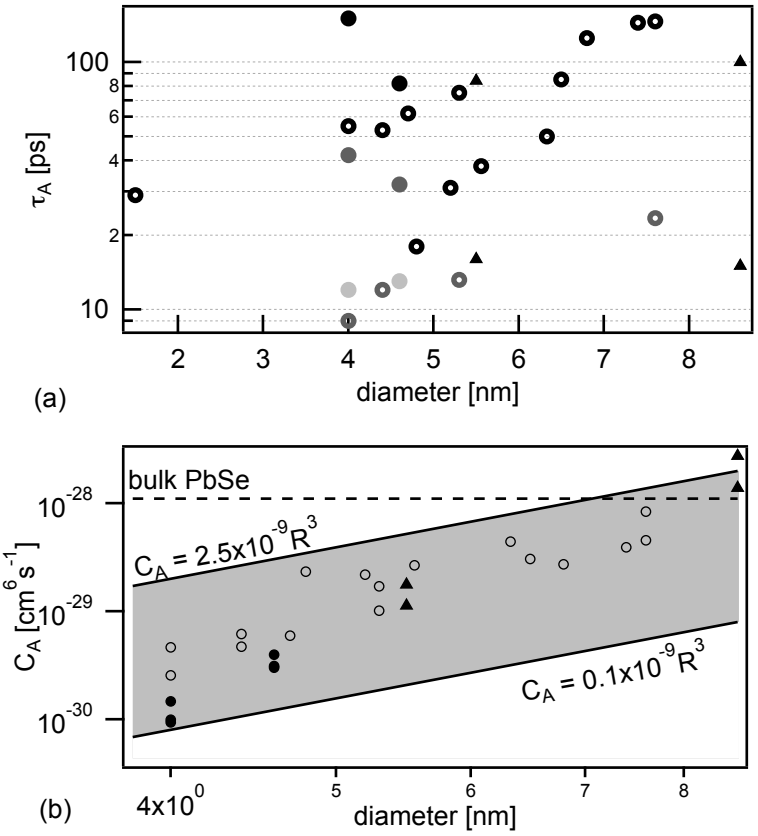

Figure 6.13: **(a)** Auger lifetimes for biexcitons (black), triexcitons (grey) and quadrexcitons (lightgrey) from personal data (full symbols) and from literature[2;4;6;10;64;67;70] (open symbols). PbSe QDs are circles, PbSe/CdSe QDs are triangles. **(b)** Auger constant C_A, calculated from the data in (a) shows the universal volume scaling, as outlined by Robel et al.[53]. The shaded area shows the range of volume scaling constants γ (see Section 3.3.2) reported by Robel et al.[53]. The value of the C_A for bulk PbSe is plotted with a dashed line.

values of the degeneracy g. The maximum value for $\Delta\alpha/\alpha_0$ is 2, where $\Delta\alpha/\alpha_0 > 1$ means net gain for the QD ensemble. If stimulated emission is not possible (*eg.* in charged QDs), the dashed line in Figure 6.14(a) indeed saturates at transparency $\Delta\alpha/\alpha_0 = 1$. The initial slope ($\sim 2/g$) of the $\Delta\alpha/\alpha_0$ *vs.* N_{eh} trace and the gain threshold are determined by g.

As mentioned before, the cubic scaling of the Auger recombination rate with the number of excitons quickly becomes similar to the carrier cooling time and could therefore inhibit population inversion and gain in PbSe and PbSe/CdSe QDs. Hence, the Poissonian state-filling model for short delay times of Equation 6.4 needs to be modified to include the effect of carrier cooling. We replace $\mathcal{P}(n, N_{eh})$ in Equation 6.4 with:

$$\mathcal{P}'(n, N_{eh}) = \frac{\tau_c^{-1}}{\tau_c^{-1} + \tau_{A,n}^{-1}} \left(\mathcal{P}(n, N_{eh}) + \sum_{k=n+1}^{\infty} \frac{\tau_{A,k}^{-1}}{\tau_c^{-1} + \tau_{A,k}^{-1}} \mathcal{P}(k, N_{eh}) \right) \tag{6.7}$$

Here τ_c is the carrier cooling time and $\tau_{A,n}$ is the Auger recombination lifetime for n excitons. The last factor expresses the sum of all QDs that have n high energy excitons for an average of N_{eh} per QD and all QDs that have more than n high energy excitons, but which didn't cool to the band gap and instead recombined. This factor we multiply by the probability that n high energy excitons in each of these QDs cool to the band gap before recombining through Auger recombination.

In Figure 6.14(b) the grey curve shows the effect of the competition between Auger recombination and carrier cooling on the power-dependent $\Delta\alpha/\alpha_0$ for $g = 8$. We have used $\tau_{A,2} = 85$ ps and the carrier cooling lifetime $\tau_c = 5$ ps. The initial slope remains the same, and while gain is still achievable, the maximum gain is lower and the transparency threshold ($\Delta\alpha/\alpha_0 = 1$) is higher.

This model does not take multiexcitonic shifts or the band gap fine structure into account. These effects will make $\Delta\alpha/\alpha_0$ wavelength dependent. To include multiexciton shifts we adapt Equation 6.4:

$$\begin{aligned} \Delta\alpha_{5ps} =& G(E_G, \sigma_G) \\ & - \sum_{n=0}^{g} \mathcal{P}'(n, N_{eh}) \\ & \quad \left[\frac{(g-n)}{g} G(E_G - n\Delta_{xx}, \sigma_G) - \frac{n}{g} G(E_G + (n-1)\Delta_{xx}, \sigma_G) \right] \\ & - \sum_{n=g+1}^{\infty} \mathcal{P}'(n, N_{eh}) G(E_G + (n-1)\Delta_{xx}, \sigma_G)) \end{aligned} \tag{6.8}$$

Here G is a gaussian function to model the first exciton feature at the band gap E_g and with width σ_g. Δ_{xx} is the biexciton shift. Note that the first G represents the absorption spectrum for a QD with one exciton, the second G represents the stimulated emission spectrum for a QD with one exciton. The effect of biexciton attraction ($\Delta_{xx} = 5$ meV) is shown in Figure 6.14(c) for $g = 8$ at three different probe wavelengths. Clearly, a small biexciton shift, together with the effect of carrier cooling, will completely inhibit gain at the blue side of the gaussian exciton peak. Moreover, the slope is steaper. At the red side, the behaviour is completely different. At low pump fluences, the shift creates PA, which turns into absorption bleaching above $N_{eh} = 2$. Again, the slope is much steaper than expected from a model without multiexcitonic interaction. The gain threshold is unchanged, but the maximum gain is not limited to $\Delta\alpha/\alpha_0 = 2$.

Finally, Figure 6.14(d) illustrates the effect of the fine structure on $\Delta\alpha/\alpha_0$. To model this, we assume the probability to have a carrier in a given band gap state to follow a Boltzmann distribution. We simplified this model by assuming the Boltzmann distribution of carriers results in a shift $\Delta_{fs} = 20$ meV in the excited absorption and emission spectrum, which gradually becomes smaller with increasing pump fluence (contrary to the multi-exciton shift) to accomodate state-filling:

$$\Delta\alpha_{5ps} = \sum_{n=0}^{g} \frac{2n}{g} \mathcal{P}'(n, N_{eh}) G(E_G + \frac{g-n}{g}\Delta_{fs}, \sigma_G) + \sum_{n=g+1}^{\infty} 2\mathcal{P}'(n, N_{eh}) G(E_G, \sigma_G) \quad (6.9)$$

Figure 6.14(d) shows that the initial slope is therefore much lower on the blue side of the α_0 spectrum and larger on the red side. The gain threshold also shifts to lower values on the red side and higher on the blue side. Again the maximum gain is higher than in a model without taking the fine structure into account.

Experimental Evidence of Fine Structure Splitting in TA spectra

For both PbSe QDs ($d = 4.6$ nm, Figure 6.15(a)) and PbSe/CdSe QDs (4.5 nm core, 0.5 nm shell, Figure 6.15(c)) the experimental traces of $\Delta\alpha/\alpha_0$ *vs.* N_{eh} at short delay times (5 ps) agree qualitatively with the last model, which includes the fine structure of the band gap (see Figure 6.15(a,c)). For both materials, the slope of the traces is much higher on the red side of the band gap spectrum than on the blue side and the extrapolated gain threshold is therefore clearly lower on the red side.

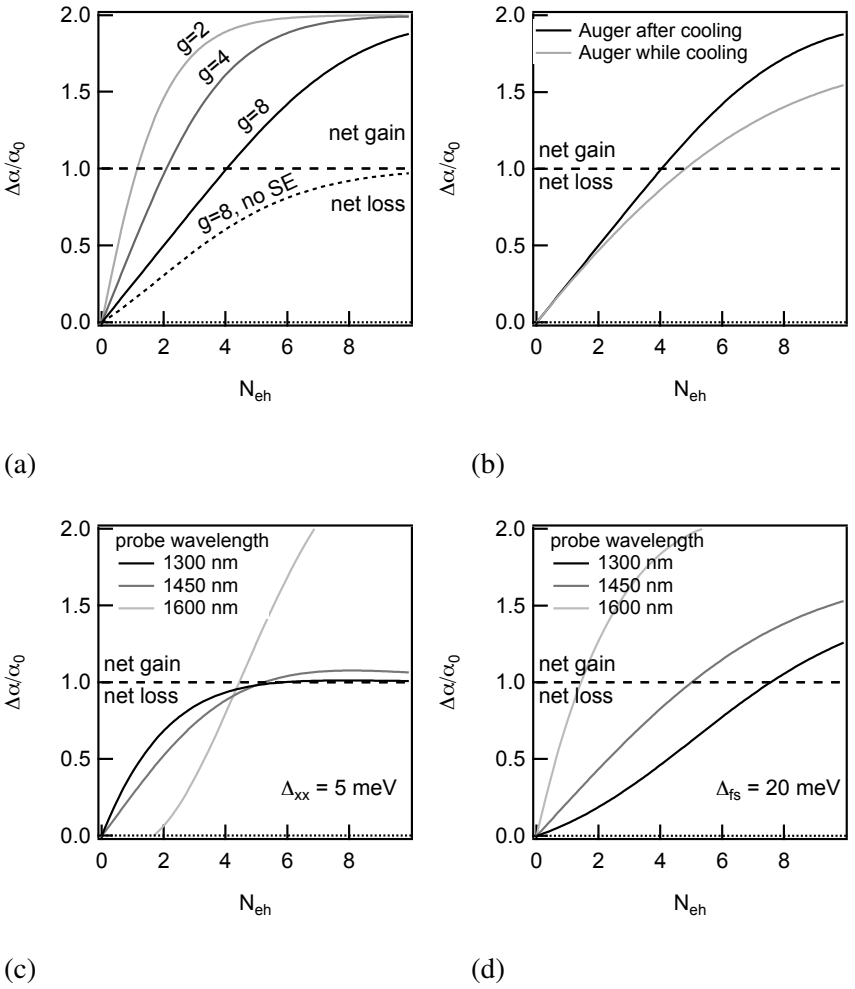

Figure 6.14: (a) Normalized differential absorbance $\Delta\alpha/\alpha_0$ *vs.* N_{eh} according to the Poissonian state-filling model (Eq. 6.4) for different degeneracies g. The dotted line shows the case where stimulated emission is not possible. (b) $\Delta\alpha/\alpha_0$ with (grey line) and without carrier cooling (black line). (c) $\Delta\alpha/\alpha_0$ taking carrier cooling and multi-excitonic shifts ($\Delta_{xx} = 5$ meV) into account for three different probe wavelengths around the band gap ($\lambda_G = 1420$ nm). (d) $\Delta\alpha/\alpha_0$ including carrier cooling and fine-structure splitting ($\Delta_{fs} = 20$ meV).

A notable difference between the model of Figure 6.14(d) and the experimental results is that we do not observe gain for either PbSe and PbSe/CdSe QDs. This is due in part to the limited pump power that was available and the stability of the setup. However, at the blue side of the band gap spectrum, the traces saturate around $\Delta\alpha/\alpha_0 = 0.5$. An extrapolation of the intraband absorption at the band gap cannot account for this effect. A setup artefact, such as a bad overlap between the probe beam and the pump beam in the sample, can be a possible cause. In that case the probe beam is probing unexcited QDs, that do not contribute to $\Delta\alpha$. Other, more photophysical, effects can have a similar impact on the signal. Some QDs might be charged and hence do not contribute to the bleach by stimulated emission[6]. Also, as outlined in Section 5.1.3 (see p. 103), due to the fine structure, the average oscillator strength of the emitting transition can be lower than the ground state absorbing transition. All these effects are modeled with the same parameter. Setting this parameter to 0.5 (*i.e.* all QDs are charged, or the oscillator strength of the emitting transition is 50% lower,...), the model agrees very well with our experimental results. This is illustrated for PbSe/CdSe QDs in Figure 6.16. Moreover, the normalized differential absorbance $\Delta\alpha/\alpha_0$ as a function of power N_{eh} at long (500 ps) delay times (see Figure 6.15(b,d)) saturate below the expected 0.25 for an 8-fold degenerate ground state. This further confirms the influence of these effects on the TA spectra.

Our model shows that both the carrier cooling and fine structure are important in understanding carrier dynamics around the band gap. However, our current data set cannot fully explain which effect is the chief reason for the lack of gain in our experiments.

6.3.3 Conclusion

We have compared the carrier dynamics of PbSe QDs with and without a CdSe shell. We did not observe a significant difference in the lifetime of multiexcitons. To understand the pump-dependent TA signal around the band gap, we extended the state-filling model of TA with multiexcitonic shifts[27;64], carrier cooling[8;71] and band gap fine structure[29]. The agreement of our model with the experimental results showed that the fine structure of the band gap cannot be neglected in understanding the wavelength dependence of the TA signal around the band gap, especially for PbSe/CdSe, where fine structure splitting is enhanced. None of the samples studied showed gain. The competition of Auger recombination with carrier cooling, resulting in a lower effective N_{eh} at the band gap, and intraband absorption can account for some reduction, but definitely not all. Our mea-

PbSe

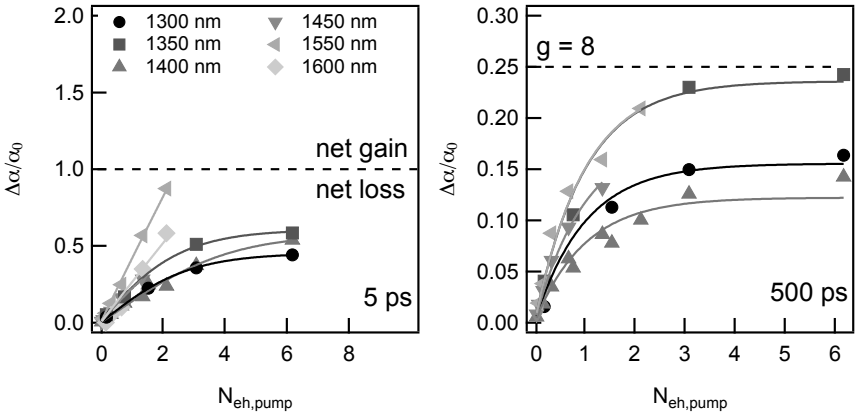

(a) (b)

PbSe/CdSe

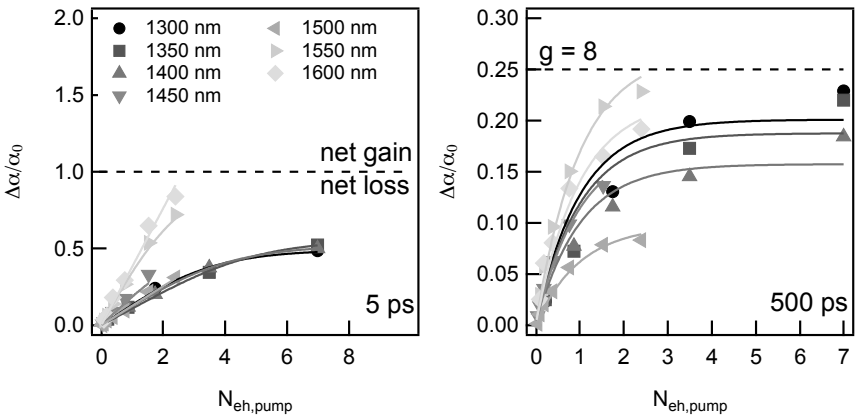

(c) (d)

Figure 6.15: Normalized differential absorbance $\Delta\alpha/\alpha_0$ *vs.* N_{eh} for PbSe QDs (top, 4.6 nm,$\lambda_g = 1420$ nm) and PbSe/CdSe QDs (bottom,4.5 nm core, 0.5 nm shell, $\lambda_g = 1450$ nm) (a,c) 5 ps after the pump pulse and (b,d) 500 ps after the pump pulse.

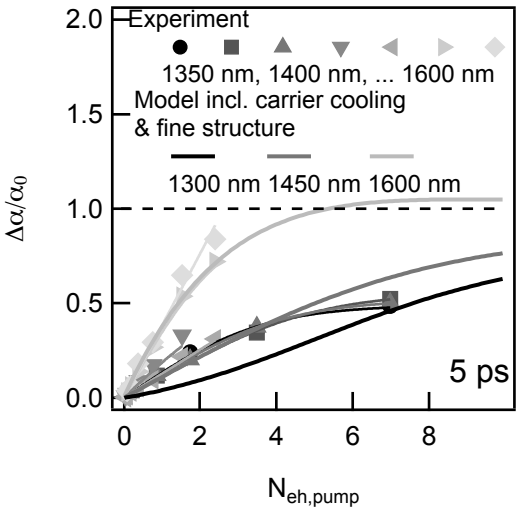

Figure 6.16: Comparison of the normalized differential absorbance $\Delta\alpha/\alpha_0$ *vs.* N_{eh}, calculated using a state-filling model, including the effects of fine structure and carrier cooling (full lines) and experimental results on PbSe/CdSe QDs.

surements cannot conclusively identify the possible causes that were mentioned, although more than likely the reduced average oscillator strength of the emitting transition, especially in PbSe/CdSe QDs, is detrimental to the observation of gain in these QDs.

References

[1] Klimov, V.; McBranch, D. Femtosecond high-sensitivity, chirp-free transient absorption spectroscopy using kilohertz lasers. *Optics Letters* **1998**, *23*, 277–279.

[2] Trinh, M. T. Ph.D. thesis, Technische Universiteit Delft, 2010.

[3] Klimov, V. Optical nonlinearities and ultrafast carrier dynamics in semiconductor nanocrystals. *Journal of Physical Chemistry B* **2000**, *104*, 6112–6123.

[4] Schaller, R.; Klimov, V. High efficiency carrier multiplication in PbSe nanocrystals: Implications for solar energy conversion. *Physical Review Letters* **2004**, *92*, 186601.

[5] Klimov, V.; Mikhailovsky, A.; McBranch, D.; Leatherdale, C.; Bawendi, M. Quantization of multiparticle Auger rates in semiconductor quantum dots. *Science* **2000**, *287*, 1011–1013.

[6] McGuire, J. A.; Sykora, M.; Robel, I.; Padilha, L. A.; Joo, J.; Pietryga, J. M.; Klimov, V. I. Spectroscopic Signatures of Photocharging due to Hot-Carrier Transfer in Solutions of Semiconductor Nanocrystals under Low-Intensity Ultraviolet Excitation. *ACS Nano* **2010**, *4*, 6087–6097.

[7] Schins, J. M.; Trinh, M. T.; Houtepen, A. J.; Siebbeles, L. D. A. Probing formally forbidden optical transitions in PbSe nanocrystals by time- and energy-resolved transient absorption spectroscopy. *Physical Review B* **2009**, *80*, 035323.

[8] An, J. M.; Califano, M.; Franceschetti, A.; Zunger, A. Excited-state relaxation in PbSe quantum dots. *Journal of Chemical Physics* **2008**, *128*, 164720.

[9] Harbold, J. M.; Wise, F. W. Photoluminescence spectroscopy of PbSe nanocrystals. *Physical Review B* **2007**, *76*, year.

[10] Wehrenberg, B.; Wang, C.; Guyot-Sionnest, P. Interband and intraband optical studies of PbSe colloidal quantum dots. *Journal of Physical Chemistry B* **2002**, *106*, 10634–10640.

[11] Guyot-Sionnest, P.; Hines, M. Intraband transitions in semiconductor nanocrystals. *Applied Physics Letters* **1998**, *72*, 686–688.

[12] Wang, C.; Shim, M.; Guyot-Sionnest, P. Electrochromic nanocrystal quantum dots. *Science* **2001**, *291*, 2390–2392.

[13] Pandey, A.; Guyot-Sionnest, P. Intraband spectroscopy and band offsets of colloidal II-VI core/shell structures. *The Journal of chemical physics* **2007**, *127*, 104710.

[14] An, J. M.; Franceschetti, A.; Dudiy, S. V.; Zunger, A. The peculiar electronic structure of PbSe quantum dots. *Nano Letters* **2006**, *6*, 2728–2735.

[15] Yang, Y.; Rodríguez-Córdoba, W.; Lian, T. Ultrafast Charge Separation and Recombination Dynamics in Lead Sulfide Quantum Dot–Methylene Blue Complexes Probed by Electron and Hole Intraband Transitions. *Journal of the American Chemical Society* **2011**, *133*, 9246–9249.

[16] Malko, A.; Mikhailovsky, A.; Petruska, M.; Hollingsworth, J.; Htoon, H.; Bawendi, M.; Klimov, V. From amplified spontaneous emission to microring lasing using nanocrystal quantum dot solids. *Applied Physics Letters* **2002**, *81*, 1303–1305.

[17] Cretí, A.; Zavelani-Rossi, M.; Lanzani, G.; Anni, M.; Manna, L.; Lomascolo, M. Role of the shell thickness in stimulated emission and photoinduced absorption in CdSe core/shell nanorods. *Phys. Rev. B* **2006**, *73*, 165410.

[18] Sewall, S. L.; Cooney, R. R.; Anderson, K. E. H.; Dias, E. A.; Sagar, D. M.; Kambhampati, P. State-resolved studies of biexcitons and surface trapping dynamics in semiconductor quantum dots. *Journal of Chemical Physics* **2008**, *129*, 084701.

[19] Ginger, D. S.; Ginger, D.; Dhoot, A. S.; Dhoot, A.; Finlayson, C. E.; Finlayson, C.; Greenham, N. C.; Greenham, N. Long-lived quantum-confined infrared transitions in CdSe nanocrystals. *Applied Physics Letters* **2000**, *77*, 2816.

[20] Huang, J.; Huang, Z.; Jin, S.; Lian, T. Exciton Dissociation in CdSe Quantum Dots by Hole Transfer to Phenothiazine. *The Journal of Physical Chemistry C* **2008**, *112*, 19734–19738.

[21] Zhu, H.; Song, N.; Rodríguez-Córdoba, W.; Lian, T. Wave Function Engineering for Efficient Extraction of up to Nineteen Electrons from One CdSe/CdS Quasi-Type II Quantum Dot. *Journal of the American Chemical Society* **2012**, *134*, 4250–4257.

[22] Leventis, H. C.; O'Mahony, F.; Akhtar, J.; Afzaal, M.; O'Brien, P.; Haque, S. A. Transient Optical Studies of Interfacial Charge Transfer at Nanostructured Metal Oxide/PbS Quantum Dot/Organic Hole Conductor Heterojunctions. *Journal of the American Chemical Society* **2010**, *132*, 2743–2750.

[23] Yang, Y.; Rodríguez-Córdoba, W.; Xiang, X.; Lian, T. Strong Electronic Coupling and Ultrafast Electron Transfer between PbS Quantum Dots and TiO2 Nanocrystalline Films. *Nano Letters* **2012**, *12*, 303–309.

[24] Allan, G.; Delerue, C. Confinement effects in PbSe quantum wells and nanocrystals. *Physical Review B* **2004**, *70*, 245321.

[25] Thomson, D.; Gardes, F.; Fedeli, J.-M.; Zlatanovic, S.; Hu, Y.; Kuo, B.; Myslivets, E.; Alic, N.; Radic, S.; Mashanovich, G.; Reed, G. 50-Gb/s Silicon Optical Modulator. *Photonics Technology Letters, IEEE* **2012**, *24*, 234 –236.

[26] Liu, A.; Jones, R.; Liao, L.; Samara-Rubio, D.; Rubin, D.; Cohen, O.; Nicolaescu, R.; Paniccia, M. A high-speed silicon optical modulator based on a metal–oxide–semiconductor capacitor. *Nature* **2004**, *427*, 615–618.

[27] Trinh, M. T.; Houtepen, A. J.; Schins, J. M.; Piris, J.; Siebbeles, L. D. A. Nature of the Second Optical Transition in PbSe Nanocrystals. *Nano Letters* **2008**, *8*, 2112–2117.

[28] Moreels, I.; Hens, Z. On the Interpretation of Colloidal Quantum-Dot Absorption Spectra. *Small* **2008**, *4*, 1866–1868.

[29] De Geyter, B.; Justo, Y.; Moreels, I.; Lambert, K.; Smet, P. F.; Van Thourhout, D.; Houtepen, A. J.; Grodzinska, D.; de Mello Donega, C.; Meijerink, A.; Vanmaekelbergh, D.; Hens, Z. The Different Nature of Band Edge Absorption and Emission in Colloidal PbSe/CdSe Core/Shell Quantum Dots. *ACS Nano* **2011**, *5*, 58–66.

[30] De Geyter, B.; Hens, Z. The absorption coefficient of PbSe/CdSe core/shell colloidal quantum dots. *Applied Physics Letters* **2010**, *97*, 161908.

[31] De Geyter, B.; Houtepen, A. J.; Carrillo, S.; Geiregat, P.; Gao, Y.; ten Cate, S.; Schins, J. M.; Van Thourhout, D.; Delerue, C.; Siebbeles, L.

D. A.; Hens, Z. Broadband and Picosecond Intraband Absorption in Lead-Based Colloidal Quantum Dots. *ACS Nano* **2012**, *6*, 6067–6074.

[32] Hwang, Y.-N.; Je, K.-C.; Kim, D.; Park, S.-H. Observation of enhanced biexcitonic effect in semiconductor nanocrystals. *Phys. Rev. B* **2001**, *64*, 041305.

[33] Hu, Y. Z.; Koch, S. W.; Lindberg, M.; Peyghambarian, N.; Pollock, E. L.; Abraham, F. F. Biexcitons in semiconductor quantum dots. *Phys. Rev. Lett.* **1990**, *64*, 1805–1807.

[34] Kang, K. I.; Kepner, A. D.; Gaponenko, S. V.; Koch, S. W.; Hu, Y. Z.; Peyghambarian, N. Confinement-enhanced biexciton binding energy in semiconductor quantum dots. *Phys. Rev. B* **1993**, *48*, 15449–15452.

[35] Woggon, U.; Giessen, H.; Gindele, F.; Wind, O.; Fluegel, B.; Peyghambarian, N. Ultrafast energy relaxation in quantum dots. *Phys. Rev. B* **1996**, *54*, 17681–17690.

[36] Klimov, V.; Hunsche, S.; Kurz, H. Biexciton effects in femtosecond nonlinear transmission of semiconductor quantum dots. *Phys. Rev. B* **1994**, *50*, 8110–8113.

[37] Gesuele, F.; Sfeir, M.; Koh, W.-k.; Murray, C. B.; Heinz, T. F.; Wong, C. W. Ultrafast supercontinuum spectroscopy of carrier multiplication and biexcitonic effects in excited states of PbS quantum dots. *Nano Letters* **2012**, *12*, 2658–2664.

[38] Malko, A.; Mikhailovsky, A.; Petruska, M.; Hollingsworth, J.; Klimov, V. Interplay between optical gain and photoinduced absorption in CdSe nanocrystals. *Journal of Physical Chemistry B* **2004**, *108*, 5250–5255.

[39] Zhang, J.; Jiang, X. Steady state photoinduced absorption of PbS quantum dots film. *Applied Physics Letters* **2008**, *92*, 141108.

[40] Cooney, R.; Sewall, S.; Sagar, D.; Kambhampati, P. Gain Control in Semiconductor Quantum Dots via State-Resolved Optical Pumping. *Physical review letters* **2009**, *102*, 127404.

[41] Qu, Y.; Jia, W.; Zheng, Y.; Ying, J. Y. Auger recombination and intraband absorption of two-photon-excited carriers in colloidal CdSe quantum dots. *Applied Physics Letters* **2007**, *90*, 133112.

[42] Padilha, L. A.; Robel, I.; Lee, D. C.; Nagpal, P.; Pietryga, J. M.; Klimov, V. I. Spectral Dependence of Nanocrystal Photoionization Probability: The Role of Hot-Carrier Transfer. *ACS Nano* **2011**, *5*, 5045–5055.

[43] Schaller, R.; Pietryga, J.; Goupalov, S.; Petruska, M.; Ivanov, S.; Klimov, V. Breaking the phonon bottleneck in semiconductor nanocrystals via multiphonon emission induced by intrinsic nonadiabatic interactions. *Physical Review Letters* **2005**, *95*, 196401.

[44] Efros, A.; Rosen, M. The electronic structure of semiconductor nanocrystals. *Annual Review of Materials Science* **2000**, *30*, 475–521.

[45] Franceschetti, A. Structural and electronic properties of PbSe nanocrystals from first principles. *Physical Review B* **2008**, *78*, 075418.

[46] An, J. M.; Franceschetti, A.; Zunger, A. The excitonic exchange splitting and radiative lifetime in PbSe quantum dots. *Nano Letters* **2007**, *7*, 2129–2135.

[47] An, J. M.; Franceschetti, A.; Zunger, A. Pauli blocking versus electrostatic attenuation of optical transition intensities in charged PbSe quantum dots. *Physical Review B* **2007**, *76*, 161310.

[48] Moreels, I.; Lambert, K.; De Muynck, D.; Vanhaecke, F.; Poelman, D.; Martins, J. C.; Allan, G.; Hens, Z. Composition and size-dependent extinction coefficient of colloidal PbSe quantum dots. *Chemistry of Materials* **2007**, *19*, 6101–6106.

[49] Soref, R.; Bennett, B. Electrooptical effects in silicon. *Quantum Electronics, IEEE Journal of* **1987**, *23*, 123–129.

[50] Schroder, D.; Thomas, R.; Swartz, J. Free carrier absorption in silicon. *Ieee Journal of Solid-State Circuits* **1978**, *13*, 180–187.

[51] Kekatpure, R. D.; Brongersma, M. L. Quantification of Free-Carrier Absorption in Silicon Nanocrystals with an Optical Microcavity. *Nano Letters* **2008**, *8*, 3787–3793.

[52] Kekatpure, R. D.; Brongersma, M. L. Near-infrared free-carrier absorption in silicon nanocrystals. *Optics Letters* **2009**, *34*, 3397–3399.

[53] Robel, I.; Gresback, R.; Kortshagen, U.; Schaller, R. D.; Klimov, V. I. Universal Size-Dependent Trend in Auger Recombination in Direct-Gap and Indirect-Gap Semiconductor Nanocrystals. *Phys. Rev. Lett.* **2009**, *102*, 177404.

[54] Klimov, V. I.; Ivanov, S. A.; Nanda, J.; Achermann, M.; Bezel, I.; McGuire, J. A.; Piryatinski, A. Single-exciton optical gain in semiconductor nanocrystals. *Nature* **2007**, *447*, 441–446.

[55] Talapin, D.; Murray, C. PbSe nanocrystal solids for n-and p-channel thin film field-effect transistors. *Science* **2005**, *310*, 86.

[56] Trinh, M. T.; Houtepen, A. J.; Schins, J. M.; Hanrath, T.; Piris, J.; Knulst, W.; Goossens, A. P. L. M.; Siebbeles, L. D. A. In spite of recent doubts carrier multiplication does occur in PbSe nanocrystals. *Nano Letters* **2008**, *8*, 1713–1718.

[57] Nootz, G.; Padilha, L. A.; Levina, L.; Sukhovatkin, V.; Webster, S.; Brzozowski, L.; Sargent, E. H.; Hagan, D. J.; Van Stryland, E. W. Size dependence of carrier dynamics and carrier multiplication in PbS quantum dots. *Phys. Rev. B* **2011**, *83*, 155302.

[58] McGuire, J.; Sykora, M.; Joo, J.; Pietryga, J.; Klimov, V. Apparent versus true carrier multiplication yields in semiconductor nanocrystals. *Nano letters* **2010**, *10*, 2049–2057.

[59] McGuire, J.; Joo, J.; Pietryga, J.; Schaller, R.; Klimov, V. New aspects of carrier multiplication in semiconductor nanocrystals. *Accounts of chemical research* **2008**, *41*, 1810–1819.

[60] Trinh, M. T.; Houtepen, A. J.; Schins, J. M.; Hanrath, T.; Piris, J.; Knulst, W.; Goossens, A. P. L. M.; Siebbeles, L. D. A. In Spite of Recent Doubts Carrier Multiplication Does Occur in PbSe Nanocrystals. *Nano Letters* **2008**.

[61] Klimov, V. I. Mechanisms for photogeneration and recombination of multiexcitons in semiconductor nanocrystals: Implications for lasing and solar energy conversion. *Journal of Physical Chemistry B* **2006**, *110*, 16827–16845.

[62] Schaller, R. D.; Sykora, M.; Jeong, S.; Klimov, V. I. High-efficiency carrier multiplication and ultrafast charge separation in semiconductor nanocrystals studied via time-resolved photoluminescence. *Journal of Physical Chemistry B* **2006**, *110*, 25332–25338.

[63] Schaller, R.; Petruska, M.; Klimov, V. Effect of electronic structure on carrier multiplication efficiency: Comparative study of PbSe and CdSe nanocrystals. *Applied Physics Letters* **2005**, *87*, 253102.

[64] Gdor, I.; Sachs, H.; Roitblat, A.; Strasfeld, D. B.; Bawendi, M. G.; Ruhman, S. Exploring Exciton Relaxation and Multiexciton Generation in PbSe Nanocrystals Using Hyperspectral Near-IR Probing. *ACS Nano* **2012**, *6*, 3269–3277.

[65] Ellingson, R.; Beard, M.; Johnson, J.; Yu, P.; Micic, O.; Nozik, A.; Shabaev, A.; Efros, A. Highly efficient multiple exciton generation in colloidal PbSe and PbS quantum dots. *Nano Letters* **2005**, *5*, 865–871.

[66] Schaller, R.; Petruska, M.; Klimov, V. Tunable near-infrared optical gain and amplified spontaneous emission using PbSe nanocrystals. *Journal of Physical Chemistry B* **2003**, *107*, 13765–13768.

[67] Sykora, M.; Koposov, A. Y.; McGuire, J. A.; Schulze, R. K.; Tretiak, O.; Pietryga, J. M.; Klimov, V. I. Effect of Air Exposure on Surface Properties, Electronic Structure, and Carrier Relaxation in PbSe Nanocrystals. *Acs Nano* **2010**, *4*, 2021–2034.

[68] Harbold, J. M.; Du, H.; Krauss, T. D.; Cho, K.-S.; Murray, C. B.; Wise, F. W. Time-resolved intraband relaxation of strongly confined electrons and holes in colloidal PbSe nanocrystals. *Phys. Rev. B* **2005**, *72*, 195312.

[69] Cragg, G. E.; Efros, A. L. Suppression of Auger Processes in Confined Structures. *Nano Letters* **2010**, *10*, 313–317.

[70] Beard, M. C.; Midgett, A. G.; Law, M.; Semonin, O. E.; Ellingson, R. J.; Nozik, A. J. Variations in the Quantum Efficiency of Multiple Exciton Generation for a Series of Chemically Treated PbSe Nanocrystal Films. *Nano Letters* **2009**, *9*, 836–845.

[71] Guyot-Sionnest, P.; Wehrenberg, B.; Yu, D. Intraband relaxation in CdSe nanocrystals and the strong influence of the surface ligands. *Journal of Chemical Physics* **2005**, *123*, 074709.

Part III

Applications of Colloidal QDs as Optical Emitters in Integrated Photonics

7

Theory and Simulation of Optical Interaction of Colloidal QDs and Photonic Resonators

7.1 Introduction

An optical resonator is a structure in which light is trapped and allowed to interfere with itself. Optical resonators provide the necessary feedback to make an optical amplifier into a laser. The feedback can be provided by reflecting mirrors or gratings, or by making a ring shaped waveguide. In the latter case outcoupling of light is either provided by radiative loss and scattering or by evanescently coupling another waveguide to the resonator.

These microdisks or microrings have become the transistor of integrated photonics. They are easy to fabricate with lithographic techniques, have a small footprint and provide high-Q and very low loss optical resonances.

For the same reasons, we have chosen the microdisk to study the interaction of optical resonators with colloidal QDs. We use hybrid colloidal QD silicon nitride microdisks, supported by a silicon pillar. In this Chapter we will introduce the basic microdisk concepts, discuss the design parameters of the microdisks and simulate the rate equations of the colloidal QDs coupled to the microdisk. In Chapter 8 we go into detail about the fabrica-

tion of these microdisks and discuss the experimental results.

7.2 Theory of Microdisks

7.2.1 Important Microdisk Parameters

Q-factor

The quality or Q-factor of an optical mode is the ratio of the energy stored in an optical mode to the energy lost per roundtrip:

$$Q = 2\pi \frac{E_{stored}}{-\Delta E_{roundtrip}} = -2\pi\nu_r \frac{\phi_{stored}}{\frac{d\phi}{dt}} \tag{7.1}$$

Here we have used the resonant frequency ν_r and the amount of photons ϕ. As a consequence, in the absence of a source, the number of photons in the cavity will decay expontentially. In the frequency domain, this becomes a Lorentzian function. In practice, it is usually easier to determine the Q-factor in the frequency domain, i.e. by measuring the spectrum. Hence we rewrite it to the more practical form:

$$Q = \frac{\lambda_0}{FWHM_\lambda}$$

The Q-factor is a direct way to quantify the quality of a cavity for storage of photons. The higher the Q-factor, the lower the cavity losses and the longer a photon stays inside the cavity mode.

Photon Cavity Lifetime τ_{cav}

The lifetime of a photon in a cavity mode is a direct measure of the losses in the cavity mode. We can therefore directly relate it to the Q-factor of the optical mode. For an unloaded optical cavity, we define τ_{cav} as the typical time constant for the decay of the amount of photons ϕ in the cavity:

$$\frac{d\phi}{dt} = -\frac{\phi}{\tau_{cav}} \tag{7.2}$$

Plugging this equation into Equation 7.1, we get:

$$\tau_{cav} = \frac{Q}{2\pi\nu_0} = \frac{Q\lambda_0}{2\pi c} \tag{7.3}$$

Here λ_0 is the resonance wavelength in free space. As an example, at the wavelength of 650 nm, the photon cavity lifetime is:

$$\tau_{cav} = Q \times 0.35\text{fs}(@650\ \text{nm})$$

Free Spectral Range

Since the resonance condition in a microdisk states that the wavelength in the microdisk λ needs to be an integer multiple m of the cavity perimeter πd:

$$m\lambda = m\frac{\lambda_0}{n_{eff}} = \pi d$$

the free spectral range or spectral distance between two consecutive resonances becomes:

$$FSR = \lambda_{m-1} - \lambda_m = \frac{\lambda_0^2}{\pi d n_g} \tag{7.4}$$

Here n_g is the group index, defined as:

$$n_g = n_{eff} - \frac{\partial n_{eff}}{\partial \lambda}\lambda \tag{7.5}$$

with n_{eff} the effective index. Note that the FSR is a direct way of measuring the group velocity $v_g = c/n_g$, i.e. the speed at which a light packet travels through the microdisk. With this definition, it is easy to calculate the cavity round trip time $\tau_{rt} = \pi d/v_g$.

Finesse

The finesse describes the buildup of photons or power in the cavity and is defined as:

$$\mathcal{F} = \frac{FSR}{FWHM} = \frac{n_{eff}}{n_g}\frac{Q}{m}$$

The finesse is also the inverse of the round trip loss:

$$\alpha\pi d = \mathcal{F}^{-1}$$

where α is the loss coefficient through absorption, scattering, radiation,...

7.2.2 Maxwell's equations for Cylindrical symmetry

Starting from Maxwell's equations in the absence of sources and assuming a sinusoidal time-dependence $exp(-i\omega t)$, we can derive the master equation for the electrical field $\mathbf{E}$:

$$\nabla \times \nabla \times \mathbf{E}(\mathbf{r}) = k_0^2 n^2(\mathbf{r})\mathbf{E}(\mathbf{r}) \tag{7.6}$$

Here $k_0 = \frac{2\pi}{\lambda_0}$ is the free space wave vector and $n(\mathbf{r}) = \sqrt{\frac{\epsilon(\mathbf{r})}{\epsilon_0}}$ is the refractive index.

A microdisk possesses cylindrical symmetry. Therefore $n(\mathbf{r}) = n(r, z)$ only depends on the radial coordinate r and the axial coordinate z. If we also assume the materials to be homogeneous, Equation 7.6 reduces to the Helmholtz equation:

$$\nabla^2 \mathbf{E}(\mathbf{r}) = k_0 n(r, z) \mathbf{E}(\mathbf{r}) \tag{7.7}$$

Since in the equation above n does not depend on the azimuthal coordinate ϕ, the shape of the field will not change, as it travels around the disk. Hence, only its phase will change:

$$\mathbf{E}(\mathbf{r}) = \mathbf{E}(r, z) e^{-im\phi}$$

Here m is the azimuthal eigenvalue, a measure of how many times the wavelength fits into the microdisk perimeter. This assumption reduces the problem from 3D to 2D.

We need to solve the 2D Helmholtz equation for each of the field components $\{E_r, E_z, E_\phi\}$. In a 1D slab waveguide, the invariance of the fields in the in-plane direction divides the solutions into two orthogonal subsets: tranverse electrical modes (TE) which only have non-zero $\{E_y, H_x, H_z\}$ field components and transverse magnetic modes (TM) with only non-zero $\{H_y, E_x, E_z\}$ components. This means the Helmholtz equation only needs to be solved for one of the field components.

In a microdisk, the structure is finite in both the r and z direction. Since the microdisk is quite thin compared to its radius, the solutions will still be predominantly TE or TM in nature. Here (quasi)-TE means that the $\{E_r, H_\phi, H_z\}$ components dominate in magnitude, while (quasi)-TM means that the $\{H_r, E_\phi, E_z\}$ are the largest field components. Hence in good approximation we can solve for only the E_r(H_r component for the TE (TM) solution respectively:

$$[\frac{\partial^2}{\partial z^2} + \frac{\partial^2}{\partial r^2} + \frac{1}{r}\frac{\partial}{\partial r} - \frac{m^2}{r^2} + k_0 n(r, z)]\Phi_r(r, z) = 0$$

Here Φ_r is the electrical field for the case of TM and the magnetic field in the case of TE.

Through separation of the variables r and z, we get two scalar equations ($\Phi(r, z) = R(r)Z(z)$). One is the slab mode equation:

$$[\frac{\partial^2}{\partial z^2} + k_0(n(z) - n_{eff})]Z(z) = 0$$

Here n_{eff} is the axial eigenvalue, commonly called the effective index of the slab waveguide. The other equation is the Bessel equation for the radial

dependence of the field:

$$[\frac{\partial^2}{\partial r^2} + \frac{1}{r}\frac{\partial}{\partial r} - \frac{m^2}{r^2} + k_0 n_{eff}(r)]R(r) = 0$$

While approximate, this solution does give significant insight in how to engineer a microdisk. We solve the slab equation above numerically using the numerical mode solver CAMFR.[1] Figure 7.1.a shows the dispersion of the effective index for a slab waveguide consisting of 80 nm of high-index Si_3N_4, 30 nm of CdSe QDs and 80 nm of low-index Si_3N_4. The refractive index dispersion for $Si_3N_4$was measured using ellipsometry (see p. 189). For the CdSe QDs, we use the dispersion of bulk CdSe[2], where we assume closest packing of the QDs, with a 25% volume fraction of QDs, 50% of ligands (n = 1.5) and 25% of air. Since the TE modes are the fundamental modes, the TM mode always has a lower effective index and goes towards cutoff for wavelengths above 1.5μm. Note that because of this TM cutoff, the group index n_g (see p. 161) of the TM mode is larger. Therefore TM modes with the same radial order will have a lower FSR than the TE modes.

The layer thickness of the QDs is an important parameter to control the modal gain of the microdisk. At the same time, the increasing layer thickness also raises the effective index of the modes (see Figure 7.1). The effect is much larger for the TM modes than for the TE modes. Only the fundamental TE and TM modes are guided up to a total microdisk thickness of 260 nm.

The solution of the Bessel equation is the Bessel function of the first kind for the radial distribution inside the microdisk $J_m(k_0 n_{eff} r)$ and the Hankel function $H_m(k_0 n_0 r)$ outside the microdisk. Requiring the continuity of the tangential components of the field at the microdisk edge, results in a transcendental equation from which we can calculate the free-space resonance wavelength, knowing the dispersion of n_{eff}:

$$k_0 n_{eff}(k_0) J_{m+1}(k_0 n_{eff} R) = (\frac{m}{R} + \eta k_0 \sqrt{n_{eff}^2 - n_0^2}) J_m(k_0 n_{eff} R)$$

Here $\eta = \frac{n_{eff}^2}{n_0^2}$ for the TE and $\eta = 1$ for the TM mode. The solution of this transcendental equation allows for easy and reasonably accurate calculation of the free space resonance wavelengths for the microdisks.

The modes in a microdisk are therefore fully described by a dominant polarization and three mode numbers:

- *the polarization* is either TE or TM
- *the azimuthal mode number* m describes the number of times the material wavelength fits into the disk perimeter.

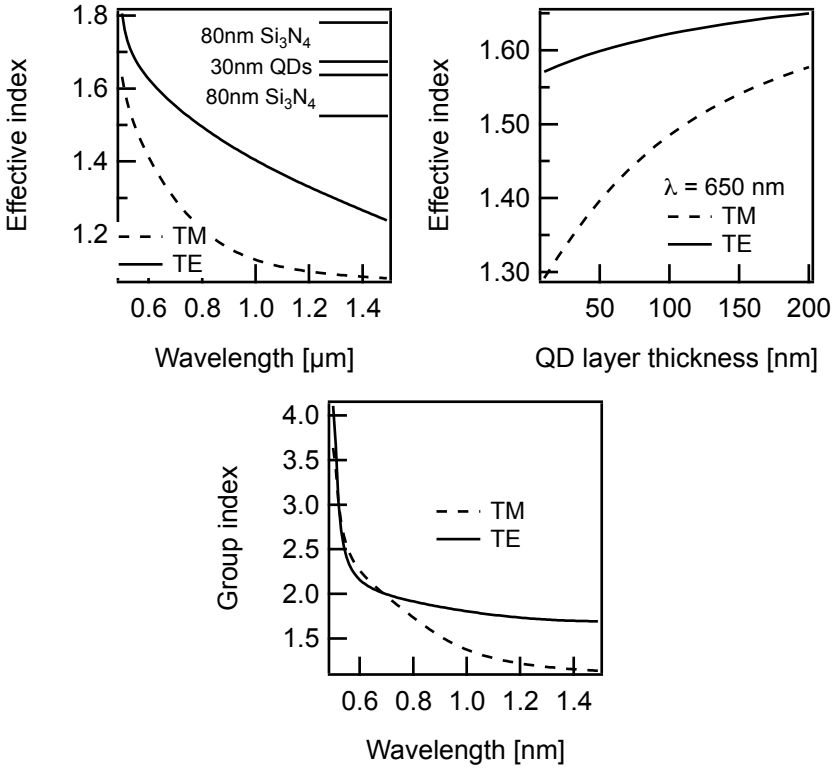

Figure 7.1: (a) The dispersion of the effective index for a slab waveguide with the layer stack as drawn above. (b) The effective index for different thickness of the QD layer.(c) The group index n_g as a function of wavelength.

- *the radial mode number* l describes the amount of field lobes in the radial direction

- *the axial mode number* h describes the amount of field lobes in the axial direction. Note that for all our microdisks the disk thickness was small enough only to support the fundamental slab-TE and TM modes.

7.2.3 FDTD simulations

In Finite Difference Time Domain simulations, the Maxwell equations are discretized both in space and time. We use the rotational symmetry of the microdisks to simplify the problem from 3D to 2D. This drastically reduces the simulation complexity and time. The microdisk cross section, including the silicon pillar is thus implemented in MEEP, an open source FDTD solver from MIT.[3]

Effect of the underetching depth on the radiative Q factor

A magnetic or electric dipole source excites the resonant mode at the given frequency. For the TM modes ($\mathbf{H} \simeq H_r$) a E_z dipole source is applied, for the TE modes ($\mathbf{E} \simeq E_r$) a H_z dipole source is applied. The time response of the electromagnetic field is monitored. Since the Q factor is directly proportional to the photon cavity lifetime τ_{cav} (see 7.2.1 on p. 160), the radiative Q factor can be extracted from this simulation.

Since the pillar that supports the freehanging microdisk is made of silicon, its high refractive index can suck the mode into the pillar and induce losses to the optical mode. Figure 7.2 shows the influence of the underetch depth, which is the proximity of the pillar to the edge of the microdisk, on the Q factor of the fundamental TE and TM mode. For both the TE and TM mode, the Q factor drops significantly when the underetch depth goes below 1250 nm, or roughly 2λ. Higher order modes are expected to leak more rapidly into the pillar.

7.2.4 FE eigenmode solver simulations using COMSOL

The model

COMSOL is a finite-element (FE) solver for systems of coupled partial differential equations. While it has built-in support for the solving eigenmode solution of Maxwell's equations in the *RF module*, it does not allow

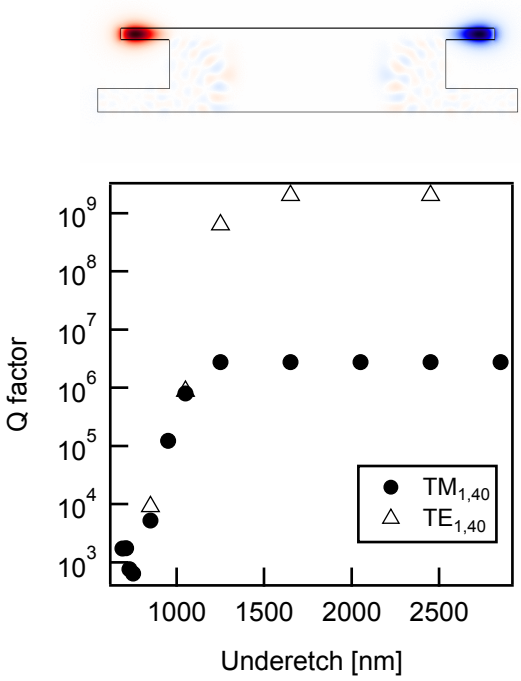

Figure 7.2: Influence of the underetch depth on the Q factor of the fundamental TE and TM modes shows the radiative loss of the optical mode to the silicon pillar and substrate, when the pillar is not small enough.

solving the axisymmetric problem with propagation invariance in the ϕ direction and take advantage of its consequent reduction from a 3D to a 2D problem.

We use an implementation [4] of the vectorial Helmholtz equation derived above, but described in the weak form to avoid numerical instability. It solves for the magnetic field strength $\mathbf{H}$, since it is continuous across all interfaces. The $\mathbf{D}$ and $\mathbf{E}$ field are then derived from $\mathbf{H}$, using Maxwell's equations.

Modes in a microdisk resonator

Figure 7.3 shows the field mode profile for all three field components of the first order $TE_{46,1}$ mode of a 5.5 μm diameter microdisk. The microdisk layer stack consists of 80 nm of high-index Si_3N_4, 30 nm of QD, and 80 nm of low-index Si_3N_4. The arrows indicate the $\mathbf{H}$ field, which clearly shows that it is perpendicular to the transverse $\mathbf{E}$ field. However, the field profiles indicate that the E_z and E_ϕ components are non-zero, and hence this underlines the *quasi*-character of the TE and TM polarization.

Figure 7.4 shows a logarithmic plot of the intensity $\|\mathbf{E}\|^2$ for the first and second order TE and TM mode for the same microdisk. The TE modes can be clearly indentified by their field discontinuity at the microdisk edge, while for the TM modes there is a jump in the intensity at the microdisk top surface. The low refractive index of the QD layer (n_{QD}=1.71 @650 nm, where we used the refractive index of bulk CdSe [2] – see Section A.5–, with a volume fraction of 25%) creates a horizontal slot for TM mode, where most of the mode's intensity is located in the QD layer. However, the refractive index of a QD layer is only an approximate value, that cannot be measured accurately using ellipsometry. Moreover, as will be discussed later, it is difficult to compare the coupled PL intensity between TE and TM modes experimentally, so the existence of this slot effect in our microdisks could not be confirmed.

Figure 7.5.a shows a dispersion diagram for a 5.5 μm microdisk. It plots the azimuthal mode number m versus the free space wavelength, as calculated with COMSOL, for the first six modes. TE modes are represented by blue dots and TM modes are represented by red dots. The light line is also plotted, with the unphysical area below it shaded out in black. The TE_2 and the TM_1 cross in the dispersion diagram around 580 nm. Here these modes are degenerate and two hybrid TEM modes exist. Similar hybrid crossing points are present for the higher radial order modes.

Figure 7.5.b mimics the expected emission spectrum from this microdisk. For clarity, we have only plotted the first four modes. Each resonance is

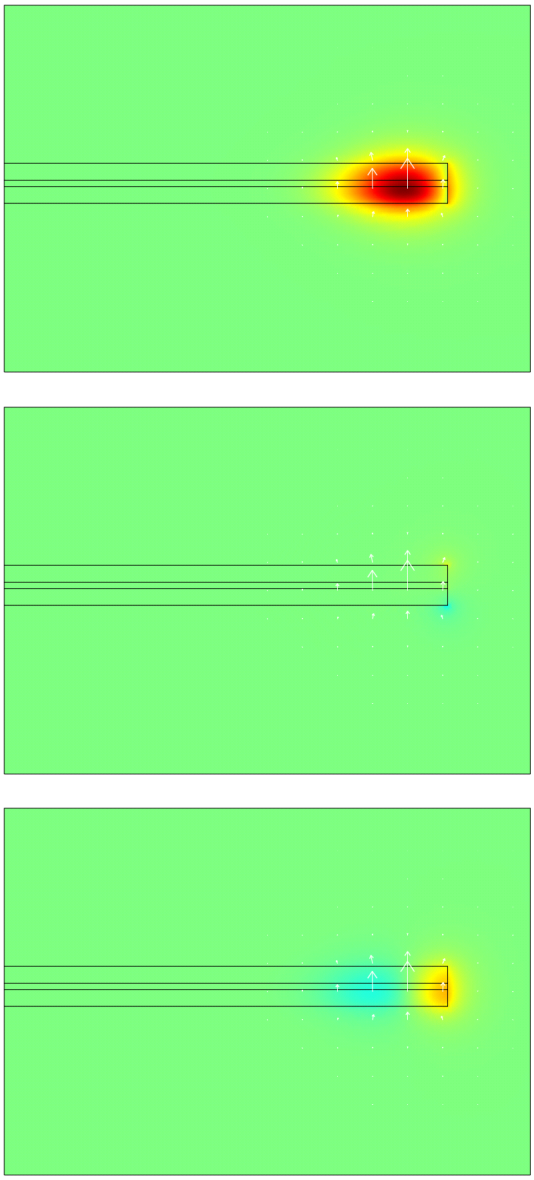

Figure 7.3: From top to bottom the E_r, E_z and E_ϕ for the $TE_{46,1}$ mode plotted on the same colour scale, as to compare the field strength. The microdisk has a 5.5μm diameter and consists of a 80 nm high-index Si_3N_4, 30 nm QD, 80 nm low-index Si_3N_4layer stack. The white arrow indicates the $\mathbf{H}$ field.

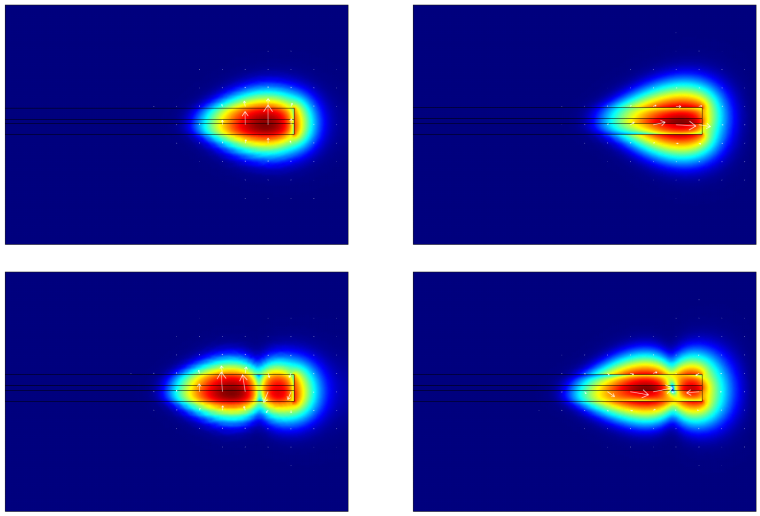

Figure 7.4: From left to right, $log\|\mathbf{E}\|^2$-plot of the $TE_{46,1}$, $TM_{46,1}$, $TE_{46,2}$ and $TM_{46,2}$. The arrow indicates the $\mathbf{H}$ field.

broadened with a Lorentzian function with a FWHM of 1 nm. This results in a dense modal spectrum, in which the overlap of the lorentzian functions creates a background emission and in which separate modes are hard to distinguish. This will be illustrated experimentally in the following chapter.

The group index for these modes is shown in Figure 7.6.a. The TM_1 has the largest group index and therefore the smallest FSR in this spectral range. Within the family of TE modes, the lowest radial order has the highest group index. The same goes for n_{eff} (see Figure 7.6). Note the similar effective index between TE_2 and TM_1. Where both graphs cross, two hybrid TEM modes will form.

7.3 Microdisks and Colloidal QDs

7.3.1 Laser Rate Equations

We use a rate equation model[5] to study the properties of microdisks that contain an active colloidal QD layer. The change in N, the number of

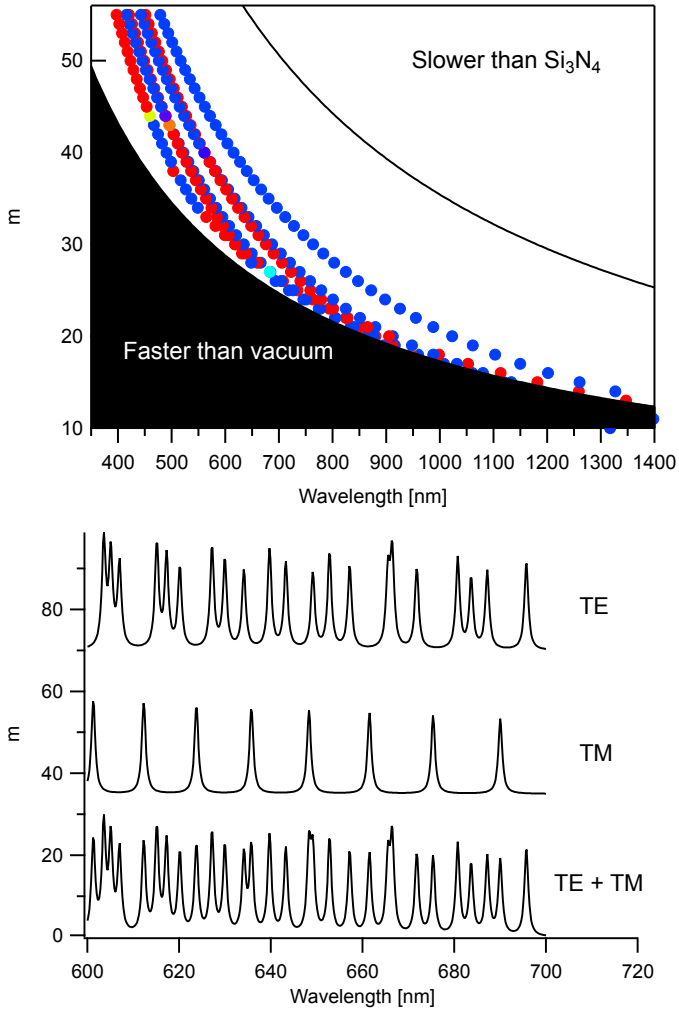

Figure 7.5: (a) Dispersion diagram for a 5.5 μm microdisk depicting the azimuthal mode number m versus the free space wavelength for six modes, as calculated using COMSOL. Blue dots are TE modes, red dots are TM modes. (b) Microdisk emission spectrum, simulated using COMSOL for the TE modes (top), the TM modes (middle) and both polarizations together (bottom). The peaks were artificially broadened with 1 nm FWHM Lorentzian lineshape.

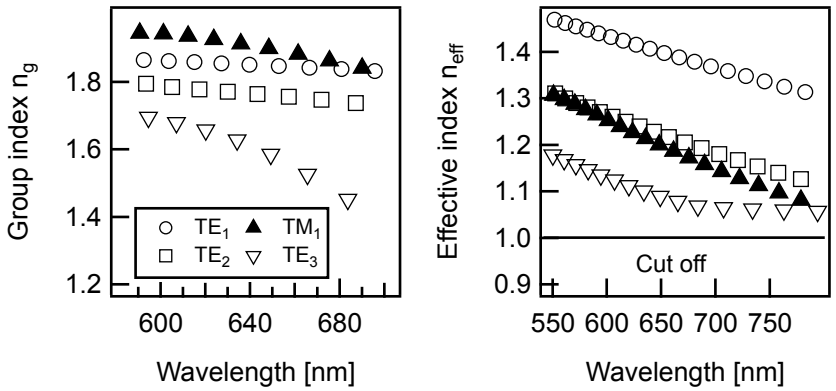

Figure 7.6: (a) Group index n_g and (b) effective index n_{eff} for a 5.5 μm microdisk for the first four modes

excitons per QD:

$$\begin{aligned}\frac{dN}{dt} &= -\frac{N}{\tau_{PL}} - \frac{(N-1)}{\tau_{PL}}\phi - \frac{C_A}{V_{QD}^2}N^3 + \sigma_P\phi_P \\ &= -\frac{N}{\tau_{PL}} - \frac{(N-1)}{\tau_{PL}}\phi - \frac{3\gamma}{4\pi V_{QD}}N^3 + \sigma_P\phi_P \\ &= -\frac{N}{\tau_{PL}} - \frac{(N-1)}{\tau_{PL}}\phi - \frac{N^3}{8\tau_{A,2}} + \sigma_P\phi_P \end{aligned} \tag{7.8}$$

is caused by spontaneous emission, stimulated emission and absorption, non-radiative decay through Auger recombination and the creation of excitons by the pump laser respectively. Here we have used Equation 3.21 for the Auger rate of colloidal QDs. τ_{PL} is the spontaneous emission rate into the cavity mode [1], C_A is the Auger constant, V_{QD} is the QD volume, σ_P is the absorption cross section at the pump wavelength, γ is the QD Auger constants (see Eq. 3.20) and $\tau_{A,2}$ is the biexciton lifetime.

This rate equation for N is coupled with the rate of change of the number of photons in a particular cavity mode ϕ:

$$\frac{d\phi}{dt} = N_{QD}\beta\frac{N}{\tau_{PL}} + N_{QD}\frac{N-1}{\tau_{PL}}\phi - \frac{\phi}{\tau_{cav}} \tag{7.9}$$

through spontaneous emission (with the spontaneous emission coupling factor β), stimulated emission and absorption, and loss of photons from

[1] which can be different from the free space rate because of the Purcell Effect

the cavity (see Equation 7.2) respectively. Here, N_{QD} is the number of QDs, for which the emission dipole is coupled to the cavity mode. Note that because of the inhomogeneous broadening typically only a subset of all QDs will be coupled.

7.3.2 Pulsed Excitation

We solve the coupled rate equations 7.8-7.9 numerically. We look at the case of pulsed excitation with a femtosecond pulsed laser. We assume that the pulse duration is much smaller than the cavity dynamics. The pump pulse is therefore modelled as an initial exciton number N_0. We further assume the cavity to be empty upon arrival of pump pulse (i.e. $\phi_0 = 0$). The values for the parameters we used in each sweep are summarized in Table 7.1. The values for τ_{PL} and $\tau_{A,2}$ were measured experimentally for CdSe/CdSe dot-in-rods. N_{QD} was estimated from the QD layer thickness in the microdisk, using a size broadening of 5% and a linewidth related to τ_{cav}. The value for N_0 were typical experimental conditions as reported in Section 8.3.3.

Sweep of	τ_{PL} [ns]	$\tau_{A,2}$ [ns]	$\sigma_P\phi_P$ [ns^{-1}]	N_{QD}	τ_{cav} [ns]	β	N_0
N_{QD}	3	0.1	0	-	0.001	1	3.4
τ_{PL}	-	0.1	0	4000	0.001	1	3.4
τ_{PL}, N_{QD}	-	0.1	0	-	0.001	1	3.4
τ_{cav}	3	0.1	0	4000	-	1	3.4
τ_A	3	-	0	4000	0.001	1	3.4
N_0	3	0.1	0	4000	0.001	1	-
β	3	0.1	0	4000	0.001	-	3.4

Table 7.1: Parameters used in the different rate equation simulation sweeps.

In Figure 7.7 we show the amount of photons ϕ in a cavity mode as a function of time for different QD loading conditions. If only 1000 QDs emit into the cavity mode, not enough photons enter the cavity for stimulated emission to become the dominant decay process. In other words, lasing does not occur. The dynamics are governed by Auger recombination and spontaneous emission. When we double the amount of coupled QDs, the number of photons in the cavity goes up by two orders of magnitude and a burst of laser light exits the cavity with a pulse width of ~ 30 ps. Stimu-

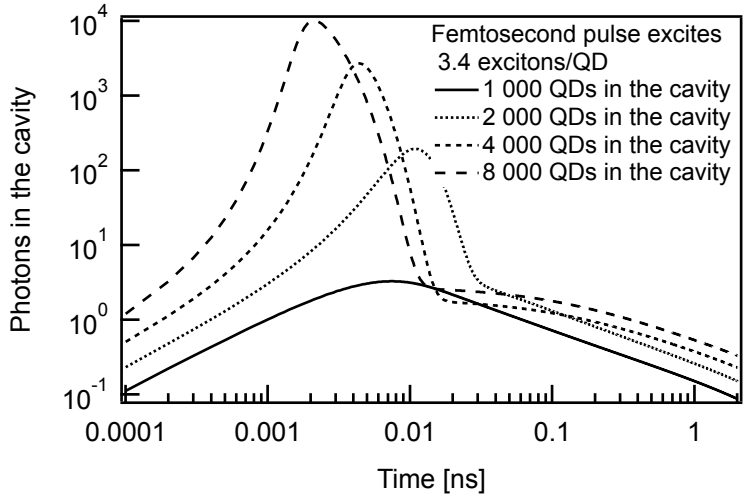

Figure 7.7: Number of photons ϕ in a certain cavity mode as a function of time for different values of the amount coupled QDs N_{QD} shows that there is a clear threshold QD loading in order for lasing to occur.

lated emission during this burst depletes the amount of excitons per QD N. When N drops below 1, lasing action stops and the dynamics 30 ps after the pump pulse are governed again by Auger recombination and spontaneous emission. Further increasing the QD loading results in shorter pulses with higher peak energy.

Increasing N_{QD} increases the modal gain (see Equation 7.9 on p 171). Similarly, we can increase the modal gain by lowering the radiative lifetime τ_{PL}. This effect is shown in the bottom graph of Figure 7.8. For long radiative lifetimes, the modal gain becomes to low to overcome cavity losses and no laser pulse is observed.

In the top graph of Figure 7.8 we keep the modal gain constant (i.e. ratio $N_{QD}/\tau_{PL} = \mathrm{cst}$), while increasing τ_{PL}. This comes down to decreasing the gain per QD. This is relevant, since spherical QDs have different absorption and gain cross sections than QRods. Moreover, QRods have anisotropic cross sections, which means that control over the QRod orientation within the cavity will change the modal gain of the cavity[6]. Decreasing the QD gain, while keeping the modal gain constant results in a higher peak energy and larger pulse width. A smaller gain cross section depletes the number of excitons N in a QD less fast. Hence, more photons are needed in the cavity to lower N below 1.

The influence of the photon cavity lifetime is shown in Figure 7.9.

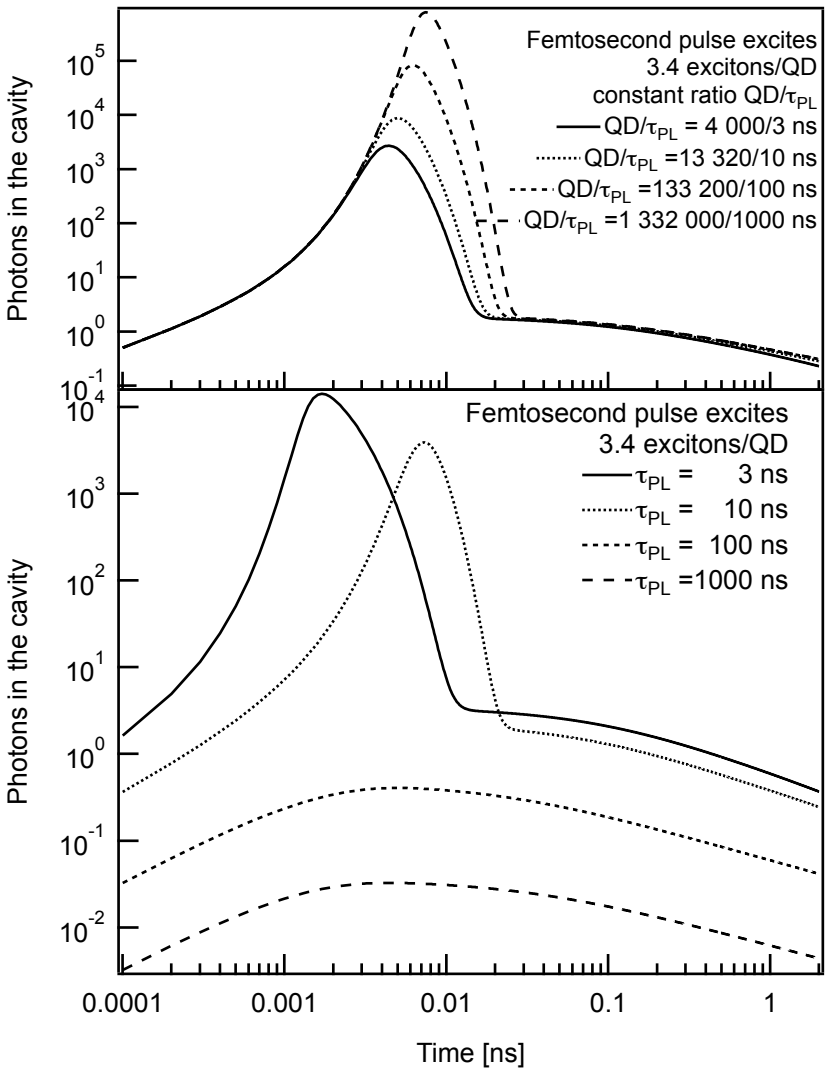

Figure 7.8: (top) Number of photons ϕ in a certain cavity mode as a function of time for different values of the amount coupled QDs N_{QD} shows that there is a clear threshold QD loading in order for lasing to occur.(bottom

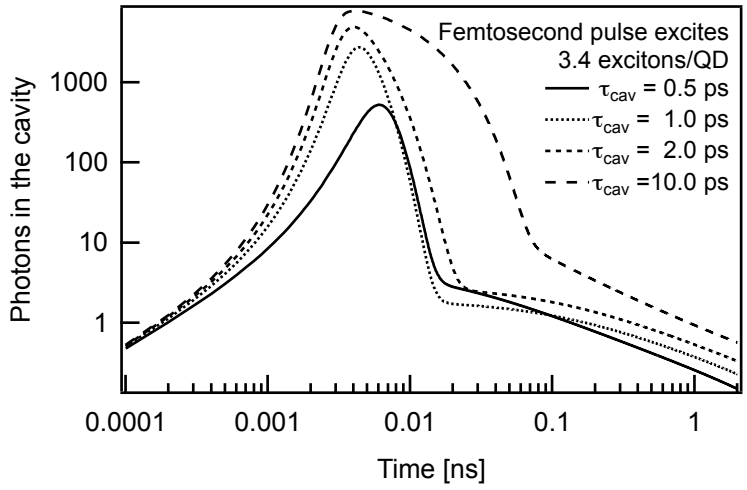

Figure 7.9: Number of photons ϕ in a certain cavity mode as a function of time for different values of the photon cavity lifetime τ_{cav} shows that the laser pulse duration in the cavity is directly determined by τ_{cav}.

While the laser build-up time becomes limited by the stimulated emission rate, the width of the resulting laser pulse is directly proportional to the photon cavity lifetime and to the Q-factor (see Section 7.2.1 on p 160).

While a reduction of the Auger recombination rate has received a lot of attention in literature, we show in Figure 7.10 that the laser pulse is marginally influenced by an order of magnitude change in the biexciton lifetime $\tau_{A,2}$. The peak energy increases slightly. The peak width is unaltered. This result is to be expected, since the presence of lasing implies that the principal loss mechanism of excitons in the QDs is through stimulated emission, and not through Auger recombination. Hence, we can conclude that the Auger rate is not the limiting factor for achieving pulsed laser operation of QD loaded microdisks. We stress that the Auger rate does have implications for CW operation of QD loaded lasers though.

The influence of the spontaneous emission coupling factor β is obvious in Figure 7.11. With a higher β more spontaneously emitted photons are fed into the cavity mode to jump start the stimulated emission and lasing. Therefore the build-up time becomes progressively shorter, combined with a slightly higher peak photon flux. Even when only 1% of the spontaneous emission goes into the cavity mode, lasing is still possible.

Finally, we present a sweep of the pump energy in Figure 7.12. The top graph shows the photon transient for different initial number of excitons

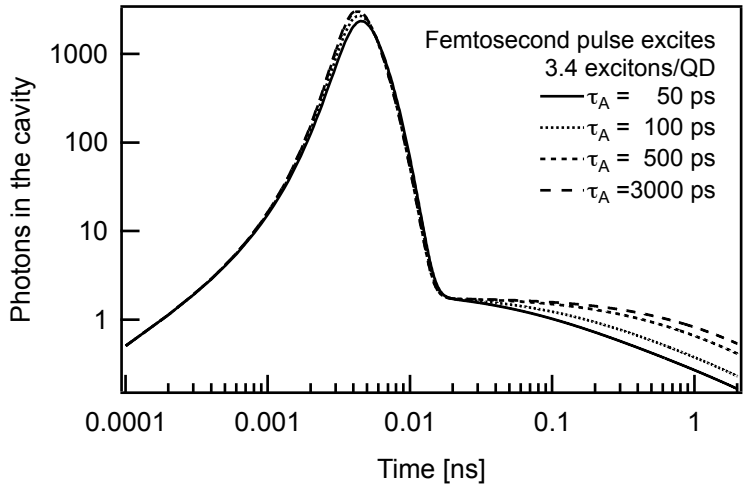

Figure 7.10: Number of photons ϕ in a certain cavity mode as a function of time for different values of the biexciton lifetime $\tau_{A,2}$ shows that the laser pulse is marginally influenced $\tau_{A,2}$.

N_0. We observe a clear threshold around $N_0 = 2$. Integration of the transients over the top graph gives the total number of photons emitted in the simulation time window (see bottom graph of Figure 7.12). It shows the characteristic change in slope of energy-out-vs-energy-in for lasing. The threshold is clearly distinguishable, despite the spontaneous emission coupling factor β being equal to 1. In high-beta lasers, the threshold is usually barely visible[7]. Here, however, the dominant non-radiative loss through Auger recombination results nonetheless in a threshold behaviour.

7.3.3 CW excitation

Under continuous wave (CW) excitation, Equations 7.8-7.9 reduce to a coupled set of stationary equations. An analytical solution is possible, yet complicated because of the cubic dependence of the Auger rate on the number of excitons N. We therefore solve the equation numerically to identify the right parameters to obtain CW lasing.

Figure 7.13 shows the number of photons in the cavity as a function of the pump power, expressed in number of excitons created per nanosecond for different QD cavity loading N_{QD}. Note that the pump rate depends on the laser photon flux and the absorption cross section of the QDs, which in turn depends on the size and shape of the particular nanocrystals. For

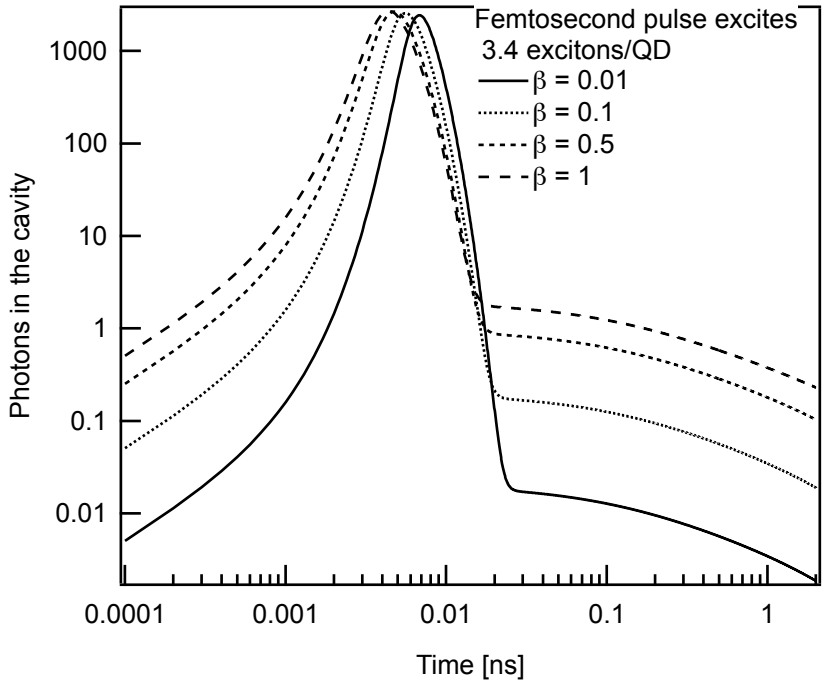

Figure 7.11: Number of photons ϕ in a certain cavity mode as a function of time for different values of the spontaneous emission coupling factor $beta$ shows that the laser pulse builds up faster for increasing β.

CW param.	τ_{PL} [ns]	$\tau_{A,2}$ [ns]	N_{QD}	τ_{cav} [ns]	β
	3	0.1	100 000	0.001	1

Table 7.2: Parameters used in the CW simulations, unless mentioned otherwise in the graphs.

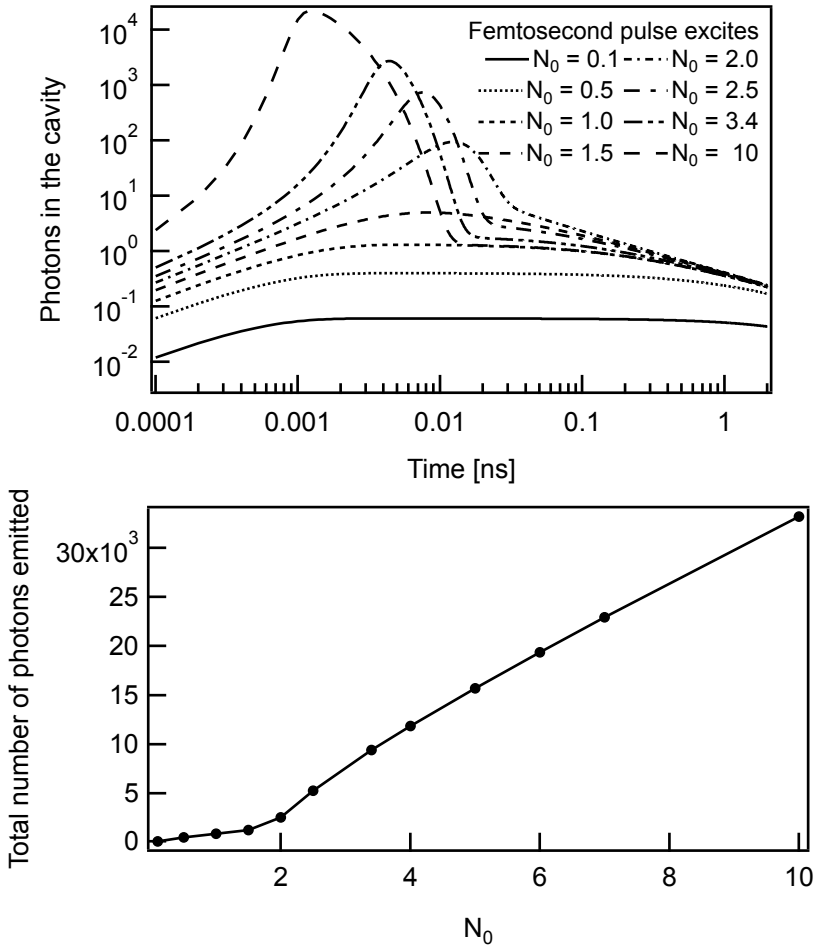

Figure 7.12: (top) Number of photons ϕ in a certain cavity mode as a function of time for different values of the initial exciton population N_0 shows a clear threshold for laser operation. (bottom) The total number of photons emitted in the 2 ns simulation window shows the typical lasing threshold.

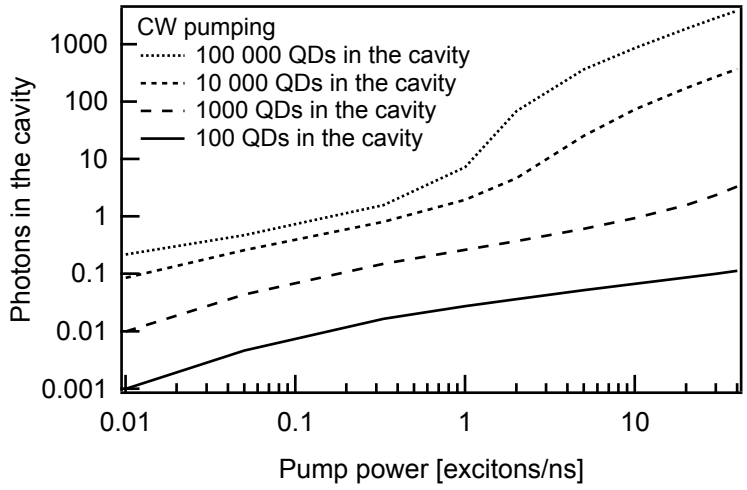

Figure 7.13: Log-log plot of the number of photons ϕ in the cavity as a function of the amount of excitons created per nanosecond by a CW pump laser for four different amounts of QDs coupled to a cavity mode.

very low QD loading, ϕ increases linearly at low pump power and eventually saturates at high power, always staying below the threshold for lasing. For $N_{QD} = 10000$, a sublinear increase is observed below threshold. Around the threshold of 2 excitons/ns, ϕ starts to increase superlinearly and again saturates at higher powers when maximum gain is reached. The $(log(\phi), log(P))$-curve for 100 000 QDs coupled to the cavity mode shows the typical S shape for a laser, with threshold between $0.3-0.4$ excitons/ns.

The influence of the Q-factor and the photon cavity lifetime τ_{cav} on the laser performance is shown in Figure 7.14.a. As we increase τ_{cav} from 1 ps to 10 ps, the amount of photons in the cavity above threshold go up by a factor of ten.

The main influence on the lasing threshold is the reduction of the non-radiative losses in the QDs through Auger recombination. The effect is shown in Figure 7.14.b. The threshold decreases from 1 excitons/ns to 0.1 exciton/ns as the biexciton lifetime increases from 100 ps to 1 ns. Note that in this simulation, we have set $\beta = 0.5$ to keep a clear threshold in the $(log(\phi), log(P))$-curve.

To compare the performance of cadmium chalcogenides, with a typical radiative lifetime in the nanosecond range, with lead chalcogenides, with τ_{PL} in the μs range, the effect on the threshold is shown in Figure 7.14.c.

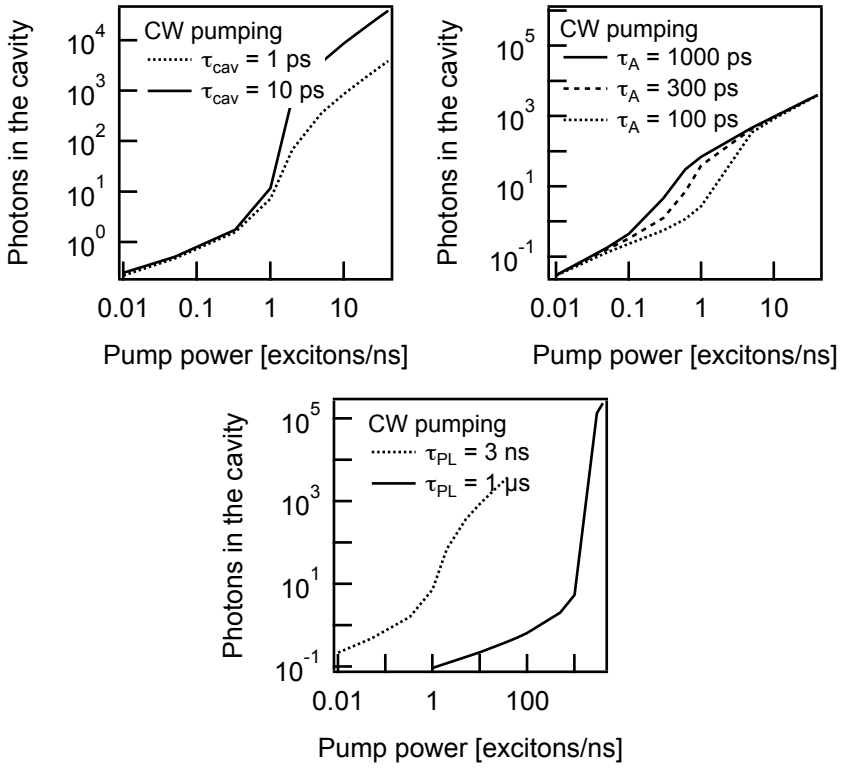

Figure 7.14: Log-log plot of the amount of photons in the cavity as a function of pump power for (a) two different photon cavity lifetimes, (b) three different biexciton lifetimes (note:$\beta = 0.5$), and (c) the spontaneous emission lifetime.

For the lead chalcogenides, the threshold would be about 1000$\times$ higher, close to 1000 excitons/ns, making CW lasing impossible without a significant reduction of the Auger recombination rate.

References

[1] Bienstman, P. Ph.D. thesis, Universiteit Gent, 2001.

[2] Bass, M.; DeCusatis, C.; Li, G.; Mahajan, V.; Enoch, J.; Van Stryland, E. *Handbook of Optics: Optical properties of materials, nonlinear optics, quantum optics*; McGraw-Hill Professional, 2009; Vol. 4.

[3] Oskooi, A. F.; Roundy, D.; Ibanescu, M.; Bermel, P.; Joannopoulos, J. D.; Johnson, S. G. MEEP: A flexible free-software package for electromagnetic simulations by the FDTD method. *Computer Physics Communications* **2010**, *181*, 687–702.

[4] Oxborrow, M. How to simulate the whispering-gallery modes of dielectric microresonators in FEMLAB/COMSOL. *Proc. SPIE*, 2007.

[5] Svelto, O. *Principles of Lasers*; Springer, 2009.

[6] Kamal, J. S.; Gomes, R.; Hens, Z.; Karvar, M.; Neyts, K.; Compernolle, S.; Vanhaecke, F. Direct determination of absorption anisotropy in colloidal quantum rods. *Phys. Rev. B* **2012**, *85*, 035126.

[7] Yokoyama, H.; Brorson, S. Rate-equation analysis of microcavity lasers. *Journal of Applied Physics* **1989**, *66*, 4801–4805.

8

Experimental Study of Optical Interaction of Colloidal QDs and Photonic Resonators

8.1 Literature Review of colloidal QDs coupled to microcavities

From the very start of colloidal QD research, the tunability of the emission wavelength, the high quantum yield and the solution processability sparked the interest of using colloidal QDs as novel gain media for integrated photonics. Several authors have reported on the coupling of QD emission to optical microcavities.[1–15]

Artemyev et al.[16] put ZnS-coated CdSe QDs on a glass microsphere and showed coupling of the QD emission to the optical modes in the microsphere. This was used to illustrate the Purcell effect with colloidal QDs. This was optimized by Snee et al.[17], who showed lasing using these QD-microsphere composites. Eisler et al.[4] embedded QDs ZnS-coated CdSe QDs in a titania-matrix and spincoated this solution onto a Bragg grating in SiO_2. Under femtosecond pulsed excitation, they demonstrated lasing at 80 K and room temperature. Min et al.[11] reported the first QDs coupled to a toroidal microcavity on a chip. Using a tapered fiber setup, they claim lasing, although the data shown is not convincing. Kazes et al.[18] dipped a

glass microcapillary into a solution of CdSe/ZnS QRods and showed polarized lasing under pulsed excitation. Hoogland et al. [1] used a similar configuration using near-infrared emitting PbSe QDs to show lasing at 1530 nm operating at 80 K. Wu et al. [19] was able to couple the emission of PbSe QDs to a silicon photonic crystal cavity, however without lasing. Schaefer et al. [9] managed to optically trap a QD solution droplet and make it lase under pulsed excitation. Finally, Zavelani-Rossi et al. [20] showed pulsed lasing from CdSe/CdS dot-in-rods, using a self-assembled *coffee stain* laser.

Most the QDs are neither embedded into the resonator material closest to the whispering gallery modes (WGM), nor does the technology provide the possibility of coupling to other integrated optical components. We report on the fabrication of free-standing and optically active microdisks with QDs embedded directly into Si_3N_4. We show that the process optimization results in low-loss silicon nitride microdisks. The Si_3N_4 matrix provides the stability necessary to preserve the optical properties of the QDs and observe efficient coupling of the photoluminescence (PL) to the resonating microdisk modes.

8.2 Fabrication

In Section 8.2.1 we give an overview of the fabrication flow and parameters used to fabricate the Si_3N_4 microdisks with embedded colloidal QDs. We comment on failed fabrication flows and possible improvements for future fabrication runs.

In subsequent sections we discuss certain fabrication steps in greater detail and comment on the optimizations that were performed.

8.2.1 Fabrication Flow

Standard Method

After optimization of the individual steps, a standard fabrication flow (see Figure 8.1) was set for all samples:

1. **Deposition of high-index Si_3N_4**: A 70-90 nm layer was deposited on a clean silicon substrate using PECVD at 300 °C (see Section 8.2.2 on p. 188).

2. **UV photolithography**: Immediately after Si_3N_4 deposition, *AZ5214E* photoresist was deposited by spincoating at 3000 rpm, followed by a

pre-bake at 90°C for 90 s. Next, a mask with microdisks is illuminated onto the sample for 18 s and developed in AZ100 developer in water (1:3).

3. **Dry etch**: Using RIE (see Section 8.2.3 on p. 191), the pattern in the photoresist is etched into the Si_3N_4 layer. The etching gases were optimized for the lowest sidewall roughness. A 30/30 sccm CF_4/O_2 mixture was used at 40 mTorr pressure and 50 W RF power. The etch mixture is selective and stops at the silicon substrate. At a 130 nm/min etch rate, the RIE is stopped after one minute.

4. **Wet etch**: Wet etching using KOH (see Section 8.2.4 on p. 193) is used to selectively etch the silicon substrate and obtain a free-hanging microdisk supported by a silicon pillar. 30 g of KOH is mixed with 120 ml deionized water and heated to 60 °C. The etch rate is approximately 500 nm/min, but is monitored each time with a microscope to obtain the correct pillar size for the required microdisk diameter.

5. **QD spincoating**: Spincoating was used to obtain a monolayer or up to layers several tens of nms thick of colloidal QDs. Spinning is done at 2000 rpm for 40 s, typically with a 0.1% volume fraction of QDs in toluene (see Section 8.2.5 on p. 195).

6. **Deposition of low-index Si_3N_4**: A final layer of 70-80 nm Si_3N_4 was deposited using PECVD at 120 °C .

Failed method

While the previous fabrication method yields good results, it inherently has the drawback that part of the collected emission comes from QDs on the substrate, and hence is not coupled to the microdisk. For this reason, another method was tested, in which all deposition (step 1, 5 and 6) was carried out first, followed by lithography (step 2), dry etching (step 3) and wet etching (step 3). This way, all QDs outside of the microdisk are removed by dry etching.

While ideal in theory, the method fails in the wet etching step. KOH not only etches silicon, but also the QDs themselves. While KOH is not a known etchant for CdX or PbX (X=S, Se, Te)[21], the evidence of etching is clear from SEM (see Figure 8.2).

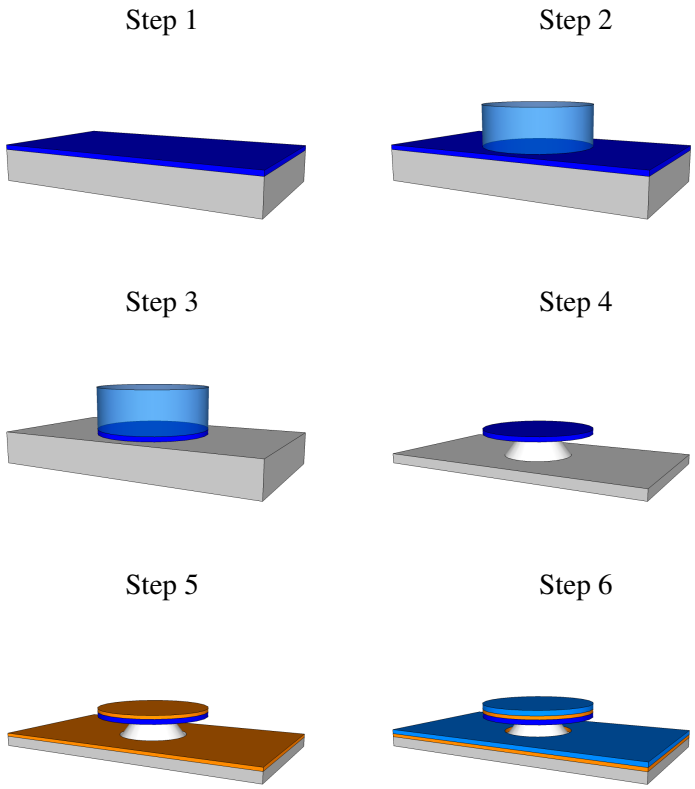

Figure 8.1: Illustration of the standard fabrication steps: 1) Si_3N_4 deposition 2) lithography 3) RIE dry etch 4) KOH wet etch 5) QD spincoating 6) Si_3N_4 deposition

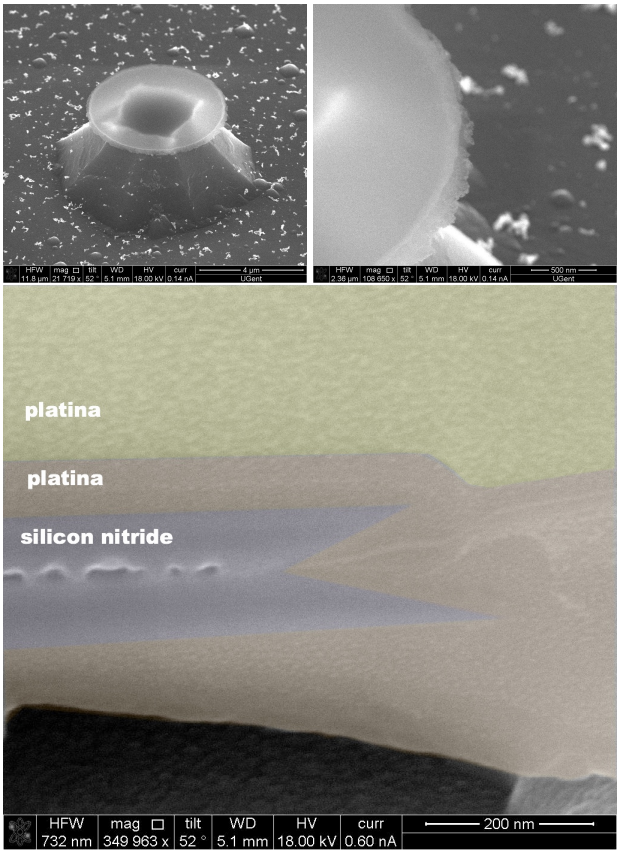

Figure 8.2: (a) Microdisk etched after QD and low-index Si_3N_4 deposition shows a diffuse edge, eaten away by KOH. (b) The brittle edge is clearer at higher magnification (c) A cross section of the microdisk shows that the QDs and part of Si_3N_4 has been etched away by KOH. Deeper in the layer voids are visible where QDs were etched away.

8.2.2 Deposition of Silicon Nitride

The material

Silicon nitride is a chemical compound containing silicon and nitrogen. Although the composition depends strongly on the deposition technique[22], the most stable form is Si_3N_4. It's a hard ceramic with low coefficient of thermal expansion and high fracture strength. Its ability to withstand high temperatures therefore makes it ideally suited as a passive laser cavity material.

In its stoichiometric form, it is also an excellent electrical insulator (resistivity $10^6 - 10^{15}\Omega$ cm and dielectric strength 1 to 5 MV/cm[23]). It is therefore heavily used in the microelectronics industry as a passivation layer.

As a chemical insulator it is also preferred over silicon dioxide to protect certain materials from degradation through diffusion of water molecules and sodium ions.

As an optical material, it combines high refractive index ($n \simeq 2.0$) with transparency in the visible to mid-infrared region, due to its large band gap[22] ($\sim 4 - 5$ eV).

Silicon nitride is therefore a perfect matrix material for colloidal quantum dots. The high band gap provides passivation and long term optical stability under illumination. Moreover, the nitride forms a chemical barrier for oxidation of the quantum dots.

Plasma-Enhanced Chemical Vapor Deposition of Si_3N_4

Chemical Vapour Deposition (CVD) is a deposition technique for thin films, whereby a mixture of volatile and reactive gases undergo a chemical reaction at the substrate surface to form the thin film. Si_3N_4 can be deposited using either low pressure CVD (LPCVD) or plasma enhanced CVD (PECVD). The latter increases the reactivity of the gases by forming a plasma. Subsequently, the process can be carried out at lower temperatures, between 100 °C and 300 °C, compared to LPCVD, and is therefore preferred for making hybrid QD-Si_3N_4 films.

During PECVD, a radiofrequent (RF) source creates a nitrogen plasma. A preset mixture of silane (SiH_4) and ammonia (NH_3) is pumped into the chamber right above the sample. Subsequently, the following reaction takes place:

$$3\mathrm{SiH_4}(g) + 4\mathrm{NH_3}(g) \rightarrow \mathrm{Si_3N_4}(s) + 12\mathrm{H_2}(g)$$

However, the ratio of the flow rates, the RF power, and addition of hydrogen gas will change the exact content of the deposited layer. In general,

a-$Si_xN_yH_z$ is formed. The content of the layers made in this work was not further investigated.

LF power	W	50
RF power	W	30
pressure	mTorr	810
SiH_4	sccm	31
NH_3	sccm	28
N_2	sccm	1500

Table 8.1: PE-CVD parameters for Si_3N_4

The PECVD parameters used to deposit Si_3N_4 in this work are summarized in Table 8.1. The substrate temperature influences the density of the Si_3N_4 film. Hence, keeping the flow rates constant, the deposition rate decreases with increasing substrate temperature (see Figure 8.3).

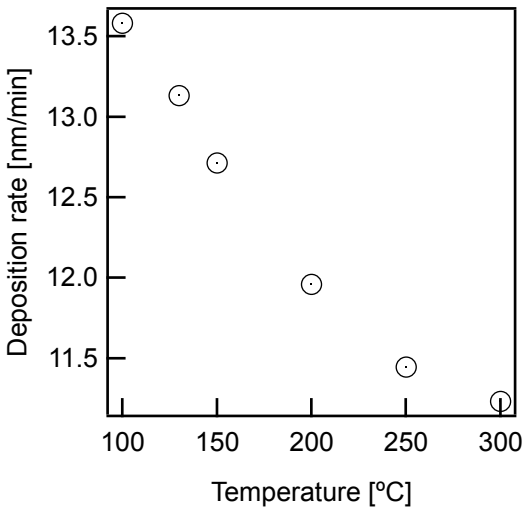

Figure 8.3: The rate of deposition of Si_3N_4 in PE-CVD for different substrate temperatures.

Optical and Electrical Properties

The refractive index of the silicon nitride can be tuned by varying the temperature of the substrate during deposition. The Cauchy coefficients for

Temperature [°C]	100	130	150
A	1.796	1.813	1.836
B	0.0178	0.01972	0.02116
C	0.00046113	0.00040571	0.00038368
Temperature [°C]	200	250	300
A	1.878	1.927	1.968
B	0.02409	0.02704	0.0308
C	0.00034454	0.00035629	0.00029276

Table 8.2: Cauchy coefficients for Si_3N_4 at different deposition temperatures

each temperature are extracted from a fit to the ellipsometry data (see Table 8.2. The Cauchy dispersion law, defined as:

$$n(\lambda) = A + \frac{B}{\lambda^2} + \frac{C}{\lambda^4}$$

is plotted in Figure 8.4.a for different temperatures. For a given wavelength, the refractive index can be changed linearly with substrate temperature (see Figure 8.4.b). For all wavelengths, the refractive index goes up by 10^{-3} refractive index units per degree Celsius.

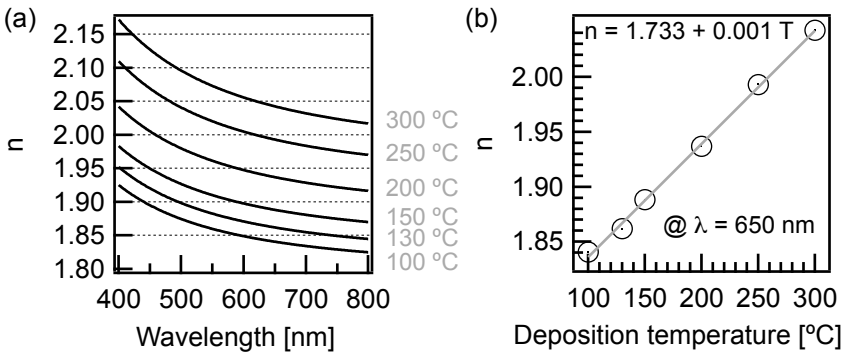

Figure 8.4: (a) Cauchy Dispersion Law for Si_3N_4 deposited at different substrate temperatures. (b) Linear increase in the refractive index as a function of substrate temperature.

8.2.3 Reactive Ion Etching of Si_3N_4

8.2.3.1 Reactive Ion Etching

In a reactive ion etching (RIE) machine, a plasma is created by applying an RF field between two parallel plates. A mixture of reactive gases is added to the low-pressure chamber. The gas becomes ionized in the plasma and a subsequent buildup of charge on the bottom wafer plate creates a field in which the ions in the plasma drift towards the wafer or sample. At the sample surface, the active ions chemically react with the surface atoms, as well as physically etch by transfer of their kinetic energy to the surface atoms. The balance between both processes will determine the etch profile, ranging from isotropic (chemical etching) to fully anisotropic (physical etching). To etch waveguides and microdisks, typically a vertical profile is preferred.

Optimization of the gas mixture

Typical etch gases for silicon and silicon nitride contain fluor, like CF_4 and SF_6[24], where F-radicals and ions react chemically with silicon to form SiF_4. While small amounts of O_2 tends to increase the etch rate because of higher F density, at higher O_2 levels a protective SiO_2 layer forms which slows down Si etching and increases selectivity between Si and Si_3N_4.

A few tests were done to optimize the gas mixture. Figure 8.5 shows three different etch results using a mixture of SF_6:O_2. At a ratio of 50:3 sccm, a clear undulating roughness is visible in the SEM micrograph. This type of etch profile, with evidence of isotropic etching in each of the undulations, is typical for chemical etching by SF_6[24]. The second micrograph, with gas ratios of 30:30 sccm, has a straight etch profile with much reduced edge roughness. In this regime, the physical bombardement with oxygen ions and radicals balances out the chemical etching by SF_6, an ideal regime known as synergetic etching. Finally, the third micrograph shows a sample etched with 5:30 sccm ratio. The etch profile is sloped, indicative of physical etching by oxygen[24].

A similar optimization run was done using CF_4:O_2. Again similar flow rates for both gases yield the ideal synergetic etching regime. Figure 8.6 shows an SEM micrograph of an etch result using the ideal 30:30 sccm gas ratio. The etch profile is vertical and edge roughness is even lower than using SF_6

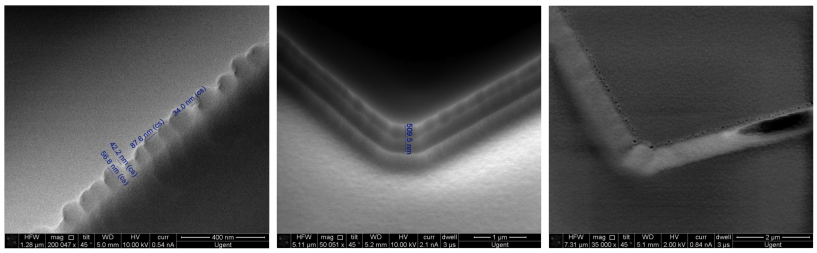

(a) (b) (c)

Figure 8.5: RIE of 80 nm of Si_3N_4 on top of a silicon substrate. From left to right, the gas mixture is changed: SF_6:O_2 (a) 50:3 sccm (b) 30:30 sccm (c) 5:30 sccm. The etching mechanism goes from chemical, over synergetic to full physical etching.

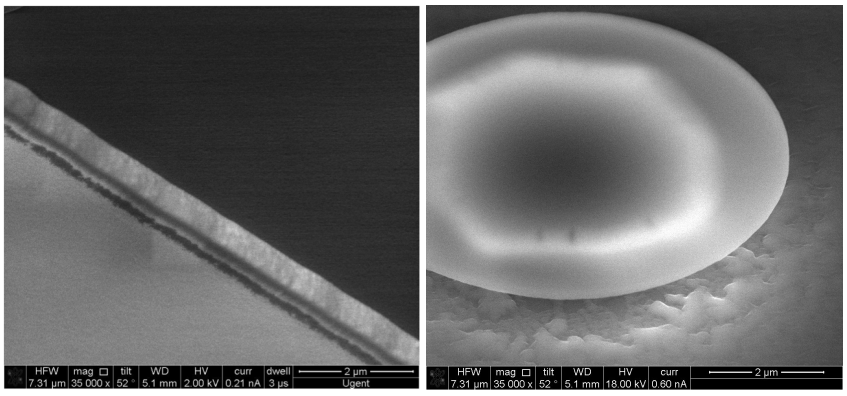

(a) (b)

Figure 8.6: (a) RIE of 80 nm of Si_3N_4 on top of a silicon substrate using CF_4:O_2 30:30 sccm. (b) A finished microdisk shows the smooth edge of the disk when using this gas ratio.

Standard process

After optimization, etching was done using the parameters summarized in Table 8.3. The etch rate is about 130 nm/min.

RF	W	150
pressure	mTorr	40
CF_4	sccm	30
O_2	sccm	30

Table 8.3: RIE parameters used for etching of Si_3N_4.

8.2.4 Selective wet etching of silicon using KOH

Silicon wet etching using KOH

Potassium hydroxide (KOH) is a selective, anisotropic wet etchant. Selectivity between Si_3N_4 and silicon is about 500. Moreover, KOH dissolved in water does not etch along the $< 111 >$ direction of silicon. Hence using a Si_3N_4 mask on top of $< 100 >$ silicon substrate, an etch profile 54.74° will form, i.e. the 111 plane.

The etch rates for other planes besides the 111 plane are equal. Therefore, the microdisk shaped layer of Si_3N_4 on top of the silicon substrate will be underetched significantly. The distance of the pillar from the microdisk edge is approximately equal to the distance from the microdisk to the substrate. This ratio can be tuned by adding isopropyl alcohol to the solution[25], which will result in less undercut for similar etch depths.

Pillar shape

A variety of shapes can form during etching, going from eight faces for large pillars to four faces for the smallest pillars, with a 54.74° angle for the 111 and a 45° angle for the 110 planes. We note that in theory this etching should be uniform, while in practice pillars can be off-center and have more irregular shapes. Figure 8.7 shows some common shapes, angles and locations of the pillar etched using KOH.

The pillar shape is important for multiple reasons. It should be far enough away from the disk edge to allow WGM, yet it can also act as a suppressor for higher radial order modes. Lastly, it should be large enough to provide adequate support for the microdisk.

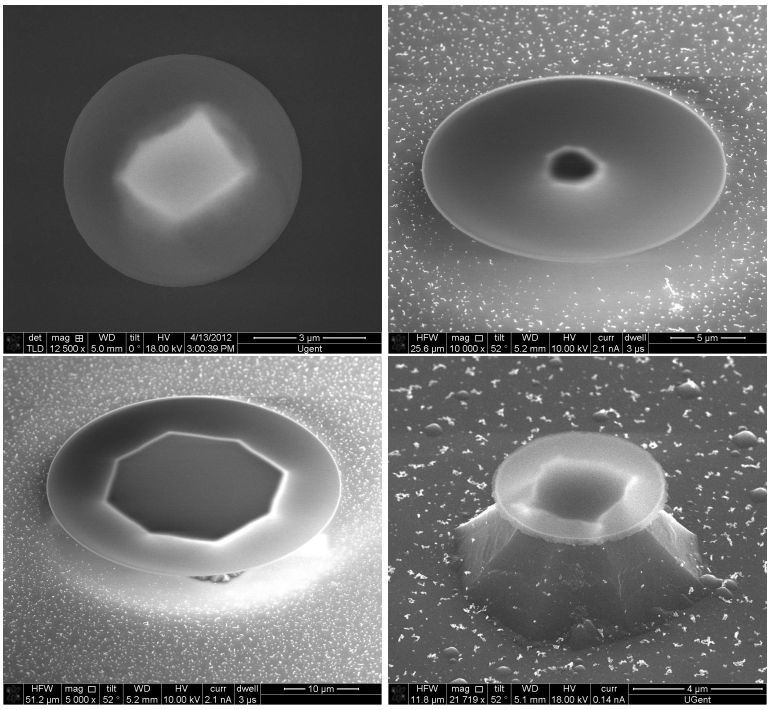

Figure 8.7: Common pillar shapes from KOH wet etching.

8.2.5 Spin coating of colloidal QDs

QD deposition

Different techniques for depositing colloidal QDs exist. For one to five layers, the langmuir-blodgett technique[26–28] is often preferred, with the advantage of forming perfectly packed layers and having precise control over the number of layers. The drawback is the complexity and time needed for deposition. For thick layers, dropcasting[29] can be used. However, drying typically induces cracks in dropcasted layers. Therefore, while being simple, fast and economic on QD usage, it is not preferred for optical applications, where the layer morphology is important. Spincoating[29] delivers the appropriate thickness and morphology, and is simple and fast. The drawback is that a large percentage of the material is lost during deposition, although this loss can be reduced significantly by choosing a small enough droplet of the QD solution, just large enough to cover the active area of the chip.

Spin coating

Spin coating is the technique whereby a suspension is deposited on a substrate. Before the suspension evaporates, the substrate is rotated at high speed. The centrifugal forces, balanced by the surface tension of the suspension create a certain thickness of the suspension. During the rotation the solvent evaporates and a solid film is deposited. The thickness of this final film h depends on the rotation speed Ω, the volume fraction f of solid material in the suspension before spin coating, the viscosity v and the diffusivity D[30]:

$$h[nm] = Af\frac{\sqrt[4]{vD}}{\sqrt{\Omega}} \tag{8.1}$$

where A is a proportionality constant.

In this work, we keep the solvent (toluene) and the spin speed (2000 rpm) constant. The only variables are the QD volume fraction and the QD shape. We assume the volume fraction to be low enough not to influence the viscosity of the suspension significantly. Figure 8.8 shows a plot of the thickness of a layer of spin coated QRods (4.5 nm by 22.3 nm) as a function of the volume fraction. The thickness increases linearly with increasing volume fraction of the QRod suspension as expected from Equation 8.1:

$$h = 45580f$$

A SEM micrograph of the surface morphology is shown in Figure 8.9. The left image shows the local structuring of the QRods in the layer. For

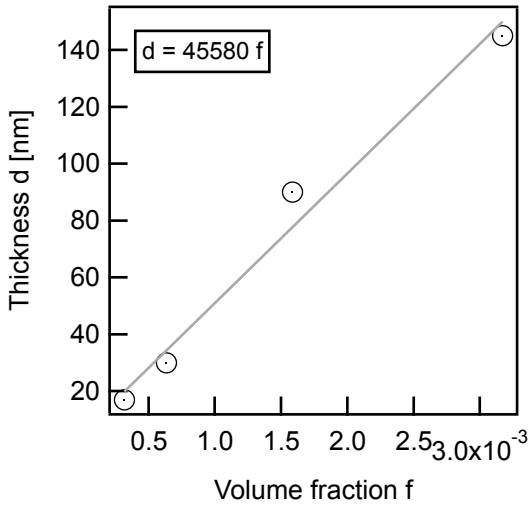

Figure 8.8: Thickness as measured using AFM for a spincoated suspension of QRods (4.5 nm by 22.3 nm) in toluene increases linearly with increasing volume fraction of the QRods.

AFM, a cut is made in the layer using a doctor blade. This is shown on the right. It shows the thickness and surface morphology of the layer.

8.2.6 SEM imaging

Real versus designed diameter

In designing the microdisks, one has to account for a discrepancy between the designed diameter on the lithographic mask and the actual diameter of the fabricated microdisk. The actual diameter, measured using SEM (see Figure 8.10), is 0.5 μm larger than the designed diameter of 6.0 μm . This is caused more than likely by overexposure and other lithographic aberrations.

Problems with layer adhesion

Using SEM imaging, it became clear that there is a problem of adhesion between the low-index Si_3N_4 layer and the QD layer beneath it. A difference in thermal expansion coefficient between both layers can induce stress and result in an inflated microdisk, during SEM, as evidenced from Figure 8.11.

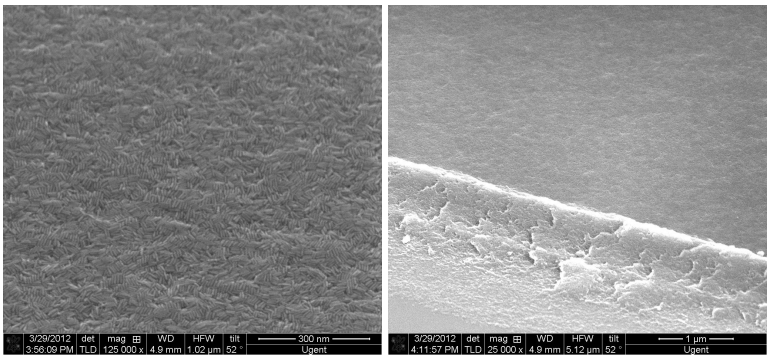

Figure 8.9: SEM of a spincoated layer of QRods (4.5 nm by 22.3 nm) of 28 nm thickness. The image on the left shows the morphology and local structuring of the rods in the spincoated layer. The right image shows the cut in the layer made using a doctor blade to measure the thickness using AFM. It shows the smoothness of the layer.

Likely, this will present a problem for high-flux optical pumping and laser operation of the microdisks as well.

Perceived QD layer thickness

In a cross section view using SEM (see Figure 8.12), it is hard to identify the QD layer and estimate the layer thickness. FIB, used to make the cross section, is known to melt and anneal the QD layer, which can result in a 60 to 80% reduction of the layer thickness.

However, due to the standard fabrication method (see Section 8.2.1 on p. 184), the spin coating could be non-uniform due to the microdisk structures on the sample. A back-of-the-envelope calculation makes this unlikely. A 0.1% volume fraction suspension yields a closest-packed film (volume fraction 74%) with a layer thickness of 50 nm. This means that the film of suspension that forms, when the spin coater starts turning (i.e. before evaporation), will have an estimated thickness:

$$h_{susp} = \frac{0.74}{0.001} h_{solid} \simeq 37.5 \mu m$$

Therefore, the height of the microdisk (between 1 μm and 2 μm) is only a small perturbation and should not alter the thickness by much.

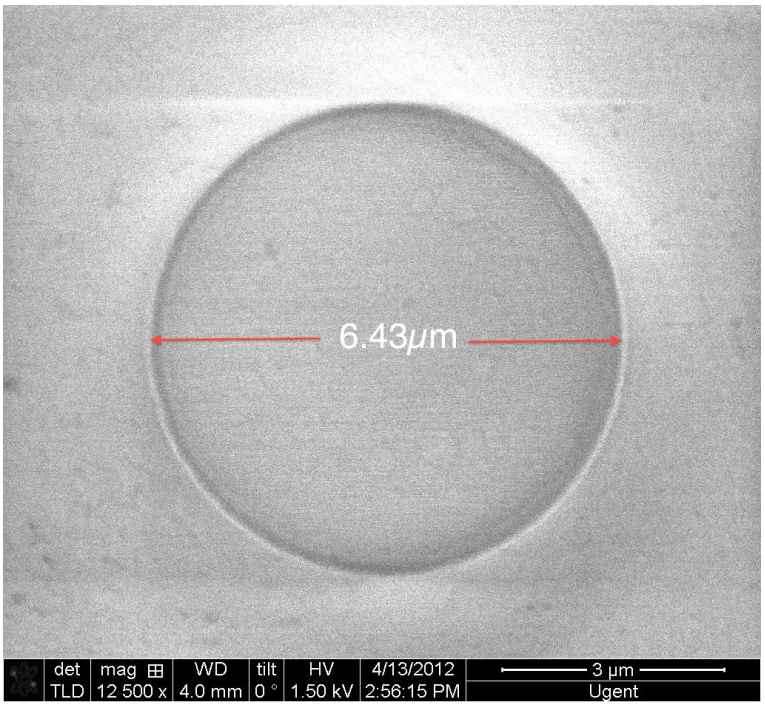

Figure 8.10: The diameter of the indicated microdisk measured using SEM is larger than the designed diameter of 6.0 μm .

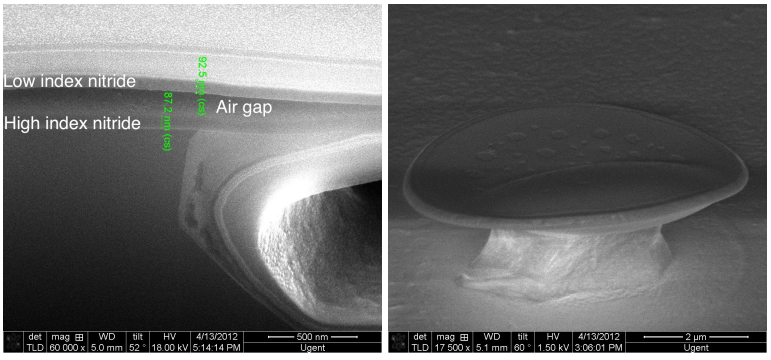

(a) (b)

Figure 8.11: (a) Cross section using SEM shows how the bottom and top Si_3N_4 layer have detached under SEM electron bombardement. (b) The microdisk *inflates* or *blows up* under SEM.

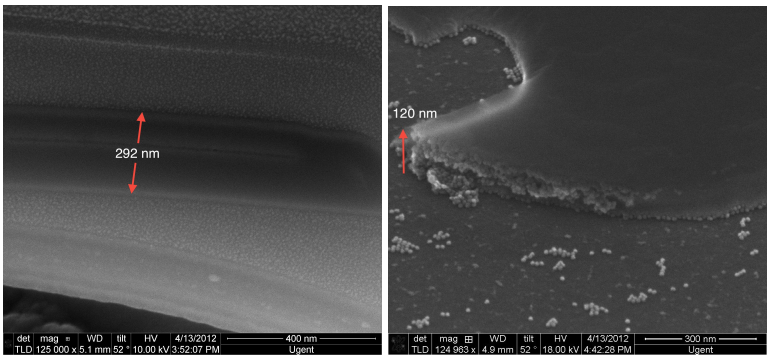

(a) (b)

Figure 8.12: (a) Cross section view of a microdisk with 80 nm of low and high index Si_3N_4, and a QD layer, which should have similar height as the layer thickness on the substrate, depicted in (b).

8.2.7 PL Quenching

We assess whether the deposition of Si_3N_4 using PECVD on a QD layer affects the optical quality of the QD film. We measure the total PL intensity before and after deposition of Si_3N_4at 120°C and 300°C for several different QD films. For the *giant* CdSe/14CdS QDs, 27% (partially in trap emission) of the PL remained after Si_3N_4 deposition at 120°C (see Figure 8.13(b)), whereas only 19% remained after Si_3N_4 deposition at 300°C. The effect was more dramatic for smaller ZnS passivated CdSe QDs, where 49% of the PL was recovered after deposition at 120°C, whereas only 7% remained at 300°C (see Figure 8.13(c)). To highlight the versatility of our fabrication technique, Figure 8.13(d) shows that it can be extended to near-infrared emitting PbS/CdS QDs[31].

8.3 Measurement Results

8.3.1 Imaging

Setup

Imaging of the fabricated microdisks was done on a standard scanning confocal PL microscope from Nikon. In this type of microscope, dichroic mirrors separate the excitation light from the PL signal. It can be used with a broadband source and a standard silicon array detector to form an image,

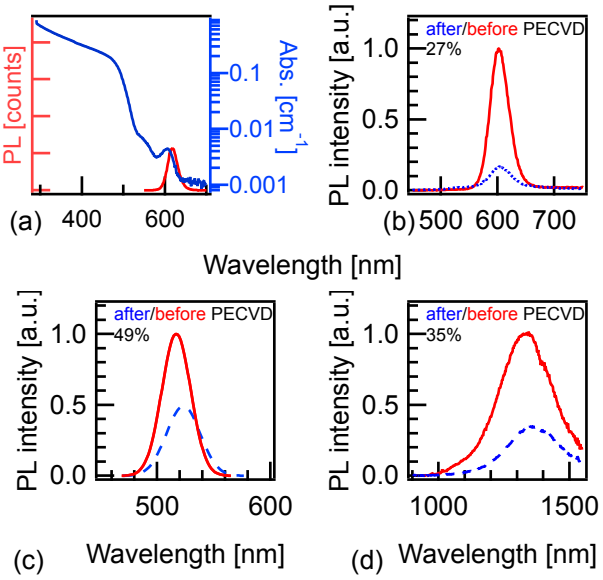

Figure 8.13: (a) PL (red) and absorption (blue) spectrum of 12 nm *giant* CdSe/14CdS QDs used in the microdisk experiment. (b) PL spectrum of spincoated CdSe/16CdS QDs before (red) and after (blue) deposition of low-index Si_3N_4 shows that 27% of the emission remains after Si_3N_4 deposition. (c) A similar experiment for CdSe/2ZnS QDs illustrates that 50% of the PL remains after deposition. (d) Also for near-infrared emitting PbS/CdS QDs 35% of the PL is recovered after Si_3N_4 deposition.

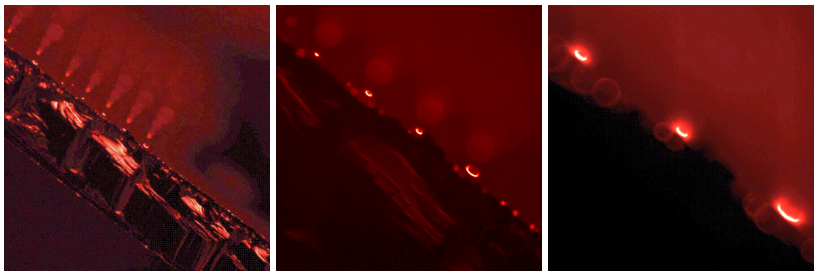

Figure 8.14: Emission imaged with the PL microscope at a 10° angle between the direction of view and the sample plain.

or in scanning confocal mode. In confocal mode, it is equipped with diaphragms that reject any PL that is not emitted from the focal point of the excitation beam. The excitation consists of the laser lines of an argon laser, and an additional diode laser, both operated in CW. The laser is imaged to a diffraction limited spot onto the sample and the collected PL is sent through a fiber to a monochromator equipped with an array of visible photomultiplier tubes. The highest spectral resolution is 2.5 nm, too large to obtain an accurate spectrum of the WGMs. To form an image, the laser is scanned over the sample.

Microdisk images

A typical sample with microdisks contains several rows of differently sized microdisks. The sample is cleaved along one row and mounted at a 10° angle between the direction of view and the sample plain to increase the collection efficiency of light emitted from the WGMs.

Figure 8.14 shows the emission collected using the PL microscope in regular imaging mode for a sample containing CdSe/CdS/ZnS, made using the SILAR technique. Several rows of disks can be seen. With only the edge column in focus (right figure), we clearly see bright emission from the edge of the microdisks.

Figure 8.15.a shows a confocal scanning image of a 7 μm microdisk. The sample is excited with the 454.6 nm Argon laser line on a spot size of about 300 nm and imaged using a 20x objective (NA=0.75). At the center of the disk, the darker spot outlines the silicon pillar, which absorbs or guides most of the emitted light in that region. Around the pillar, a first bright ring can be seen, followed by a slightly larger second ring. From the spectrum in Figure 8.15.b of the different regions of interest (ROI) indicated

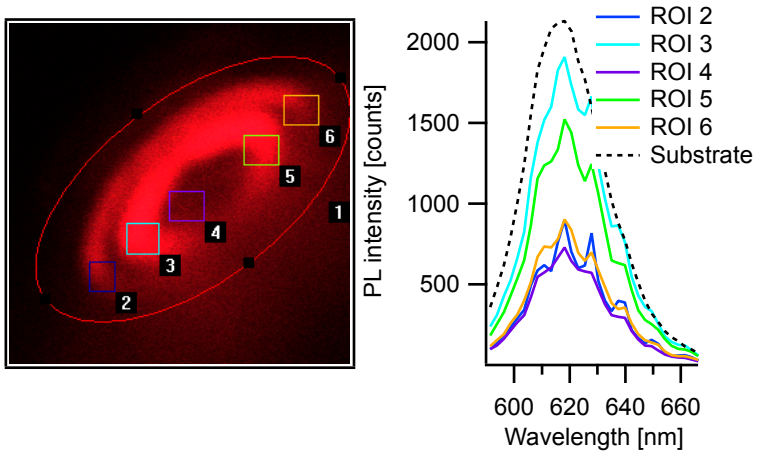

Figure 8.15: (a) Confocal image of a 7 μm microdisk with CdSe/CdS/ZnS QDs at a 10° angle. The Regions of Interest (ROI) are indicated on the image. (b) The spectrum from each of these ROI.

on Figure 8.15.a we see modulations in the spectrum from the coupling of emission to the WGMs for all ROIs, yet most strongly from ROI 2 at the bottom edge of the disk. Note that the spectral resolutation is only 2.5 nm, so the peak width is limited by the setup's resolution. The size of the second ring correlates well with the microdisk diameter. We therefore concluded that the outer ring is mostly emission from WGMs. The explanation of the inner ring is not fully clear. It could be from reflection or scattering of the WGM at the pillar edge, or from a non-uniform QD layer around the pillar due to spincoating on fully pre-etched microdisks, some emission of which still couples to WGMs, since the spectrum from this region still shows WGM-like modulations.

8.3.2 Spatial and spectral mode mapping

Selective Excitation Setup for Spatial and Spectral Imaging - ULB

In this Section we describe the spatial and spectral mode mapping. These measurements were done in collaboration with Edouard Brainis from Université Libre de Bruxelles (ULB), who built and operates a custom microphotoluminescence imaging setup. The spectrally and spatially resolved microphotoluminescence setup (see Figure 8.16) consists of a picosecond

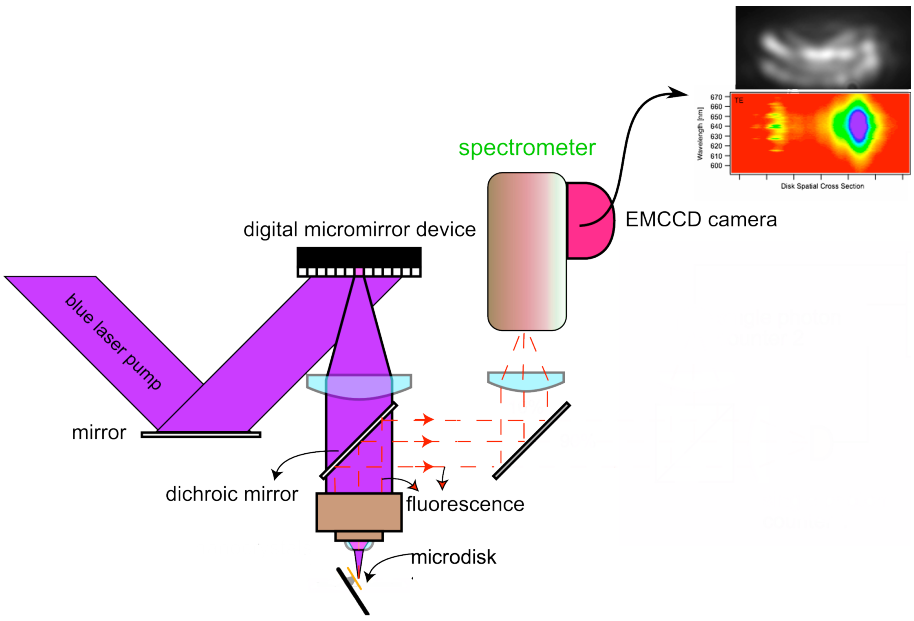

Figure 8.16: Selective Excitation Setup for Spatial and Spectral Imaging at the ULB shows the laser beam incident on the DMD. A pixel on the DMD is imaged onto the sample plane by a 100x objective. The PL is collected using the same lens and sent to a dichroic mirror. An image of the sample is formed on the entrance slit of the spectrometer, which can be used to collect a spatial image of the microdisk (top graph) or hybrid spatial/spectral image (bottom graph)

pulsed laser ($\lambda = 408$ nm) incident on a digital micromirror device (DMD). The micromirror plane is imaged onto the sample plane using a 100x-objective (NA=[@EDOUARD]), enabling us to determine the shape, size and position of the excitation spot, without moving the sample itself. The emission is collected using the same objective, separated from the excitation light with a dichroic filter, polarized using a Glan-Thompson polarizer and sent to an imaging spectrograph.

With open slits and the grating turned to the 0^{th} diffraction order (i.e. mirror), a full spatial image is formed on an EMCCD (electron multiplying charged coupled device) camera(see top graph in Figure 8.16). With closed slits (typically 30-50 μm) and the grating turned to the right diffraction order a hybrid spatial/spectral image forms on the 2D detector (see bottom graph in Figure 8.16). The spatial axis is oriented along the length of

the slit, whereas the spectral axis is perpendicular to the slit length. The sample is mounted with a 10° angle between the substrate and the setup's optical axis, since the radiation pattern from WGM's is directed preferentially along this axis.[32]

Spectral and spatial mapping of WGM modes

Figure 8.17(a) shows a tranverse-electrical-polarized (TE, *i.e.* $\mathbf{E} \sim E_r \mathbf{e_r}$) mode map collected from a 6.0 μm diameter microdisk. We position the sample in such a way that the slit of the imaging spectrograph takes a spatial cross section through the middle of the disk (see the drawing at the top of Figure 8.17(a)). This is plotted on the x-axis. The spectrograph grating then images the slit, spectrally separated along the direction perpendicular to the slit onto the EMCCD. In this way, of each point of the microdisk cross section, a spectrum is taken and plotted on the y-axis.

We pump with a spot size of 1.5 μm, which we carefully direct at the right side of the microdisk. The PL of the excitation spot lights up, together with a bright spot of PL at the left side of the microdisk. This secondary PL spot is well out of the range of the excitation spot, since moving the excitation spot towards the left reduces rather than increases the brightness of the left spot. Hence, it cannot be attributed to direct excitation of the QDs by the pump spot. As the distance between the right edge of the excitation spot and the left spot is equal to the diameter of the disk (see Figure 8.17(a)), it suggest that the secondary PL spot on the left side comes from WGM, resonating in the microdisk.

That the PL indeed comes from WGMs becomes even clearer when we take a look at a line section through the spectral mode map at the left edge (see Figure 8.17(b)). The spectrum exhibits some clearly distinguishable resonances, both in TE and TM (tranverse magnetic) polarization, illustrating the modified density of optical modes the QDs can couple to, once they are embedded in the optical cavity (see Figure 8.17(a-b)). Given the small excitation spot size and the low pump fluence used, we can therefore conclude that the emission coming from the left side of the microdisk is the spontaneous emission of the excited QDs on the right side of the microdisk that is coupled to a resonant microdisk mode and eventually leaks or scatters away from the disk into the collection optics.

Two WGM families stand out in the TE spectrum. They have slightly different free spectral range (FSR), indicating a different radial order (TE_1, TE_2). In the TM spectrum three sets of modes are visible, of which only the one dominant mode is quasi-TM. We identify the other WGMs as the same quasi-TE modes seen in the TE spectrum, given that the wavelengths

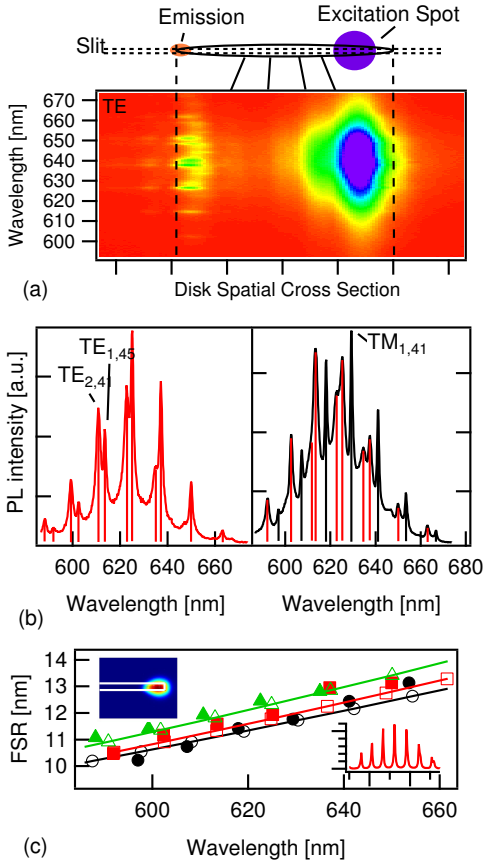

Figure 8.17: (a)Mode map collected from a 6.0μm microdisk containing *giant* CdSe/14CdS QDs by selective excitation of the right side of the disk. The cross section from where the PL is collected is drawn in the microdisk drawing above. Only TE polarized light is collected here. (b) Spectrum at the left edge of the microdisk for TE and TM polarized light. The two TE modes are also visible in the TM spectrum, as indicated by the red lines. The mode's radial and azimuthal order is indicated for one of the resonances. (c) FSR as measured (full symbols) and as calculated (open symbols) as a function of the resonance wavelength for the first order TM (black), first order TE (red) and second order TE (green) mode. The inset at the top left shows the intensity mode profile of the $TE_{1,45}$ calculated using COMSOL. The inset at the bottom right shows the calculated TE spectrum, using a 1 nm linewidth.

match with the peak positions of the quasi-TE modes.

To compare our mode mapping results with simulations, we solve the axisymmetric form of Maxwell's equations in cylindrical coordinates numerically.[33] As illustrated in Figure 8.17(c), using the dimensions and refractive indices as mentioned above, we can predict the spectral positions and the FSR of the resonances for the first order quasi-TM and the first and second order quasi-TE modes within the emission band of the QDs. For the QD layer, we have taken a refractive index of 1.69 to obtain the best fit with our experimental results. A perfect match between simulations and experiment is not possible, since we neglect the QD and other material dispersion, and approximate the shape of the disk cross section with a rectangle.

To understand why the quasi-TE modes show up in the TM spectrum (see Figure 8.19 for more detail), we look at the field line plots ($\mathbf{E_t} = E_r\mathbf{e_r} + E_z\mathbf{e_z}$) of the TE_1, TE_2 and TM_1 modes from simulations (see Figure 8.18). Because of the asymmetry of the microdisk structure, the TE and TM modes are hybrid. The TE mode have a non-negligible E_z component at the corners of the disk cross section. The same goes for the E_r component of the TM mode at the corners, and along the top surface of the disk. Scattering of the quasi-TE modes at the microdisk corner would therefore couple to an almost pure TEM free space mode.

Apart from the observation that the scattered modes are hybrid, two more things are striking in Figure 8.19. Note that the intensity in both maps cannot be compared, because of slightly different experimental conditions, integration times and camera gain settings:

- the TM collects more *background* emission
- in the TE map, the TM_1 mode is spatially shifted compared with the TE modes. However, in the TM map, the TM_1 is spatially aligned with the TE modes.

Further investigation is needed to rule out any setup artefacts and identify the physical origin of these effects.

Scattering is the main mechanism coupling photons out of the microdisk cavity, rather than WGM radiation or direct PL coupling to free space modes. This is further confirmed by the very localized spot of WGM-modulated PL, coming from the left edge of the microdisk (see Figure 8.17(a)). Other, non-radiative loss mechanisms, such as reabsorption and Stokes-shifted re-emission outside the WGM resonance by the QDs, will further reduce the Q-factor of the cavity. A Lorentzian fit to the quasi-TM peaks yields Q-factors of 600, while the peaks in the TE spectrum yield

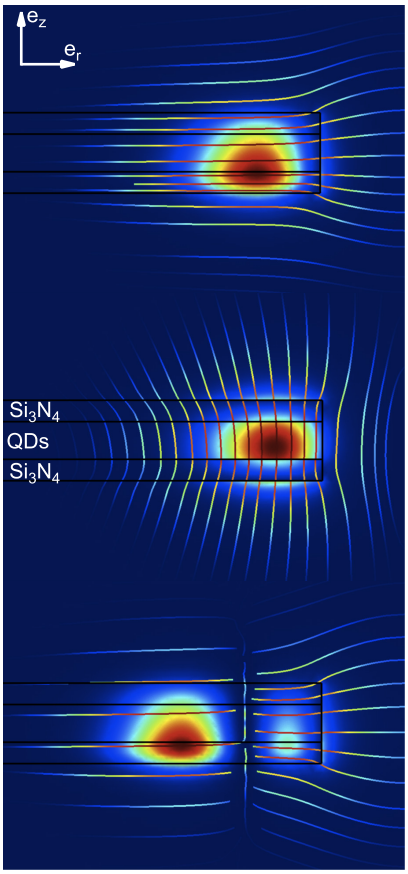

Figure 8.18: Field lines $\mathbf{E_t} = E_r\mathbf{e_r} + E_z\mathbf{e_z}$ for the TE_1 (top), TM_1 (middle) and TE_2 (bottom) modes, plotted against the background of the mode intensity $|\mathbf{E}|^2$, show that both modes are hybrid, especially at the corners of the structure.

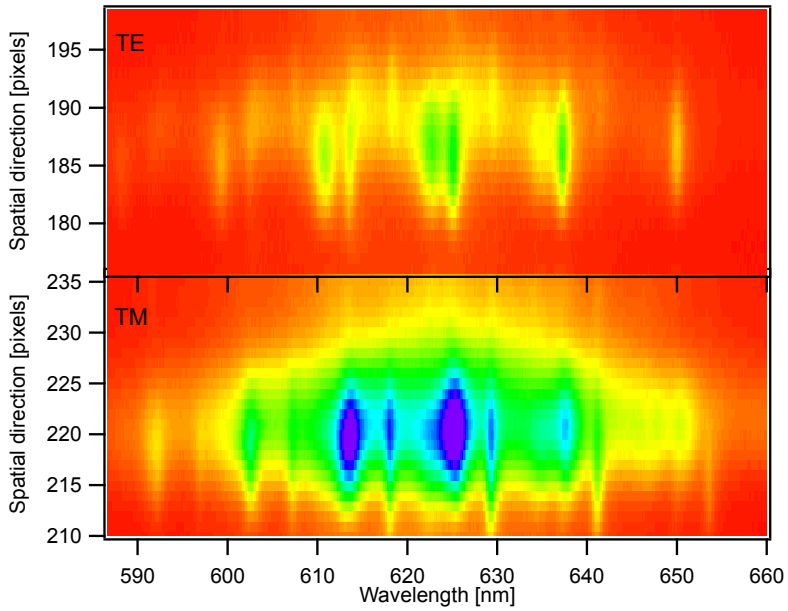

Figure 8.19: Mode map of a 6.0 μm microdisk for the TE polarization (top) and TM polarization (bottom)

Q-factors of 450 and 300 for the first and the second order modes respectively.

Since we only pump a small part of the microdisk and keep the flux below one exciton per QD, it might seem surprising that light resonates in the microdisk at wavelengths where it is absorbed by the QDs. Even without exact knowledge of the local field factor in these densely packed QD layers,[34], we can still estimate the absorption coefficient between a lower limit of 40 and an upper limit of 2000 cm^{-1} (taking the confinement factor into account). This puts the expected Q-factors in the range of 5000 to 100, in agreement with our experimental results.

Both loss mechanisms could be engineered to improve the Q-factor for the desired applications. However, our main aim was to showcase the succesful embedding colloidal QDs into a CMOS-compatible solid matrix and putting them to work in an active and complex, integrated photonic device. While the photophysics of the interaction between the QD and the optical microcavity are interesting in their own right and merit further study, this work smooths the path towards other active photonic structures, such as waveguides, ring resonators and interferometers, and more complex active photonic circuits.

Influence of the spot size

The DMD in this setup allows us to change the excitation spot size and position without changing the collection optics or the sample position. Figure 8.20.a shows the mode maps collected for a 6.5 μm microdisk, containing SILAR CdSe/CdS/ZnS QDs (30 nm layer thickness), recorded using a 600 lines/mm grating (resolution = 0.084 nm). The position and size of the excitation spot is clear from the large 2D-gaussian spot in each mode map. The excitation spot is directed at one side of the microdisk. The emission pattern at the top clearly shows the WGMs scattering from the other side of the microdisk. From right to left, we increase the diameter of the circular exciation spot on the DMD from 30 pixels over 50 pixels to 80 pixels. Even though we keep the laser power constant, the multimode nature of the excitation laser creates a non-uniform spot on the DMD. We can therefore not guarantee that the exciting photon flux density remains constant while changing the spot size.

From the mode maps it is clear that exciting a larger area of the microdisk and therefore more QDs increases the intensity of the WGMs. Figure 8.20.b shows the spectra at the WGM position. The spectra are normalized to the highest WGM intensity. It shows that the background emission grows faster than the WGM intensity as the excitation spot becomes larger.

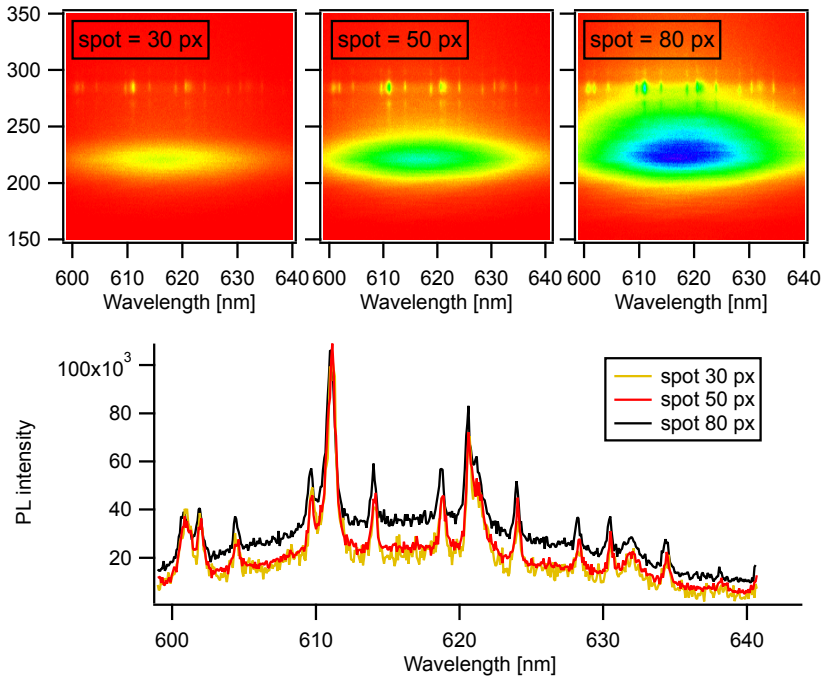

Figure 8.20: (a) Mode maps of a 6.5 μm microdisk, containing 30 nm thick layer of SILAR CdSe/CdS/ZnS QDs, using a 600 lines/mm grating for three different excitation spot sizes. All maps are shown on the same scale, so the emission intensities can be compared. (b) Spectrum for the different spot sizes by normalizing the peak intensities shows the faster growth of the background emission.

For the largest spot size, the QDs at the WGM position are excited as well. Their emission couples partly to free space modes, i.e. the background emission. The spectrum is therefore the sum of the emission of all excited QDs that are coupled to the WGMs and the emission of the excited QDs at the spatial position where the spectrum is taken that is coupled to free space modes directly.

Pump power sweep

Figure 8.21 shows the spectrum of a 6.5 μm microdisk, containing SILAR CdSe/CdS/ZnS QDs (30 nm layer thickness), recorded using a 600 lines/mm

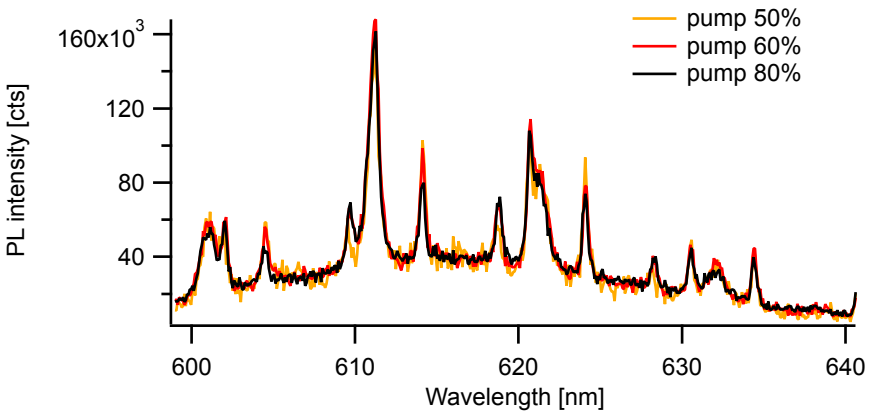

Figure 8.21: Spectrum of a 7.5 μm microdisk, containing 30 nm thick layer of SILAR CdSe/CdS/ZnS QDs, using a 600 lines/mm grating for three different pump powers of the excitation laser, normalized to the background emission shows the linear increase of the output spectrum.

grating (resolution = 0.084 nm) for three different pump powers. All spectra have been normalized to the background emission. The peaks follow the same power-dependent trend as the background emission, illustrating the absence of strong stimulated emission. Moreover, neither the spectral position, nor the Q-factor change with increasing pump power. From a lorentzian fit to the sharpest peak in the spectrum, we extract a Q-factor of 1800.

8.3.3 Spectral and Temporal Characterization

Microdisk Pump Setup - Trento, Italy

These measurements were done in cooperation with the Silicon Photonics Group of Prof. Lorenzo Pavesi at the University of Trento, Italy. Their setup can be used to study the spectral and temporal behaviour of the microdisk emission intensity as a function of the pump power. We excite the microdisk using a 532 nm CW diode laser, delivering a maximum power of 4 mW (5 kW/cm^2) or a femtosecond pulsed Titanium:Sapphire laser (50 fs, 80 MHz), frequency-doubled to 400 nm, delivering a maximum average power of 30 mW (under ideal conditions) or 0.3 nJ (120 μJ/cm^2). Both beam paths are combined into a single 20x achromatic objective (designed to have the same focal point for both 400 nm and 534 nm), which focuses

the laser light down to a 10 μm spot. The sample is mounted with its surface perpendicular to the excitation beam path.

The collection path is mounted at a 90° angle and uses a 40x objective to collect the microdisk emission. The microdisk sample needs to be cleaved in such a way that the microdisks are less than 100 μm from the sample edge in order for the lens to be able to focus on the microdisk. Behind the objective, a polarizer is mounted, used to distinguish between TE and TM modes and a dichroic mirror to filter out the excitation light, before sending the collected emission to a monochromator. Similar gratings as on the spatial and spectral imaging setup at ULB are available (300 l/mm and 600 l/mm).

The diffracted light is imaged onto the slit of a *streak camera* (Hamamatsu). The streak camera delivers the temporal resolution of the setup by transforming the temporal profile into a spatial profile on a 2D array detector. The light entering the device falls onto a photocathode, which emits electrons through the photo-electric effect. Similar to a CRT television, the electrons are deflected using a time-varying electric field, triggered using the excitation pulse of the laser. At the start of the trigger, the electrons hit the top of a phospor screen and over time are swept over the entire height of the screen, thus transforming the time profile into a spatial profile. Since the speed or time resolution of the camera is determined by the electronics, it has a huge dynamic range with time windows from 10 ms to 2 ns, while the sensitivity is close to the single-photon regime, thanks to the efficient photocathode materials in the visible range of the spectrum.

Spectral analysis under CW excitation

We investigate a sample containing CdSe/CdS dot-in-rods (22.3 nm by 5.3 nm). These type of nanocrystals were selected for their qualities as a gain material. Their Auger recombination rate was reported to be reduced, resulting in longer gain lifetimes and lower lasing thresholds[35–37]. However, due to technical issues at the time of processing, the desired layer thickness of 50 nm was not obtained. Instead, from SEM, we estimate only a sub-monolayer was deposited.

We estimate the cross section of the dot-in-rods[38] as:

$$\begin{aligned} \sigma &= \mu V && (8.2)\\ &\simeq 5e^{6}m^{-1}\frac{\pi(5.3e^{-9}m)^{2}}{4}22.3e^{-9}m\ @532nm && (8.3)\\ &= 2.5e^{-14}\,cm^{2}\ @532nm && (8.4) \end{aligned}$$

CW pumping using the 532 nm diode laser results in a maximum power

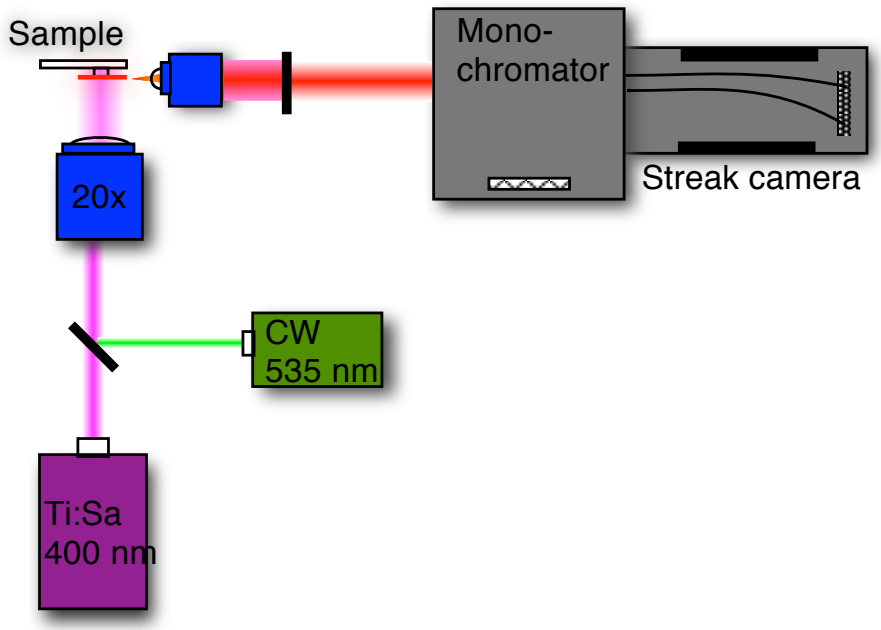

Figure 8.22: Microdisk pump setup used in Trento, Italy.

of 4 mW on a spot of 10 μm, or a power density of 5 kW/cm^2. Using the cross section above, this gives a maximum exciton pump rate of one exciton every 2.93 ns.

Figure 8.23 shows the TE and TM spectra from three 6.5 μm microdisks on this sample. All spectra clearly exhibit WGM resonances in both TE and TM. While polarization suppression is not perfect for reasons highlighted above (see Section 8.3.2 on p. 204), there are two or three mode families clearly belonging to a different polarization in each spectrum. As Figure 8.23 shows spectra of three different 6.5 μm microdisks, it illustrates the reproducibility of the spectra. Both in TE (black) and TM (red) the position of the resonances matches well throughout the spectral bandwidth. As both position and FSR line up, it shows that the modes have the same effective refractive and group index. However, the top spectrum (TM) was shifted by 3.8 nm towards the blue side of the spectrum (left) to match the WGM positions with the other spectra. Moreover, there is a clear difference in Q-factor and exctinction with the background emission. These measurements illustrate the challenges we still face to optimize the uniformity of the fabrication process.

To extract more information from the spectra, we perform a multi-peak fitting algorithm (using Igor Pro) on the bottom (see Figure 8.24) and top spectrum (see Figure 8.26) of Figure 8.23. To each WGM we manually assign a lorentzian peak. A gaussian function accounts for the background emission coupled directly to free space modes. The result of the fitting procedure is shown in the top graph of Figure 8.24 for TE (left) and TM (right) as a solid red line. We deconvolute the spectrum in separate WGM peaks in the middle graph. We colour each WGM family differently and also plot the gaussian background emission. The TE spectrum contains three mode families, while in the TM spectrum we can only identify two. From the middle graph, it is clear that the amplitudes of the peaks for each mode family form a gaussian-like envelope. These amplitudes are plotted in the bottom graph, together with a gaussian fit. The central wavelength is indicated for each mode family. Each envelope is significantly shifted by 10-30 nm.

To identify the modes, we plot the FSR in the top graphs of Figure 8.25. For the TE modes, the green modes have the highest FSR and are therefore the highest radial order. The black and red modes have a very similar FSR, that is too close to be of a different radial order, according to simulations. Moreover, their Q factors are very similar for all wavelengths. We therefore speculate that these are non-degenerate clockwise and counter-clockwise propagating first order modes. For the TM modes the FSRs (see top right graph of Figure 8.25) are clearly different for both modes and we therefore

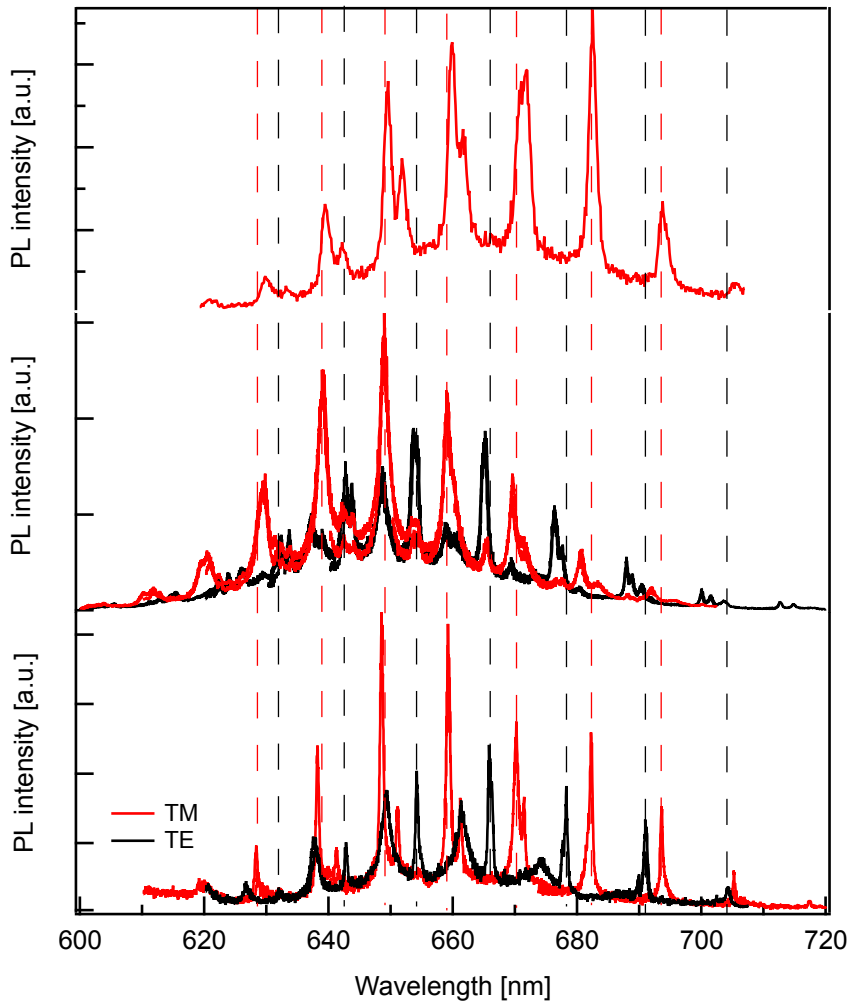

Figure 8.23: TE and TM spectra of three disks of 6.5 μm on the same sample. All disks contain CdSe/CdS dot-in-rods (22.3 nm by 5.3 nm) and are excited using a 532 nm CW laser at low power. Lines are drawn as guides to the eye, showing the corresponding WGMs in each spectrum. The top spectrum was moved by 3.8 nm towards the blue (left) side. It illustrates the reproducibilty and quality of the microdisks on one sample.

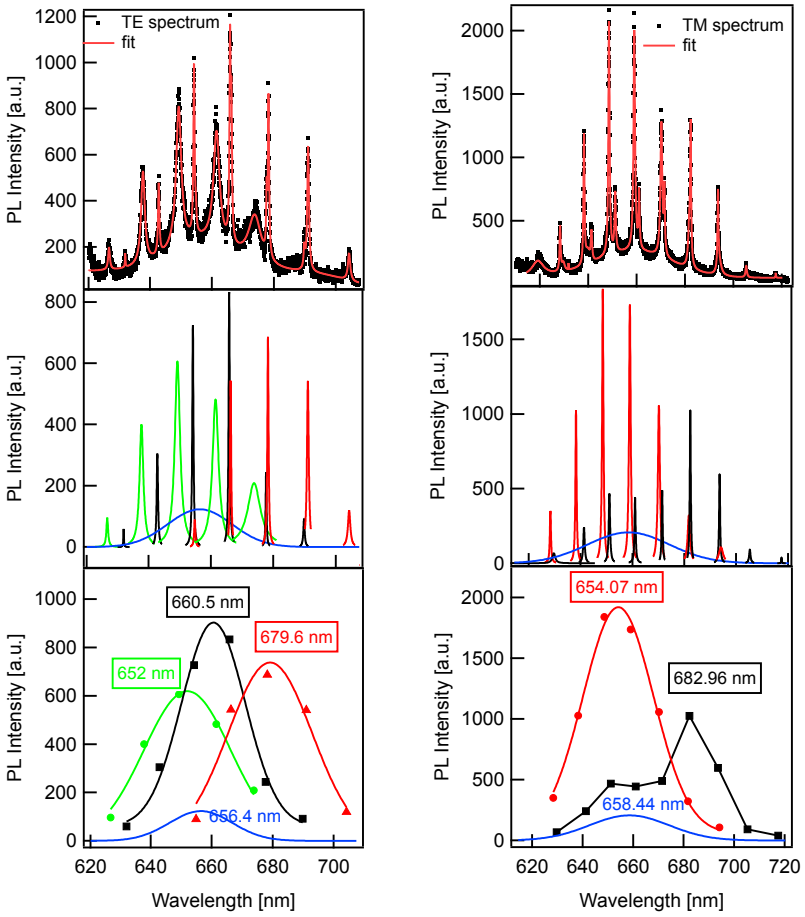

Figure 8.24: (top) The spectrum (TE on the left, TM on the right) of a 6.5 μm microdisk containing CdSe/CdS dot-in-rods is fitted using a multipeak fitting algorithm. The sum of all the separate peaks is shown as a red line. (middle) Deconvolution of the spectrum in separate Lorentzian peaks together with a Gaussian background for the uncoupled spontaneous emission. Peaks belonging to the same mode family are coloured in the same way. (bottom) The amplitude of each peak is plotted. The amplitude-envelope of each mode family is fitted using a Gaussian function. The central wavelength is indicated in the boxes.

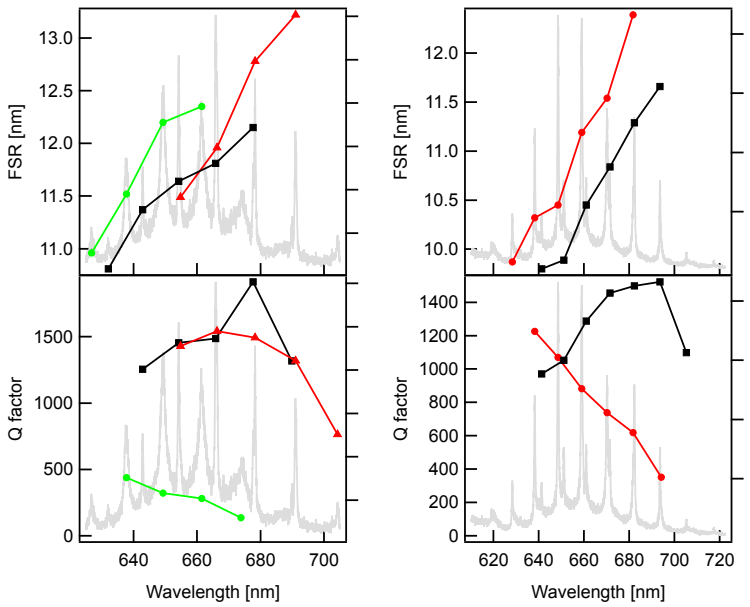

Figure 8.25: FSR and Q factor for the TE (left) and TM modes (right) of a 6.5 μm microdisk.

identify these as first and second order TM modes.

With this identification, we come to a general observation that:

- the first order mode envelope is significantly redshifted compared to the gaussian background emission.
- the second order mode envelope is slightly blueshifted compared to the gaussian background emission.

This observation is corroborated by the TM spectrum of another microdisk on the sample (see Figure 8.26) on which we performed the same fitting procedure, and in fact qualitatively by all spectra collected, even for samples containing different QDs.

The origin of this is not well understood at this time. We found no reports in literature describing this behaviour. A redshift would be caused by a higher coupling or lower mode loss (i.e. higher Q factor) on the red side of the spectrum, and inversely for a blueshift. The Q factor dependence on the wavelength indeed follows this trend. The bottom graphs of Figure 8.25 show an increasing Q factor with wavelength for the blueshifted modes, and a decreasing Q factor for the redshifted modes.

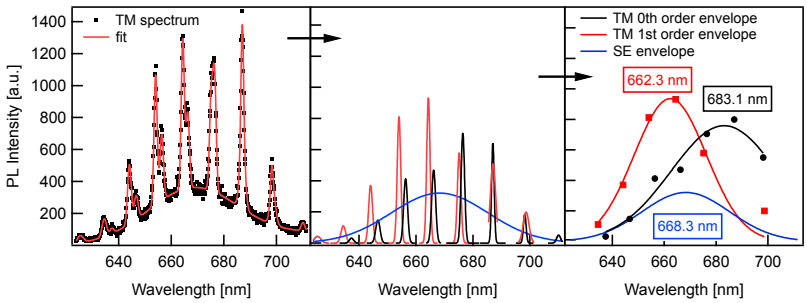

Figure 8.26: Another 6.5 μm microdisk, with similar analysis was done as in Figure 8.24 shows the reproducibility of the processing and measurement.

The Q factor reaches a maximum of 1500, and is very similar for both TE and TM WGMs. We note that these Q factors are limited by the spectral resolution of the setup. The full-width-at-half-maximum extracted from the fit is below 0.5 nm, whereas the resolution of the grating was measured using the excitation laser to be 0.8 nm.

Stability under 400 nm pulsed excitation

A pulsed laser can deliver pulses with a much higher power than the CW diode laser used here. The Ti:Sa femtosecond pulsed laser delivers a maximum average power of 30 mW in the frequency-doubled 400 nm line. While the average power P_{avg} is in the same order of magnitude, this power is concentrated in a short femtosecond pulse, calculated easily:

$$P_{pulse} = \frac{P_{avg}}{\tau_{pulse} f_{rep}} = \frac{30\ \text{mW}}{1\ \text{ps}\ 82\ \text{MHz}} = 0.37\ \text{kW}$$

Here τ_{pulse} is the pulse width and f_{rep} is the repetition rate. When this is focused down to a 20 μm spot, we get a power density of 120 MW/cm^2. Assuming the pulse width to be shorter than all internal QD processes, we express this as an energy density of $E_{pulse} = 120\ \mu\text{J/cm}^2$ per pulse. At 400 nm, the dot-in-rod cross section is $\sigma_{QD} = 6e^{-14}$ cm^2, larger than at 532 nm. The number of excitons created by a single pulse therefore becomes:

$$N_{ex} = \sigma_{QD} E_{pulse} \frac{\lambda}{hc} = (6e^{-14}\ \text{cm}^2)\ (2.34e^{14}\ \text{photons/cm}^2) = 14.1$$

This high photon flux and energy density can however also have adverse effects. Spectra taken using CW excitation were stable over the course of hours. On the contrary, excitation using the Ti:Sa pulsed laser resulted almost immediately in a spectral blueshift over the course of minutes, and a slower decrease of the intensity of the WGM peaks.

To illustrate this effect, Figure 8.27 shows the evolution of the spectra taken from a 6.5 μm microdisk containing CdSe/CdS dot-in-rod over the course of twenty minutes (from top to bottom). A line is drawn as a guide to the eye connecting one WGM peak. Clearly, a strong blueshift over nearly 10 nm (i.e. one FSR) is observed. The position of one WGM resonance is plotted in Figure 8.28, showing a strong shift of 1 nm/min in the first 5 min, slowly decreasing to a lower shift rate beyond 5 min. The intensity, shape and Q factor of the WGMs does not seem to change much in the first 5 min, but clearly worsens after 10 mins.

We note that we observed this effect on all microdisks under study on this sample, and also on microdisks containing different QDs. Since the initial shift is usually not accompanied by a degradation of the PL, we assume that the intense excitation beam alters the disk shape. Given the problems with adhesion between the low-index top Si_3N_4 layer and the spincoated QD layer, which we observed under SEM (see Section 8.2.6 on p. 196), we speculate that the intense excitation beam creates thermal stress between these layers, which is partially released by *inflating* the microdisk. As air replaces Si_3N_4 as the top layer, this will result in a lower effective index (air vs Si_3N_4) and blueshift of the spectrum.

Power analysis under CW and pulsed excitation

In Figure 8.29(a) we show the increase of the collected PL intensity for several TE modes with increasing CW pump power. The top axis also shows the exciton pump rate. For comparison, the power dependence off-resonance is also shown for one wavelength (open circles). The intensity initially increases linearly. Around 1 mW, the intensity begins to saturate into a square-root power law. A further increase of power shows a sudden superlinear increase in the intensity, which could be due to stimulated emission. However, the increase is at the limit of the pump power, and could therefore not be confirmed with additional data points.

The CW laser creates a steady-state population of excitons in the rods, according to the model developed in Section 7.3.3 (see p. 176). The number of photons in the cavity as a function of the CW pump power is plotted in Figure 8.29(b) for a cavity containing 1000 QDs coupled to the cavity resonance. The trend of the experimental and simulated traces agrees well

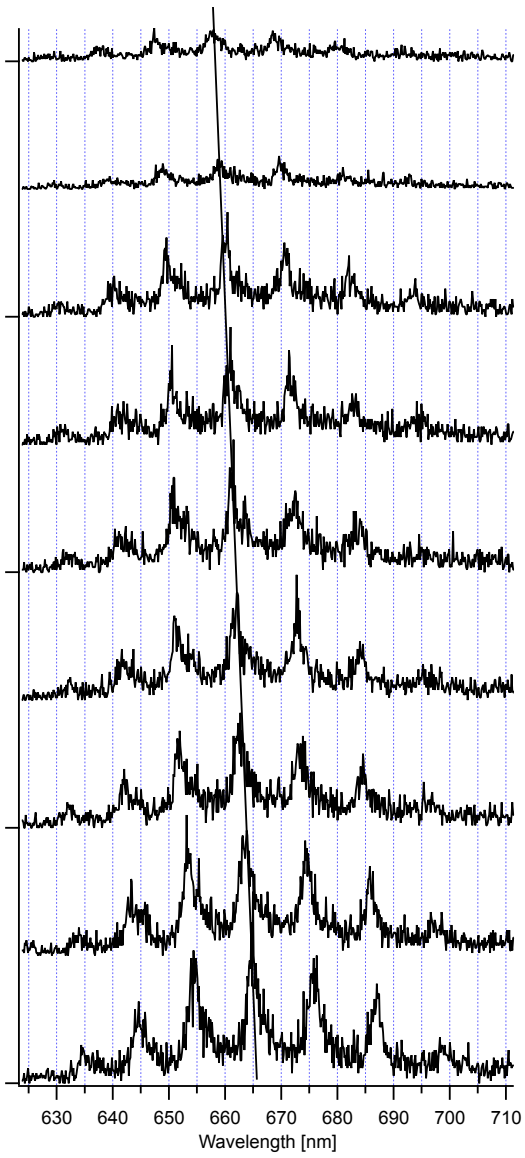

Figure 8.27: Spectra of a 6.5 μm microdisk under 400 nm pulsed excitation (27 mW average power) shifts in time. The time axis increases from the bottom spectrum to the top spectrum.

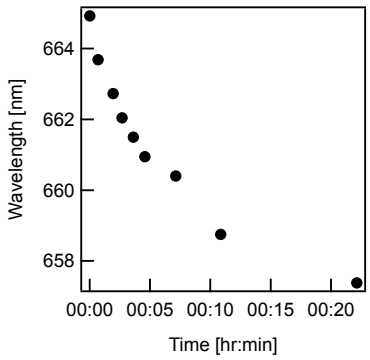

Figure 8.28: Blueshift of one of the WGM peaks as a function of time of excitation using a 400 nm pulsed excitation at full power (27 mW) for a 6.5 μm microdisk.

qualitatively. We find the same linear increase at low power and a saturation to a square-root power law at higher power. A sudden superlinear increase, indicative of stimulated emission, is also observed. The agreement between experiment and theory is however not perfect, as the theoretical trace is spread over several pump power decades, whereas the experimental trace is concentrated to just two decades.

Under pulsed excitation using the Ti:Sa pulsed laser, the collected PL intensity increases linearly. Figure 8.30 shows a log-log plot of the intensity as a function (left axis, dots) of average power of the fs-pulse laser for the peak wavelength indicated on the right axis with the squares. The solid line is a power law fit to the PL data. The exponent that was extracted from the fit is 0.92 ± 0.03 and hence almost perfectly linear. The top axis indicates the number of excitons per QD created by each laser pulse.

As we have seen in Section 7.3.2 on p. 172, the PL intensity increases linearly both below and well above threshold. Given the number of excitons that we were able to create (due to low excitation laser output that day), the lower than expected number of QDs in the cavity and the blueshift of the WGM resonance locations (see Figure 8.30 open squares on the right axis), we conclude that we are in a linear regime below full bleach and in the regime where the amount of QDs is too low to provide sufficient gain to start lasing action.

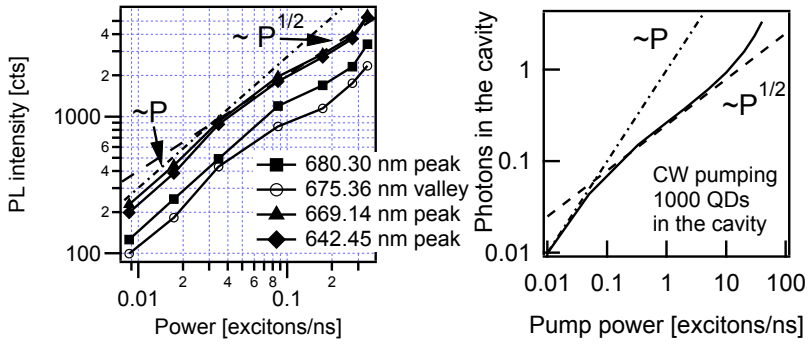

Figure 8.29: (a) Collected PL intensity as a function of CW pump power for several TE modes and one off-mode wavelength shows initially a linear increase, saturating to a square-root dependence. The maximum power indicates a superlinear increase. The dash-dotted line is a guide to eye for a linear dependence, the dashed line indicates a square-root dependence. (b) Simulation of the number of photons in the microdisk cavity as a function of CW pump power, as discussed in Section 7.3.3 (see p. 176) for an underloaded cavity with 1000 QDs shows the same linear increase at low power and sublinear increase at higher power.

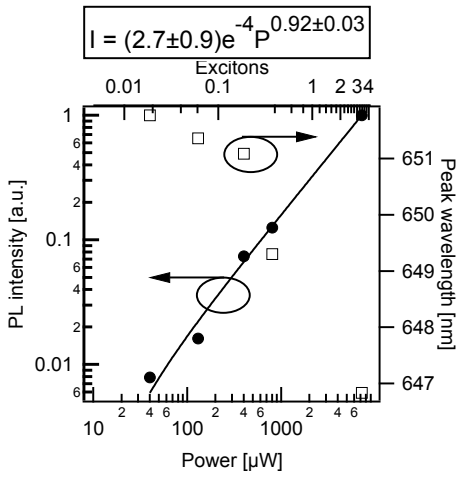

Figure 8.30: Log-log plot of the intensity as a function (left axis, dots) of average power of the fs-pulse laser for the peak wavelength indicated on the right axis with the squares, increases almost linearly. The line is a power law fit to the intensity data as a function of average pump power. The fitting coefficients are given in the box above the graph. The peak wavelength blueshifts over almost the entire FSR for high pump power.

Time resolved analysis under pulsed excitation

Besides the relationship between the output and the input power, the decay dynamics of the output of the microdisk after an excitation pulse can teach us more about the interaction between the QDs and the microdisk cavity.

First of all, the rate of spontaneous emission Γ_{SE} depends on the strength of the optical dipole transition on the one hand and on the density of final states in the photon field on the other hand. Especially in a microcavity, where the modal volume is small, the density of optical states can be increased, an effect known as the *Purcell effect*. The increase in the SE rate in the cavity compared to free space is quantified by the *Purcell factor* F_P[39]:

$$F_P = \frac{\Gamma_{SE,cav}}{\Gamma_{SE,\infty}} = \frac{3}{4\pi^2}\frac{Q}{V_m}\eta$$

It depends on the Q factor and the normalized modal volume[40]:

$$V_m = \frac{n^3}{\lambda^3}\frac{\int_V \epsilon_r |\mathbf{E}(\mathbf{r})|^2 dV}{max(\epsilon_r |\mathbf{E}(\mathbf{r})|^2)}$$

The normalized mode volume as calculated using Comsol for the first and second order TE and TM modes of a 6.0 μm microdisk is summarized in Table 8.4. It can be estimated easily by making the assumption that in the axial direction the mode is confined by the thickness of the disk, in the radial direction the mode is half the wavelength in the microdisk and in the azimuthal direction the resonance condition means the $m\lambda/n_{eff}$ needs to fit in the disk perimeter:

$$V_m \simeq \frac{h_{\text{disk}}(\frac{\lambda}{2n_{eff}})(\frac{m\lambda}{n_{eff}})}{(\lambda/n_{eff})^3} = \frac{n_{eff}h_{disk}m}{2\lambda} = 13.9$$

which is in good agreement with the values calculated using Comsol.

	$TE_{1,42}$	$TM_{1,42}$	$TE_{2,42}$	$TM_{2,42}$
λ_0 (nm)	649.25	619.36	591.55	567.858
V_m	11.3	14.1	11.93	15.07
F_P	10.1	8.1	9.6	7.6

Table 8.4: Normalized modal volumes for a 6.0 μm microdisk calculated using COMSOL.

The Purcell factor is in the order of 10 (see Table 8.4) for a Q factor of 1500. However, this is the idealized Purcell factor, the conditions on

the basis of which the Purcell factor was derived, do not all apply. The conditions[41] state that:

- the emitter and the cavity WGMs are spectrally tuned and $\Delta\omega_{em} \ll \Delta\omega_{cav}$
- the emitted field is aligned with that of the cavity and placed in a cavity-field antinode
- the nonradiative recombination rate is negligible.

Due to the large homogeneous linewidth of several meV (or nm) of CdSe QDs, related to acoustic phonon assisted transitions[42–44], the cavity linewidth is easily of the same order as the QD linewidth. Moreover, the thick QD layer implies that the Purcell enhancement will depend on the spatial position of the QD and result in a ensemble of different enhancement factors. Lastly, both in the low and in the high pump fluence regime, non-radiative recombination through surface recombination and Auger recombination respectively is not negligible. The deviation from the ideal regime is quantified by the non-ideality factor η dropping below one.

The Purcell effect on a microdisk containing an ensemble of QDs coupled to the cavity is simulated using the rate equations in Figure 8.31. The QDs are excited with 3.4 excitons per pulse. While this is above population inversion, there are not enough QDs coupled to the cavity to start lasing. The decay curves clearly show the fast Auger dynamics and the longer radiative recombination time. The Purcell effect is still clearly distinguishable as a shortening in the radiative lifetime.

An experimental decay curve recorded on a 6.5 μm microdisk excited with 3.4 excitons per QD is plotted in Figure 8.32.a. The dynamics, with the fast Auger component in the beginning and the long radiative tail are reminiscent of the simulation for $F_p \sim 1$ (Figure 8.31). They suggest that a lack of QDs coupled to the cavity inhibits lasing in this microdisk. Similar to the procedure followed by Pitanti et al.[41], we perform a fit of the decay curve on resonance and off resonance (i.e. in a dip). As the decay is not single-exponential, we fit the curves using a stretched exponential function:

$$I(t) = A \exp -(t/\tau)^{\beta} \tag{8.5}$$

The average decay time can be calculated as:

$$\langle \tau \rangle = \frac{\tau}{\beta} \Gamma \left(\frac{1}{\beta} \right) \tag{8.6}$$

On-resonance we extract an average lifetime of 150 ps. Off-resonance the fit yields an average lifetime of 250 ps. This is a factor 1.7 difference. The

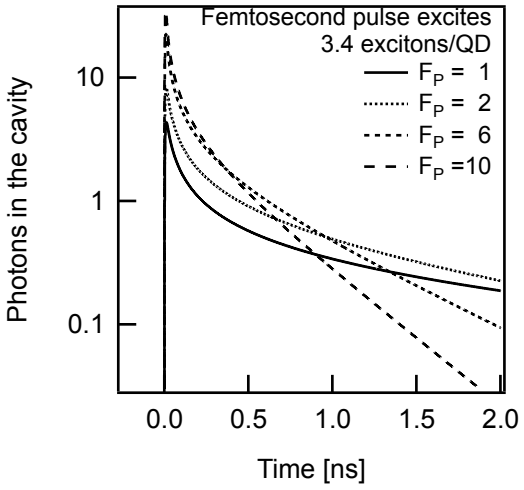

Figure 8.31: Simulated decay curve of a microdisk excited with a pulse of 3.4 excitons/QD for different Purcell factors shows the Purcell effect at high pump fluences.

β-factor gives an indication for the spread on the lifetime distribution. $\beta = 1$ for a single-exponential function. The lower β, the higher the deviation on the lifetime distribution. Both decay curves exhibit strong non-exponential decay. The on-resonance distribution is slightly broader, with $\beta = 0.42 \pm 0.01$ than the off-resonance distribution, with $\beta = 0.49 \pm 0.01$.

The difference between the on and off peak lifetime is evident both from the graph as from the stretched exponential fit. However, our model and understanding of the interaction of the QD ensemble with the WGMs is not developed enough to relate this difference in lifetime to the Purcell factor.

Moreover, Figure 8.32.b shows that the average lifetime is shorter at the blue side of the spectrum and increases monotonically with wavelength (Figure 8.32.c). To prove that this effect is related to the interaction of the QDs with the cavity, the decay traces at the blue and red side of the spectrum of QDs on the sample substrate (i.e. not coupled to the cavity) overlap (see Figure 8.32.d).

Since the effect is clearly due to the presence of the cavity, the physical origin is any or a combination of:

- stimulated emission

- cavity lifetime
- Purcell effect

The gain spectrum for QDs typically has a gaussian lineshape. We therefore wouldn't expect a linear increase in the average lifetime from stimulated emission. The cavity lifetime (proportional to the Q factor) on the other hand shows a different trend depending on the radial mode family (see Figure 8.26). Lastly, if the increasing trend is due to the Purcell effect, the trend would not be observed for the off resonance lifetimes.

Conclusion

In conclusion, the power dependence and decay dynamics of the emission spectrum of dot-in-rods coupled to a microdisk cavity were studied. We showed that the amount of QRods coupled to the cavity is too low to start lasing. A thorough spectral deconvolution showed interesting behaviour for different radial mode families. Clear differences in the average lifetime between on and off resonance were observed, together with a linearly increasing trend with wavelength.The Purcell effect is more than likely at the origin of this behaviour. However, more measurements and analysis are necessary to provide a full understanding.

8.4 Conclusion and Perspective

We developed a fabrication process to embed colloidal QDs into a Si_3N_4 matrix and etch pillar-supported microdisks. The PL of the QDs is preserved and coupled to the microdisk, as evidenced by the spectrum showing clear WGM resonances.

We studied the microdisks using three different setups. This provides us with a good understanding of the interaction of the QDs with the cavity from spatial, spectral and temporal measurements.

The ultimate goal of making a hybrid QD-microdisk laser was not reached. Two chief reasons can be identified. The amount of QDs coupled to the microdisk in the studied samples was too low to provide sufficient gain to overcome cavity losses and the microdisk layer stack is not stable under 400 nm pump light.

The first problem is easy to solve by spincoating a more concentrated QD solution and has already been tackled in samples which are under test at the time of writing. The second problem needs more work to investigate the true reason for the instability. More than likely it is related to the adhesion problem between the low-index Si_3N_4 and the QD layer beneath it. The

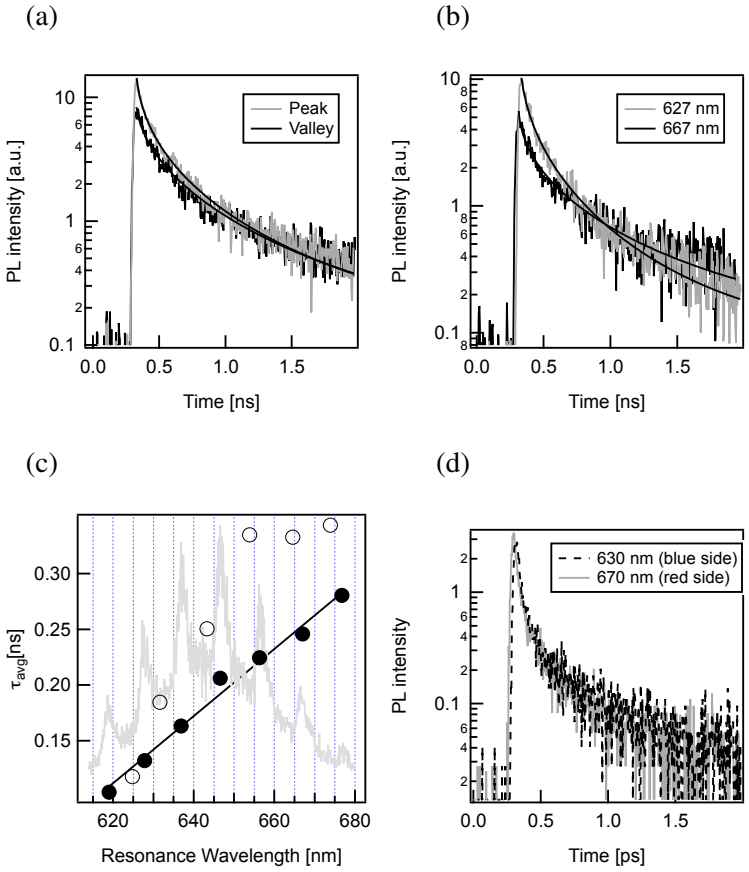

Figure 8.32: (a)The PL decay after excitation with a fs-pulsed laser is shown on resonance (grey) and off resonance (black). The decay curves are fitted using a stretched exponential function.(b)The PL decay after excitation with a fs-pulsed laser is shown at the resonance of 627 nm and 667 nm. We observe a faster decay at the blue side of the spectrum. (c) The average PL decay time for each resonance in the spectrum increases linearly with increasing wavelength (full circles). The decay times off-resonance are also plotted (open circles) and show that decay is enhanced for on-resonance wavelengths. (d) Comparison of the dynamics of the QDs on the sample substrate, *i.e.* not coupled to the microdisk at the blue and at the red side of the PL spectrum.

role of the ligands surrounding the QDs and the influence of the PECVD deposition needs to be studied further to identify the problem and ultimately solve it.

At the same time, further improvements in the etching quality and the uniformity of the QD deposition are necessary. Moreover, a new fabrication flow should be developed that allows QDs to be selectively deposited only inside the microdisk and not on the entire sample substrate. A masked anti-adhesion treatment for selective deposition could be an interesting route to reach this goal.

This work has laid the foundations for many opportunities for interesting research. The first opportunity is to achieve lasing under optical pumping using the extensive library of QDs that is available today. In the visible part of the spectrum, both pulsed and CW operation should be achievable, while in the infrared more material research is necessary to provide an adequate gain material. In parallel, efforts should be made to couple the emission to a bus waveguide and integrate it with photonic circuitry. We would like to stress here that a laser is a necessary light source for many, but definitely not all applications. In trying to solve the problems with QDs in a multi-exciton regime, it is sometimes overlooked that QDs are excellent emitters (and absorbers) in the single-exciton regime. With further engineering the cavity, high β factors can be reached using microdisks, making them an excellent, broadband light source while still providing sharp linewidths.

From a more fundamental viewpoint, the interaction of a single or ensemble of QDs with a high-Q cavity is very interesting. More research is necessary to understand the Purcell effect with these emitters and prove that the enhancement we see is indeed related to the Purcell effect. Moreover, both at low and room temperature, a few QDs coupled to a microdisk are an interesting testbed to explore the fully quantum mechanical light-matter interaction.

Lastly, the advances that have been made recently to electrically excite the QDs should be combined with the microdisk cavities. Especially the technique of field-driven electroluminescence[45] is ideally suited for our device architecture. The insulating Si_3N_4 acts as a capacitator, putting a large field over the QDs. The first steps of mask design have already been made to make electrical contacts on the top of the microdisk and on the silicon substrate. This would be the first demonstration of QD electroluminescence coupled to an optical microcavity and a major step forward in the QD and photonics research fields.

References

[1] Hoogland, S.; Sukhovatkin, V.; Howard, I.; Cauchi, S.; Levina, L.; Sargent, E. A solution-processed 1.53 mu m quantum dot laser with temperature-invariant emission wavelength. *Optics Express* **2006**, *14*, 3273–3281.

[2] Chan, Y.; Steckel, J.; Snee, P.; Caruge, J.; Hodgkiss, J.; Nocera, D.; Bawendi, M. Blue semiconductor nanocrystal laser. *Applied Physics Letters* **2005**, *86*, 073102.

[3] Le Thomas, N.; Woggon, U.; Schops, O.; Artemyev, M.; Kazes, M.; Banin, U. Cavity QED with semiconductor nanocrystals. *Nano Letters* **2006**, *6*, 557–561.

[4] Eisler, H.; Sundar, V.; Bawendi, M.; Walsh, M.; Smith, H.; Klimov, V. Color-selective semiconductor nanocrystal laser. *Applied Physics Letters* **2002**, *80*, 4614–4616.

[5] Moller, B.; Woggon, U.; Artemyev, M. Coupled-resonator optical waveguides doped with nanocrystals. *Optics Letters* **2005**, *30*, 2116–2118.

[6] Woggon, U.; Wannemacher, R.; Artemyev, M.; Möller, B.; LeThomas, N.; Anikeyev, V.; Schöps, O. Dot-in-a-dot: electronic and photonic confinement in all three dimensions. *Applied Physics B: Lasers and Optics* **2003**, *77*, 469–484.

[7] Malko, A.; Mikhailovsky, A.; Petruska, M.; Hollingsworth, J.; Htoon, H.; Bawendi, M.; Klimov, V. From amplified spontaneous emission to microring lasing using nanocrystal quantum dot solids. *Applied Physics Letters* **2002**, *81*, 1303–1305.

[8] Chan, Y.; Caruge, J.; Snee, P.; Bawendi, M. Multiexcitonic two-state lasing in a CdSe nanocrystal laser. *Applied Physics Letters* **2004**, *85*, 2460–2462.

[9] Schaefer, J.; Mondia, J. P.; Sharma, R.; Lu, Z. H.; Susha, A. S.; Rogach, A. L.; Wang, L. J. Quantum dot microdrop laser. *Nano Letters* **2008**, *8*, 1709–1712.

[10] Artemyev, M.; Woggon, U. Quantum dots in photonic dots. *Applied Physics Letters* **2000**, *76*, 1353–1355.

[11] Min, B.; Kim, S.; Okamoto, K.; Yang, L.; Scherer, A.; Atwater, H.; Vahala, K. Ultralow threshold on-chip microcavity nanocrystal quantum dot lasers. *Applied Physics Letters* **2006**, *89*, 191124.

[12] Pattantyus-Abraham, A. G.; Qiao, H.; Shan, J.; Abel, K. A.; Wang, T.-S.; van Veggel, F. C. J. M.; Young, J. F. Site-Selective Optical Coupling of PbSe Nanocrystals to Si-Based Photonic Crystal Microcavities. *Nano Letters* **2009**, *9*, 2849–2854.

[13] Fan, X.; Lonergan, M. C.; Zhang, Y.; Wang, H. Enhanced spontaneous emission from semiconductor nanocrystals embedded in whispering gallery optical microcavities. *Phys. Rev. B* **2001**, *64*, 115310.

[14] Giebink, N.; Wiederrecht, G.; Wasielewski, M. Strong exciton-photon coupling with colloidal quantum dots in a high-Q bilayer microcavity. *Applied Physics Letters* **2011**, *98*, 081103–081103.

[15] Luk, T. S.; Xiong, S.; Chow, W. W.; Miao, X.; Subramania, G.; Resnick, P. J.; Fischer, A. J.; Brinker, J. C. Anomalous enhanced emission from PbS quantum dots on a photonic-crystal microcavity. *J. Opt. Soc. Am. B* **2011**, *28*, 1365–1373.

[16] Artemyev, M.; Woggon, U.; Wannemacher, R.; Jaschinski, H.; Langbein, W. Light trapped in a photonic dot: Microspheres act as a cavity for quantum dot emission. *Nano Letters* **2001**, *1*, 309–314.

[17] Snee, P.; Chan, Y.; Nocera, D.; Bawendi, M. Whispering-gallery-mode lasing from a semiconductor nanocrystal/microsphere resonator composite. *Advanced Materials* **2005**, *17*, 1131–+.

[18] Kazes, M.; Lewis, D.; Ebenstein, Y.; Mokari, T.; Banin, U. Lasing from semiconductor quantum rods in a cylindrical microcavity. *Advanced Materials* **2002**, *14*, 317–+.

[19] Wu, Z.; Mi, Z.; Bhattacharya, P.; Zhu, T.; Xu, J. Enhanced spontaneous emission at 1.55 mu m from colloidal PbSe quantum dots in a Si photonic crystal microcavity. *Applied Physics Letters* **2007**, *90*, 171105.

[20] Zavelani-Rossi, M.; Lupo, M.; Krahne, R.; Manna, L.; Lanzani, G. Lasing in self-assembled microcavities of CdSe/CdS core/shell colloidal quantum rods. *Nanoscale* **2010**, *2*, 931–935.

[21] Tuck, B. The chemical polishing of semiconductors. *Journal of Materials Science* **1975**, *10*, 321–339.

[22] Bruno, G.; Capezzuto, P.; Madan, A. *Plasma Deposition of Amorphous Silicon-Based Materials*; Plasma-Materials Interactions; Elsevier Science, 1995.

[23] Sze, S. *Semiconductor devices: physics and technology*; John Wiley & Sons, 2008.

[24] Jansen, H.; Gardeniers, H.; de Boer, M.; Elwenspoek, M.; Fluitman, J. A survey on the reactive ion etching of silicon in microtechnology. *Journal of Micromechanics and Microengineering* **1996**, *6*, 14.

[25] Seidel, H.; Csepregi, L.; Heuberger, A.; Baumgartel, H. Anisotropic Etching of Crystalline Silicon in Alkaline Solutions. *Journal of The Electrochemical Society* **1990**, *137*, 3612–3626.

[26] Lambert, K.; Wittebrood, L.; Moreels, I.; Deresmes, D.; Grandidier, B.; Hens, Z. Langmuir-Blodgett monolayers of InP quantum dots with short chain ligands. *Journal of Colloid and Interface Science* **2006**, *300*, 597–602.

[27] Justo, Y.; Moreels, I.; Lambert, K.; Hens, Z. Langmuir-Blodgett monolayers of colloidal lead chalcogenide quantum dots: morphology and photoluminescence. *Nanotechnology* **2010**, *21*, 295606.

[28] Lambert, K.; Capek, R.; Bodnarchuk, M.; Kovalenko, M.; Van Thourhout, D.; Heiss, W.; Hens, Z. Langmuir- Schaefer Deposition of Quantum Dot Multilayers. *Langmuir* **2010**, *26*, 7732–7736.

[29] Hanrath, T.; Choi, J. J.; Smilgies, D.-M. Structure/Processing Relationships of Highly Ordered Lead Salt Nanocrystal Superlattices. *ACS Nano* **2009**, *3*, 2975–2988.

[30] Lawrence, C. The mechanics of spin coating of polymer films. *Physics of Fluids* **1988**, *31*, 2786.

[31] Pietryga, J.; Werder, D.; Williams, D.; Casson, J.; Schaller, R.; Klimov, V.; Hollingworth, J. Utilizing the Lability of Lead Selenide to Produce Heterostructured Nanocrystals with Bright, Stable Infrared Emission. *Journal of the American Chemical Society* **2008**, *130*, 4879–4885.

[32] Peter, E.; Dousse, A.; Voisin, P.; Lemaitre, A.; Martrou, D.; Cavanna, A.; Bloch, J.; Senellart, P. Highly directional radiation pattern of microdisk cavities. *Applied Physics Letters* **2007**, *91*, 151103.

[33] Oxborrow, M. How to simulate the whispering-gallery modes of dielectric microresonators in FEMLAB/COMSOL. *Proc. SPIE*, 2007.

[34] Hens, Z.; Moreels, I. Light absorption by colloidal semiconductor quantum dots. *J. Mater. Chem.* **2012**, *22*, 10406–10415.

[35] Zavelani-Rossi, M.; Lupo, M.; Tassone, F.; Manna, L.; Lanzani, G. Suppression of biexciton Auger recombination in CdSe/CdS dot/rods: role of the electronic structure in the carrier dynamics. *Nano letters* **2010**, *10*, 3142–3150.

[36] Cretí, A.; Zavelani-Rossi, M.; Lanzani, G.; Anni, M.; Manna, L.; Lomascolo, M. Role of the shell thickness in stimulated emission and photoinduced absorption in CdSe core/shell nanorods. *Phys. Rev. B* **2006**, *73*, 165410.

[37] Krahne, R.; Zavelani-Rossi, M.; Lupo, M. G.; Manna, L.; Lanzani, G. Amplified spontaneous emission from core and shell transitions in CdSe/CdS nanorods fabricated by seeded growth. *Applied Physics Letters* **2011**, *98*, 063105.

[38] Kamal, J. S.; Gomes, R.; Hens, Z.; Karvar, M.; Neyts, K.; Compernolle, S.; Vanhaecke, F. Direct determination of absorption anisotropy in colloidal quantum rods. *Phys. Rev. B* **2012**, *85*, 035126.

[39] Purcell, E. M. Proceedings of the American Physical Society. *Phys. Rev.* **1946**, *69*, 681.

[40] Kippenberg, T. Ph.D. thesis, California Institute of Technology, 2004.

[41] Pitanti, A.; Ghulinyan, M.; Navarro-Urrios, D.; Pucker, G.; Pavesi, L. Probing the spontaneous emission dynamics in Si-nanocrystals-based microdisk resonators. *Physical review letters* **2010**, *104*, 103901.

[42] Tittel, J.; Göhde, W.; Koberling, F.; Basche, T.; Kornowski, A.; Weller, H.; Eychmüller, A. Fluorescence spectroscopy on single CdS nanocrystals. *The Journal of Physical Chemistry B* **1997**, *101*, 3013–3016.

[43] Fernee, M. J.; Littleton, B. N.; Cooper, S.; Rubinsztein-Dunlop, H.; Gomez, D. E.; Mulvaney, P. Acoustic Phonon Contributions to the Emission Spectrum of Single CdSe Nanocrystals. *The Journal of Physical Chemistry C* **2008**, *112*, 1878–1884.

[44] Masia, F.; Accanto, N.; Langbein, W.; Borri, P. Spin-Flip Limited Exciton Dephasing in CdSe/ZnS Colloidal Quantum Dots. *Physical Review Letters* **2012**, *108*, 87401.

[45] Wood, V.; Panzer, M.; Caruge, J.; Halpert, J.; Bawendi, M.; Bulovic, V. Air-Stable Operation of Transparent, Colloidal Quantum Dot Based LEDs with a Unipolar Device Architecture. *Nano letters* **2009**, *10*, 24–29.

9 General Conclusion

9.1 Conclusion

Colloidal QDs are an attractive new class of materials with promising properties. First of all, the ease with which an entire wavelength range is accessible with just one material, one synthesis technique and just one parameter to adjust, the QD size, makes them highly versatile, both in fundamental physical studies as more engineering oriented applications. Secondly, their capping ligands not only provide protection to their delicate optical properties, but also yield their solubility in various solvents. This makes the embedding or processing the easy part of the road from QD synthesis over identifying the optical and electrical properties to designing and optimizing their use in LEDs, lasers, solar cells and other applications. Their short non-radiative lifetime of Auger recombination together with their small size, which requires high carrier densities, have so far hampered their succesful use in CW lasers and efficient LEDs and their application in integrated photonic circuits.

On the other hand the field of silicon photonics has significant merit in realizing very small and low loss optical components with very reproducible, low-cost and high-volume fabrication methods from the CMOS industry. The obvious drawback of the platform is the lack of direct generation of light due to silicon's indirect and silicon nitride's overly large band gap. Along with the success of passive silicon photonics came the success

of heterogeneous integration of active materials on silicon. Mature technology, using III-V bonding [1], already exist. In that sense, the combination of silicon photonics and colloidal QDs is more a testbed for the limits and properties of these new materials rather than as a direct competitor to the III-V/silicon photonics platform.

In this thesis we have aimed to take some of the key hurdles on the way to an active hybrid colloidal QD integrated photonic light source. We have extended the understanding of the hot-injection synthesis. Our simulation model shows good agreement with an experimental CdSe synthesis. We thereby proved that besides nucleation and growth, the generation of monomers from precursors is key to the dynamics of the hot injection synthesis. As the rates of nucleation and growth are limited by the generation of the monomer, this rate will determine the balance between nucleation and growth and therefore the balance between concentration and diameter at full yield. We then showed that we could use the initial precursor concentration as a strategy to tune this final QD diameter at full yield, rather than stopping the synthesis at the required size, yet before all precursors are consumed. Further comparison of the simulation and experimental synthesis taught us the role of free fatty acids in the hot injection synthesis. Careful analysis established a direct relation between the free acid concentration and the solubility of the monomers. Control over the free acid concentration therefore yields a second way of tuning the diameter at full yield. These results established two of many reaction chemistry/nanocrystal property relations and offer a more profound understanding of the hot injection synthesis method. This is needed as a tool to engineer the properties of QDs in smarter, more cost-effective and efficient way and will result in a faster turn-around time of the methodological cycle of designing a synthesis, optimizing the new material, characterizing its properties and feeding the results back into the design phase.

Furthermore, we studied a new class of infrared emitting QDs, heterostructured PbSe/CdSe dot-in-dot and ran them through in-depth optical testing. We showed that the sizing curve and the absorption oscillator strength remain unaltered by the addition of a CdSe shell to PbSe QDs. However, the change in the local dielectric environment by the CdSe shell makes the absorption coefficient at energies well above the band gap dependent on the ratio between the shell volume and the total QD volume Vshell/VQD. The spontaneous emission lifetime of highly luminescent PbSe/CdSe QDs ($QY \simeq 30-60\%$) is longer than their PbSe QD counterpart. This is caused by a lower emission oscillator strength compared to PbSe QDs. This reduction is more than likely due to an increased fine-structure splitting of the 8-fold degenerate bulk band gap because of the addition of

a CdSe shell.

With transient absorption spectroscopy we studied their intraband absorption after photoexcitation, which is forbidden in first order for bulk semiconductors, but allowed in colloidal QDs. The intraband absorption both in PbSe and PbSe/CdSe QDs contributes to the difficulty of achieving transparency and gain in these QDs, yet below the band gap, in the energy range between 1600 nm and 2200 nm, intraband absorption could be used for zero-insertion loss optical modulators.

Finally we looked at the transient absorption signal around the band gap as well. The Auger lifetime for PbSe/CdSe QDs is not prolonged by the addition of the CdSe shell. This shows that the spatial separation between the electron and hole in these heterostructured QDs is insufficient to create significant biexciton repulsion. We further explained the spectral shape of the bleaching signal using a state-filling model which was extended to include the effects of multi-exciton shifts and increased fine-structure splitting.

At last we developed, tested and simulated a platform technology for embedding QDs in silicon nitride. We explored the theory of these microdisks and investigate the coupling of the active QDs to the resonator using a QD-microdisk rate equation model. These highlight the conditions needed to achieve lasing using these QDs. The main conclusion is that pulsed lasing should be possible with the current materials, but only if a sufficient number of QDs is coupled to the cavity resonance.

We designed and optimized a fabrication flow for hybrid QD-silicon nitride photonic structures. The active microdisks were tested using several techniques. Using a spatially and spectrally resolved photoluminescence setup we were able to identify the optical modes in the microdisk and determine scattering as the main photon loss mechanism. Finally, we showed that the QDs couple very well to the whispering gallery modes of the resonators, yet that the loading conditions, the gain properties and the stability of the QD-silicon nitride stack is insufficient to sustain QD-microdisk lasing at this point.

9.2 Perspective

While some dreams and ideas in this PhD research were deemed too hopeful or unrealistic, the answers to some of the puzzles we managed to solve in this work sprouted many more new questions of their own.

Due to the dedication and hard work of a talented team, the combination of experimental synthesis with synthesis modeling has been nothing short of a success, which surely does not end with this text. The goal remains to identify all of the reaction chemistry/nanocrystal property relations and

be able to link them quantitatively to one or several parameters in the simulation model. In parallel the model itself also requires more work. The implementation could be improved and the theoretical expression for nucleation and growth could be further refined to include other unknown size-dependent effects. Furthermore, the theoretical model could be extended to include non-anisotropic growth, such as QRods and platelets. The ultimate goal is to be able to design and predict the outcome of a synthesis. Automated synthesis systems could for example allow a more optimal form of the monomer generation rate than zero, first or second order dynamics.

The study on the optical properties of PbSe/CdSe QDs was valuable. In the mean while, most properties have been confirmed in PbS/CdS QDs as well. Ongoing theoretical work also confirms the splitting of the fine-structure we observed experimentally. From a practical point of view, these heterostructured QDs are not adequate. The Auger recombination rate remains unchanged and the cation exchange induces significant size broadening. However, the lessons learned in these optical studies are bound to be valuable in the ongoing characterization of new heterostructured and differently shaped materials. The most promising route at this point is to develop and test doped colloidal QDs as they are able to offer a true four-level gain material.

Finally, a platform technology, spanning a very large possible wavelength range was developed and is ready to be used as a testbed for new materials to come out of the chemistry labs. A few problems remain, such as the fate of the ligands during silicon nitride deposition and the — probably related — issue of adhesion of the silicon nitride layer to the QDs. As a next step, integration of access waveguides to the microdisk structures should allow much easier characterization of their properties and more efficient optical pumping. Moreover, the demonstration of electrical field induced LEDs[2] using colloidal QDs should be followed up by our demonstration of electrically pumped colloidal QD microdisks, as both knowhow and technology are already present.

As a closing argument, we may have focused too much on solving the negative aspects of colloidal QD properties to see the opportunities of its positive aspects. It is by now well established that gain in colloidal QDs is very difficult to achieve, yet in the low pump regime of one exciton or less, colloidal QDs are very efficient, tunable, stable and versatile emitters. Focusing on engineering the coupling of this spontaneous emission (*i.e.* the β factor) to optical circuits could allow the fabrication of very efficient, low cost, broadband and tunable classical light sources, using colloidal QDs. As this is a key component needed in gas- and biosensors for cheap and high-volume lab-on-a-photonic-chip applications,[3] we believe that this use of

colloidal QDs together with integrated photonics provides the ideal hybrid system to sustain a bright future for both research fields.

References

[1] Roelkens, G.; Van Campenhout, J.; Brouckaert, J.; Van Thourhout, D.; Baets, R.; Romeo, P. R.; Regreny, P.; Kazmierczak, A.; Seassal, C.; Letartre, X.; Hollinger, G.; Fedeli, J. M.; Di Cioccio, L.; Lagahe-Blanchard, C. III-V/Si photonics by die to wafer bonding. *Materials Today* **2007**, *10*, 36–43.

[2] Wood, V.; Panzer, M.; Caruge, J.; Halpert, J.; Bawendi, M.; Bulovic, V. Air-Stable Operation of Transparent, Colloidal Quantum Dot Based LEDs with a Unipolar Device Architecture. *Nano letters* **2009**, *10*, 24–29.

[3] Claes, T. Ph.D. thesis, Universiteit Gent, 2012.

A

Basic Properties of Colloidal QDs

A.1 PbS

Bulk Band Gap

$$E_{g,bulk} = 0.41 \text{ eV} = 3024 \text{ nm}$$

Sizing Curve

$$E_g(d) = 0.41 + \frac{1}{0.0252d^2 + 0.283d}$$

from Moreels et al. [1]

Crystal Parameters

PbS has the rock salt crystal structure with 4 Pb and 4 S atoms per unit cell and with the lattice constant:

$$a = 0.5936 \text{ nm}$$

Dielectric Function

At 400 nm:

$$\epsilon = 4.25 + 26.4i$$

$$n = 3.96$$

$$k = 3.34$$

Well below the band gap of the QD, *i.e.* the electronic dielectric constant:

$$\epsilon_0 = 16.2$$

and the refractive index:

$$n_0 = 4$$

For the exact spectral dependence, we refer to Moreels[2].

Molar Extinction Coefficient

At 400 nm in C_2Cl_4:

$$\epsilon_{400\text{ nm}} = 0.0233 d^3 \text{ cm}^{-1}/\mu\text{m}$$

At the band gap, integrated — on an energy scale — over the first exciton transition in C_2Cl_4:

$$\epsilon_{\text{gap}} = 1.8 d^{1.3} \text{ cm}^{-1}\text{meV}/\mu\text{m}$$

Absorption Coefficient

At 400 nm, in C_2Cl_4:

$$\mu_{400\text{ nm}} = 1.71 \times 10^5 \text{ cm}^{-1}$$

Local Field Factor

At the band gap, in C_2Cl_4:

$$|f_{LF}|^2 = 0.0725$$

Oscillator Strength of the Band Gap Transition

$$f_{if} = 2.23 d$$

A.2 PbSe

Bulk Band Gap

$$E_{g,bulk} = 0.278 \text{ eV} = 4460 \text{ nm}$$

Sizing Curve

$$E_g(d) = 0.278 + \frac{1}{0.0156d^2 + 0.209d + 0.445}$$

[1]

Crystal Parameters

PbSe has the rock salt crystal structure with 4 Pb and 4 Se atoms per unit cell and with the lattice constant:

$$a = 0.61255 \text{ nm}$$

Dielectric Function

At 400 nm:

$$\epsilon = 10.66 + 20.53i$$

$$n = 2.50$$

$$k = 4.11$$

Well below the band gap of the QD, *i.e.* the electronic dielectric constant:

$$\epsilon_0 = 20.8$$

and the refractive index:

$$n_0 = 4.6$$

For the exact spectral dependence, we refer to Moreels[2].

Molar Extinction Coefficient

At 400 nm in C_2Cl_4:

$$\epsilon_{400\text{ nm}} = 0.0311d^3 \text{ cm}^{-1}/\mu\text{m}$$

At the band gap, integrated — on an energy scale — over the first exciton transition in C_2Cl_4:

$$\epsilon_{\text{gap}} = 1.8d^{1.3} \text{ cm}^{-1}\text{meV}/\mu\text{m}$$

Absorption Coefficient

At 400 nm, in C_2Cl_4:

$$\mu_{400\text{ nm}} = 2.273 \times 10^5 \text{ cm}^{-1}$$

Local Field Factor

At the band gap, in C_2Cl_4:

$$|f_{LF}|^2 = 0.0446$$

Oscillator Strength of the Band Gap Transition

$$f_{if} = 3.35d$$

A.3 PbTe

Bulk Band Gap

$$E_{g,bulk} = 0.32 \text{ eV} = 3875 \text{ nm}$$

Sizing Curve

$$E_g(d) = 0.32 + \frac{1}{0.0341d^2 + 1.03}$$

from Murphy et al. [3] and own data.

Crystal Parameters

PbTe has the rock salt crystal structure with 4 Pb and 4 Te atoms per unit cell and with the lattice constant:

$$a = 0.64606 \text{ nm}$$

Dielectric Function

At 400 nm:

$$\epsilon = -8.891 + 9.398i$$

$$n = 1.422$$

$$k = 3.304$$

Well below the band gap of the QD, *i.e.* the electronic dielectric constant:

$$\epsilon_0 = 33.3$$

and the refractive index:

$$n_0 = 4.6$$

For the exact spectral dependence, we refer to Moreels [2].

Molar Extinction Coefficient

At 400 nm in C_2Cl_4:

$$\epsilon_{400\text{ nm}} = 0.0616 d^3 \text{ cm}^{-1}/\mu\text{m}$$

Absorption Coefficient

At 400 nm, in C_2Cl_4:

$$\mu_{400\text{ nm}} = 4.49 \times 10^5 \text{ cm}^{-1}$$

A.4 CdS

Bulk Band Gap

$$E_{g,bulk} = 2.41 \text{ eV} = 514.46 \text{ nm}$$

Crystal Parameters

CdS has the zinc blende crystal structure with 4 Cd and 4 S atoms per unit cell and with the lattice constant:

$$a = 0.5833 \text{ nm}$$

Note that it can also have the hexagonal wurtzite structure.

A.5 CdSe

Bulk Band Gap

$$E_{g,bulk} = 1.74 \text{ eV} = 712.56 \text{ nm}$$

Crystal Parameters

CdSe has the zinc blende crystal structure with 4 Cd and 4 Se atoms per unit cell and with the lattice constant:

$$a = 0.6077 \text{ nm}$$

Note that it can also have the hexagonal wurtzite structure.

Dielectric Function

Well below the band gap of the QD, *i.e.* the electronic dielectric constant:

$$\epsilon_0 = 7.4529$$

and the refractive index:

$$n_0 = 2.73$$

For the spectral dependence of bulk CdSe, we refer to Bass et al. [4].

A.6 CdTe

Bulk Band Gap

$$E_{g,bulk} = 1.5 \text{ eV} = 826.57 \text{ nm}$$

Crystal Parameters

CdTe has the zinc blende crystal structure with 4 Cd and 4 Te atoms per unit cell and with the lattice constant:

$$a = 0.64805 \text{ nm}$$

Note that it can also have the hexagonal wurtzite structure.

References

[1] Moreels, I.; Lambert, K.; Smeets, D.; De Muynck, D.; Nollet, T.; Martins, J. C.; Vanhaecke, F.; Vantomme, A.; Delerue, C.; Allan, G.; Hens, Z. Size-Dependent Optical Properties of Colloidal PbS Quantum Dots. *Acs Nano* **2009**, *3*, 3023–3030.

[2] Moreels, I. Ph.D. thesis, Universiteit Gent, 2009.

[3] Murphy, J.; Beard, M.; Norman, A.; Ahrenkiel, S.; Johnson, J.; Yu, P.; Micic, O.; Ellingson, R.; Nozik, A. PbTe colloidal nanocrystals: Synthesis, characterization, and multiple exciton generation. *Journal of the American Chemical Society* **2006**, *128*, 3241–3247.

[4] Bass, M.; DeCusatis, C.; Li, G.; Mahajan, V.; Enoch, J.; Van Stryland, E. *Handbook of Optics: Optical properties of materials, nonlinear optics, quantum optics*; McGraw-Hill Professional, 2009; Vol. 4.